



**AALBORG UNIVERSITY**  
DENMARK

**Aalborg Universitet**

## **Controller Development for a Separate Meter-In Separate Meter-Out Fluid Power Valve for Mobile Applications**

Nielsen, Brian

*Publication date:*  
2005

*Document Version*  
Early version, also known as pre-print

[Link to publication from Aalborg University](#)

*Citation for published version (APA):*  
Nielsen, B. (2005). *Controller Development for a Separate Meter-In Separate Meter-Out Fluid Power Valve for Mobile Applications*. Institut for Energiteknik, Aalborg Universitet.

### **General rights**

Copyright and moral rights for the publications made accessible in the public portal are retained by the authors and/or other copyright owners and it is a condition of accessing publications that users recognise and abide by the legal requirements associated with these rights.

- Users may download and print one copy of any publication from the public portal for the purpose of private study or research.
- You may not further distribute the material or use it for any profit-making activity or commercial gain
- You may freely distribute the URL identifying the publication in the public portal -

### **Take down policy**

If you believe that this document breaches copyright please contact us at [vbn@aub.aau.dk](mailto:vbn@aub.aau.dk) providing details, and we will remove access to the work immediately and investigate your claim.

# Controller Development for a Separate Meter-In Separate Meter-Out Fluid Power Valve for Mobile Applications

by

Brian Kongsgaard Nielsen

Dissertation submitted to the Faculty of Engineering & Science at Aalborg University in  
partial fulfillment of the requirements for the degree of Doctor of Philosophy in  
Mechanical Engineering

Aalborg University, Denmark  
Institute of Energy Technology  
December 2005

Aalborg University  
Institute of Energy Technology  
Pontoppidanstræde 101  
DK-9220 Aalborg East

Copyright ©Brian Kongsgaard Nielsen, 2005

# Preface

This dissertation has been submitted to the Faculty of Engineering and Science at Aalborg University in partial fulfilment of the requirements for the Ph.D. degree in Mechanical Engineering. The work has been carried out in a commercial company, which is hereafter named 'The Company', and at the Institute of Energy Technology at Aalborg University. The work has been partially funded by the Danish Ministry of Science Technology and Innovation under the Industrial PhD initiative record no. 2002-503/0080-82. Without this financial support the work would not have been possible.

I would like to thank my colleagues at *The Company* and in particular the project team members for their enthusiastic support and suggestions. Thanks goes also to my supervisors Director Leif Børge Tandrup and Professor Torben Ole Andersen for their support, advice, comments and suggestions. Thanks goes in particular to my family for their patience. A special thanks goes to my wife, Lene, for her invaluable support and patience.

Nordborg, December 2005

Brian Kongsgaard Nielsen



# Abstract

In most mobile vehicles which are used within construction, agriculture, material handling, forestry, garbage handling etc. a fluid power system is used for power transport and power distribution. The transported/distributed power is usually generated by a diesel engine or from an electrical battery. The largest advantages of the fluid power system are its high energy density and its robustness. Currently there is no cost effective and robust alternative to using a fluid power system for the power transport in the kilowatt range necessary to establishing a linear motion of tools in mobile machinery. For a rotary motion electrical motors controlled by using power electronics is a competing technology because of their high energy efficiency. Additionally, the energy density of electrical devices is still increasing.

In fluid power systems where more consumers (cylinders or motors) are supplied by a single pump the fluid is distributed through valves. A valve works by controlling a fluid stream through the valve by varying the opening of an orifice. The disadvantage by this is that when controlling the fluid flow rate a pressure drop is created across the orifice. This results in a throttle loss equal to the controlled flow rate times the pressure drop across the orifice. By a constant flow rate the best energy efficiency is therefore obtained by keeping the pressure drop across the orifice as low as possible. More orifices are commonly included in a single valve.

A specific type of valve, which is commonly used in many types of mobile applications, is a 4-way proportional valve. In this type of valve two fluid streams are controlled: One fluid stream from a pump to a fluid consumer and one fluid stream from the fluid consumer to a fluid reservoir. In a 4-way proportional valve it is necessary to use a separate control of the two fluid streams to minimise the throttling losses. The purpose of the research documented in this dissertation is to investigate how a 4-way proportional valve may be build to fulfil the increasing demands with regard to energy efficiency and functionality. And to develop controllers for a valve prototype whereby the two mentioned fluid streams may be controlled separately.

First an introduction to mobile fluid power systems is given. It is explained that the future trend within mobile fluid power systems goes towards integration of sensors and microprocessors into the components. The particular research area is motivated by the use of two examples. They explain how a separate control of the meter-in and the meter-out flow of proportional valves, together with integration of sensors, may minimise throttling losses and give increased functionality of the fluid power system.

## VI

Next the hydraulic functionality, which is anticipated to be integrated into proportional valves in the future, and additionally also influences on the layout of a future valve, is described. Existing valve concepts are evaluated with regard to their functionality, compared to the number of degrees of freedom which must be controlled. New valve concepts are also suggested and evaluated. A single valve concept is selected for further study.

A parametrised model of the selected valve concept is derived and verified experimentally by means of a prototype valve. A linearised model, which is to be used in the subsequent development of controllers, is derived from the verified non-linear. The demands for compensation of varying load pressure across the valve is examined by measuring the static performance of state of the art valves. Next the dynamical demands for valve are examined qualitatively.

Controllers for the individual control of the spools of the prototype valve are designed. The design involves two different methods for pilot operation of the spools. The pilot control method by which the best performance is at first obtained, compared to the static demands put forward, is rejected. This is because it has a low relative stability due to design restrictions. Robust controllers for the valve using the remaining pilot control method are developed. The robustness is evaluated by simulations and afterwards the controllers are tested experimentally.

A model of a hydraulic actuator system with a flexible load structure is derived. For the establishment of the equivalent parameters for the model, basis is taking in a real life loader crane. Subsequently, the multivariable interactions of the actuator system are analysed by means of a linearised model. Two controllers based on separate meter-in separate meter-out are developed and subsequently tested by using the non-linear simulation models of both the valve and the loader crane.

The research documented in this dissertation has contributed to the identification of valve concepts which are suitable as a platform for future proportional valves. It has contributed to the development of a parametrised model of a pilot operated spool valve, which may be used by engineers in design work involving spool valves. Additionally, by the research different controllers for the control of a pilot operated spool valve have been developed and tested. Because pilot operation of spools is generic in fluid power systems, it is anticipated that by a modification of parameters the controllers may also be used for the control of other fluid power components. Finally, the research has contributed with two new methods whereby a decoupled control of the velocity and the pressure level of a hydraulic actuator may be obtained.

# Resumé

I de fleste køretøjer, der anvendes indenfor anlægsarbejde, landbrug, godshåndtering, skovbrug, affaldshåndtering m.m., benyttes et hydrauliksystem til transport og distribuering af effekten, der som regel enten leveres af en dieselmotor eller fra et elektrisk batteri. De største fordele ved et hydrauliksystem er systemets høje energitæthed og systemets robusthed. Der er p.t. ikke noget kosteffektivt og robust alternativ til at anvende et hydrauliksystem til effekttransporten på kilo-watt niveau, som er nødvendig for at tilvejebringe en lineær bevægelse af redskaber på mobile køretøjer. For roterende bevægelse er elektriske motorer styret vha. effektelektronik en konkurrerende teknologi pga. høj energieffektivitet, og energitætheden af elektriske systemer bliver stadig bedre.

I hydrauliske systemer, hvor flere forbrugere (cylindre eller motorer) forsynes af en enkelt pumpe, distribueres det hydrauliske trykmedie til forbrugerne vha. ventiler. En ventil fungerer ved, at en fluidstrøm gennem ventilen kan reguleres ved at variere åbningen af en blænde. Ulempen ved dette er, at reguleringen af fluidstrømmen per tid skaber et trykfald over blænden. Dette resulterer i et drøvletab, der er lig den regulerede fluidmængde per tid gange trykfaldet over blænden. For en konstant fluidmængde per tid opnås den bedste energieffektivitet derfor ved, at trykfaldet over blænden holdes så lavt som muligt. Ventiler inkluderer typisk flere blænder.

En specifik ventiltipe, der anvendes generelt i mange typer af mobile applikationer, er en 4-vejs proportionalventil. I en sådan ventil reguleres to fluidstrømme: Et fremløb fra pumpen til den hydrauliske forbruger og et returløb fra den hydrauliske forbruger til et reservoir indeholdende det hydrauliske trykmedie. I en 4-vejs proportionalventil er det nødvendigt, at benytte en separat regulering af de to fluidstrømme for at minimere drøvletabet. Formålet med forskningsprojektet, der er dokumenteret i denne afhandling, er at undersøge, hvordan en 4-vejs proportionalventil med separat regulering af de to fluidstrømme kan opbygges for at imødekomme stigende krav med hensyn til energieffektivitet og funktionalitet; samt at designe regulatorer til en ventilprototype, der er opbygget med mulighed for separat regulering af de to nævnte fluidstrømme.

Først gives en introduktion til mobilhydrauliske systemer, og der redegøres for den fremtidige udviklingstendens indenfor mobilhydraulik, der går imod en større integration af sensorer og mikroprocessorer i de hydrauliske komponenter. Ved hjælp af to eksempler forklares det som motivation for det pågældende forskningsområde, hvordan separat styrbare fremløb og returløb i proportionalventiler sammen med integration af sensorer kan minimere drøvletab samt tilføre øget funktionalitet til det hydrauliske system.



## VIII

Dernæst beskrives de hydrauliske funktioner, der forventes integreret i proportionalventiler i fremtiden, og som samtidigt har indflydelse på, hvordan en given ventiltopologi udformes mekanisk. Eksisterende ventiltopologier evalueres, mht. funktionaliteten i forhold til antallet af mekaniske frihedsgrader der skal styres. Nye ventiltopologier foreslås og evalueres også, og en enkelt ventiltopologi udvælges til videre studie.

En parametriseret model af den udvalgte ventiltopologi opbygges og verificeres eksperimentelt vha. en ventilprototype. På baggrund af den verificerede model udledes en lineiriseret model, som skal anvendes til det efterfølgende design af regulatorer. Kravene til kompensering af varierende lasttryk over ventilen undersøges ved hjælp af eksperimentel undersøgelse af eksisterende ventilers statiske ydelse mht. lastkompensering. Dernæst undersøges de dynamiske krav til ventilen kvalitativt.

Regulatorer til individuel styring af prototypeventilens to ventilglidere designes indebærende to forskellige metoder til pilotstyring af ventilgliderne. Den metode, der umiddelbart giver den bedste ydelse i forhold til de opstillede statiske krav, har pga. af designrestriktioner en lav relativ stabilitet og forkastes. Robuste regulatorer til den tilbageværende pilotstyringsmetode udvikles efterfølgende. Robustheden af regulatorerne undersøges vha. simulering, og efterfølgende afprøves regulatorerne eksperimentelt.

En model af et hydraulisk reguleringsystem med fleksibel mekanisk laststruktur udledes. For tilvejebringelse af systemets ækvivalentparametre tages der udgangspunkt i en aktuel lastbilkran. I det efterfølgende analyseres de multivariable koblinger i det hydrauliske reguleringsystem vha. en lineiriseret model. To regulatorer baseret på separat styring af fluidstrømmene til og fra cylinderen der aktiverer det hydrauliske reguleringsystem udvikles, hvorefter de udviklede regulatorer afprøves vha. simuleringsmodeller af ventil og lastbilkran.

Forskningen dokumenteret i denne afhandling har bidraget til identifikation af ventiltopologier, der er egnede som platform til fremtidens proportionalventil. Den har bidraget til udviklingen af en parameteriseret model af en pilotstyret gliderventil, der kan anvendes af ingeniører i designarbejde, som involverer gliderventiler. Endvidere er der gennem forskningen udviklet og afprøvet forskellige regulatorer til styring af en pilotstyret gliderventil. Da pilotstyring af glidere er generisk for hydrauliske systemer, forventes det, at regulatorerne ved modifikation af parametre kan anvendes til styring af andre hydrauliske komponenter også. Endelig har forskningen bidraget med to nye metoder, hvormed der kan opnås en afkoblet styring af en hydraulisk cylinders eller motors hastighed og trykniveau.

# Contents

<b>1</b>	<b>Introduction</b>	<b>1</b>
1.1	Introduction to mobile fluid power systems and load sensing . . . . .	1
1.1.1	Pump configurations for working hydraulics . . . . .	2
1.1.2	Closed circuit transmission . . . . .	5
1.1.3	Load sensing proportional valves . . . . .	6
1.2	Future trends in mobile fluid power . . . . .	9
1.3	Motivating examples for using programmable separate metering valves . .	11
1.3.1	Minimising throttle losses by combined pump and valve control . .	12
1.3.2	Transmission by combined open circuit pump and valve control . .	13
1.4	Demarcation of research and outline of thesis . . . . .	14
1.5	Main results of this work . . . . .	16
1.6	Reading instructions . . . . .	17
<b>2</b>	<b>Separate meter-in separate meter-out valve concepts</b>	<b>19</b>
2.1	Criteria for selection of valve concept . . . . .	20
2.2	Hydraulic functionality . . . . .	21
2.3	State of the art separate meter-in separate meter-out valve concepts . . .	26
2.4	New separate meter-in separate meter-out valve concepts . . . . .	30
2.5	Actuation methods . . . . .	33
2.6	Summary and conclusion . . . . .	36
<b>3</b>	<b>Mathematical models of separate meter-in separate meter-out valve</b>	<b>39</b>
3.1	State of the art - Modelling of spool valves . . . . .	39
3.2	Pilot and main spool interaction . . . . .	40
3.3	Non-linear model description . . . . .	42
3.3.1	Non-linear flow equation . . . . .	43
3.3.2	Pilot valve model . . . . .	45
3.3.3	Main valve model . . . . .	49
3.3.4	Effective bulk modulus . . . . .	51
3.4	Prototype of spool valve . . . . .	51
3.5	Verification of non-linear model . . . . .	53
3.5.1	Orifice parameters . . . . .	53
3.5.2	Verification of orifice leakage model for large radial clearances . .	54
3.5.3	Verification of orifice model for round fluid ports . . . . .	55
3.5.4	Verification of hysteresis model . . . . .	57
3.5.5	Verification of flow force model associated with main spool . . . .	58
3.5.6	Verification of combined dynamic model of pilot valve . . . . .	59

3.5.7	Discussion on model verification . . . . .	63
3.6	Linear model descriptions . . . . .	63
3.6.1	Valve with pressure control pilot . . . . .	65
3.6.2	Valve with flow control pilot . . . . .	69
3.6.3	Disturbance interaction between pilot circuit and main circuit . .	70
3.7	Summary and conclusion . . . . .	75
<b>4</b>	<b>Electrohydraulic pressure compensation</b>	<b>77</b>
4.1	Introduction to electrohydraulic pressure compensation . . . . .	78
4.2	Requirements for flow controller . . . . .	79
4.2.1	Steady state accuracy . . . . .	80
4.2.2	Dynamic flow control requirements . . . . .	83
4.3	Preliminary controller design for valve with pressure control pilot . . . .	85
4.3.1	Absolute stability of pressure control pilot valve . . . . .	85
4.3.2	Controller design . . . . .	95
4.4	Preliminary controller design for valve with flow control pilot . . . . .	98
4.5	Performance specification and analysis in the frequency domain . . . . .	102
4.5.1	Disturbance rejection of SISO plant . . . . .	104
4.5.2	Minimum bandwidth due to RHP-poles . . . . .	105
4.6	Performance demands for closed loop position controller . . . . .	106
4.6.1	Decoupling of dead-zone in pilot valve . . . . .	107
4.6.2	Decoupling of pilot drain pressure disturbances . . . . .	109
4.6.3	Bandwidth requirements for negative damping of main spool . . .	111
4.6.4	Summary of performance demands . . . . .	111
4.7	Improved robust controller designs . . . . .	111
4.7.1	State of the art and choice of controller types . . . . .	112
4.7.2	Gain scheduling Proportional-Integral-Lead-Feedforward (G-PILF) controller . . . . .	113
4.7.3	Robust 2 d.o.f. $\mathcal{H}_\infty$ (R2H) controller . . . . .	116
4.7.4	Frequency shaping Sliding Mode (F-SM) controller . . . . .	122
4.7.5	Modified Frequency shaping Sliding Mode (MF-SM) controller . .	130
4.7.6	Sliding Mode controller with Prefilter (SM-P) . . . . .	131
4.8	Robustness of controllers . . . . .	134
4.8.1	Robustness to disturbances . . . . .	135
4.8.2	Robustness to parameter variations . . . . .	139
4.9	Experimental results . . . . .	141
4.10	Summary and conclusion . . . . .	145
<b>5</b>	<b>Generic model of hydraulic application with flexible load structure</b>	<b>147</b>
5.1	Presentation of selected application . . . . .	147
5.2	Models of main lift axis and base rotational axis . . . . .	149
5.2.1	Equivalent parameters for main lift axis . . . . .	150
5.2.2	Equivalent parameters for base rotational axis . . . . .	154
5.3	Summary and conclusion . . . . .	155
<b>6</b>	<b>Multivariable pressure/velocity control</b>	<b>157</b>
6.1	State of the art - Separate metering control . . . . .	157

6.2	Introduction to the multivariable control problem . . . . .	158
6.3	Tools for decentralised controller design . . . . .	162
6.3.1	Relative gain array . . . . .	162
6.3.2	Structured singular value interaction measure . . . . .	163
6.4	Linear models for controller development . . . . .	164
6.4.1	Linear model representation of hydraulic actuator system . . . . .	164
6.4.2	Linear valve dynamics . . . . .	166
6.5	Decentralised pressure/velocity control structures . . . . .	166
6.5.1	Plant interactions . . . . .	167
6.5.2	Pseudo SISO control strategy for meter-in . . . . .	169
6.5.3	Pseudo SISO control strategy for meter-out . . . . .	176
6.5.4	Output selecting pressure control strategy for meter-out . . . . .	177
6.5.5	Simulation results . . . . .	182
6.6	Summary and conclusion . . . . .	190
<b>7</b>	<b>Conclusion and recommendations for further work</b>	<b>193</b>
7.1	Summary of work . . . . .	193
7.2	Contributions . . . . .	194
7.3	Recommendations for further work . . . . .	195
<b>A</b>	<b>Parameter values</b>	<b>197</b>
A.1	Parameters associated with chapter 3 . . . . .	197
A.2	Parameters used in chapter 4 . . . . .	199
A.3	Parameters used in chapter 5 . . . . .	202
A.4	Parameters used in chapter 6 . . . . .	202
<b>B</b>	<b>Orifice area equations</b>	<b>205</b>
B.1	Rectangular fluid port . . . . .	205
B.2	Circular fluid port . . . . .	205
<b>C</b>	<b>Derivation of flow and pressure gains</b>	<b>207</b>
C.1	Rectangular fluid port . . . . .	208
C.2	Circular fluid port . . . . .	208
<b>D</b>	<b>Selected operating points for valve model linearisation</b>	<b>211</b>
<b>E</b>	<b>Development and verification of loader crane model</b>	<b>213</b>
E.1	Introduction to the modelled system . . . . .	214
E.2	Model of hydraulic subsystem . . . . .	216
E.2.1	Hydraulic cylinder model . . . . .	216
E.2.2	Model of flow resistances in jib extension cylinders . . . . .	217
E.2.3	Over centre valve model . . . . .	219
E.3	Model of mechanical subsystem . . . . .	220
E.3.1	Model of structural flexibility . . . . .	220
E.3.2	Coupling between flexible, rigid and hydraulic models . . . . .	222
E.3.3	Model of prismatic joint friction . . . . .	223
E.4	Model verification . . . . .	224

F Publications	227
Bibliography	228

# Nomenclature

## Chapter 1

$\eta_{hm}$	Hydro-mechanical efficiency of pump
$\eta_t$	Total efficiency of pump
$D_r$	Rated displacement of the pump per revolution
$n$	Engine rpm
$P$	Power
$p_0$	LS pressure margin
$p_{ts}$	Pressure required by load sensing system
$p_{max}$	Maximum pump pressure
$p_p$	Pump pressure
$q_{ts}$	Flow rate required by load sensing system
$q_{max}$	Maximum pump flow

## Chapter 3

$\beta_a$	Bulk modulus of air
$\beta_e(\cdot)$	Effective bulk modulus
$\beta_f$	Bulk modulus of fluid
$\beta_h$	Bulk modulus of hose
$\Delta p$	Pressure drop
$\delta x_{m0}$	Maximum relative main spool displacement
$\delta x_m$	Relative main spool displacement
$\delta x_{p0}$	Maximum relative pilot spool displacement
$\delta x_p$	Relative pilot spool displacement
$\Delta_a$	Overlap between P-port (T-port) and A-port of main spool
$\Delta_b$	Overlap between P-port (T-port) and B-port of main spool
$\Delta_{DZ}$	Total length to dead-zone due to port lap on pilot spool
$\Delta_{pa}$	Overlap length between P-port and A-port on pilot spool
$\Delta_{pb}$	Overlap length between P-port and B-port on pilot spool
$\delta_q$	Dimensionless factor
$\Delta_{ta}$	Underlap length between A-port and T-port on pilot spool
$\Delta_{tb}$	Underlap length between B-port and T-port on pilot spool
$\delta_{vc}$	Radial coil clearance
$\epsilon_{rm}$	Eccentricity of main spool in housing
$\epsilon_{rp}$	Eccentricity of pilot spool in housing
$\epsilon_r$	Eccentricity of spool in housing
$\Gamma$	Propagation constant associated with fluid line
$\kappa$	Polytropic exponent/adiabatic exponent
$\lambda_q$	Flow number
$\mu$	Dynamic viscosity of fluid

$\nu$	Kinematic viscosity of fluid
$\rho$	Mass density of fluid
$\theta_q$	Fluid jet angle
$A_m$	Main spool end face area
$A_o(\cdot)$	Orifice opening area
$A_p$	Pressure feedback area associated with feedback pins in pilot spool
$A_{vc}$	End face area of voice coil
$C^1$	Fluid line capacitance per unit length
$C_d$	Orifice discharge coefficient
$C_{rm}$	Radial clearance between the housing and the main spool
$C_{rp}$	Radial clearance between housing and pilot spool
$C_r$	Radial clearance between spool and housing
$C_{vc}$	Friction factor for laminar flow past voice coil
$d$	Spool diameter
$d_h(\cdot)$	Hydraulic diameter
$d_m$	Main spool diameter
$d_p$	Pilot spool diameter
$D_{vc}$	Outer coil diameter
$d_{vc}$	Inner coil diameter
$f_a$	Actuator force input
$f_{cm_0}$	Magnitude of stiction force associated with main spool
$f_{cm_1}$	Magnitude of Coulomb friction force on main spool at non-zero velocity
$f_{cm}$	Coulomb friction force associated with main spool
$f_{cp_0}$	Magnitude of stiction force associated with pilot spool
$f_{cp_1}$	Magnitude of Coulomb friction force on pilot spool at non-zero velocity
$f_{cp}$	Coulomb friction force on pilot spool
$f_{fm}$	Static flow force + dynamic flow force due to main pressure gradients
$f_{fp}$	Static flow force + dynamic flow force due to pilot pressure gradients
$f_{pp}$	Pressure feedback force
$f_{sm_0}$	Spring prestress force associated with main spool
$f_{sm}$	Spring force associated with main spool
$f_{sp_0}$	Spring prestress force associated with pilot spool
$f_{sp}$	Spring force associated with pilot spool
$f_{vc}$	Viscous damping due to voice coil
$f_{vm}$	Viscous friction force + dynamic flow force associated with main spool velocity
$f_{vp}$	Viscous friction force + dynamic flow force associated with pilot spool velocity
$k_p$	Pressure gain of orifice
$k_q$	Flow gain of orifice
$k_{sm}$	Spring constant associated with main spool
$k_{sp}$	Spring constant associated with pilot spool
$k_{vc}$	Viscous damping length coefficient associated with coil
$L^1$	Fluid line inductance per unit length
$L_1$	Length of pilot spool land
$L_2$	Length of pilot spool land
$L_3$	Length of main spool land
$L_4$	Maximum overlap length of main spool land
$L_5$	Length of pilot fluid leakage channel past main spool

$L_d$	Damping length of dynamic flow force
$L_h$	Length of fluid line/hose
$L_{vc}$	Length of voice coil
$m_m$	Main spool mass
$m_p$	Pilot spool + voice coil mass
$p$	Pressure
$p_{a_0}$	Atmospheric pressure
$p_a$	A port pressure
$p_b$	B port pressure
$p_{pa}$	Pressure in pilot chamber A
$p_{pb}$	Pressure in pilot chamber B
$p_{pp}$	Pilot supply pressure
$p_{pt}$	Pilot drain pressure
$p_p$	Main valve supply pressure
$q$	Flow rate
$q_{ac}$	Flow to pilot chamber A
$q_{bc}$	Flow to pilot chamber B
$R^1$	Fluid line resistance per unit length
$Re$	Reynolds number
$Re_t$	Transition Reynolds number
$s(i)$	Coefficient which is either 1 or -1
$V_{a_0}$	Volume percentage of air in fluid at atmospheric pressure
$V_a$	Volume percentage of air in fluid
$V_{c0}$	Main spool control chamber volumes for $x_m = 0$
$V_h$	Hose volume
$V_q$	Average flow velocity through orifice
$V_t$	Total volume of fluid + hose + air
$x_l$	Axial orifice opening length
$x_m$	Main spool position
$x_p$	Pilot spool position
$x_t$	Axial orifice opening at transition to turbulent flow
$Z_c$	Characteristic impedance of fluid line

**Chapter 4 (for model parameters see also nomenclature for chapter 3)**

$\Delta$	Complex perturbation
$\pm\Delta_0$	Assumed positions of pilot spool where drain ports close.
$\tau_d$	Time constant.
$\tau_f$	Time constant.
$k_v(t)$	Time varying flow gain of pilot spool.
$S$	Sensitivity function
$T$	Complementary sensitivity function
$W_m$	Multiplicative weight for uncertainty
$W_p$	Performance weight
$W_u$	Performance weight

**Chapter 5**

$\alpha$	Differential area coefficient of actuator $0 < \alpha \leq 1$
$\alpha_b$	Base rotation angle in global coordinates
$\alpha_m$	Main boom rotation angle in global coordinates



$\beta_e$	Effective bulk modulus
$\zeta_l$	Damping coefficient of mechanical structure
$A$	Largest actuator area
$A_j$	Piston area of jib actuator
$c_a$	Viscous damping associated with actuator
$c_l(\cdot)$	Equivalent damping coefficient of load structure
$f_e$	External force applied onto equivalent load mass
$f_l$	Load force on actuator
$J_O$	Mass moment of inertia with respect to point $O$
$k_l(\cdot)$	Equivalent spring coefficient of load structure
$k_{\tau_0}$	Torsional spring stiffness as a function of jib length
$k_{\tau_1}$	Torsional spring stiffness for shortest jib length
$k_\tau$	Torsional spring stiffness around main rotational axis
$L$	Length of main boom + jib
$L_c$	Total stroke length of base rotation cylinder
$L_\tau$	Moment arm of attachment point of jib actuator
$m_a$	Movable mass of actuator
$m_p$	Lumped mass of payload
$m_s$	Lumped mass of jib
$p_i$	Pressure in the $i$ th actuator chamber
$q$	Flow into the $i$ th actuator chamber
$V_{is}$	Static volume of the $i$ th actuator chamber
$V_j$	Compressed fluid volume of jib actuator
$x_a$	Actuator position
$x_l$	Load position

**Appendix B and C (see also nomenclature for chapter 3)**

$d_g$	Metering notch diameter
$h_g$	Length of circular metering notch
$N_g$	Number of notches

# Chapter 1

## Introduction

### Contents

---

1.1	Introduction to mobile fluid power systems and load sensing	1
1.2	Future trends in mobile fluid power . . . . .	9
1.3	Motivating examples for using programmable separate metering valves . . . . .	11
1.4	Demarcation of research and outline of thesis . . . . .	14
1.5	Main results of this work . . . . .	16
1.6	Reading instructions . . . . .	17

---

This thesis is dealing with controller development for a separate meter-in separate meter-out valve for the control of hydraulic actuators for mobile applications. A separate meter-in separate meter-out valve is characterised by having at least two separately controllable orifices. These orifices are connected to each work port of a hydraulic actuator being either a cylinder or a hydraulic motor. An introduction to the subject is given in this chapter where a description of what has initiated this research is given, and the use of flexible programmable separate meter-in separate meter-out valves is motivated.

### 1.1 Introduction to mobile fluid power systems and load sensing

Fluid power systems in mobile applications are characterised by the fact that they are controlled directly by human interaction with only a few semi-automated working cycles. Commonly the operator controls the movement of a hydraulic actuator by operating a control valve or a pump. The hydraulic actuator is characterised by carrying out a rotational or linear motion. Indirectly the operator controls the movement of a tool which is mechanically connected to the hydraulic actuator through a kinematic linkage. Such a tool could be the bucket of a wheel loader, the boom of a loader crane, the basket of a manlift or the caterpillar tracks of an excavator, there are numerous examples.

Due to the operator being in the loop of the velocity control system, the velocity of the tool need not be proportional to the velocity of the hydraulic actuator as long as the movement is repeatable for a given operator input. The operator acts as a feedback controller and compensates for the non-linear transmission ratio. That is, as long as the transmission ratio between the movement of the hydraulic actuator and the tool is not too non-linear. Due to this compensation by the operator it is adequate that the force (torque) or the velocity of the piston (shaft) of the hydraulic actuator may be controlled proportionally to the operator input.

The load applied onto the piston (shaft) of the hydraulic actuator changes as a function of the external forces or torques on the tool. The load also changes as a function of piston (shaft) position if the kinematic linkage connecting the tool to the hydraulic actuator comprises a non-linear transmission ratio between the tool and the actuator. Simplified, the direct cause for the load change on the hydraulic actuator is the working cycle of the machine which is decided by the operator. This working cycle is unknown prior to being carried out. If the operator should experience a system that is easy to control independently of the load conditions, the fluid power system must adapt to the load conditions. That is, due to the demands for repeatability the input power must be matched to the load power requirements. This is one of the main reasons for applying load sensing systems in mobile fluid power applications.

### 1.1.1 Pump configurations for working hydraulics

In a mobile application the functions operated through the fluid power system are working functions (operating tools such as buckets, booms and winches), propelling, cooling by fan drives, steering and braking. If propelling is periodically a large part of the applications working cycle, a closed circuit transmission with its own pump is commonly installed for propelling. One or more separate pumps are then used for the working functions, steering and braking. The number of installed pumps may vary dependent on the load conditions of particular working cycles of a machine, and the cost of installed pump capacity. If for example one working function is always operated, irrespective of the operation of other functions. Then, due to energy efficiency, it may be beneficial to install a specific pump for the function which is always in service.

The capacity of the installed pumps also depends on the working cycle of a machine. At low engine rpm the installed pump displacement of an application is often not adequate to operate all functions simultaneously. For safety reasons priority should then be given to steering and braking prior to working functions. This functionality is handled by priority valves which maintain sufficient pressure levels at the steering and braking circuits, before directing fluid towards the working functions. Basically a priority valve reacts on the load pressure of the fluid device which has first priority and the outlet pressure of the pump. If the outlet pressure of the pump raises above the required load pressure of the fluid device having first priority, the priority valve directs fluid towards functions having secondary priority.

For some applications there is a poor match between the flow consumption requirements

and the engine rpm. Ayres addressed the issue in [14] for mobile construction equipment, but the issue is not limited to this class of applications. In general energy is unnecessarily wasted if the pump is of a constant displacement type and the flow rate demanded by the working cycle is small compared to the actual pump flow rate. To increase energy efficiency a variable displacement pump may be used. An internal control circuit in a variable displacement pump maintains the pump outlet pressure at  $p_p = p_{ls} + p_0$ , by adjusting the pump displacement, where  $p_{ls}$  is the highest pressure level, which is present among the fluid consumers. The LS pressure margin,  $p_0$ , is often chosen in the range of 10 – 20 [bar]. At a flow consumption of  $q_{ls}$  the power fed into the system using a variable displacement pump is

$$P = \frac{q_{ls} p_p}{\eta_t} \quad (1.1)$$

where  $\eta_t$  is the total efficiency of the pump composed of the volumetric efficiency and hydro-mechanical efficiency. For variable displacement pumps one may question whether it makes sense to consider efficiency of the pump itself. For example, if the pump is only maintaining a constant pressure when the connected system has no flow consumption, then the volumetric efficiency is infinitely poor due to internal losses of the pump. Anyway it is more efficient than the constant displacement pump. For a constant displacement pump with load pressure compensation the power fed into the system is

$$P = \frac{n D_r p_p}{\eta_{hm}} \quad (1.2)$$

where  $n$  is the rpm of the engine,  $D_r$  is the rated displacement of the pump per revolution and  $\eta_{hm}$  is the hydro-mechanical efficiency. The difference in energy consumption is best illustrated by figure 1.1 below where the scenario described above corresponds to the two most right figures b and c.

As illustrated by the figure, using load sensing and adapting the pump outlet pressure of a constant displacement pump to the load pressure gives a power saving of  $P = q_{max}(p_{max} - p_p)$ . This is the step taking from figure 1.1a to figure 1.1b. In the second step, from figure 1.1b to figure 1.1c, the load sensing system is combined with a variable displacement pump whereby further power savings may be obtained. The loss denoted leakage loss in figure 1.1c is due to the fluid consumption of the pump itself. If additionally the displacement of the pump may be controlled directly, the amount of fluid metered from the pump may be matched exactly to the demand of the system. Hereby the pressure loss in figure 1.1c may be avoided [106, 115].

In a system with a variable displacement pump the feedback of the highest load pressure to the pump is carried through by a system of shuttle valves and fluid lines. If the fluid path for the load sensing signal between the consumer carrying the highest load pressure and the pump is sufficiently long, a delay in the pump command may occur. Another delay, due to pump stroke dynamics, pump suction performance and the length of the fluid line between the pump outlet and the consumer, may occur, before the consumer in control of the pump receives the commanded pressure level. In worst case this behaviour results in instability of the hydraulic system. This is a well known but non-trivial problem of using variable displacement pumps. A simplified example of how an axial piston pump with variable displacement is connected to a set of proportional valves with load sensing circuit is sketched in figure 1.2.

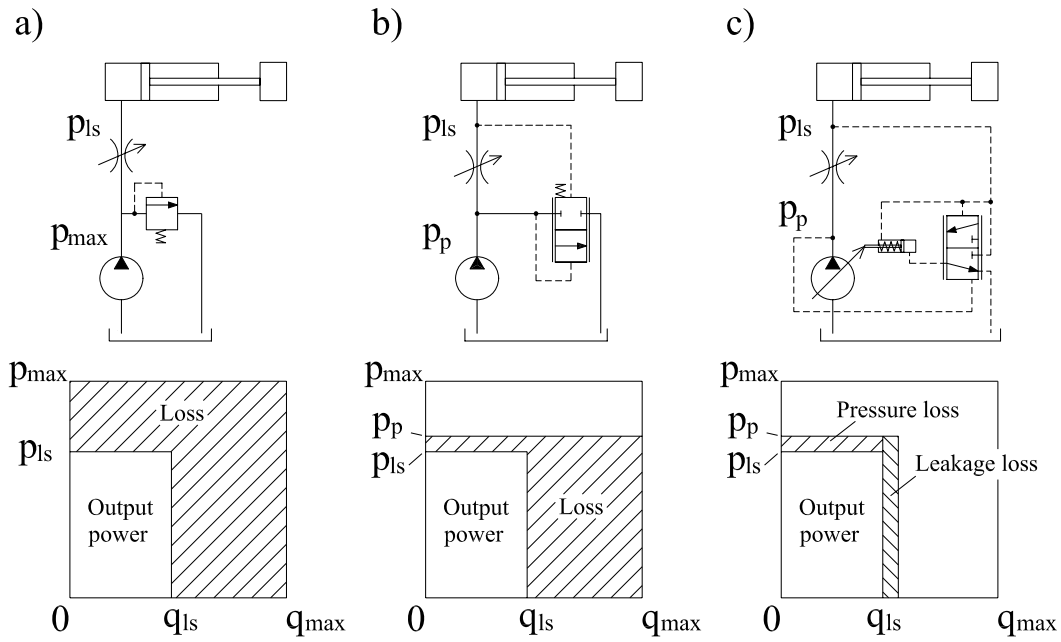


Figure 1.1: Illustration of the power savings obtained by using two different types of load sensing systems.

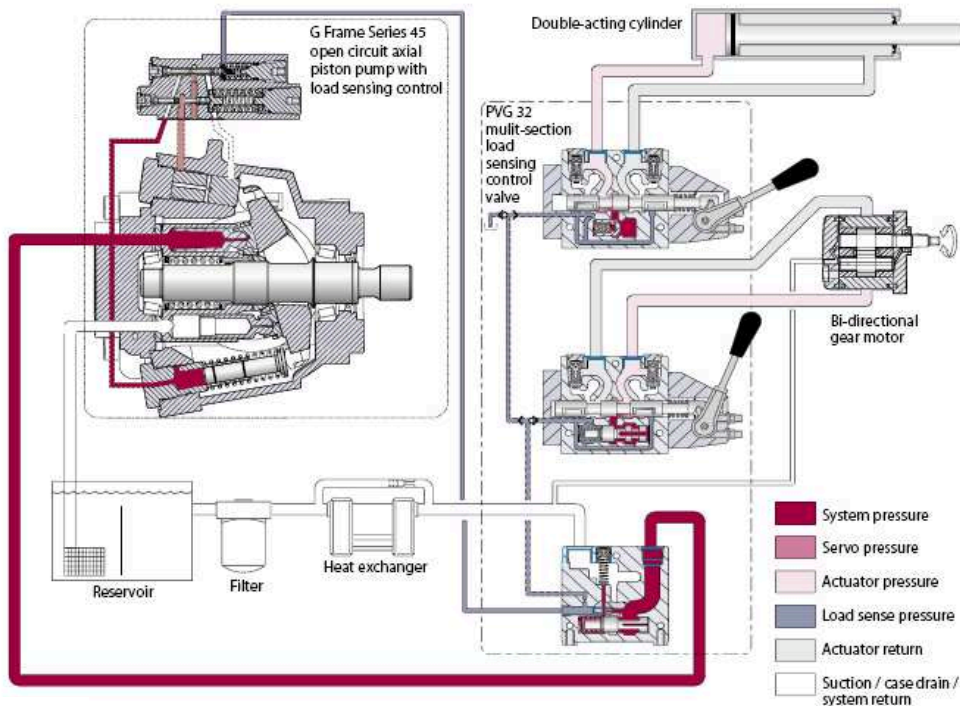


Figure 1.2: Load sensing circuit with variable displacement pump.

Open circuit pump configurations as those described above are only used for propelling of a vehicle, if the propel function and the working functions are not to be operated

simultaneously; and for systems where only low performance from the transmission is demanded. An excavator is an example of an application where propel functions and working functions are not operated simultaneously. For vehicles such as skid steer loaders and small to medium sized construction machinery a closed circuit transmission is commonly used.

### 1.1.2 Closed circuit transmission

A closed circuit transmission has its own hydraulic circuit separate from other hydraulic circuits on a machine (hereby the name closed circuit transmission). Fundamentally it is therefore not a part of the load sensing system. Commonly closed circuit transmissions are used for propelling, but for heavy duty working hydraulics they may also be used with some improvement of energy efficiency compared to a conventional valve system [85, 86]. A sketch of a closed circuit transmission is shown in figure 1.3. For the

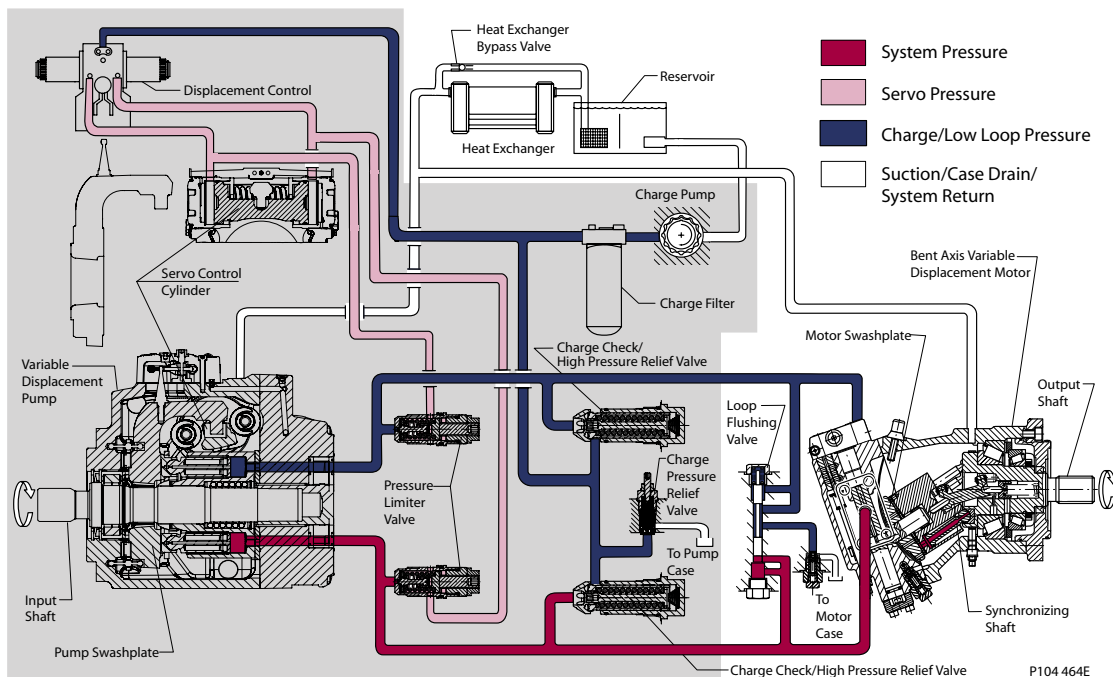


Figure 1.3: Closed circuit transmission.

particular configuration which is shown both the pump and the driven motor are of variable displacement types. To simplify the explanation assume that the displacement of the motor is constant. Then the rotational velocity of the motor is varied by changing the displacement of the pump. Hereby the pump motor configuration is a displacement controlled circuit why fundamentally a high efficiency may be obtained. However, a charge pump is necessary due to flushing of hot oil from the closed circuit, due to avoiding cavitation of the low pressure side of the circuit, due to internal leakage of components and due to standby supply pressure for the pilot control of the pump. The charge pump is a fixed displacement pump and it operates at a fixed standby pressure.

Thus the power loss due to the charge pump is comparable to the case sketched in figure 1.1a. For small displacements the closed circuit transmission therefore has a poor energy efficiency. The capacity of the charge pump is chosen in correspondence to the need for flushing hot oil from the closed circuit. Ideally the charge pump could be of a variable displacement type and be controlled as a function of the oil temperature in the closed circuit.

A difference between a variable load-sensing pump and a variable transmission pump is that the latter operates in a bidirectional mode. The transmission pump does not have a mechanical end stop in the neutral position as the load sensing pump<sup>1</sup>. Because of the high volumetric efficiency the control of the transmission pump around neutral therefore has to be accurate. That is, to the limit where the displacement flow is not larger than the leakage of the closed circuit. To limit the gain around the neutral position some types of closed transmission circuits feature a by-pass orifice inserted between the high pressure side and the low pressure side. This gives a more smooth control of the system at small displacements, but at the cost of energy efficiency as pointed out in [29].

### 1.1.3 Load sensing proportional valves

Commonly proportional valves for mobile applications have a modular structure where more valve modules are stacked into a group sharing the common oil supply from the pump or a priority valve. A group with four stacked valve sections is shown in figure 1.4. The valve sections share a common inlet module interfacing to the fluid supply.



Figure 1.4: Sauer-Danfoss PVG32 proportional valve group.

---

<sup>1</sup>In practice the load sensing pump may go slightly past zero to negative displacement.

The fluid flow rate through a proportional control valve is basically controlled by a set of variable orifices for example shaped between a spool and a housing. Simplified the flow rate through an orifice is governed by the equation

$$q = kA_o\sqrt{\Delta p} \quad (1.3)$$

where  $\Delta p$  is the pressure drop across the orifice,  $A_o$  is the cross sectional area of the orifice and  $k$  is a constant. In the proportional valve type known as a Closed Centre Load Sensing (CCLS) valve a pressure compensating spool maintains a constant pressure drop across the orifice controlling the fluid flow from the valve to the hydraulic actuator. Hereby the pressure drop under the square root of equation (1.3) is kept constant and the flow rate is only a function of the orifice area.

Generally load sensing valves with pressure compensating spools may be divided into two types. One type where the pressure compensating spool is located upstream compared to the main spool (pre-compensated valve). A hydraulic diagram of this type is sketched in figure 1.5. The other type has the pressure compensating spool located downstream

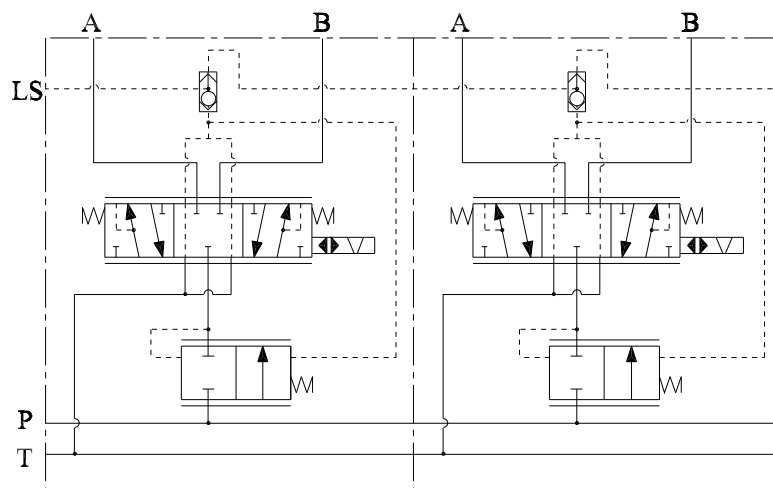


Figure 1.5: Pre-compensated valve modules.

compared to the main spool (post-compensated valve). The hydraulic diagram of this type is shown in figure 1.6. In both types of valves the pressure compensating spool maintains a constant pressure drop across the meter-in orifice independently of the load pressure. A pre-compensated valve has the advantage that the valve design is mechanically less complex than that of the post-compensated valve. The advantage of a post-compensated valve is that more valve sections sharing a common pressure source are able to share the available flow between each other relative to their inputs if the pressure source is saturated. Saturating the pressure source means that the maximum needed load pressure cannot be maintained at the desired flow rate. For the pre-compensated valve the highest loaded valve modules will not be adequately supplied at supply pressure saturation. By this case the valve module carrying the smallest load has first priority on getting flow.



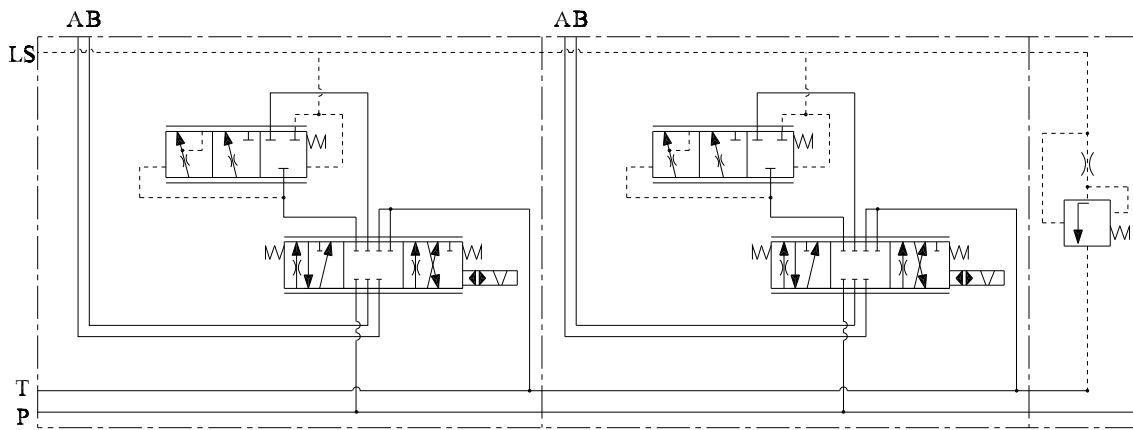


Figure 1.6: Post-compensated valve modules.

Common for both pre- and post-compensated valves are that they only control the meter-in flow from the valve to the hydraulic actuator independently of the load pressure. The meter-out flow from the hydraulic actuator to the valve is not pressure compensated. For positive loads, which act in the direction of the actuator movement, the orifice controlling the meter-out flow has to throttle to avoid cavitation of the meter-in side. By cavitation the load will be overrunning (moving too fast) because it is uncontrollable by the meter-in flow. If the meter-out orifice becomes too narrow the pump pressure has to be raised to lower a load. This is explained by figure 1.7.

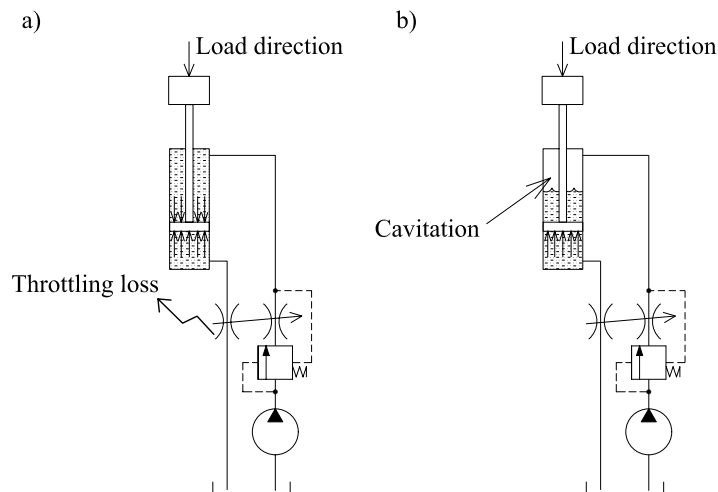


Figure 1.7: a) The area of the meter-out orifice is too small and throttling loss occurs. b) The area of the meter out orifice is too large and cavitation of the meter-in side occurs.

Solving the above problem may be done by pressure compensating both the meter-in flow and the meter-out flow. By this solution it must be assured that the meter-out flow

is always larger than the meter-in flow. Otherwise, power loss by unnecessary throttling will still occur. Because the meter-out flow must always be larger than the meter-in flow suction valves in parallel with the meter-in orifices are necessary to avoid cavitation.

Valves with both pressure compensated meter-in and meter-out flows have been manufactured by Eaton [2, 3]. The hydraulic diagram of one of these, the Eaton EMV valve, is sketched in figure 1.8. It may be seen from the hydraulic diagram that the valve

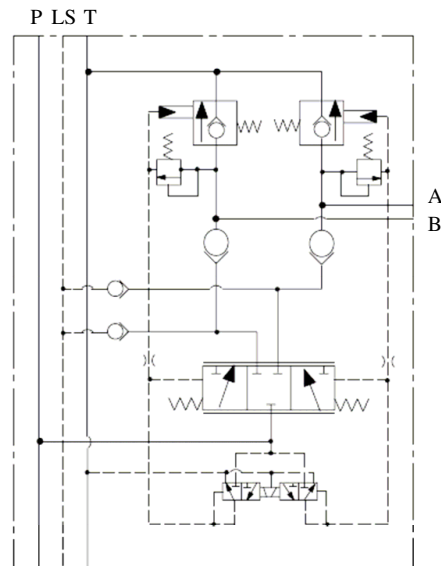


Figure 1.8: Eaton/Vickers EMV valve topology.

does not have pressure compensating spools. This is due to the valve being pressure compensated by using the flow forces. This is possible since the valve uses a pressure control pilot stage. Pressure compensation by flow forces are usually not as accurate at low pressure drops as using a pressure compensating spool. However, it should be noted that a variable displacement pump effectively performs the pressure compensation for the valve module carrying the highest load, which is also the valve module having the lowest pressure drop across the main spool. Thus, inaccuracy of pressure compensation by flow forces at low pressure drops is necessarily not a problem in a real system.

In some applications a load pressure dependent flow rate is desirable. For these applications the type of directional valves known as Open Centre Load Sensing (OCLS) valves are commonly used. In these valves the load pressure is adjusted according to the valve input signals. Andersson and Ayres gives a good description of these valves in [12].

## 1.2 Future trends in mobile fluid power

The evolution (and sometimes innovation) of mobile fluid power components and systems is market driven and contain factors such as costumer demands for increasing energy

efficiency, performance and functionality, increased power density (envelope reduction), cost reduction and fulfilment of environmental demands and legal requirements [52, 78].

To meet these requirements the route for a manufacturer of fluid power components is to design smarter products by the integration of valves sensors and on board electronics [52], but at the same time reduce the constructional effort. Improvements are often obtained due to advances in other technologies [16]. Recent key advancements is for example that the cost of powerful DSPs and reliable pressure sensor elements are nearing a price level in favour of integrating these components into products. This seems to be verified by industry as pressure sensor integration in both industrial and mobile fluid power valves has already taken place [4, 20, 79]. With regard to the mobile valves the full potential of these new solutions still remains to be seen.

The leading research authority within fluid power in China suggests that future research areas (among several more) should be [111]:

- Increased reliability by simplifying structure and using real time control.
- Increased accuracy by real time closed loop control and raising system stiffness.
- Improvement of dynamic response applying distributed control and using advanced control strategies.
- Improvement of efficiency by raising energy efficiency of components, better distribution of the primary energy, and implementation of innovative functionality.

Hans-Heinrich Harms which is one of the leading authorities within mobile fluid power in Europe suggests that priorities within research should be (secondary source: [25]):

- Increased energy and density performance of components.
- Increased energy efficiency and cost-effectiveness of systems.
- Improved static and dynamic properties.
- Increased controllability and convenience of operation.
- Requirement of greater integration of sensors and progressive development of control systems.

Helduser and Djurovic also suggest that energy efficiency of load sensing systems is to be improved [46]. They have addressed the problem by improving the energy efficiency of working hydraulics through a combined pump and valve control. In their approach they make use of a variable displacement pump where the flow rate is the controlled variable instead of the pressure as conventionally. The pump is then controlled to deliver exactly the required flow which is similar to the flow sum method suggested in other references, e.g. see [106, 115, 116].

The flow through the highest loaded valve section is controlled by the pump since this valve section is opened fully. Helduser and Djurovic gives several interesting ways of detecting if the system is entering into flow saturation. The only downside of their approach seem to be that it is based around conventional pre-compensated or post-compensated proportional valves, see figures 1.5 and 1.6. Hereby the same problem of controlling bidirectional loads as with conventional valves using only one pressure compensating valve for the meter-in flow is faced. In fact Lang and Harms whom suggest that the entire hydraulic system is rearranged and comprises an intelligent supply, intelligent controls and intelligent actuators state that ".....in case of pulling loads, the disintegration of all control edges is desirable." [56].

Seen in relation to the key focus areas outlined above, hydraulic valves is one of the most innovative areas in the field of mobile fluid power. This is for example seen by the fact that integrated position sensors and electronics with custom designed ASICs has been present in mobile valves through the past 20 years. In recent years the effective integration of microprocessors and CAN bus systems has also taken place. Within the area of displacement machines such an integration is first happening at the moment. However, using the experience from the valves there is reason to believe that this will happen at a faster pace than has been the case with valves.

### 1.3 Motivating examples for using programmable separate metering valves

In this section two examples are given, explaining some of the new functionality that a separate meter-in separate meter-out valve offer in combination with sensors and improved pump control, compared to a conventional load sensing pump. By using pressure sensors a number of the auxiliary valves, which are present in conventional pressure compensated proportional valves, may be replaced by software control algorithms. Some of the auxiliary valves which are no longer necessary are:

- Check valves for preventing drop before lift
- Work port pressure limitation valves
- Mechanical feature for kick-out (Release of automatic spool holding function at over pressure)

Examples of the new functions which may be implemented when the pressures are available for a control are:

- Electronic load sensing
- Electronic shift between pressure/flow control
- Active damping

- Programmable flow sharing
- Power management

If in addition the control of the valve orifices, e.g. by the positioning of a spool, is sufficiently fast, electrohydraulic pressure compensation may be implemented. Hereby the conventional pressure compensating spools may also be replaced by software. An advantage of this is that by pressure sensors the metering orifices may be pressure compensated for flow in both directions allowing for regenerative functions if the valve concept is sufficiently flexible. To illustrate the flexibility of a programmable separate meter-in separate meter-out valve and motivate the use of such a valve in the future, two examples are given in the following.

### 1.3.1 Minimising throttle losses by combined pump and valve control

In the following an example is given as to how bidirectional loads may be controlled while keeping the pump pressure at a minimum. Assume that the variable displacement pump in figure 1.9 is operating in flow control mode. Both cylinders are extending and the load direction of the left cylinder is positive whereas the load direction of the right cylinder is negative. The operator demands cylinder velocities such that the required flow rate from the pump is  $q_p = q_1 + q_2$ . To control the load of the left cylinder  $V_{12}$  must be throttling and hereby controlling the speed of the cylinder. To avoid a large pressure level in the pressure chambers of the left cylinder,  $V_{11}$  keeps the pressure in the bottom chamber of the cylinder low. Due to the fact that the pump is operating in flow control mode the pump controller may control the pump flow at  $q_p = q_1 + q_2$ . Hereby the valves  $V_{21}$  and  $V_{22}$  may be opened fully as the pump automatically controls the velocity of the right cylinder. By using the flow controlled pump, the throttling losses, which normally occur because a conventional variable load sensing pump generates a slightly higher pressure than required, are minimised.

The described control method is perhaps the most intuitive, but pump flow may be saved by using the regenerative features of the sketched valve set-up. Suppose that the load and velocity directions are as described above. Then, the left actuator may be moved without using pump flow by still throttling the meter-out flow through  $V_{12}$ , but instead of connecting the meter-in chamber to the pump line,  $V_{11}$  is moved in the opposite direction connecting the associated chamber to the drain line. Hereby the pressure chamber is filled by regenerating flow through the drain line. To accomplish this regenerative function, a counter pressure valve in the drain line may be necessary to improve suction performance. If using a counter pressure valve in the drain line it should be secured that sufficient fluid in the drain line is present. This may, however, be checked by monitoring the pressure of the drain line.

Suppose the load directions of both cylinders are negative and the pump still controls the flow. Then both meter-out valves  $V_{12}$  and  $V_{22}$  and the meter-in valve of the cylinder which is at the highest pressure level may be opened fully. The meter-in flow of the

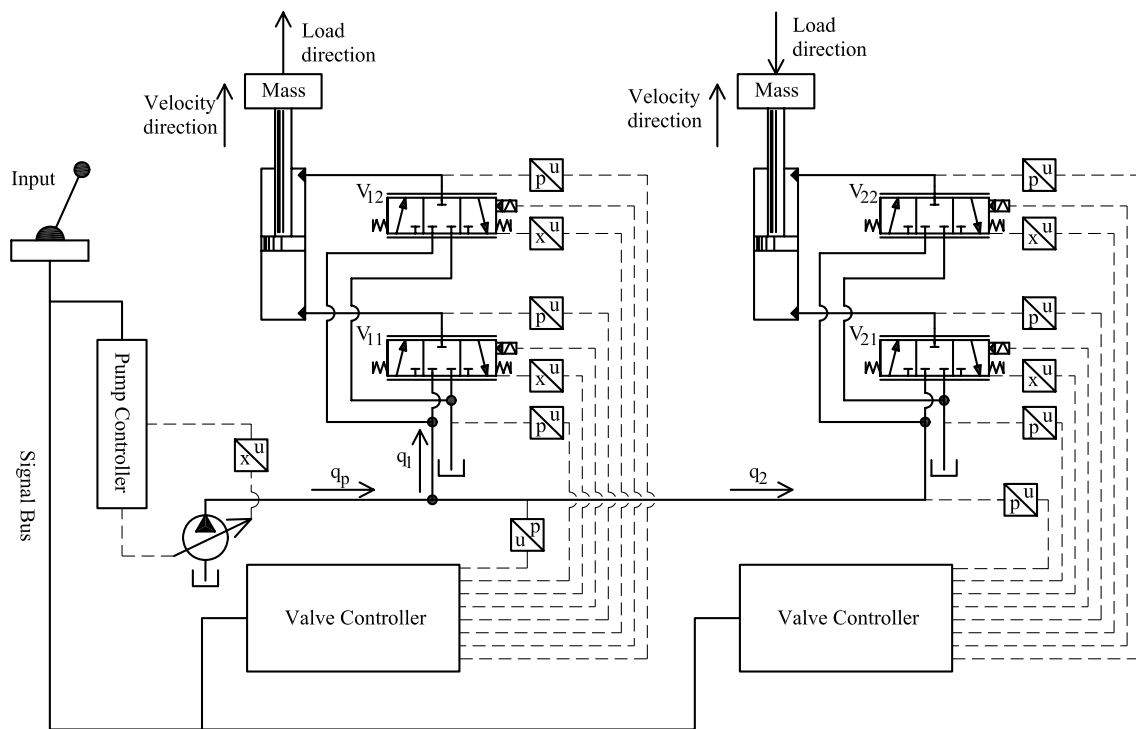


Figure 1.9: Combined pump and valve control set-up.

cylinder carrying the lowest pressure should throttle. In the case that both loads are positive the velocities are controlled by throttling across the valves  $V_{12}$  and  $V_{22}$  and filling the meter-in chambers at a low pressure. Essentially the described example where the pump controls the velocity of one cylinder, except for the case that both load directions are positive, is similar to the control method proposed in [46]. However, the separate meter-in separate meter-out set-up in figure 1.9 is able to control bidirectional loads while minimising throttle losses as opposed to the set-up suggested in [46]. Furthermore advanced regenerative functions may also be implemented.

### 1.3.2 Transmission by combined open circuit pump and valve control

Combined open circuit pump and valve control is also a candidate for use in transmission circuits. Valve controlled transmissions are for example already used in excavators. Due to the fact that the open circuit pump is not reversible a valve system which controls the flow direction as well as the back pressure is needed. A separate meter-in separate meter-out valve is a good candidate for this due to the separate orifices. Consider the hydraulic system in figure 1.10. The pump operates in flow control mode. For one rotational direction of the hydraulic motor  $V_{11}$  may be opened fully connecting the pump to one work port of the hydraulic motor.  $V_{12}$  then controls the back pressure in the opposite work port of the motor. For reversing operation the roles of  $V_{11}$  and  $V_{12}$  are opposite. Thus in the transmission system the variable displacement pump controls the

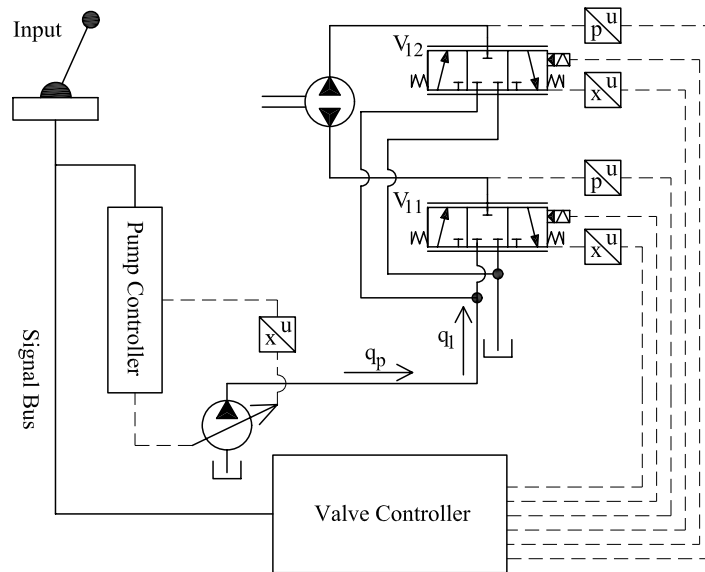


Figure 1.10: Combined pump and valve control for transmission.

flow rate and the separate meter-in separate meter-out valve controls the flow direction and the back pressure on the drain side of the motor. The separate meter-in separate meter-out valve in the transmission system sketched in figure 1.10 could be one of several in a group, where the remaining ones control ordinary working functions.

Digital displacement pumps which may control the flow quite accurately and which has fast response times are currently under development [1]. Such a pump could be a good candidate for use in an open circuit transmission as the above.

## 1.4 Demarcation of research and outline of thesis

Motivated by the flexibility that programmable separate meter-in separate meter-out valves offer in combination with other intelligent hydraulic components, the research presented in this dissertation has been funded by *The Company* and is intended to fulfil the following purposes:

1. Establishing an overview of valve concepts on a hydraulic diagram level, which fulfils the future needs for energy efficient programmable valves.
2. Develop a model of the one of several valve concepts which fits best into requirements and technologies available within *The Company*.
3. Develop controllers for this valve concept and identify parameters critical to controller performance.

The research is limited to considering a single separate meter-in separate meter-out valve section interfacing to the remaining hydraulic system through a supply pressure and a drain pressure connection. With this demarcation the considered valve section could be actuator mounted, that is distributed on a machine, or mounted centrally in group along with more valves sections.

The dissertation is organised as follows:

### **Chapter 2: Separate meter-in separate meter-out valve concepts**

A criterion for how to select a specific separate meter-in separate meter-out valve concept out of several is stated. The chapter partly takes its basis in an internal confidential market analysis, which has been partly initiated by the author, and in which the author has participated. The hydraulic functionality which influences on the mechanical valve topology of a separate meter-in separate meter-out valve is described. State of the art separate meter-in separate meter-out valve concepts are analysed with regard to the selected criterion. Some of the state of the art valve concepts are protected by patents and others do not fit into the priorities of *The Company*. Therefore several new valve concepts are suggested. A single valve concept is selected for further study.

### **Chapter 3: Mathematical models of separate meter-in separate meter-out valve**

A detailed parametric model of the selected valve concept is derived. The model is verified by means of measurements made on a physical prototype of the selected valve concept. The non-linear model is linearised with the purpose of using the linear model for controller design.

### **Chapter 4: Electro-hydraulic pressure compensation**

Flow controllers are developed for the selected spool valve concept. The preliminaries for the developed controllers are that the differential pressure across the valve and the opening of the main orifice controlling the flow may be determined. A minimum knowledge of certain design parameters of the valve is assumed. The controller performance is evaluated both by simulations and by measurements made using the prototype.

### **Chapter 5: Generic model of hydraulic application with flexible load structure**

A simulation model of a single degree of freedom of a loader crane is developed for the purpose of being used in a simulations for evaluating separate meter-in separate meter-out controllers. The model incorporates structural flexibility of the mechanical crane structure. The model is written on a generic form which makes it applicable to a wide range of single degree of freedom hydraulic applications.



**Chapter 6: Multivariable pressure/velocity control**

Decentralised control structures for separate meter-in separate meter-out control are analysed and verified by simulations. The chapter gives an insight into the multivariable directions of a hydraulic actuator controlled by separate meter-in separate meter-out. Although one of the initiators of this work is the increased functionality a programmable valve offers, only basic separate meter-in separate meter-out control is considered.

**Chapter 7: Conclusion and recommendations for further research**

This chapter summarises the presented work and contains the conclusion and recommendations for further work.

## 1.5 Main results of this work

This dissertation gives an overview of different separate meter-in separate meter-out valve concepts on a hydraulic diagram level and puts forward several new ones.

The reference in the field of modelling hydraulic components is the book by Blackburn, Reethof and Shearer [19] and the book by Merritt [70]. This dissertation establishes and verifies an accurate parametric spool valve model partly on the basis of these books but also by using earlier research in the field.

Quantitative steady state requirements for electrohydraulic pressure compensation of proportional valves are established with basis in experimental work, and dynamical requirements are discussed qualitative.

Spool position controllers are developed for two generic pilot operated spool valve configurations. One of those valve configurations is based on a pressure control pilot stage, the other valve configuration uses a flow control pilot stage. In this connection parameters impacting the relative stability of the valve with a pressure control pilot are identified. Dynamical performance limitations due to the design of the valve with flow control pilot are also identified.

The different spool position controllers for the valve with flow control pilot are developed using linear,  $\mathcal{H}_\infty$  and sliding mode controller design tools. The developed controllers for this valve are implemented on a valve prototype and evaluated experimentally.

Two MIMO controllers are developed, one based on meter-in, the other based on meter-out. Both controllers may control bidirectional loads. The controllers are tested in a simulation environment using simplified simulation models of two of the degrees of freedom of a loader crane incorporating structural flexibility.

Published work either primarily made by the author or to which the author has contributed during his Ph.D. study are listed in appendix F. These publications reflect the broad interest of the author with co-workers.

## 1.6 Reading instructions

The symbolic explanation of the referred to variables throughout the thesis may be found in the nomenclature before this chapter. A few variables, which are composite of other variables and constants or appear due to linearisation of an equation, are not listed to simplify the nomenclature. Hopefully, it should be apparent from the text what is meant in these cases.

Numerical values for constants are found in appendix A. Unless appearing specifically from the text, these numerical values have been used to obtain the presented results. Appendices are not intended to be readable without consulting the main text first with the exception of appendices E and F.

Small introductions are given to the methodologies used throughout the thesis where such introductions are found appropriate.



# Chapter 2

## Separate meter-in separate meter-out valve concepts

### Contents

---

2.1	Criteria for selection of valve concept . . . . .	20
2.2	Hydraulic functionality . . . . .	21
2.3	State of the art separate meter-in separate meter-out valve concepts . . . . .	26
2.4	New separate meter-in separate meter-out valve concepts . . . . .	30
2.5	Actuation methods . . . . .	33
2.6	Summary and conclusion . . . . .	36

---

The functionality of a separate meter-in separate meter-out valve has to match the requirements of the application which is to be controlled. The purpose of this chapter is to clarify the functional requirements for a single valve section. Focus is directed towards the few hydraulic functions which pose restrictions on how the valve members (poppet valves, spool valves etc.) are connected hydraulically. When referring to valve concepts in this chapter, what is meant is the specific mechanical combination of valve members, e.g. spool valves and poppet valves.

Because this research is made as an industrial Ph.D. study, a pragmatic approach to concept selection is taken considering market demands, and combining these with the priorities of *The Company* that has funded the research. Detailed market data is not presented as this is the confidential property of *The Company*, but hydraulic functions which are of relevance to the mechanical concept of a single programmable valve section are presented. Hence, excluding functionality required to be implemented in a common inlet module of a valve group, which is necessary if the valve section is not to be actuator mounted.

## 2.1 Criteria for selection of valve concept

The success criteria for selecting a mechanical separate meter-in separate meter-out valve concept is subjective from manufacturer to manufacturer. This is because the favoured choice depends on which technologies the valve manufacturer manages. In general the favoured choice incorporates weighting of the following objectives:

- Use existing core technologies in the valve, which are not new to the manufacturer. These technologies should preferably give increased performance and reliability compared to competitive products. To secure a technological entry barrier these technologies should preferably also be difficult to copy.
- Minimising cost of ownership for the end user. In measurable terms cost of ownership is related to required service cost (reliability), product lifetime and energy efficiency.
- Offering to the end user the expected controllability of a hydraulic machine. This is more difficult to measure and may be subjective from end user to end user. However, as a starting point flexibility to offer a variety of hydraulic functions must be present in a valve concept.
- Low manufacturing cost. This may for example be obtained due to few and simple components, but also because the incorporated technologies are well known to the manufacturer. A low cost maximises both the competitive advantage for the valve manufacturer and the manufacturer of a hydraulic machine as the latter may obtain the product (the valve) at a lower price.

Since separate meter-in separate meter-out valves are considered on a conceptual level in this chapter, reliability and product lifetime is clearly outside the scope. It has already been motivated in the introduction that separate meter-in separate meter-out control may increase energy efficiency due to lowering of throttle losses. Thus focus will be at the required functionality of a single separate meter-in separate meter-out valve section as mentioned.

Regarding the choice between suitable candidate technologies incorporated into a valve concept, it has been a clear priority of *The Company* to focus the research on separate meter-in separate meter-out valve concepts making use of the following technologies/components:

- Pressure sensors for measuring the pump drain and work port pressures. These pressure sensors shall be used for electrohydraulic pressure compensation, and to give basis for a simple valve concept.
- Position sensors for implementing closed loop control of the variable orifices, because closed loop control gives advantages with regard to disturbance rejection.

As one of the focus points of this research is development of closed loop controllers it is quite natural to include these components in the considered valve concepts.

The lowest possible cost is mostly not obtained for a product from start of production, but by cost reductions after production has begun. Such reductions may be obtained by refinement of production methods, improvement of internal and external logistics of the manufacturing process and to some degree by redesign. However, some focus on cost must remain in the process of concept development, to avoid ending up with a concept where cost reduction means a total redesign of the product. In this connection the following success criterion for evaluating a valve concept on a hydraulic diagram level has been identified in cooperation with design engineers at *The Company*.

*Increase functionality while reducing the number of required continuously controllable independent mechanical valve members with flow metering orifices. Hereby reducing the number of position sensors and mechanical degrees of freedom in the actuating system.*

Regarding the number of degrees of freedom of the actuating system, a single acting (unidirectional) and a double acting (bidirectional) actuator are both defined to have one mechanical degree of freedom. From a cost point of view this makes sense as one cannot state that a double acting actuator is twice as expensive to manufacture as a single acting one. The reverse case may not hold either.

## 2.2 Hydraulic functionality

Although this dissertation is only concerned with the control of one valve section, the required functionality of the fluid power system as a whole has to be considered when choosing a sufficiently flexible separate meter-in separate meter-out valve concept. Hydraulic functions that are related to proportional valves may be split up into different groups, which depend on the considered level of detail that the complete hydraulic system is looked upon. The following split is found useful:

### **Inlet/outlet functions**

These functions are concerned with the case that more proportional valve sections share a common inlet module. The inlet/outlet functions determine how a group of valve sections interfaces to the remaining hydraulic system, e.g. to a constant or a variable displacement pump.

### **Metering functions**

These functions are concerned with specific metering capability of a single valve section. For example meter-in/meter-out and regenerative functions are within this group. They are related to the control of a single hydraulic actuator, and they may be seen as independent of whether more valves are distributed on the application (actuator mounted) or mounted centrally in a group.

### Flow distribution functions

These functions are concerned with flow sharing between more hydraulic actuators. For example flow sharing by pump saturation, regeneration of flow from one valve section to another and prioritisation of flow, e.g. to steering and braking systems.

### Protection functions

These function relates to the safe operation of a mobile application. Functions in this group are for example pressure limitation, prevent drop before lift, zero leakage functionality etc.

### Auxiliary functions

These functions are application specific and mainly includes programmable functions. Examples are programmable flow characteristics, active damping of vehicle oscillations, bucket shake, external sensor control, customer specific software etc.

When counting functions already offered by current state of the art proportional valves and functions which are found to be beneficial to offer in the future, 61 functions are foreseen that relates to the above grouping<sup>1</sup>. Here concern is directed towards the functions which affects the mechanical concept of a single valve section, omitting the programmable ones of the 61 functions, which are realisable with any separate meter-in separate meter-out valve. Within the above grouping the considered functions are:

### Metering functions

- Both work ports of the controlled actuator are connected to the drain line. This function is denoted as float.
- Reuse of oil for the fast extension of an actuator carrying a small load. This function is denoted as regenerative lift.
- Reuse of oil for lowering of gravitational loads, hereby saving pump flow. This function is denoted as regenerative lower.

### Flow distribution functions

- Reuse of oil from one valve section to another. This function is denoted as sectional regeneration.

---

<sup>1</sup>As part of this research, demands for hydraulic functionality for specific applications within the material handling, construction and agricultural sectors have been analysed. This has been done, in cooperation with *The Company's* technical sales department and key account managers, to establish the necessary baseline for determining the required flexibility of a separate meter-in separate meter-out valve section. The results are however excluded from this thesis as they are confidential property of *The Company*.

### Protection functions

- A load may be held in position without using pump pressure. This function is denoted as zero leak.
- Venting of fluid from the work ports of the controlled actuator in case of pressure peaks. This function is denoted as shock valve functionality.

The float and regenerative lift metering functions are shown in figure 2.1. These func-

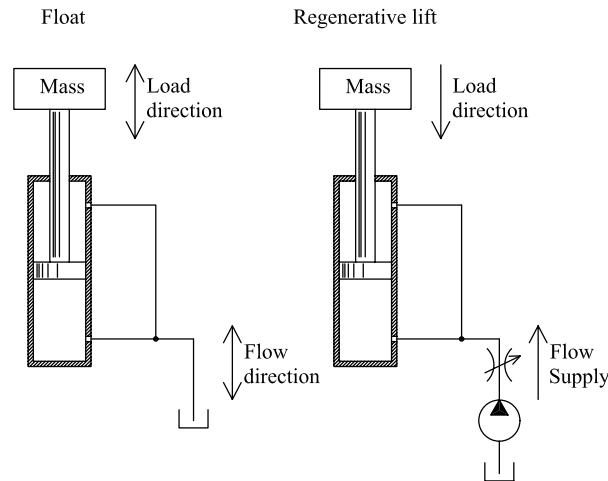


Figure 2.1: Float and regenerative lift.

tions both use a fully open connection between the work ports of the actuator as shown. The float function is used with both hydraulic motors and cylinders whereas the regenerative lift function is a function for use with differential area cylinders only.

Regenerative lower may be realised in several ways as sketched in figure 2.2. The most

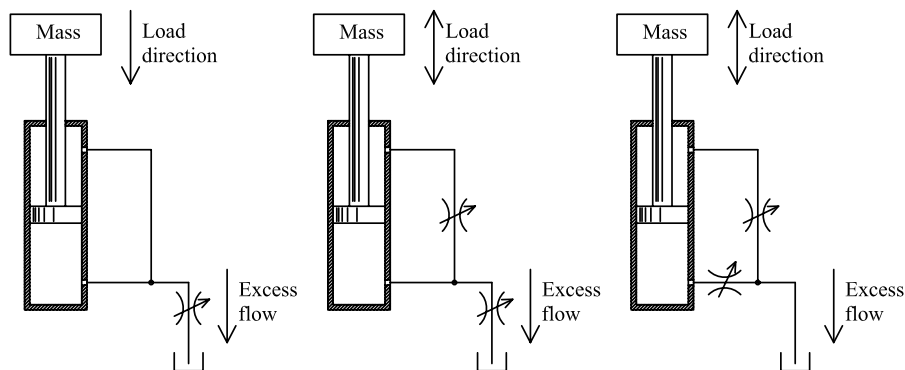


Figure 2.2: Ways realising regenerative lower.

left sketch of the figure shows regenerative lower using only one control variable. This way of realising regenerative lower gives less loading capability of the actuator as it only carries the load on the piston rod area. Therefore, it may only be used with differential



area actuators with unidirectional loads. The sketch in the middle shows regenerative lower using two variable orifices. The advantage is that bidirectional load may be controlled regardless of the area ratio of the actuator. The most right sketch of figure 2.2 shows regenerative lower with two orifices opening into a common drain connection. By this orifice combination bidirectional loads may also be controlled regardless of the area ratio of the actuator. However, the low pressure side of the actuator will be filled by suction, which may be a problem in systems with long fluid lines. Often gravity gives a unidirectional load on an actuator why the ability to control bidirectional loads with regenerative lower may be of little use in these cases.

Sectional regeneration may be obtained by connecting the meter-out side of an actuator, which is lowered by gravity, to either the pump line or the drain line. If connected to the drain line this corresponds to the regenerative lower just explained above. If connecting the lowering actuator to the pump line, this may only be done if the lowering actuator is at the highest pressure level among the consumers supplied by the particular pump line. This case is explained by considering figure 2.3, where flow directions are shown by the arrows marked with a  $q$ . In the figure the actuator to the right is lowered. The upper pressure chamber of this actuator which is expanding may then be supplied either through  $v_{bp}$ , or it may be supplied through  $v_{bt}$ , if there is an excess of fluid in the drain line.

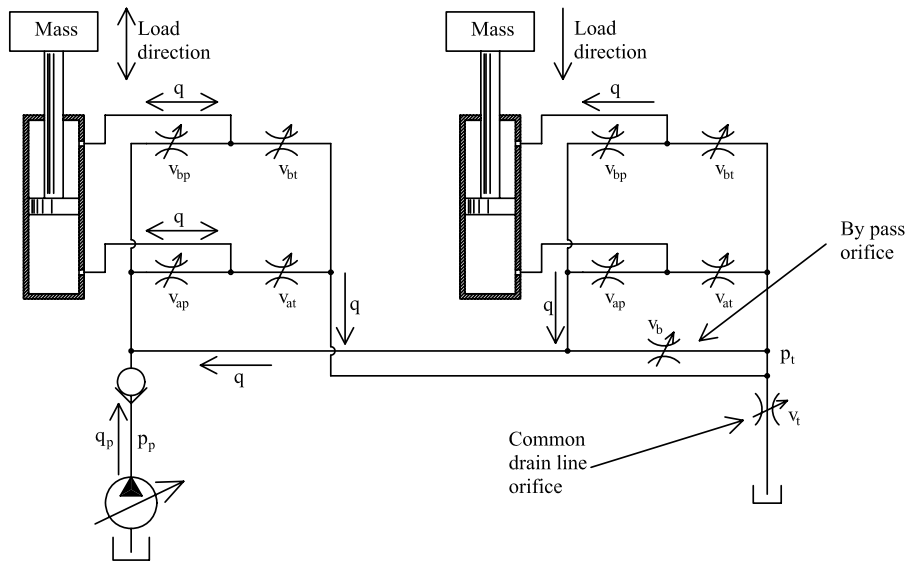


Figure 2.3: Sectional regeneration.

If there is also an excess of fluid in the pump line, then some of this fluid must be metered to the drain line. This is handled by the by pass orifice. This by pass orifice could be located in the inlet module of a valve group. If there is insufficient fluid supply, make up fluid has to be delivered by the pump. In this case a variable load sensing pump should be used as the pump will be at full load pressure, and due to energy efficiency, throttling of excess flow from the pump to the drain line shall be avoided. The consumers which are supplied from the lowering actuator may in principle be any consumers, as long as

they require a pressure in the supply line which is lower than that generated by lowering actuator.

There is a variety of possibilities of supplying fluid from the lowering actuator to other consumers through the pump line. Again with reference to the right actuator in figure 2.3, these possibilities are listed in table 2.1. The table should be read in the way that M means metering, O means fully open and C means closed. The "Load carrying capability" column refers to the right (lowering) actuator in the figure. The "Velocity controlled by" column refers to the valves which determine the velocity of the right (lowering) actuator. In this column "cfr" means the consumed flow rate of other fluid consumers than the lowering actuator.

No.	$v_{ap}$	$v_{bp}$	$v_{at}$	$v_{bt}$	$v_t$	$v_b$	Velocity controlled by	Load carrying capability	Conditions
1	M	O	C	C	O	M	$v_{ap}$	Reduced	None
2	M	O	M	C	O	C	$v_{ap} + v_{at}$	Reduced	None
3	M	O	C	M	O	C	$v_{ap}$	Reduced	None
4	O	M	C	C	O	M	$v_b + cfr$	Full	None
5	O	M	M	C	O	C	$v_{at} + cfr$	Full	None
6	O	M	C	M	O	C	$v_{bt} + cfr$	Full	None
7	M	M	C	C	O	M	$v_{ap}$	Full	None
8	M	M	M	C	O	C	$v_{ap} + v_{at}$	Full	None
9	M	M	C	M	O	C	$v_{ap}$	Full	None
10	M	C	M	O	M	C	$v_{ap}$	Full	Excess fluid in drain
11	M	C	C	O	M	M	$v_{ap}$	Full	Excess fluid in drain

Table 2.1: Metering modes for sectional regeneration.

It is desirable that the velocity of the right (lowering) actuator is independent of the flow rate consumption of other fluid consumers. By the results in the table this rules out the possibilities where  $v_{ap}$  is fully open. The metering modes where  $v_{bp}$  is fully open has the disadvantage that the upper expanding chamber of the lowering actuator is exposed to the load pressure of the remaining system. The load carrying capability of the actuator is therefore reduced. Finally, the metering modes where the upper expanding chamber is supplied through  $v_{bt}$  requires excess flow in the drain line to avoid cavitation.

If it is a requirement that full load carrying capability of the lowering actuator is maintained, for the case that there may be insufficient fluid available in the drain line, then the orifices  $v_{ap}$  and  $v_{bp}$  has to be independently controllable. In this case no. 9 in the table above is the preferred option, since compared to no. 8 the velocity of the lowering actuator is only dependent of one valve, namely  $v_{ap}$ . No. 7 requires an extra by pass orifice.

Regarding the protection functions the zero leak and shock valve functionality have more to do with mechanical design solutions than the separate meter-in separate meter-out valve concept as such. For example, zero leak may be established by pilot operated check valves or by directly using seat valves for the metering orifices. The preferred option is up to a particular valve manufacturer to decide.

### 2.3 State of the art separate meter-in separate meter-out valve concepts

In this section an overview of state of the art valve concepts is given and these are evaluated with respect to the criterion put up in section 2.1, and the metering and flow distribution functionality described in section 2.2. State of the art regarding separate meter-in separate meter-out valve concepts is found among patents and patent applications. The valve concepts described in these references may be divided into 4 basic ones, although naturally they have some variation. One of these valve concepts based on two 3-way 3-position spool valves is shown in figure 2.4. This concept is able to do float,

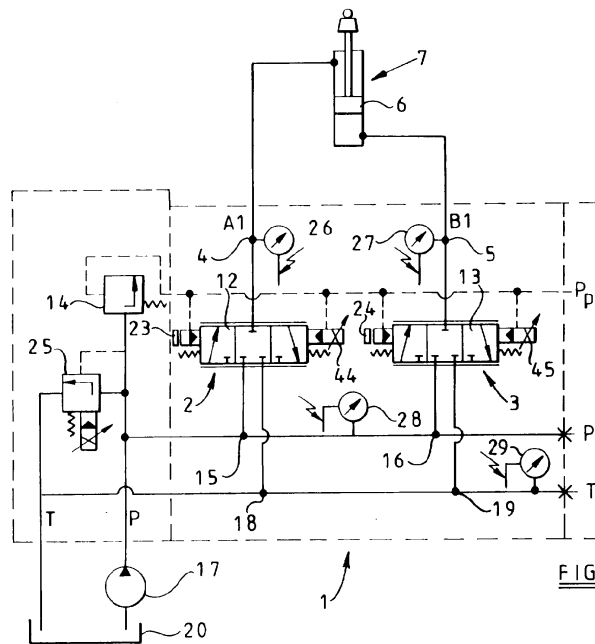


Figure 2.4: Valve concept with two 3-way spools. Source: [104].

regenerative lift and regenerative lower. The latter is done by first directing fluid to the drain line corresponding to the most right sketch in figure 2.2. Hereby the expanding pressure chamber is filled by suction with the problems that this may involve, e.g. see section 2.2. The concept may also do sectional regeneration corresponding to no. 9 in table 2.1. The sensor/actuator requirements and functionality are summarised in table 2.2. The number of actuators in the parentheses are in case single acting electromechanical actuators are used.

Float	Regen. lift	Regen. lower	Sectional regen.	No. of single acting actuators	No. of double acting actuators	No. of position sensors	Integrated zero leak
+	+	+	+	(4)	2	2	-

Table 2.2: Summary of functionality and sensor/actuator requirements.

A second valve concept which is also based on two 3-way 3-position spool valves but with an additional auxiliary circuit for realising the float function is shown in figure 2.5. The regenerative lift and regenerative lower metering functions are however not

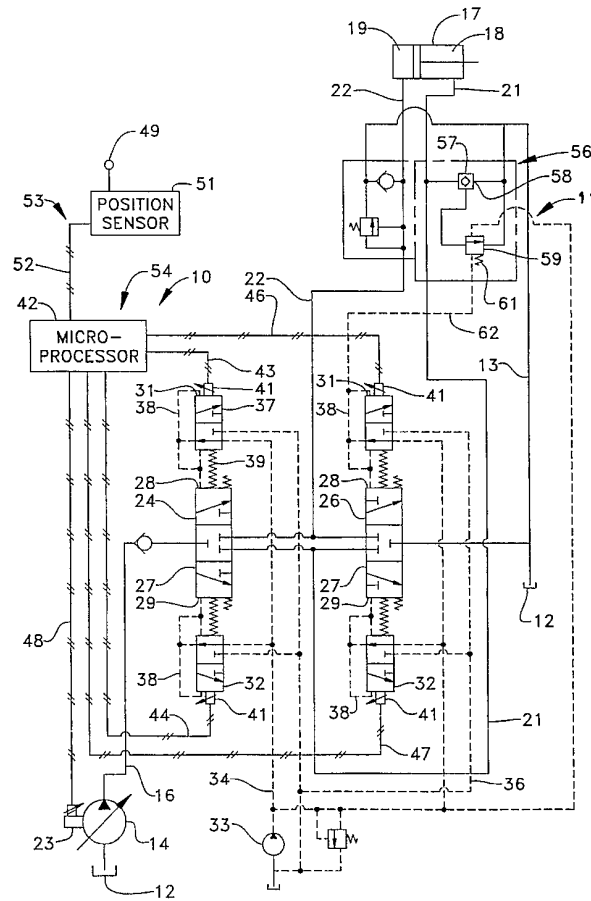


Figure 2.5: Valve concept with two 3-way spools. Source: [5].

realisable by the concept. If removing the check valve in the pump line (16), then sectional regeneration is possible corresponding to no. 11 in table 2.1. For sectional regeneration, excess fluid in the drain line is therefore necessary. By removal of the check valve a prevention of drop before lift should be implemented in software. The sensor/actuator requirements and functionality are summarised in table 2.3.

Float	Regen. lift	Regen. lower	Sectional regen.	No. of single acting actuators	No. of double acting actuators	No. of position sensors	Integrated zero leak
+	-	-	(+)	(4)	2	2	-

Table 2.3: Summary of functionality and sensor/actuator requirements.

Caterpillar among others has proposed a valve concept based on four 2-way valves. The valves are connected in the well know Wheatstone bridge as sketched in figure 2.6. Both suction and shock valves are also shown in the figure. The concept offers the same

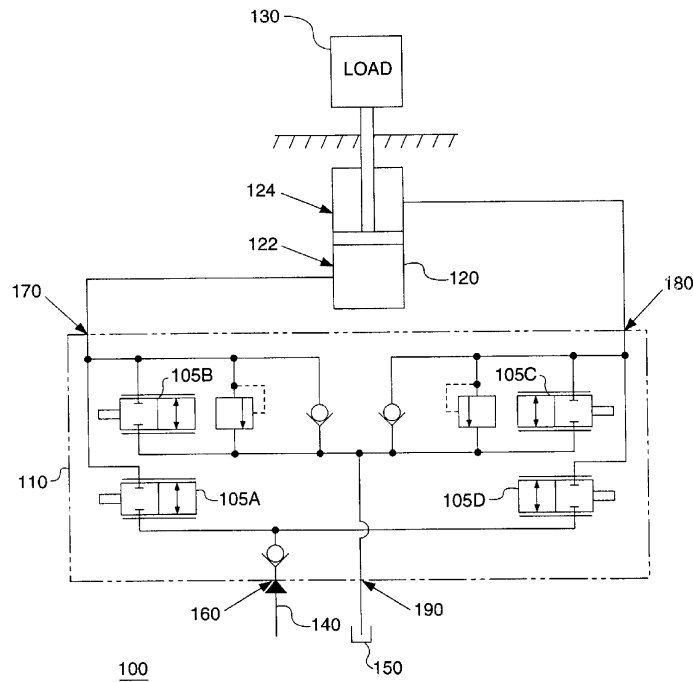


Figure 2.6: Valve concept with four 2-way valves. Source: [6].

metering functionality as the concept in figure 2.4, assuming that the check valve in the fluid line (140) is removed and prevention of drop before lift is implemented in software. Thus except that it is possible to incorporate zero leakage directly in the concept by using seat valves, it does not offer more flexibility compared to the spool valve concept in figure 2.4. If the flexible metering functions of the concept should not be lost, four single acting actuators are required. Additionally also four position sensors are necessary for closed loop control of the 2-way valves. The sensor/actuator requirements and functionality are summarised in table 2.4.

Float	Regen. lift	Regen. lower	Sectional regen.	No. of single acting actuators	No. of double acting actuators	No. of position sensors	Integrated zero leak
+	+	+	+	4	-	4	+

Table 2.4: Summary of functionality and sensor/actuator requirements.

The last of the four basic separate meter-in separate meter-out valve concepts is sketched in figure 2.7. It consists of two 2-way valves (36,38) for metering and one 4-way valve (30) for controlling the flow direction.

Provided that the 4-way valve is fitted with an extra position, whereby the 2-way valves may be connected to the drain line, then the concept can do float and regenerative lower across the drain line. This valve combination is already suggested in [92]. A position where the 4-way valve connects both of the 2-way valves to the fluid supply is necessary to do regenerative lifting.

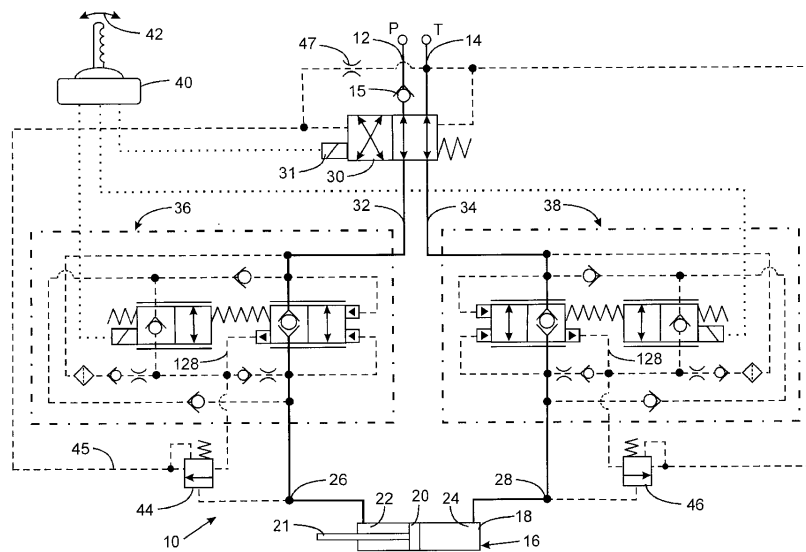


Figure 2.7: Three valve main stage valve topology. Source: [92].

If more than two positions of the 4 way valve are used, the 4-way valve shall be able to be positioned at intermediate positions. This will require some sort of feedback. Feedback is commonly implemented by spring force if the pilot stage generates pressure. For accurate positioning, position sensor feedback is commonly used. The upper row of the listing of functionality and required actuators and sensors in table 2.5 refers to the case where only two positions are available on the 4-way valve. The second and third rows refer to the case where three positions are available on the 4-way valve. Additionally it is assumed that the 4-way valve may be positioned sufficiently accurate without sensor feedback. Both regenerative lift and regenerative lower is mechanically complex to obtain by a single 4-way spool valve, and this option has been left out of the table.

Float	Regen. lift	Regen. lower	Sectional regen.	No. of single acting actuators	No. of double acting actuators	No. of position sensors	Integrated zero leak
-	-	-	-	2 + 1 on/off	-	2	+
-	+	-	+	3	-	2	+
+	-	+	-	3	-	2	+

Table 2.5: Summary of functionality and sensor/actuator requirements.

The concept may offer zero leakage if the two 2-way valves are seat valves (this is the option sketched in the figure). Sectional regeneration requires removal of the check valve (15), and again necessitates a software implementation of the prevention of drop before lift.

Among the presented concepts, the spool valve concept shown in figure 2.4 offers the most functionality with potentially the fewest electromechanical actuators and sensors. However, this valve concept with added position sensors and pressure sensors is protected

by a patent [104]. To secure that *The Company* has the free scope for utilising the technologies developed in this work it is natural to focus the work around a prototype concept, which is not protected by a patent. To obtaining the full required hydraulic functionality the work may be focused around a concept with four 2-way valves in a Wheatstone configuration. With regard to hydraulic valves this configuration has been known for years, a recent reference is [15], and is therefore no longer patentable. Due to the double up of sensors and actuators compared to the spool concept in figure 2.4, then using the Wheatstone configuration is only feasible if integration of zero leak on the metering elements by using seat valves is desirable. A number of new separate meter-in separate meter-out concepts have therefore been considered. These are presented in the following section.

## 2.4 New separate meter-in separate meter-out valve concepts

The first of the new concepts is sketched in figure 2.8. The suggested valve is inspired by the concept in figure 2.7, but two check valves (1,2) are added which passes the meter-in flow to the actuator. Additionally the 4-way valve (5) is made in the way that it decides the flow direction as well as controls the meter-in flow rate. The return path of the 4-way valve is large, such that it does only pose a negligible flow restriction compared to the two poppet valves (3,4), which control the meter-out flow rate. The concept requires three position sensors (6,7,8) and three actuators as shown. Provided the check valve functions of the poppet valves may handle full meter-in flow rate the two check valves (1,2) may be omitted.

The functionality and sensor actuator requirements are listed in table 2.6. The advantage over the concept in figure 2.7 is that sectional regeneration may be made corresponding to no. 11 in table 2.1. As mentioned, integrating both a regenerative lower position and a regenerative lift position in the 4-way valve will be mechanically complicated.

Float	Regen. lift	Regen. lower	Sectional regen.	No. of single acting actuators	No. of double acting actuators	No. of position sensors	Integrated zero leak
+	-	+	(+)	2	1	3	(+)

Table 2.6: Functionality and sensor/actuator requirements for valve concept one.

The second considered valve concept is sketched in figure 2.9. The valve concept is based on a 3-way valve (1) for controlling the meter-in flow rate, and two 2-way valves (2,3) for controlling the meter-out flow rate. Without the auxiliary valve (4) the valve concept may do regenerative lower through the drain line and float. The auxiliary valve (4) only has to be included if regenerative lift is required for a particular application, or if direct port to port regenerative lower is required. The check valves (5,6) may be omitted if zero leak is not required. Sectional regeneration is only realisable if these check valves are removed. For this case sectional regeneration corresponds to no. 11 in

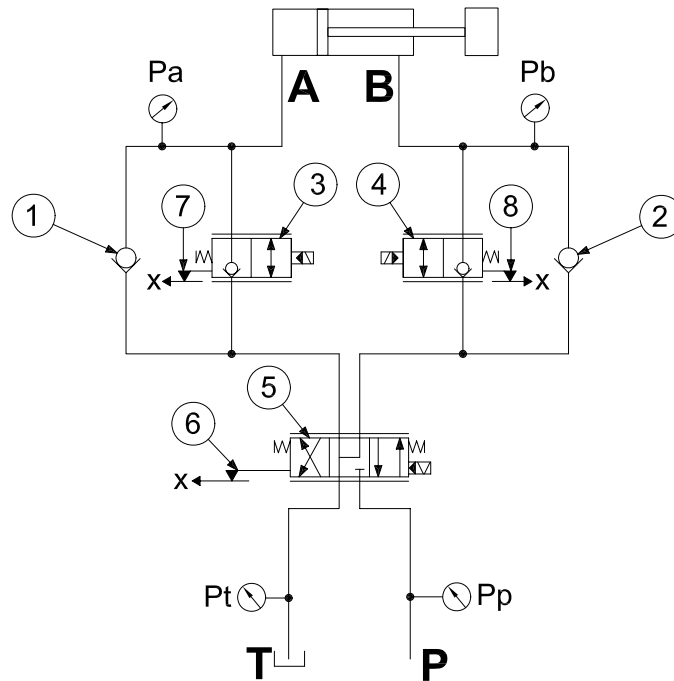


Figure 2.8: Valve concept one.

table 2.1. Sectional regeneration and integrated zero leak are not possible at the same time. The actuator and sensor requirements are listed in table 2.7.

Float	Regen. lift	Regen. lower	Sectional regen.	No. of single acting actuators	No. of double acting actuators	No. of position sensors	Integrated zero leak
+	-	+	-	2	1	3	(+)
+	+	+	-	2 + 1 on/off	1	3	(+)
+	-	+	(+)	2	1	3	-
+	+	+	(+)	2 + 1 on/off	1	3	-

Table 2.7: Functionality and sensor/actuator requirements for valve concept two.

The two valve concepts presented above mainly differ from the Wheatstone valve configuration in that a single spool valve is used for controlling the meter-in flow. One actuator and one position sensor are thus saved while zero leak may still be integrated in the valve concept, without using pilot operated check valves in the work port connections of the valve. Due these limited advantages another valve concept is proposed. This is sketched in figure 2.10.

This valve concept may do float, regenerative lower, regenerative lift and sectional regeneration due to the most right throttling position incorporated on the two 3-way valves (1,2). It should be noted that in these positions throttling may only take place for the work port denoted by B in the figure, whereas the work port denoted by A will be fully open. Thus the valve concept may only do regenerative functions for unidirectional loads which is a limitation compared to the concept in figure 2.4 and the Wheatstone



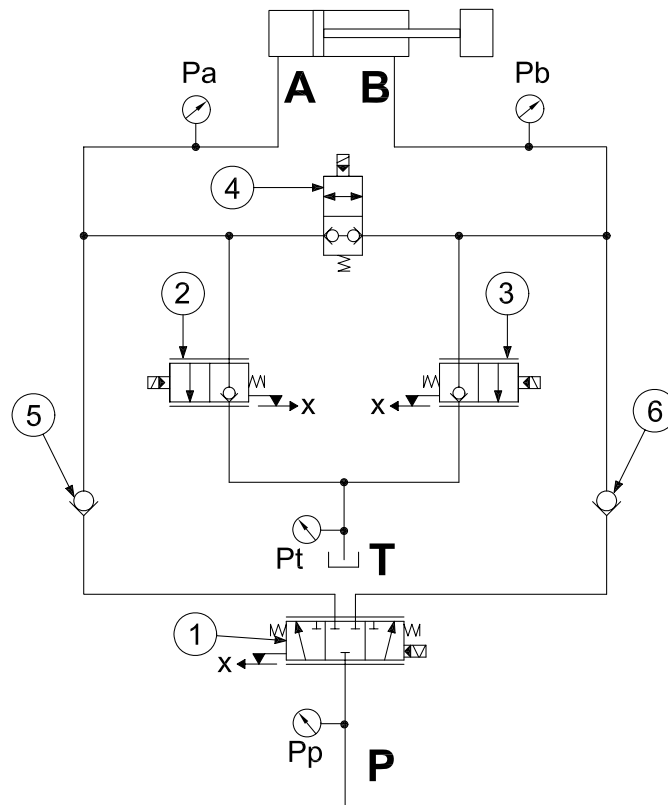


Figure 2.9: Valve concept two.

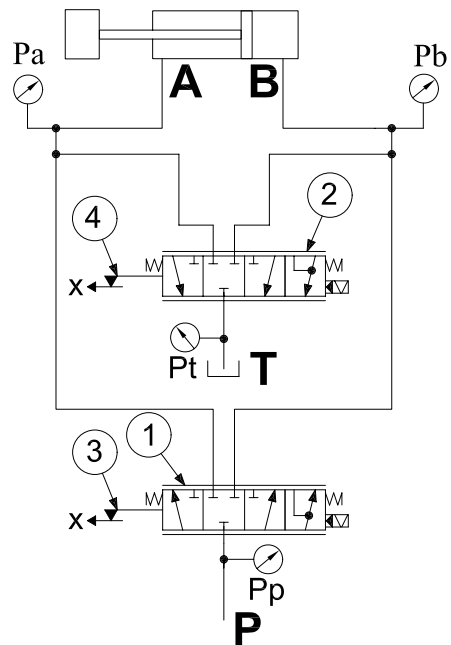


Figure 2.10: Valve concept three.

valve configuration in figure 2.6. Often gravitational loads give unidirectional loads on a hydraulic actuator and the limitation in this case is not a disadvantage. If zero leakage is a requirement pilot operated check valves in the A and B ports of the figure must be used (this is not shown). The actuator and sensor requirements are listed in table 2.8.

Float	Regen. lift	Regen. lower	Sectional regen.	No. of single acting actuators	No. of double acting actuators	No. of position sensors	Integrated zero leak
+	+	+	+	(4)	2	2	-

Table 2.8: Functionality and sensor/actuator requirements for valve concept three.

According to the selection criterion presented in section (2.1), the concept in figure 2.10 of those presented is the best alternative to the preferred concept in figure 2.4, which as mentioned is protected by a patent. The concept in figure 2.10 offers the full metering functionality, albeit for unidirectional loads only, by using two mechanical degrees of freedom to be actuated.

From a technological point of view *The Company* already has the technology for competitive manufacturing of spool valves with pilot operated check valves. Thus with respect to in-house technologies a spool valve concept seems as that most feasible for *The Company*. Therefore the valve concept in figure 2.10 is selected for further study.

Other valve concepts have been considered, however only the most feasible ones compared to the selection criterion described in section 2.1 have been shown here.

## 2.5 Actuation methods

In the above only main stage topologies of separate meter-in separate meter-out valves have been discussed. The actuation method associated with the valve members of a specific topology is another issue. In general a valve member may be directly actuated or actuated by a pilot pressure. Preferably a valve should be directly actuated if possible, due to improved dynamical properties. However, this require a number of issues to be solved due to the required force level to do so. These are:

- Current state of the art electromechanical actuators do not provide enough force for handling the flow forces in spool valves, unless flow force compensation is used. Regarding spool valves several methods for flow force compensation are possible [39]. However, the most effective of these require that the spool valve is designed with an outer sleeve. Such a design is, however, too expensive for use in mobile fluid power valves and gives a less compact envelope of the valve.
- Increasing force requires increasing electrical power and the cost of power electronics increases when the necessary power handling capacity increases.
- To drive valves requiring large power levels an increase of the voltage level of the electrical circuit of a mobile machine is necessary to keep down the current.

Due to these issues actuation via a pilot circuit is found necessary.

Different hydraulic pilot actuation circuits candidate for the actuation of spool valves. The fail safe state of valves for mobile systems (except for steering systems) is that all orifices of the main stage are closed. This fail safe state must be obtainable if electrical power fails. Thus for a spring centred spool valve this means that the spool must be forced back to the null position at power loss. This gives the one restriction on the pilot actuation circuit that it must balance the pressures in pilot chambers facing the ends of the main spool if power fails. Four pilot actuation schemes whereby this is obtained are sketched in figure 2.11. The 2-way valves of the three upper circuits are on-off valves but continuously controllable ones are also possible. As shown in [75] other combinations of fixed and variable orifices are possible, but not all of these fulfil the fail safe condition.

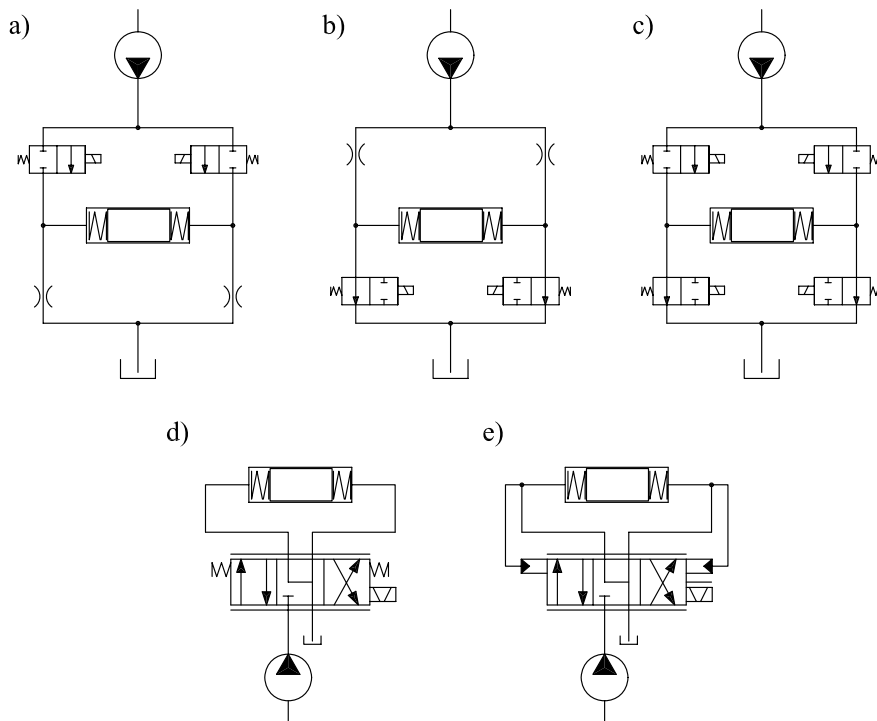


Figure 2.11: Pilot actuation circuits for spool valves.

The circuit in figure 2.11c is the one used in the current product portfolio of *The Company's* proportional valves. Therefore it will be obvious as a first choice to reuse available technologies for the actuation of the selected separate meter-in separate meter-out valve concept. However, when a pressure compensation spool is not present in the valve, the bandwidth requirement is higher than what may be obtained with the current solenoid valve technology of *The Company*. The use of a 4-way spool, e.g. as sketched in figures 2.11d and 2.11e, is therefore the preferred solution to be able to use already available electromechanical actuator technology. The fail safe position of the pilot spool which is the centre position may be established by spring centring or by feedback of the pilot pressures as shown. Both are considered in the subsequent chapter.

Several types of electromechanical actuators may be used, each having different characteristics with regard to force/torque, stroke and linearity. Electromechanical actuators which are more or less commonly used in hydraulic valves are shown in table 2.9, along with their typical force/stroke characteristic, and examples of attainable work for the full stroke. The numbers should, however, be taken with some caution as improvement of the different actuator types is continuously taking place.

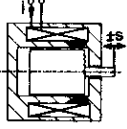
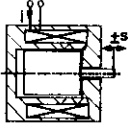
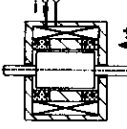

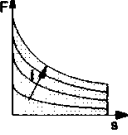
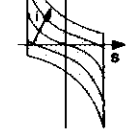
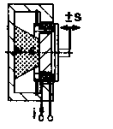
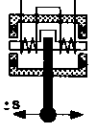
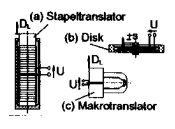

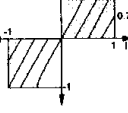
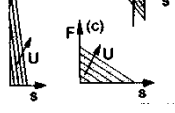
Actuator type	Proportional solenoid	On/off solenoid	Linear force motor
Example design			
Force/stroke			
Max. force [N]	55-180	55-200	$\pm 100 - 300$
Work-stroke [Nmm]	80-320	75-800	140-780
Input power [W]	18-32	16-38	7.2-65
Actuator type	Voice coil	Torque motor	Piezo actuator
Example design			
Force/stroke			
Max. force [N]	$\pm 60$	-	a) 3500 b) 35 c) 50
Force-stroke [Nmm]	$> 100$	2-40	a) 400 b) 7 c) 50
Input power [W]	30	0.02-4	typ. 50

Table 2.9: Electromechanical actuators for fluid power components, [75].

To enlarge the bandwidth of the pilot circuit the movable mass of the actuator should be low compared to the obtainable force. Furthermore, because no direct feedback of the pilot spool position is to be used the actuator should preferably have a good linearity between current and force. Both of these requirements points at the voice coil actuator as the preferred option. In the following a dual spool valve concept using voice coil actuators and a 4-way spool in the pilot circuit is studied.

## 2.6 Summary and conclusion

The chapter was started by presenting the criterion for conceptual evaluation of separate meter-in separate meter-out valve concepts according to the priorities of *The Company*. This criterion is:

*Increase functionality while reducing the number of required continuously controllable independent mechanical valve members with flow metering orifices. Hereby reducing the number of position sensors and mechanical degrees of freedom in the actuating system.*

The hydraulic functions requiring attention, when selecting the mechanical valve concept of a single programmable valve section, was explained. These functions are:

- Regenerative lowering
- Regenerative lifting
- Float
- Sectional regeneration

Next, state of the art valve concepts were evaluated, according to the required functionality and priorities of *The Company*, and new concepts were proposed. It was argued that a pilot stage for actuating the main valves of the selected valve concept is necessary, and the preferred option among different electromechanical actuation methods was pointed out. As a result of these steps the valve concept in figure 2.12 is the one which is studied further.

In addition to the spring centred pilot valves shown in the figure, ones which are moved to their fail safe positions by pressure feedback are also considered in the following. Due to the research being limited to generic separate meter-in separate meter-out control, as stated in the demarcation of research in the introduction, spools with regenerative functions as shown in figure 2.10 are not considered.

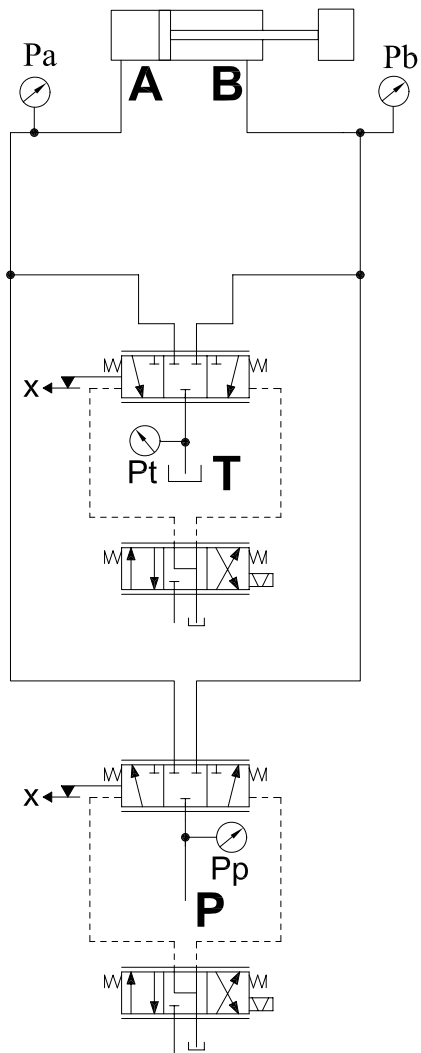


Figure 2.12: Selected valve concept.



# Chapter 3

## Mathematical models of separate meter-in separate meter-out valve

### Contents

---

<b>3.1</b>	<b>State of the art - Modelling of spool valves . . . . .</b>	<b>39</b>
<b>3.2</b>	<b>Pilot and main spool interaction . . . . .</b>	<b>40</b>
<b>3.3</b>	<b>Non-linear model description . . . . .</b>	<b>42</b>
<b>3.4</b>	<b>Prototype of spool valve . . . . .</b>	<b>51</b>
<b>3.5</b>	<b>Verification of non-linear model . . . . .</b>	<b>53</b>
<b>3.6</b>	<b>Linear model descriptions . . . . .</b>	<b>63</b>
<b>3.7</b>	<b>Summary and conclusion . . . . .</b>	<b>75</b>

---

In this chapter a non-linear and a linear mathematical model of the pilot operated spools, of the separate meter-in separate meter-out spool valve concept presented in the previous chapter, are derived. The non-linear model shall be used to test the developed controllers in a simulation environment. The linear model, which is a linearisation of the non-linear model, with some non-linearisable non-linearities omitted, is to be used for controller design. As the meter-in and the meter-out part of the selected valve concept are identical only half a valve is considered and interaction between the meter-in and meter-out parts through the pilot circuit is assumed to be negligible.

### 3.1 State of the art - Modelling of spool valves

When modelling valve devices, such as a spool valve, one of the largest difficulties is to obtain a lumped yet fairly accurate description of the flow across the variable orifice. Much work has been done modelling and analysing systems incorporating valves with flapper nozzle pilot stages. These models are often based on the turbulent flow equation, see e.g. [7, 10, 70, 77]. For other valve types, such as the two stage spool valves considered here, this approach is expected not to be applicable, since the flow rate from the pilot stage may be small. Researches have dealt with modelling flow



rates across orifices at small pressure drops and openings [107, 108]. The work was based on empirical models, and did not give a direct connection between measurable design parameters and flow rate. Others analysed the numerical problems that may arise due to the infinite flow gain, when using the turbulent flow equation at zero pressure drop [37]. The developed flow model used a quadratic polynomial in the pressure drop to model transition between laminar and turbulent flow. The model had very good numerical performance but the accuracy at small pressure drops was one of its weak points. Blackburn and others [19, 70] suggested a discharge coefficient proportional to the square root of the Reynolds number up to turbulent flow. Finally, Lebrun [58] used a modification of the orifice equation, making the discharge coefficient proportional to the flow number. Hereby, he obtained a flow rate proportional to the pressure drop as for laminar flow.

## 3.2 Pilot and main spool interaction

Two different means of pilot operation is considered, as mentioned in the previous chapter. One where the output of the pilot control unit is a differential pilot pressure in response to the applied force to the pilot spool. This will be referred to as pressure control pilot. A valve with such a pressure control pilot stage is depicted in figure 3.1. In this design the main spool is spring centred and the pilot spool is centred by pressure feedback. The pressures in the pilot chambers facing the ends of the main spool are fed back to the pilot spool. If the force input is removed from the pilot spool, the forces (being flow and spring forces) acting on the main spool will impose a force on the pilot spool, through the pressure feedback pins, moving it to a position so fluid is vented from the pilot chambers. Hereby, the main spool will move to its neutral with respect to force balance. Besides acting as a centring device for the pilot spool, the pressure feedback also acts as a proportional closed loop pilot pressure controller (therefore the name pressure control pilot).

Assuming that the pilot spool has port overlap of the pressure port and underlap of the drain port in neutral. To avoid leakage between the pressure port and the drain port by direct short circuiting, it is then required that<sup>1</sup>

$$\Delta_{pa} \geq \Delta_{ta} \wedge \Delta_{pb} \geq \Delta_{tb} \quad (3.1)$$

This condition gives two local intervals  $\Delta_{ta} < x_p < \Delta_{pa}$  and  $-\Delta_{pb} < x_p < -\Delta_{tb}$  where the pilot valve is closed of to the chambers carrying pressures  $p_{pa}$  and  $p_{pb}$  respectively due to spool overlap. The overlap has the effect of two local dead-zones. The size of the dead-zone depends on the relative sizes of the pilot spool port laps. Which of the two local dead-zones that are active depends on the sign of the actual main spool position. If  $x_m > 0$  the dead-zone is given by

$$\Delta_{DZ} = \Delta_{pa} - \Delta_{ta} \quad (3.2)$$

---

<sup>1</sup>Pressure port overlap and drain port underlap are considered positive as they are shown in figure 3.1.

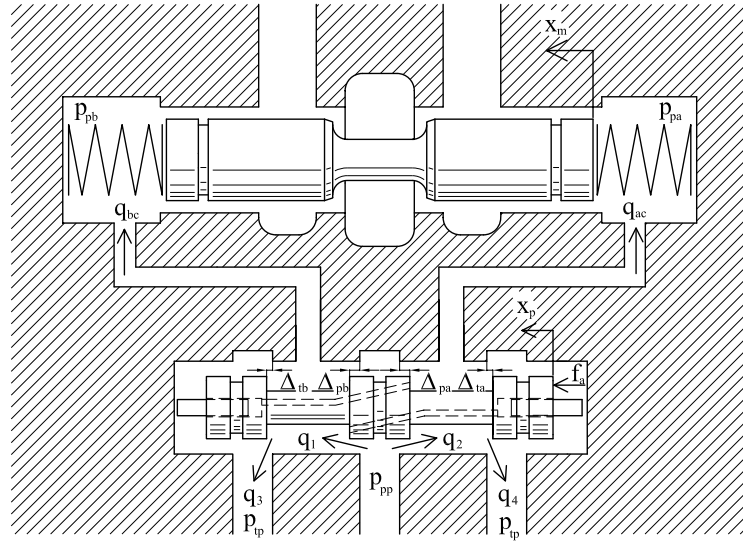


Figure 3.1: Spool valve with pressure control pilot (The voice coil actuator is not shown).

If  $x_m < 0$  the dead-zone is given by

$$\Delta_{DZ} = \Delta_{pb} - \Delta_{tb} \quad (3.3)$$

If  $x_m = 0$  and the pressure port is overlapped the dead-zone is given by

$$\Delta_{DZ} = \Delta_{pa} - \Delta_{pb} \quad (3.4)$$

If the situation where the main spool velocity is zero and the main spool shall move across its neutral position is considered, say from a positive to a negative position, then from the above, it may be realised that the main spool moves in the negative direction due to flow and spring forces when the pilot spool position is  $x_p \leq \Delta_{ta}$ . When the main spool reaches  $x_m = 0$  the pilot spool shall move to  $x_p \leq -\Delta_{pb}$ , to build up the pressure denoted  $p_{pb}$ , thus moving the main spool further in the negative direction. This means that the size of the dead-zone depends on the sign of the main spool position reference, which again is because the pilot spool operates by a combination of meter-in and meter-out.

Similarly to (3.4), if  $x_m = 0$  and the pressure port is underlapped, while (3.1) still holds, the dead-zone is given by

$$\Delta_{DZ} = \Delta_{ta} - \Delta_{tb} \quad (3.5)$$

The second considered pilot control scheme is one where the output of the pilot stage is a flow in response to the force applied to the pilot spool. This will be referred to as a flow control pilot. A valve with this pilot control scheme is depicted in figure 3.2. In this design both the pilot spool and the main spool are spring centred. In the force neutral

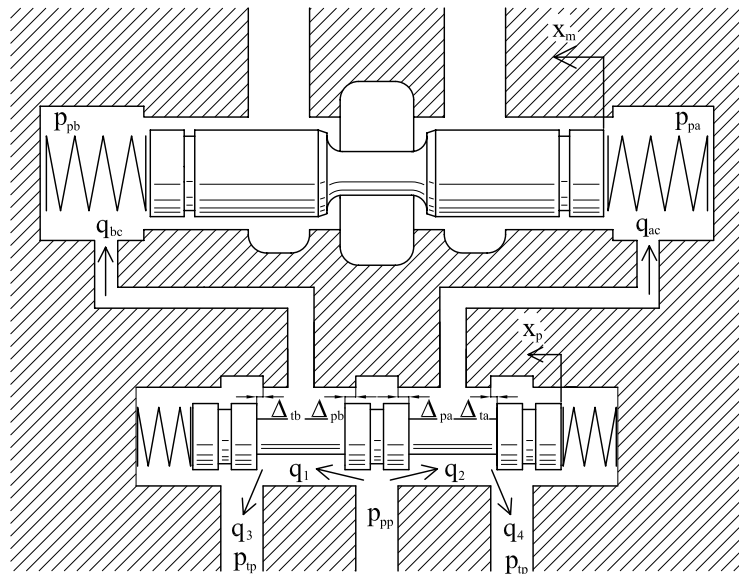


Figure 3.2: Spool valve with flow control pilot (The voice coil actuator is not shown).

position, the drain port of the pilot spool is underlapped to secure that the main spool may return to neutral at power loss. The same comments as given above regarding the dead-zone of the pilot spool applies to this design, except as mentioned the drain ports of the pilot spool are always underlapped in neutral and consequently the pressure ports are always overlapped in neutral due to (3.1).

### 3.3 Non-linear model description

In this section a non-linear model of the two pilot controlled spool valves sketched in figures 3.1 and 3.2 is derived. The assumptions made to derive the model are that

- Incompressible fluid (Bernoulli) is assumed for the derived flow equations.
- For the design with pressure control pilot, it is assumed that fluid inside the pressure chambers formed between the feedback pins and the pilot spool is incompressible.
- Due to the fact the the voice coil actuator of the prototype valve presented further below is to be current controlled, the dynamics of the electrical circuit of the actuator is omitted in the model. This may be done provided the driving voltage for the actuator is high enough.
- The force constant of the actuator is assumed independent of actuator stroke. In practice the force constant of the used actuator does not vary more than  $\pm 10\%$  according to the manufacturer, why this is a reasonable assumption

It may not be transparent how the non-linear equations presented in this section link with each other. The block diagram in figure 3.3 shows the interconnections in the model. However, the reader is encouraged to use the nomenclature given in the beginning of the thesis. A variable with an  $i$  as a sub index, such as  $X_{x_i}$ , means the variable, such as  $X_x$ , associated with the  $i$ 'th flow. Furthermore,  $i = \{1,2,3,4\}$  is used for denoting the flows associated with the pilot spool, and  $i = \{5,6,7,8\}$  is used for denoting the flows associated with the main spool.

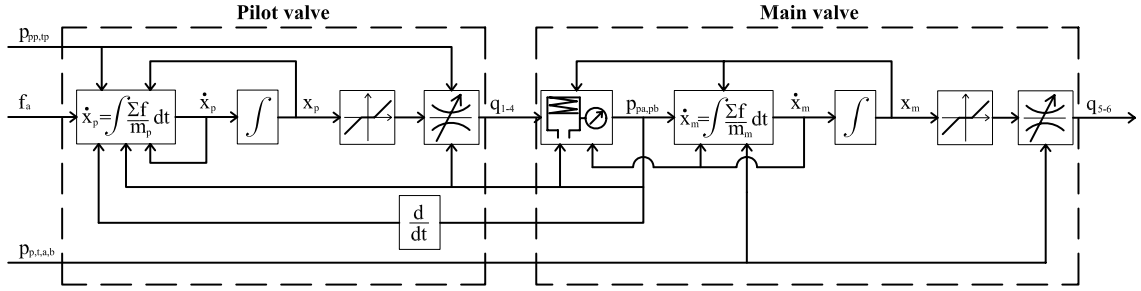


Figure 3.3: Block diagram of valve model.

### 3.3.1 Non-linear flow equation

For flow across a metering land three different flow scenarios may occur, namely

- Laminar flow
- Transition between laminar and turbulent flow
- Turbulent flow

In the present work the approach described in [58] is used to model the transition from laminar leakage to turbulent flow. This transition may be approximated by

$$q = \delta_q \lambda_q A_o(x_l) \sqrt{\frac{2}{\rho} |\Delta p| \text{sign}(\Delta p)} \quad Re < Re_t \quad (3.6)$$

where the flow number is defined by

$$\lambda_q = \frac{d_h(x_l)}{\nu} \sqrt{\frac{2}{\rho} |\Delta p|} \quad (3.7)$$

For a large spool overlap compared to the clearance between spool and housing the flow through the clearance may be modelled by [19]

$$q = \frac{\pi(d + 2C_r)C_r^3(1 + \frac{3}{2}(\frac{\epsilon_r}{C_r})^2)\Delta p}{-12\mu x_l} \quad x_l \leq -10C_r \quad (3.8)$$

It will be shown in the model verification that this equation gives fairly accurate results down to an overlap length of  $10C_r$ , why this limit is used. Lebrun [58] accounted for radial clearance in the orifice area used in (3.6) and added a coefficient to the overlapped length of (3.8), to ensure continuity between equations (3.6) and (3.8). During tests carried out obtaining results for the model verification presented in the next section, this approach has shown not to correlate well with the measured overlap for large clearances. In this work the clearance will simply be disregarded in the area used for (3.6) and the maximum leakage flow computed by (3.8) at  $x_l = -10C_r$  will be added to (3.6) instead. Additionally the theoretical opening point of the orifice is set to be at  $x_l = -10C_r$ , e.g. see (3.13) below. Effectively this means that the used overlap in the simulation model is  $10C_r$  smaller than the mechanically measured one.

At high flow rates, where the flow pattern is turbulent, the discharge coefficient is approximately constant and the flow may be computed by

$$q = C_d A_o(x_l) \sqrt{\frac{2}{\rho} |\Delta p| \text{sign}(\Delta p)} \quad Re \geq Re_t \quad (3.9)$$

Assuming that the discharge coefficient and Reynolds number at transition to turbulent flow are known<sup>2</sup>,  $\delta_q$  may be found via the Reynolds number at transition to turbulent flow. Substituting (3.9) into the equation for the Reynolds number and rearranging gives

$$Re_t = \frac{V_q d_h(x_l)}{\nu} = \frac{q d_h(x_l)}{A_o(x_l) \nu} = \frac{C_d \sqrt{\frac{2}{\rho} |\Delta p|} d_h(x_l)}{\nu} \Rightarrow \sqrt{\frac{2}{\rho} |\Delta p|} = \frac{Re_t \nu}{C_d d_h(x_l)} \quad (3.10)$$

From (3.6), (3.7), (3.9) and (3.10) we get

$$C_d = \delta_q \lambda_q = \delta_q \frac{d_h(x_l)}{\nu} \sqrt{\frac{2}{\rho} |\Delta p|} = \frac{\delta_q Re_t}{C_d} \Rightarrow \delta_q = \frac{C_d^2}{Re_t} \quad (3.11)$$

The axial orifice opening  $x_t$  at which  $Re_t$  is reached can be calculated if the inverse of the hydraulic diameter may be found, that is

$$x_t = d_h^{-1} \left( \frac{Re_t \nu}{C_d \sqrt{\frac{2}{\rho} |\Delta p|}} \right) \quad (3.12)$$

A complete set of equations describing the flow across a metering land of a spool valve from laminar leakage through transition region to turbulent flow has been derived. The equations are based on knowledge of the discharge coefficient at fully developed turbulent

---

<sup>2</sup>Experimental measurements are most often necessary to determine these numbers.

flow and the Reynolds number at which this occurs. Unfortunately these parameters are highly uncertain. The derived equations are valid for a spool valve with an arbitrary orifice area characteristic. In appendix B, area equations as a function of spool position are given for the case of rectangular fluid ports and and metering lands with circular notches.

### 3.3.2 Pilot valve model

Consider the pilot spool depicted in figure 3.4. Based on equations (3.6), (3.8) and (3.9) the flows across the four metering lands may be described by

$$q_i = \begin{cases} \left(1 + \frac{3}{2} \left(\frac{\epsilon_{rp}}{C_{rp}}\right)^2\right) \frac{\pi d_p C_{rp}^3 \Delta p_i}{12 \mu L_1} & x_{l_i} \leq -L_1 \\ -\left(1 + \frac{3}{2} \left(\frac{\epsilon_{rp}}{C_{rp}}\right)^2\right) \frac{\pi d_p C_{rp}^3 \Delta p_i}{12 \mu x_{l_i}} & -L_1 < x_{l_i} \leq -10 C_{rp} \\ \delta_{q_i} \lambda_{q_i} A_{o_i}(x_{l_i} + 10 C_{rp}) \sqrt{\frac{2}{\rho} |\Delta p_i|} \text{sign}(\Delta p_i) + q_{l_i} & Re < Re_{t_i} \wedge x_{l_i} > -10 C_{rp} \\ C_{d_i} A_{o_i}(x_{l_i} + 10 C_{rp}) \sqrt{\frac{2}{\rho} |\Delta p_i|} \text{sign}(\Delta p_i) + q_{l_i} & Re \geq Re_{t_i} \wedge x_{l_i} > -10 C_{rp} \end{cases} \quad i = \{1, 2, 3, 4\} \quad (3.13)$$

where

$$\begin{aligned} x_{l_1} &= -x_p - \Delta_{pb} & ; & \quad \Delta_{pb} > 0 \quad \text{for overlap} & \wedge & \quad \Delta p_1 = p_{pp} - p_{pb} \\ x_{l_2} &= x_p - \Delta_{pa} & ; & \quad \Delta_{pa} > 0 \quad \text{for overlap} & \wedge & \quad \Delta p_2 = p_{pp} - p_{pa} \\ x_{l_3} &= x_p + \Delta_{tb} & ; & \quad \Delta_{tb} > 0 \quad \text{for underlap} & \wedge & \quad \Delta p_3 = p_{pb} - p_{pt} \\ x_{l_4} &= -x_p + \Delta_{ta} & ; & \quad \Delta_{ta} > 0 \quad \text{for underlap} & \wedge & \quad \Delta p_4 = p_{pa} - p_{pt} \end{aligned} \quad (3.14)$$

$$q_i = \left(1 + \frac{3}{2} \left(\frac{\epsilon_{rp}}{C_{rp}}\right)^2\right) \frac{\pi d_p C_{rp}^2 \Delta p_i}{120 \mu} \quad (3.15)$$

$$\begin{aligned} q_{ac} &= q_2 - q_4 \\ q_{bc} &= q_1 - q_3 \end{aligned} \quad (3.16)$$

The pilot spool acceleration is governed by

$$\ddot{x}_p = \frac{1}{m_p} (f_a - f_{cp} - f_{vp} - f_{fp} - f_{sp} - f_{pp}) \quad (3.17)$$

where  $f_{sp}$  is the spring force, which is zero for the pressure control pilot valve, and  $f_{pp}$  is the pressure feedback force, which is zero for the flow control pilot valve.

Previous works [7, 10, 77] have been able to describe the dynamic characteristics of servo valves fairly well, without including Coulomb friction in the force balance of the spool. Whether this is due the particular valve designs, or because the driving circuits

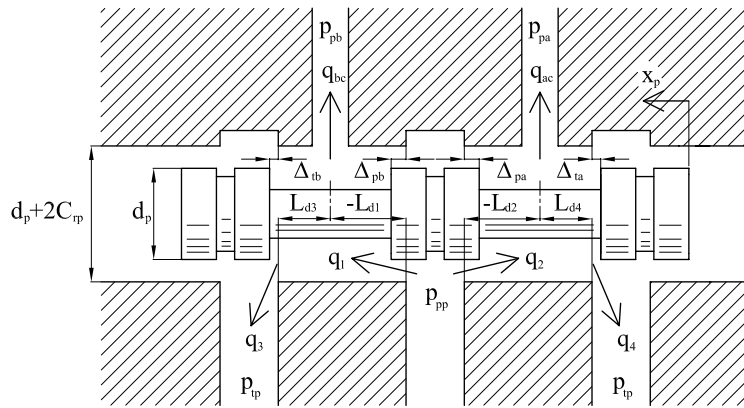


Figure 3.4: Pilot spool with designation of flows, pressures and dimensions.

of the examined valves include friction compensation is not transparent from these references. In [114], however, it is suggested that Coulomb friction is included. The latter is the approach used here, as discontinuities may have a quite crucial impact on the performance of control systems. Coulomb friction is included in this model by

$$f_{cp} = \begin{cases} \frac{f_{cp0}}{\delta x_{p0}} \delta x_p & |\delta x_p| \leq \delta x_{p0} \\ f_{cp1} \text{sign}(\dot{x}_p) & |\delta x_p| > \delta x_{p0} \end{cases} \quad (3.18)$$

Note, the friction model includes both hysteresis and stiction due to the friction forces  $f_{cp0} \geq f_{cp1}$  which may have different magnitudes. The model may be seen as a simple extension of the model reported in [87], which only used one friction force for both zero and non-zero velocity. In (3.18),  $f_{cp0}$  is the maximum Coulomb friction force and  $\delta x_{p0}$  is the length which the pilot spool must move before this force is developed. The two parameters characterises the hysteresis loop as illustrated in figure 3.5

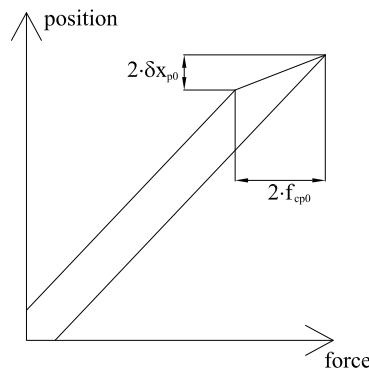


Figure 3.5: Hysteresis sketch.

Referring again to figure 3.4, the dynamic flow force associated with the  $i$ 'th flow and

adhering from the changing flow rate may, according to [19], be computed by<sup>3</sup>

$$f_{fd_i} = \rho L_{d_i} \frac{dq_i}{dt} = \rho L_{d_i} k_{p_i} \Delta p_i + \rho L_{d_i} k_{q_i} \dot{x}_{l_i} \quad (3.19)$$

In (3.19) the damping length  $L_{d_i}$  is considered constant. The part associated with the spool velocity  $\dot{x}_{l_i} = \dot{x}_p$  may be considered as a damping force. In (3.17),  $f_{vp}$  accounts for all damping forces on the pilot spool which are proportional to the spool velocity. Thus the afore-mentioned part of (3.19) is included in  $f_{vp}$ , which may be computed by

$$f_{vp} = \mu \left( \frac{2\pi d_p L_2}{C_{rp}} + k_{vc} \right) \dot{x}_p + \rho \sum_{i=1}^4 L_{d_i} k_{q_i} \frac{\partial x_{l_i}}{\partial x_p} \dot{x}_p \quad (3.20)$$

The left hand term within the closed brackets of (3.20) accounts for viscous friction on the spool and  $k_{vc}$  accounts for viscous damping acting on the coil of the voice coil actuator. The viscous damping length coefficient,  $k_{vc}$ , may be determined from the governing equations describing the flow which passes the coil as it moves. Consider the voice coil actuator depicted in figure 3.6.

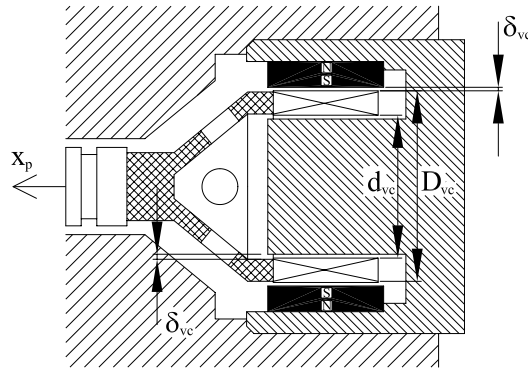


Figure 3.6: Voice coil actuator.

Assuming that drain holes are present in the coil holder (as shown). Then, the amount of oil which must pass the coil as it moves is equal to that displaced by the end face area of the coil times the moved distance. Thus, the displacement flow is given by

$$q_{vc} = A_{vc} \dot{x}_p = \frac{\pi}{4} (D_{vc}^2 - d_{vc}^2) \dot{x}_p \quad (3.21)$$

The flow must pass the radial clearances with thickness  $\delta_{vc}$  between the coil and field assembly. This may be approximated by the flow in two ducts, i.e. past the two sides of the coil, each described by a tube with a concentric cylinder. Note, depending on the

<sup>3</sup>Flow and pressure gains,  $k_{q_i} = \frac{\partial q_i}{\partial x_{l_i}}$  and  $k_{p_i} = \frac{\partial q_i}{\partial \Delta p_i}$  are derived in appendix C.



surface geometry, the coil may drag oil with it as it moves, e.g. see [103] chapter 2. This is neglected, however, as exact surface geometry of the coil is not known. By modelling the flow as laminar duct flow generated by a pressure difference, the total flow passing both coil sides may be computed by [74]

$$q_{vc} = \frac{\pi d_h^4}{2C_{vc}L_{vc}\mu} \Delta p = \frac{\pi d_h^4}{2C_{vc}L_{vc}\mu} \frac{f_{vc}}{A_{vc}} \quad (3.22)$$

In (3.22),  $d_h = 2\delta_{vc}$ , and  $C_{vc}$  is a friction factor that varies depending on the ratio between the inner and the outer duct diameters. It has been used that  $D_{vc} \gg \delta_{vc}$  and  $d_{vc} \gg \delta_{vc}$ , which, for the two flows passing the coil sides, gives approximately equal values of  $C_{vc}$ , because  $\frac{D_{vc}}{D_{vc}+\delta_{vc}} \approx \frac{d_{vc}-\delta_{vc}}{d_{vc}}$ .

From flow continuity (3.21) and (3.22) must be equal. Consequently  $k_{vc}$  may be computed as

$$\frac{\pi d_h^4}{4C_{vc}L_{vc}\mu} \frac{f_{vc}}{A_{vc}} = A_{vc} \dot{x}_p \Rightarrow k_{vc} = \frac{2C_{vc}L_{vc}A_{vc}^2}{\pi d_h^4} \quad (3.23)$$

To quantify the amount of damping that is applied to the coil compared to that applied to the spool some values are given in table 3.1<sup>4</sup>. The maximum Reynolds number associated with the results in the table is 547, for a fluid viscosity of 2 [cSt] and a pilot spool velocity of 0.35 [ $\frac{m}{s}$ ], which are used as extreme values. This indicates the validity of the laminar flow condition that was assumed for the damping force model. The coil damping force is thus expected to be much larger than the spool damping force, which is listed in the last column of the table.

$D_{vc}$	$d_{vc}$	$\delta_{vc}$	$\frac{D_{vc}}{D_{vc}+\delta_{vc}}$	$\frac{d_{vc}-\delta_{vc}}{d_{vc}}$	$L_{vc}$	$k_{vc}$	$d_p$	$L_2$	$C_{rp}$	$\frac{2\pi d_p L_2}{C_{rp}}$
30e-3	25e-3	1.00e-3	0.97	0.96	5e-3	<b>891</b>	8e-3	5e-3	3e-6	<b>84</b>
30e-3	25e-3	0.75e-3	0.98	0.97	5e-3	<b>2816</b>	8e-3	5e-3	3e-6	<b>84</b>
30e-3	25e-3	0.50e-3	0.98	0.98	5e-3	<b>14255</b>	8e-3	5e-3	3e-6	<b>84</b>
25e-3	20e-3	1.00e-3	0.96	0.95	5e-3	<b>596</b>	8e-3	5e-3	3e-6	<b>84</b>
25e-3	20e-3	0.75e-3	0.97	0.96	5e-3	<b>1885</b>	8e-3	5e-3	3e-6	<b>84</b>
25e-3	20e-3	0.50e-3	0.98	0.98	5e-3	<b>9543</b>	8e-3	5e-3	3e-6	<b>84</b>
20e-3	15e-3	1.00e-3	0.95	0.93	5e-3	<b>361</b>	8e-3	5e-3	3e-6	<b>84</b>
20e-3	15e-3	0.75e-3	0.96	0.95	5e-3	<b>1140</b>	8e-3	5e-3	3e-6	<b>84</b>
20e-3	15e-3	0.50e-3	0.98	0.97	5e-3	<b>5773</b>	8e-3	5e-3	3e-6	<b>84</b>

Table 3.1: Viscous damping length coefficients for various coil dimensions.

Referring again to the force balance of the pilot spool given by (3.17),  $f_{fp}$  describes the four static flow forces, and the pressure gradient dependent parts associated with the four dynamic flow forces. The latter is the part corresponding to the left hand term of (3.19).  $f_{fp}$  may be computed by

$$f_{fp} = \sum_{i=1}^4 \left[ q_i \sqrt{2\rho|\Delta p_i|} \cos(\theta_{q_i}) + \rho L_{d_i} \frac{\partial q_i}{\partial \Delta p_i} \Delta \dot{p}_i \right] \frac{\partial x_{l_i}}{\partial x_p} \quad (3.24)$$

<sup>4</sup>For a diameter ratio close to 1 a friction factor,  $C_{vc}$ , of 96.0 may be used [74].

The spring force acting on the pilot spool is given by

$$f_{sp} = f_{sp0} \text{sign}(x_p) + k_{sp} x_p \quad (3.25)$$

Finally, for a pilot circuit design with pressure feedback pins,  $f_{pp}$  is given by

$$f_{pp} = A_p(p_{pb} - p_{pa}) \quad (3.26)$$

Equations 3.25 and 3.26 are the only equations by which the dynamic models of the two valve designs in figures 3.1 and 3.2 differ.

### 3.3.3 Main valve model

The non-linear flow equation derived in section 3.3.1 also applies to the main spool. Hence, the flow equation for the main spool depicted in figure 3.7 is given by

$$q_i = \begin{cases} \left(1 + \frac{3}{2} \left(\frac{\epsilon_{rm}}{C_{rm}}\right)^2\right) \frac{\pi d_m C_{rm}^3 \Delta p_i}{12 \mu L_4} & x_{l_i} \leq -L_4 \\ -\left(1 + \frac{3}{2} \left(\frac{\epsilon_{rm}}{C_{rm}}\right)^2\right) \frac{\pi d_m C_{rm}^3 \Delta p_i}{12 \mu x_{l_i}} & -L_4 < x_{l_i} \leq -10 C_{rm} \\ \delta_{q_i} \lambda_{q_i} A_{o_i}(x_{l_i} + 10 C_{rm}) \sqrt{\frac{2}{\rho} |\Delta p_i|} \text{sign}(\Delta p_i) + q_{l_i} & Re < Re_{t_i} \wedge x_{l_i} > -10 C_{rm} \\ C_{d_i} A_{o_i}(x_{l_i} + 10 C_{rm}) \sqrt{\frac{2}{\rho} |\Delta p_i|} \text{sign}(\Delta p_i) + q_{l_i} & Re \geq Re_{t_i} \wedge x_{l_i} > -10 C_{rm} \end{cases} \quad i = \{5, 6\} \quad (3.27)$$

where

$$\begin{aligned} x_{l_5} &= x_m - \Delta_a \quad ; \quad \Delta_a > 0 \quad \text{for overlap} \quad \wedge \quad \Delta p_5 = p_p - p_a \\ x_{l_6} &= -x_m - \Delta_b \quad ; \quad \Delta_b > 0 \quad \text{for overlap} \quad \wedge \quad \Delta p_6 = p_p - p_b \end{aligned} \quad (3.28)$$

$$q_{l_i} = \left(1 + \frac{3}{2} \left(\frac{\epsilon_{rm}}{C_{rm}}\right)^2\right) \frac{\pi d_m C_{rm}^2 \Delta p_i}{120 \mu} \quad (3.29)$$

The main spool acceleration is found from the equation of motion

$$\ddot{x}_m = \frac{1}{m_m} (A_m (p_{pa} - p_{pb}) - f_{cm} - f_{vm} - f_{fm} - f_{sm}) \quad (3.30)$$

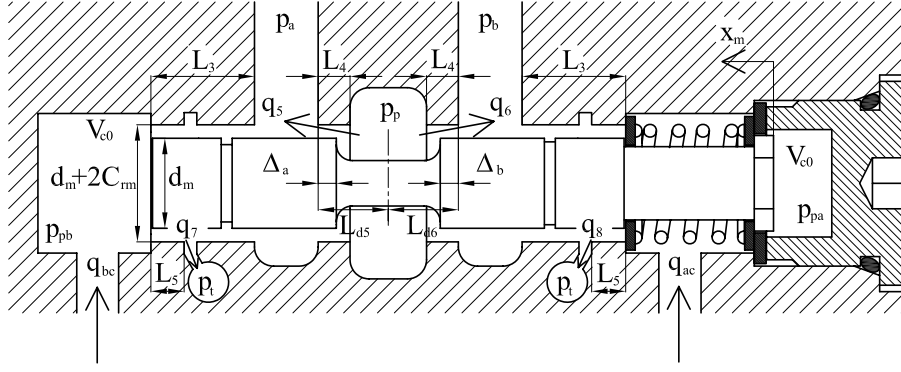


Figure 3.7: Main spool with designation of flows, pressures and dimensions.

The models of the spring force, Coulomb friction and viscous friction forces and the flow forces are similar to those already presented for the pilot spool. Thus, for the main spool these equations are presented with no further explanation.

The Coulomb friction force is given by

$$f_{cm} = \begin{cases} \frac{f_{cm0}}{\delta x_{m0}} \delta x_m & |\delta x_m| \leq \delta x_{m0} \\ f_{cm1} \text{sign}(\dot{x}_m) & |\delta x_m| > \delta x_{m0} \end{cases} \quad (3.31)$$

The sum of the viscous friction force and the velocity dependent dynamic flow force is given by

$$f_{vm} = \frac{2\mu\pi d_m L_3}{C_{rm}} \dot{x}_m + \rho L_{d_m} \sum_{i=5}^6 k_{q_i} \frac{\partial x_{l_i}}{\partial x_m} \dot{x}_m \quad (3.32)$$

The sum of the static flow force and the pressure gradient dependent dynamic flow force is given by

$$f_{fm} = \sum_{i=5}^6 \left[ q_i \sqrt{2\rho |\Delta p_i|} \cos(\theta_{q_i}) + \rho L_{d_i} \frac{\partial q_i}{\partial \Delta p_i} \Delta \dot{p}_i \right] \frac{\partial x_{l_i}}{\partial x_m} \quad (3.33)$$

The spring force is given by

$$f_{sm} = f_{sm0} \text{sign}(x_m) + k_{sm} x_m \quad (3.34)$$

The pressure build up in the pilot control chambers may be computed by

$$\dot{p}_{pa} = \frac{\beta_e(p_{pa})}{V_{c0} + A_m x_m} (q_{ac} - q_8 - A_m \dot{x}_m) \quad (3.35)$$

$$\dot{p}_{pb} = \frac{\beta_e(p_{pb})}{V_{c0} - A_m x_m} (q_{bc} - q_7 + A_m \dot{x}_m) \quad (3.36)$$

The leakage flows from the pilot control chambers are given by

$$q_i = \frac{\pi (d_m + 2C_{rm}) C_{rm}^3 \left(1 + \frac{3}{2} \left(\frac{\epsilon_{rm}}{C_{rm}}\right)^2\right) \Delta p_i}{12\mu L_5} \quad i = \{7, 8\} \quad (3.37)$$

where

$$\begin{aligned} \Delta p_7 &= p_{pb} - p_t \\ \Delta p_8 &= p_{pa} - p_t \end{aligned} \quad (3.38)$$

### 3.3.4 Effective bulk modulus

The effective bulk modulus, which is used in equations (3.35) and (3.36), is a way to represent the equivalent stiffness of the fluid together with the equivalent stiffness of other parts of the fluid power system, which deform when the pressure of the fluid increases. Common parts contributing to the equivalent stiffness are air contained in the fluid and flexibility of hoses and fluid containers, as for example the walls of a hydraulic cylinder. The model of the effective bulk modulus used here includes the stiffness of the fluid, the air in the fluid and flexibility of hoses if such are present in the modelled system<sup>5</sup>. The model is give by

$$\beta_e = \left( \frac{1}{\beta_f} + \frac{V_h}{V_i \beta_h} + \frac{V_a}{\beta_a} \right)^{-1} \quad (3.39)$$

where

$$\begin{aligned} V_a &= \left( \frac{p_{a0} V_{a0}^\kappa}{p} \right)^{\left(\frac{1}{\kappa}\right)} \\ \beta_a &= k(10^5 + p) \end{aligned}$$

and  $\kappa$  is the polytropic exponent. Fluid compression without heat loss is assumed why  $\kappa$  may be chosen equal to the adiabatic exponent. The parameters used for the model is found table A.4 of appendix A.

## 3.4 Prototype of spool valve

A prototype of the selected separate meter-in separate meter-out spool valve concept has been build with the purpose of being used for verifying the model derived above, and to be able to test various control strategies to be developed. The prototype is sketched in figure 3.8. To facilitate the manufacturing of the prototype, off the shelf components are used where possible. The main spools have been designed specifically

---

<sup>5</sup>The term modelling the hose stiffness may obviously be left out for the presented valve model, but the term is anyway included here as it is used for computations in section 3.6.3.

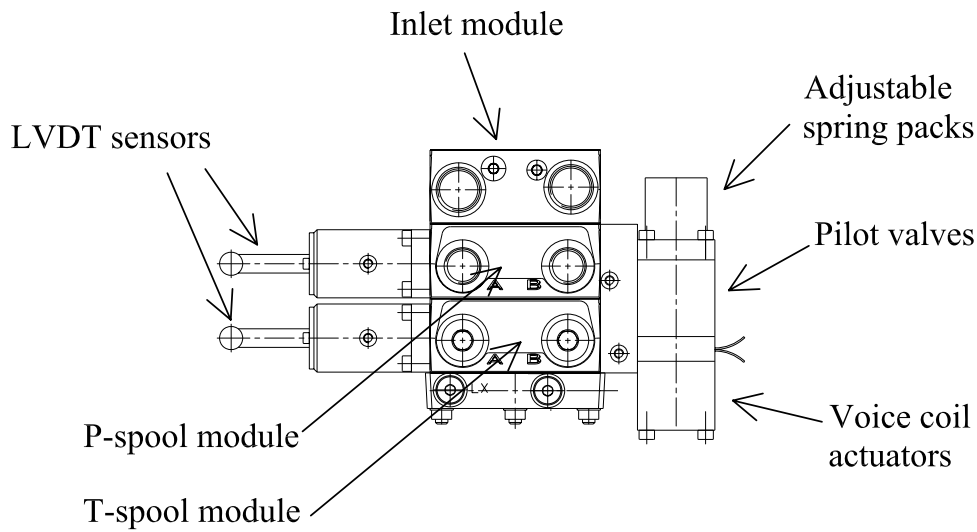


Figure 3.8: Separate meter-in separate meter-out prototype valve.

for the prototype, except that diameters are fixed, because two bulk castings from state of the art proportional valves are used for housings. Due to the component reuse, the meter-in function (P-spool) and the meter-out function (T-spool) are located in the two separate housings bolted together. The main spools have been made with sharp lands, i.e. without chamfering. For supplying the valve assembly, an inlet module from an existing proportional valve design is used as well. The main valve assembly features a cetop interface to easily fit two custom made pilot valves.

The mechanical components for the pilot valves have been designed and machined specifically for the prototype. To be able to verify the pilot valve separated from the main valve assembly, the pilot valves are of the flow control type with spring centred spools. The off the shelf components used for the prototype valve are:

- Voice coil actuators: BEI Kimco LA15-16-024A
- Voice coil amplifiers: BEI Kimco VCA10-70-000A
- LVDT amplifiers: RDP S7M
- LVDT sensors: Custom made HBM

In a addition to these bought in components a custom designed optical position sensor was used for accessing the pilot spool for position measurements.

The nominal design parameters of the prototype are listed in table A.1, A.3 and A.5 of appendix A. Note, some of these parameters in these tables are only used in the non-linear model of the valve and are therefore not design parameters. The prototype has been manufactured using ideal tolerances for low cost manufacturing to get as realistic a test object as possible.

## 3.5 Verification of non-linear model

In this section the results from the verification of the non-linear valve model are presented. The structure of the equations describing the pilot valve model and the main valve model are identical. Thus, it is assumed that verifying the model structure by conducting tests on the pilot valve separately is adequate.

### 3.5.1 Orifice parameters

Two different pilot valves have been made to verify the orifice model. One having rectangular fluid ports (sharp metering lands) and a large radial clearance, to verify the leakage model at large clearances. The other having round fluid ports (circular notches) to verify the used area equation for the round fluid ports, and the leakage model at small clearances. In the following the first mentioned pilot valve is referred to as PV-A and the latter as PV-B. Both prototypes were made with spring centred spools.

The geometric dimensions of the spools and housings, which are significant to verify the models, have been measured. The measured values associated with PV-A are listed in table 3.2. The measured values associated with PV-B are listed in table 3.3. The given sizes of the valve labs are relative to a common null position as in the model. Therefore, equal P-port valve lab size, i.e.  $\Delta_{pa} = \Delta_{pb}$ , has been chosen as the null position for the measurement.

Parameter	Value	Unit
$\Delta_{pa}, \Delta_{pb}$	0.70	[mm]
$\Delta_{ta}$	0.18	[mm]
$\Delta_{tb}$	0.42	[mm]
$d_p$	7.989	[mm]
$D_p$	8.007	[mm]
$C_{rp}$	9	[ $\mu\text{m}$ ]
Cylindricity housing	12.30	[ $\mu\text{m}$ ]
Cylindricity spool	1.90	[ $\mu\text{m}$ ]

Table 3.2: Measured parameters associated with PV-A (measuring accuracy  $\pm 1$  [ $\mu\text{m}$ ]).

Parameter	Value	Unit
$\Delta_{pa}, \Delta_{pb}$	0.74	[mm]
$\Delta_{ta}$	0.46	[mm]
$\Delta_{tb}$	0.38	[mm]
$d_p$	8.117	[mm]
$D_p$	8.122	[mm]
$C_{rp}$	2.5	[ $\mu\text{m}$ ]
Cylindricity housing	4.30	[ $\mu\text{m}$ ]
Cylindricity spool	1.45	[ $\mu\text{m}$ ]

Table 3.3: Measured parameters associated with PV-B (measuring accuracy  $\pm 1$  [ $\mu\text{m}$ ]).

### 3.5.2 Verification of orifice leakage model for large radial clearances

The measurements shown in this section have been made using PV-A. The flows across the pressure port lands have been measured to verify the orifice leakage model. The test set-up used to do this is sketched in figure 3.9.

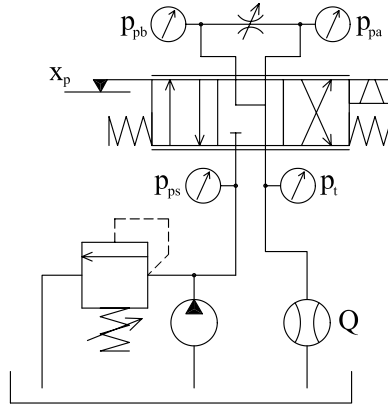


Figure 3.9: Hydraulic set-up used for testing pilot valve.

The oil temperature in the reservoir of the used hydraulic power pack was controlled why the viscosity of the oil has also been held constant during the tests. The measured flow characteristics for three different pressure drops are plotted in figures 3.10, 3.11 and 3.12 along with simulation results. It may be seen that the valve lap associated with the P-port is asymmetric in the actual neutral position (force neutral) at  $x_p = 0$  [mm].

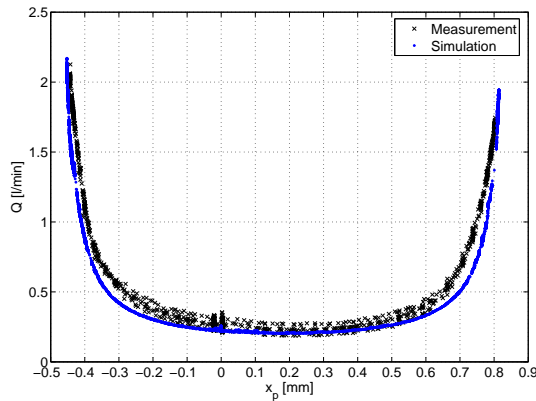


Figure 3.10: Flow characteristics of pilot valve,  $p_{pp} - p_{pa,pb} = 11$  [bar].

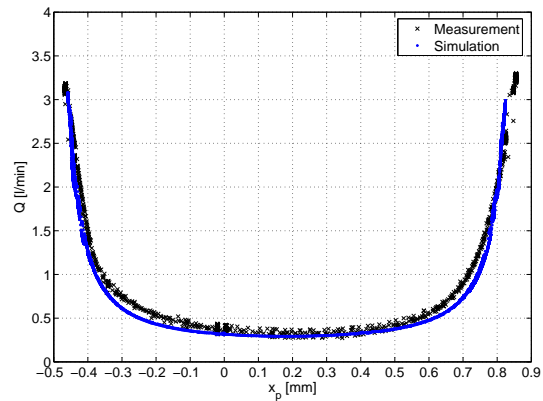


Figure 3.11: Flow characteristics of pilot valve,  $p_{pp} - p_{pa,pb} = 15$  [bar].

The parameter values used to obtain the presented simulation results are listed in table 3.4. The used values for valve overlap in the simulation model are smaller than the measured ones, e.g. see table 3.2. The difference may possibly be attributed to small

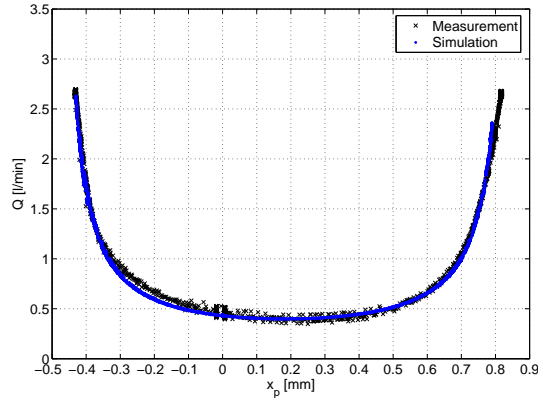


Figure 3.12: Flow characteristics of pilot valve,  $p_{pp} - p_{pa,pb} = 21$  [bar].

Parameter	Value	Unit
$\Delta_{pa}$	0.84	[mm]
$\Delta_{pb}$	0.48	[mm]
$C_{rp}$	15	[ $\mu\text{m}$ ]
$\epsilon_{rp}$	15	[ $\mu\text{m}$ ]

Table 3.4: Parameter values used in simulation.

chamfers due to deburring of the metering edges when manufacturing the spool. The total P-port spool lab measured is 1.4 [mm] and that used in the simulation is 1.32 [mm], meaning a difference of 0.04 [mm] per lab. Regarding the larger radial clearance used in the simulation, this is attributed to the cylindricity tolerances of the spool bore and the spool itself<sup>6</sup>. Taking into consideration the fairly small geometric parameter deviations necessary to make the simulated flow characteristics fit the measurements, a fair agreement between measurements and the simulation results is found for the three pressure drops. The model is found to model the leakage for overlaps  $> 10C_r$ , i.e. 10 times the radial clearance, sufficiently accurate.

### 3.5.3 Verification of orifice model for round fluid ports

The measurements shown in this section have been made on PV-B. The test set-up sketched in figure 3.9 has been used to obtain the measurements. Measurements by three different pressure drops across the valve have been made. The results in figures 3.13, 3.14 and 3.15 show that simulation results fit the measurements fairly well. Surprisingly, the Reynolds number used in the simulation to switch between the orifice equation for transition flow and the equation for turbulent flow was set as low as  $Re_t = 1$ . From a modelling point of view this means that for the considered pilot valve, the orifice equation modelling the transition between laminar and turbulent flow may be omitted. It was found that for the pressure levels of interest in the pilot circuit, the discharge

<sup>6</sup>Effectively the cylindricity tolerances mean that the bore for the spool and the spool itself are not ideally round.



coefficient is independent of pressure drop.

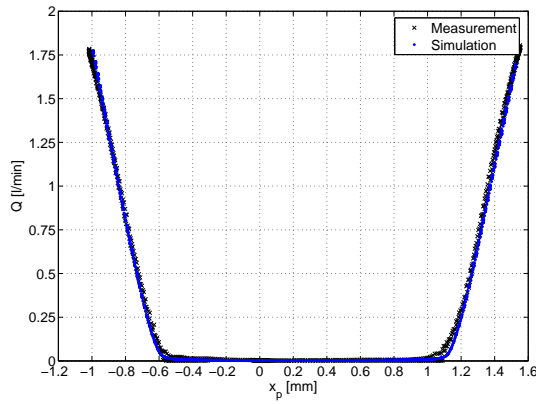


Figure 3.13: Flow characteristics of pilot valve,  $p_{pp} - p_{pa,pb} = 10$  [bar].

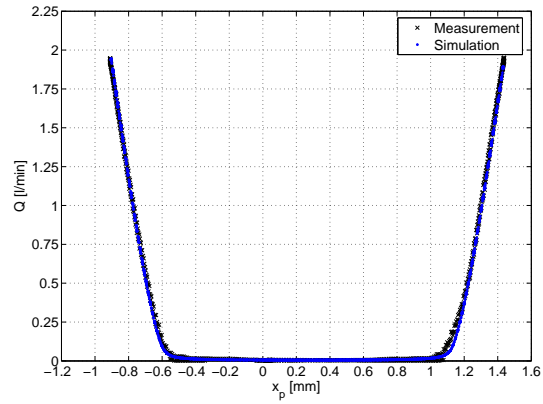


Figure 3.14: Flow characteristics of pilot valve,  $p_{pp} - p_{pa,pb} = 20$  [bar].

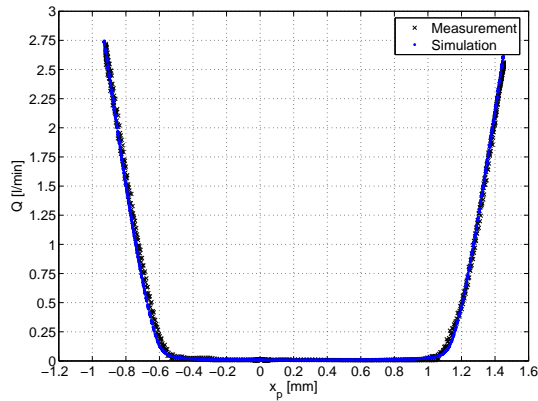


Figure 3.15: Flow characteristics of pilot valve,  $p_{pp} - p_{pa,pb} = 30$  [bar].

The parameter values used in the simulation are listed in table 3.5. By comparing the parameters with the ones in table 3.4, it may be seen that the total P-port overlap used to make the simulation results fit the measured ones is 0.29 [mm] larger than the measured total overlap. An explanation has not been found, but the error is of a size that one may expect human error to be involved<sup>7</sup>. The conclusion is that the flow characteristic relative to the opening point may be trusted but the opening point should be taken with some caution.

<sup>7</sup>Unfortunately, due to a mix of unfavourable circumstances there where no time to repeat the measurements after the error was discovered.

Parameter	Value	Unit
$\Delta_{pa}$	1.15	[mm]
$\Delta_{pb}$	0.62	[mm]
$C_{rp}$	3	[ $\mu\text{m}$ ]
$\epsilon_{rp}$	3	[ $\mu\text{m}$ ]

Table 3.5: Parameter values used in simulation.

### 3.5.4 Verification of hysteresis model

The measurements made to verify the hysteresis model was made on PV-A. The spool position as a function of a 0.05 Hz sinusoidal input current to the voice coil actuator was measured to determine the Coulomb friction associated with the pilot spool. Due to difficulty of measuring the spring pre-stress force directly at assembly of the valve, the pre-stress force has been determined from current and position measurements. Since the spring constant of the centring spring is known, the spring pre-stress length in neutral may be found from the measured spool position and applied current as<sup>8</sup>

$$x_{p0} = \frac{x_{pmax} i_0}{i_{max} - i_0} \quad (3.40)$$

where  $x_{pmax}$  is the maximum spool stroke,  $i_{max}$  is the current applied to reach the maximum spool stroke and  $i_0$  is the current required to produce a force equal to the spring pre-stress force. The spring pre-stress force may now be found by multiplying (3.40) by the known spring constant. The voice coil force constant may then be computed as

$$k_{fa} = \frac{x_{pmax}}{i_{max} - i_0} k_{sp} \quad (3.41)$$

The measured current multiplied by the force constant gives force applied to the pilot spool. This has been used to obtain the force in the graphs presented below.

Measurements have been made both without using dither and by applying a superimposed sinusoidal dither signal on the fundamental sinusoidal input signal. A dither frequency of 100 [Hz] and a current amplitude developing a maximum dither force at least equal to the friction force was found to remove the observed hysteresis. The measured hysteresis plots are shown in figures 3.16 and 3.17 along with simulation results. It should be noted that to obtain the data for plotting the simulated average position when applying dither a low pass filter was applied in the simulation.

The real system shows a varying friction level depending on position. The model has not been made to capture this, as it will depend on the local surface conditions of the valve spool and housing. Overall there is a fair agreement between measurements and simulations. With reference to figure 3.5, appropriate coefficients for the hysteresis model of the pilot stage were found to be  $f_{cp0} = 0.5$  [N] and  $\delta x_{p0} = 0.002$  [mm], these have been used in the simulations.

---

<sup>8</sup>It should be noted that to have a unique connection between the applied current and the measured spool position the effect of Coulomb friction on a low frequency average has to be removed. For this purpose dither was used.

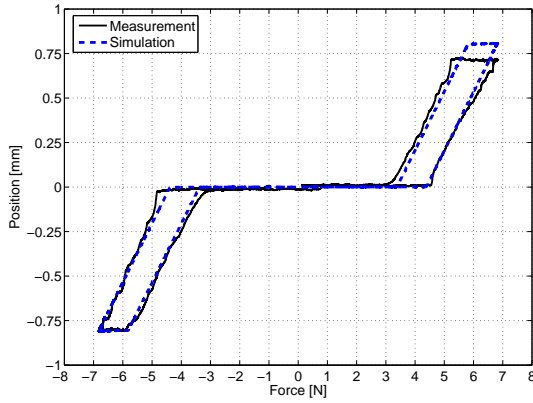


Figure 3.16: Hysteresis related to pilot spool position (no dither).

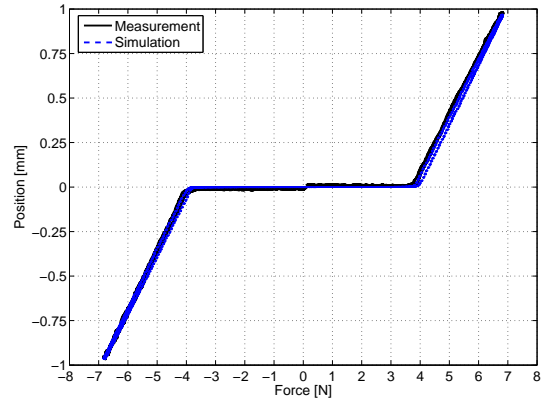


Figure 3.17: Hysteresis related to pilot spool position (with dither).

The hysteresis as a function of input force was measured for the pressurised system also. No change in the friction level was observed when varying the pressure drop. The measurement obtained at  $p_{pp} - p_{pa,pb} = 21$  [bar] is plotted in figure 3.18 along with simulation results. The Coulomb friction level is at approximately  $f_{cp0} = 0.45$  [N].

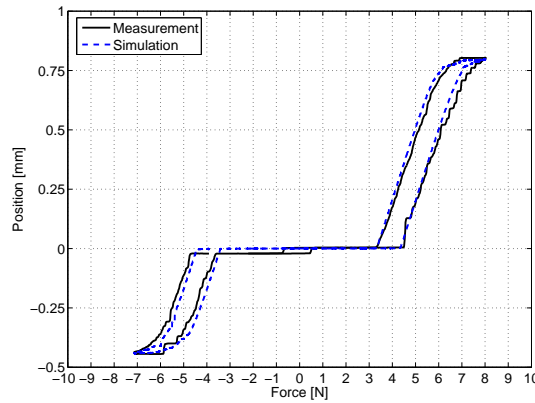


Figure 3.18: Hysteresis related to pilot valve position (no dither),  $p_{pp} - p_{pa,pb} = 21$  [bar].

Again sinusoidal dither was found to remove the hysteresis. The slope of the curve in figure 3.18 is not linear which is due to flow forces. Hence, the slope of the curve may be seen as an indirect verification of the flow force model.

### 3.5.5 Verification of flow force model associated with main spool

The prototype featured the possibility of measuring the pressures of the pilot chambers facing the ends of the main spool. Hereby, the flow forces added possible friction forces could be indirectly measured through the differential pressure operating the main spool. A simple proportional controller was implemented to control the main spool position and a slowly varying sinusoidal signal was applied as reference. In figures 3.19 and 3.20

the measured and simulated forces acting on the main spool are shown for two different pressure drops.

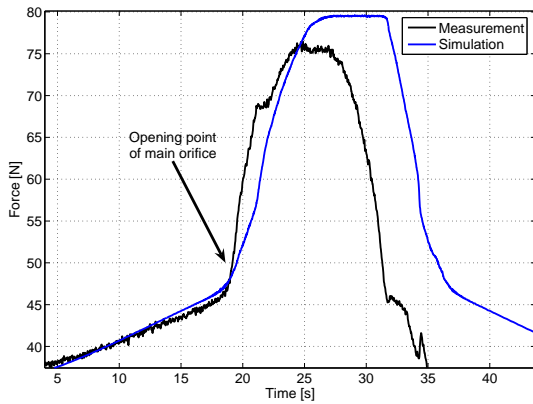


Figure 3.19: Measured and simulated force,  $\Delta p = 130$  [bar].

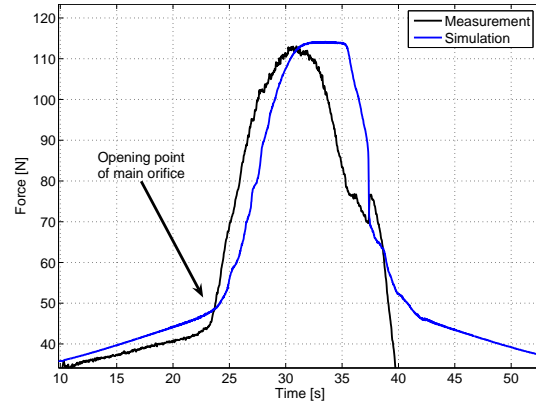


Figure 3.20: Measured and simulated force,  $\Delta p = 300$  [bar].

The plotted force contains the spring force the flow force and the friction force acting on the main spool. The simulation is made by using the measured flow rate, pressure drop and main spool position directly in the static equation for the flow force. Hereby the only unknown parameters are the jet angle of the fluid jet from the orifice and the spool friction. An estimate for the jet angle may therefore be found from the measurement. A jet angle of 79 [deg] for the sharp landed main spool was computed, which is surprising compared to the 69 [deg] which is commonly used for the considered type of spool valve [70]. The difference may be attributed the substitution of the discharge coefficient instead of the contraction coefficient when deriving the equation for the flow force. In this connection a change in the fluid jet angle has the same effect as changing the contraction/discharge coefficient, whichever is used.

The approximate opening point of the main orifice is marked by an arrow in each of the two figures 3.19 and 3.20. To the left of the respective arrow heads (approximately) the force applied is due the spring force on the main spool. Coulomb friction on the main spool is present as the measured force is larger than the simulated force when the orifice is opening and smaller than the simulated force when the orifice is closing. Without Coulomb friction the force should be approximately equal due to the slowly varying reference signal.

### 3.5.6 Verification of combined dynamic model of pilot valve

The measurements presented in this section have been made using the PV-A. Again the test set-up in figure 3.9 above has been used. Time series has been collected for different dynamic input signals. The simulation results presented below have been made by applying the measured current and the measured pressures as inputs to the simulation model. The advantage of using the measured pressures as inputs is that a model of the

dynamics of the connected fluid lines and hydraulic power pack does not have to be included in the simulation. As previously, the measured current has been converted to an actuator force in the simulations by using the force constant of the voice coil actuator.

First the current input to the voice coil actuator was constructed as a step input signal with increasing frequency. The signal was constructed as

$$i_a = K_g \cdot \text{sign} \left( \sin \left( \frac{\omega_1 - \omega_0}{t_1} t^2 + \omega_0 t \right) \right) + K_o \quad (3.42)$$

where  $\omega_0$  is the frequency at  $t = 0$  and  $\omega_1$  is the frequency at the final time  $t = t_1$ .  $K_g$  is the gain and  $K_o$  is the offset value. A run from 1 to 20 Hz without superimposed dither, and with the pilot spool offset from its null position to cancel the effect of the spring pre-stress force was made. Low respectively high frequency parts of the measurement and simulation results are shown in figures 3.21 and 3.22. Generally the model describes the damping of the pilot spool fairly well. The dominating dynamics of the pilot stage is expected to be of second order. However, comparing the size of the overshoot to the time at which oscillations have been damped, it is apparent that much of the damping adheres from Coulomb friction. The test was run with the coil in air why the viscous damping associated with the coil of the voice coil actuator was omitted in the simulation.

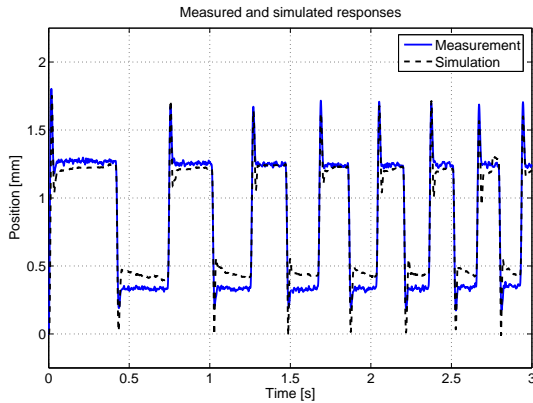


Figure 3.21: Low frequency time response.

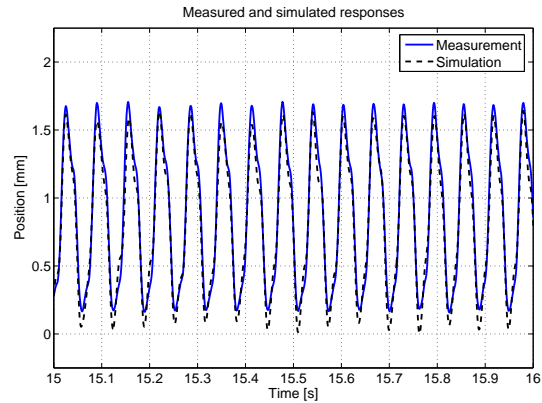


Figure 3.22: High frequency time response.

Measured and simulated responses to a chirp signal containing frequencies from 1 to 150 Hz was used to identify the frequency responses, which are shown in figure 3.23. Again the force applied to the spool was the input and the spool position was the output.

Due to influence from the dynamics of the connecting hoses and the hydraulic power pack, corresponding dynamic tests as those presented above could not be made with success when the pilot valve was pressurised. Instead step responses have been recorded for three different opening settings of the variable orifice in figure 3.9. The measured time responses of the pilot spool position obtained by having the variable orifice fully open are plotted in figures 3.24 (no dither used) and 3.25 (dither used) along with

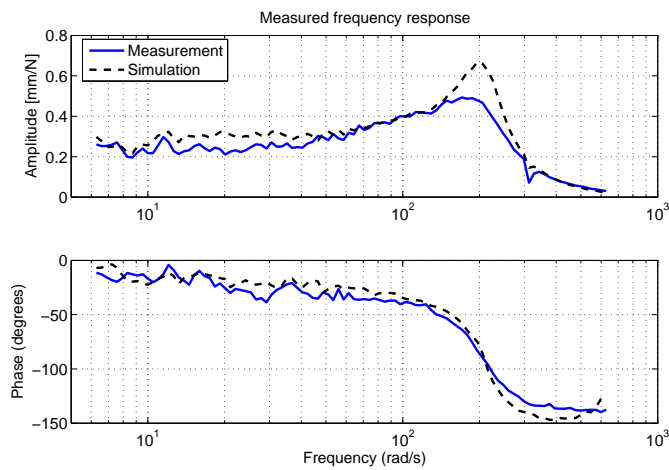


Figure 3.23: Frequency response of de-pressurised pilot stage.

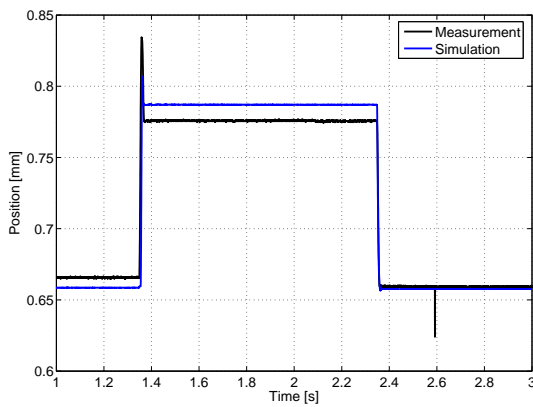


Figure 3.24: Time response of pilot spool position (no dither).

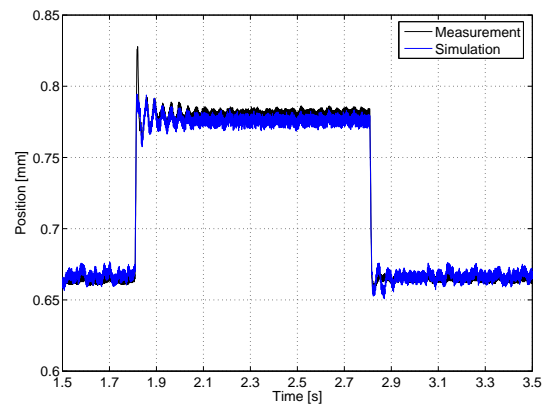


Figure 3.25: Time response of pilot spool position (with dither).

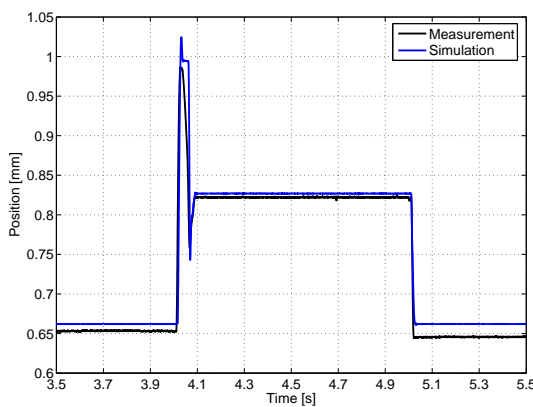


Figure 3.26: Time response of pilot spool position (no dither).

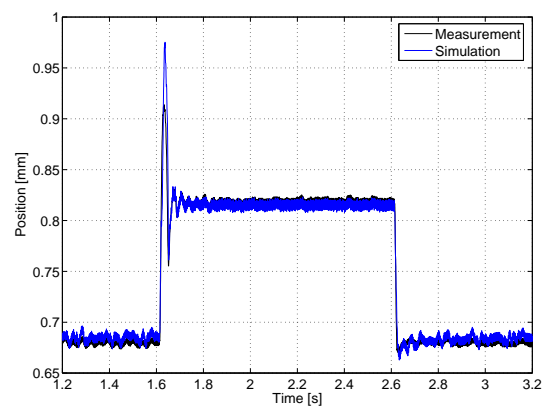


Figure 3.27: Time response of pilot spool position (with dither).

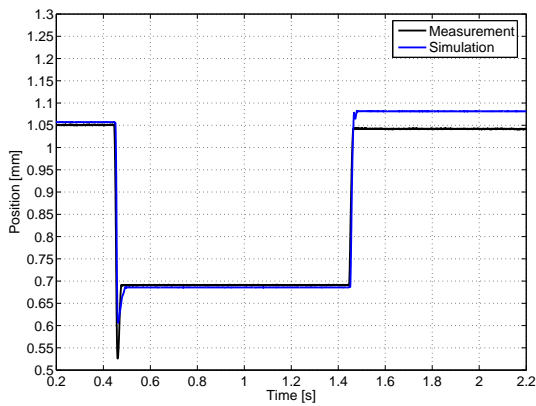


Figure 3.28: Time response of pilot spool position (no dither).

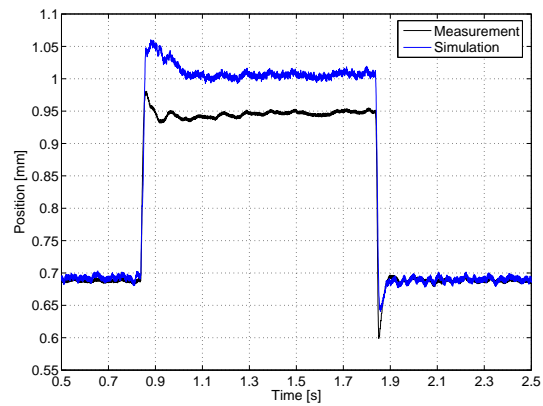


Figure 3.29: Time response of pilot spool position (with dither).

simulation results. Similar results for two other orifice openings are shown in figures 3.26, 3.27, 3.28 and 3.29.

The deviations between the spool position, regarding the measurements and simulations where no dither is used, are due to stiction. As observed in previous work [76], dither eliminates the stiction force in hydraulic valves. A stiction force in the range of 1.25 - 1.5 [N] and a friction force of 0 [N] at non-zero velocity have been found to yield the best match between simulations and measurements. This deviates from the Coulomb friction force of approximately 0.5 [N] found earlier to match the measured hysteresis. However, for rapid spool movements it is very likely that Coulomb friction is negligible and the main friction phenomenon is viscous.

The rather high level of stiction is assumed to be due to the fact that the clearance between the spool and the housing was slightly tapered. That is, the spool bore of the housing was cone formed whereas the spool was nearly perfectly cylindrical, e.g. see parameters in table 3.2. It is known that this causes larger friction forces to be overcome [19]. To check this, response tests were made on the PV-B as well (results are omitted here). These did not show the same level of overshoot as those for the PV-A. This indicates that the stiction force was not as high for the PV-B as for the PV-A. Measurements of geometric parameters of the PV-B have shown that the clearance between the spool and the housing was not tapered as for the P-VA, e.g. see table 3.3. This supports the above assumption regarding the reason for the high level of stiction in the PV-A.

Regarding the damping model associated with the voice coil actuator it has been found that the model overestimates the damping. That is, if the damping given by the model was used in the simulation, the simulated responses were overdamped.

The difference between the responses in figure 3.29 cannot be attributed stiction as dither has been used. In the figure, the dither may be seen superimposed on the measured position signal. The difference is rather that the model of the fluid jet angle is slightly erroneous giving an erroneous flow force magnitude as a result. The measured flow has

been compared to that obtained by simulation, and this was not found to be the cause for the error. Except from this, there is a good agreement between the measurements and the simulated dynamic responses.

### 3.5.7 Discussion on model verification

In the above the non-linear model has been verified. The approach taken was to fix the parameters of the model at values giving the overall best simulated response compared to the collected data series. This approach is valid since the data has not been used to directly determine the model. In general the model showed to capture both static and dynamic responses fairly well. However three issues of concern were identified:

1. There was a poor agreement between the measured overlap of the PV-B valve, and that used in the simulation to fit the simulated flow characteristics to the measured ones. The most likely reason for this is human error. However, due to a mix of unfavourable circumstances the measurements could not be recreated.
2. The model overestimated the flow forces on the main spool. A plausible reason for this was, however, explained.
3. One set of Coulomb friction parameters giving good results for both the tested pilot valves could not be found. This is of minor concern since it was found that the Coulomb friction force may be eliminated by applying dither.

Issue 1 is of the greatest concern here. But, due to the fact that there was a good agreement between the measured and the simulated flow characteristics regarding this issue, it may be expected that the model may anyway model the real valve adequately well. That is, without carrying through the measurements once more to verify whether the mismatch is due to human error. What may be questioned is the parametrisation of the overlap. Due to the parametrisation of the overlap of the PV-A is the same, and that this gave good results, indicates that the parametrisation of the overlap is implemented correctly in the model.

## 3.6 Linear model descriptions

In this section a linear model description of the valves, depicted in figures 3.1 and 3.2 is developed. The model is to be used in the controller development and is obtained by a Jacobi linearisation of the non-linear model. Additionally, at the end of the section, a simple linear model is derived for pointing out some potential interaction problems between the main circuit and the pilot circuit of the valve. We start by deriving the linear model of the valve assembly. The non-linear model may be written on the form

$$\dot{x} = f(x, u) \quad (3.43)$$

$$y = Cx \quad (3.44)$$



where  $x \in \mathcal{R}^n$  is the state vector,  $u \in \mathcal{R}$  is the input and  $y \in \mathcal{R}$  is the output. To carry out the linearisation it is required that  $f : \mathcal{R}^n \times \mathcal{R} \rightarrow \mathcal{R}^n$  is continuous. The following assumptions have to be made to make the non-linear model continuously differentiable and thus linearisable, e.g. see [90]:

- Coulomb friction forces on the spools may be ignored. This is a fairly crude assumption unless the Coulomb friction forces on the spools are small compared to other force contributions entering into the force equilibriums of the spools. If not, as may be the case for the pilot spool, it is assumed that the Coulomb friction phenomenon may be removed by superimposing dither on the input signal. The results in the previous section supports this assumption.
- Sufficient pilot pressure is present such that pilot pressure saturation may be ignored.
- The main spool does not operate across its neutral position; or the pressure differential required to overcome the main spool spring pre-stress force is negligible compared to the pressure differential available to move the main spool.

By these assumptions the hard non-linearities which are not linearisable may be neglected except from the dead-zone associated with the pilot spool orifices. This latter problem will be worked around choosing operating points at the limits of the dead-zone. For the specific problem at hand this is done by using the simulation model making it converge for a small main spool velocity, e.g. see appendix D, and afterwards reading out state values for the equilibrium. For small velocities it is assumed that the error doing this is negligible. Having handled the discontinuous terms of the non-linear model a linear model approximating the non-linear one, locally, may be obtained as

$$\dot{x} = \left. \frac{\partial f(x, u)}{\partial x} \right|_{x=0, u=0} x + \left. \frac{\partial f(x, u)}{\partial u} \right|_{x=0, u=0} u = Ax + Bu \quad (3.45)$$

$$y = Cx \quad (3.46)$$

This model is only valid locally around a specific operating point. To get a picture of how the dynamics of the valve depends on the chosen operating point, a set of operating points is therefore considered. These are listed in appendix D. Necessarily, the set of operating points results in a set of linear models. Therefore frequency responses and other results presented below are shown for the model set instead of a single plant.

In addition to the above necessary assumptions to carry out the linearisation the following simplifications are made

- Transient flow forces on both the pilot spool and the main spool due to pressure gradients are neglected to simplify the linearised model. By frequency domain analysis previous research has indicated that for low frequencies, which is normally encountered in mobile hydraulics, the error by doing this is minor [68].

- Transient flow forces on the pilot spool due to velocity are neglected. This is done as simulations made to carry out the model verification showed that transient flow forces on the pilot spool due to velocity are negligible. That is, compared to the damping due to viscous friction and damping on the voice coil.

In this section the linear model is mainly presented as transfer functions in the Laplace variable  $s$ . That is as<sup>9</sup>

$$G(s) = C(sI - A)^{-1}B + D \quad (3.47)$$

Often in the literature capital letters are used for denoting the Laplace transforms of signals. This distinction between time domain signals and Laplace transforms of signals is not used here. The model of the valve will at some points in the text be referred to as the plant model, or simply the plant.

### 3.6.1 Valve with pressure control pilot

We here consider the valve with pressure control pilot. Using the assumptions above the plant model may be described by the block diagram in figure 3.30. The transfer function  $G_1(s)$  models the pilot spool dynamics relating the force input to the pilot spool position. Transfer functions  $G_2(s)$ ,  $G_3(s)$ ,  $G_4(s)$  and  $G_6(s)$  model the pilot chamber dynamics and  $G_5(s)$  models the main spool dynamics. In addition to the linear transfer functions, the dead-zone due to the pilot spool overlap is also shown.

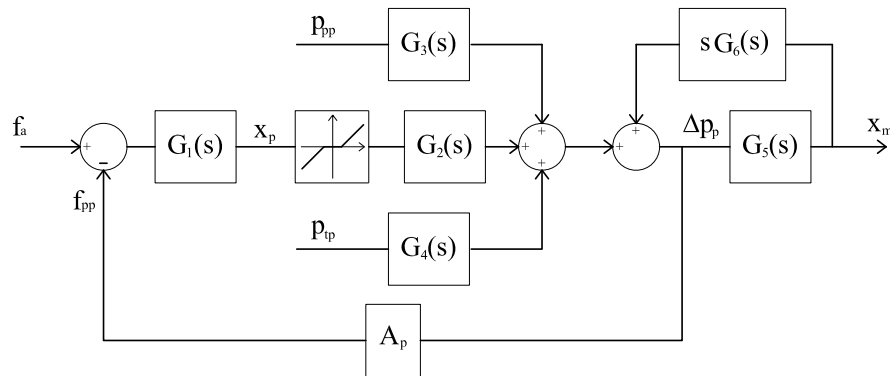


Figure 3.30: Block diagram of valve model with with pressure control pilot, showing linearised parts and the dead-zone.

A linear transfer function relating the force input to the pilot spool position may be derived from (3.17), (3.20) and (3.24), and is given by

$$G_1(s) = \frac{x_p}{f_a - f_{pp}} = \frac{1}{m_p} \frac{1}{s^2 + 2\zeta_1\omega_1 s + \omega_1^2} \quad (3.48)$$

<sup>9</sup>For the model considered here  $D = 0$  but is included in the equation for completeness.

where

$$2\zeta_1\omega_1 = \frac{1}{m_p} \frac{\partial f_{vp}}{\partial \dot{x}_p} \Big|_{x_{p0}, \Delta p_{i0}} = \frac{2\mu}{m_p} \left( \frac{\pi d_p L_2}{C_{rp}} + \frac{C_{vc} L_{vc} A_{vc}^2}{\pi (2\delta_{vc})^4} \right) \quad (3.49)$$

$$\omega_1^2 = \frac{1}{m_p} \frac{\partial f_{fp}}{\partial x_m} \Big|_{x_{p0}, \Delta p_{i0}} = \frac{1}{m_p} \sum_{i=1}^4 k_{qi} \sqrt{2\rho |\Delta p_{i0}|} \cos(\theta_{Q_i}) \quad (3.50)$$

Even though there is no spring forces acting on the pilot spool the transfer function is of type 0. This is due to the flow force gradient with respect to pilot spool position. At steady state no flow forces are acting on the pilot spool, as the main spool velocity must be zero due to steady state. The flow force gradient may, however, be non-zero. This is the case if the flow gain of the active pilot orifice is non-zero at the steady state operating point. For the operating points considered, i.e. at the limit of the dead-zone, this is the case.

The two terms within the brackets of (3.49) describe the damping acting on the spool and on the voice coil. From (3.50) it may be seen that the flow force gradient is proportional to the flow gain.

By linearising equation (3.13) the flows into the pilot chambers are given by

$$q_{ac} = k_{q_{pa}} x_p - k_{p_{pa}} p_{pa} + k_{p_2} p_{pp} + (k_{p_4} + k_{p_8}) p_{tp} \quad (3.51)$$

$$q_{bc} = k_{q_{pb}} x_p - k_{p_{pb}} p_{pb} + k_{p_1} p_{pp} + (k_{p_3} + k_{p_7}) p_{tp} \quad (3.52)$$

where<sup>10</sup>

$$k_{q_{pa}} = k_{q_2} \frac{\partial x_{l2}}{\partial x_p} - k_{q_4} \frac{\partial x_{l4}}{\partial x_p} = k_{q_2} + k_{q_4} \quad (3.53)$$

$$k_{p_{pa}} = k_{p_2} + k_{p_4} + k_{p_8} \quad (3.54)$$

$$k_{q_{pb}} = k_{q_1} \frac{\partial x_{l1}}{\partial x_p} - k_{q_3} \frac{\partial x_{l3}}{\partial x_p} = -k_{q_1} - k_{q_3} \quad (3.55)$$

$$k_{p_{pb}} = k_{p_1} + k_{p_3} + k_{p_7} \quad (3.56)$$

In the above  $k_{q_1}$  to  $k_{q_4}$  and  $k_{p_1}$  to  $k_{p_4}$  are associated with flows across the pilot spool, and  $k_{p_7}$  and  $k_{p_8}$  are associated with leakage from the pilot chambers facing the ends of the main spool, e.g. see figure 3.7.

The pressure differential of the pilot chambers is given by

$$\Delta p_p = p_{pa} - p_{pb} \quad (3.57)$$

The pilot chamber pressures may be computed as

$$p_{pa} = \frac{\beta_e (p_{pa0})}{[V_{c0} + A_m x_{m0}]_s} (q_{ac} - A_m s x_m) = \frac{c_{pa}}{s} (q_{ac} - A_m s x_m) \quad (3.58)$$

<sup>10</sup>In appendix C, flow gain coefficients  $k_q$  and pressure gain coefficients  $k_p$  as function of absolute axial orifice opening,  $x_l$ , are derived for two different orifice geometries.

$$p_{pb} = \frac{\beta_e (p_{pb0})}{[V_{c0} - A_m x_{m0}]s} (q_{bc} + A_m s x_m) = \frac{c_{pb}}{s} (q_{bc} + A_m s x_m) \quad (3.59)$$

Now the four transfer functions  $G_2$ ,  $G_3$ ,  $G_4$  and  $G_6$  may be derived using (3.51), (3.52), (3.57), (3.58) and (3.59). The following are obtained where the given approximations are valid for a pilot spool with an underlapped drain port in the null position

$$\begin{aligned} G_2(s) = \frac{\Delta p_p}{x_p} &= \frac{(c_{pa} k_{q_{pa}} - c_{pb} k_{q_{pb}}) s + c_{pa} c_{pb} (k_{q_{pa}} k_{p_{pb}} - k_{q_{pb}} k_{p_{pa}})}{(s + c_{pa} k_{p_{pa}}) (s + c_{pb} k_{p_{pb}})} \\ &\approx \frac{c_{pa} k_{q_{pa}}}{s + c_{pa} k_{p_{pa}}} \end{aligned} \quad (3.60)$$

$$\begin{aligned} G_3(s) = \frac{\Delta p_p}{p_{pp}} &= \frac{(c_{pa} k_{p_2} - c_{pb} k_{p_1}) s + c_{pa} c_{pb} (k_{p_2} k_{p_3} - k_{p_1} k_{p_4})}{(s + c_{pa} k_{p_{pa}}) (s + c_{pb} k_{p_{pb}})} \\ &\approx \frac{c_{pa} k_{p_2}}{s + c_{pa} k_{p_{pa}}} \end{aligned} \quad (3.61)$$

$$\begin{aligned} G_4(s) = \frac{\Delta p_p}{p_{tp}} &= \frac{(c_{pa} k_{p_4} - c_{pb} k_{p_3}) s + c_{pa} c_{pb} (k_{p_1} k_{p_4} - k_{p_2} k_{p_3})}{(s + c_{pa} k_{p_{pa}}) (s + c_{pb} k_{p_{pb}})} \\ &\approx -\frac{s}{s + c_{pa} k_{p_4}} \end{aligned} \quad (3.62)$$

$$\begin{aligned} G_6(s) = \frac{\Delta p_p}{s x_m} &= \frac{-A_m [(c_{pa} + c_{pb}) s + c_{pa} c_{pb} (k_{p_{pb}} + k_{p_{pa}})]}{(s + c_{pa} k_{p_{pa}}) (s + c_{pb} k_{p_{pb}})} \\ &\approx \frac{-A_m c_{pa}}{s + c_{pa} k_{p_{pa}}} \end{aligned} \quad (3.63)$$

From (3.30) a linear transfer function relating the differential pilot pressure to the main spool position may be obtained as

$$G_5(s) = \frac{x_m}{\Delta p_p} = \frac{A_m}{m_m} \frac{1}{s^2 + 2\zeta_5 \omega_5 s + \omega_5^2} \quad (3.64)$$

where

$$2\zeta_5 \omega_5 = \frac{1}{m_m} \left. \frac{\partial f_{vm}}{\partial \dot{x}_m} \right|_{x_{m0}, \Delta p_{i0}} = \frac{2\mu\pi d_m L_3}{m_m C_{rm}} + \frac{\rho L_{dm}}{m_m} \sum_{i=5}^6 k_{qi} \frac{\partial x_{li}}{\partial x_m} \quad (3.65)$$

$$\begin{aligned} \omega_5^2 &= \frac{1}{m_m} \left[ k_{sm} + \left. \frac{\partial f_{fm}}{\partial x_m} \right|_{x_{m0}, \Delta p_{i0}} \right] \\ &= \frac{1}{m_m} \left[ k_{sm} + \sum_{i=5}^6 k_{qi} \sqrt{2\rho |\Delta p_{i0}|} \cos(\theta_{Qi}) \right] \end{aligned} \quad (3.66)$$

From equation (3.65) it may be seen that if  $L_{dm} < 0$ ,  $G_5(s)$  may have an unstable set of complex poles. That is, if the dynamic damping from transient flow forces is negative and

$$\frac{2\mu\pi d_m L_3}{C_{rm}} < \left| \rho L_{dm} \sum_{i=5}^6 k_{qi} \frac{\partial x_{l_i}}{\partial x_m} \right| \quad (3.67)$$

The sign of  $L_{dm}$  depends on the flow direction through the valve chamber, e.g see [19].

The transfer functions derived above may be combined into the following transfer function, which models the dynamics between the pilot spool force input and the main spool position.

$$G_p = \frac{x_m}{f_a} = \frac{G_1 G_2 G_5}{1 - s G_5 G_6 + A_p G_1 G_2} \quad (3.68)$$

The frequency response associated with this transfer function is plotted in figure 3.31 and the pole-zero locations are plotted in figure 3.32, only the dominating dynamics is shown. The valve with pressure control pilot has a dominating dynamics of second order, as may be seen from the frequency response. For on-stroke ( $\dot{x}_m > 0$ ) the poles tend to move towards the left complex half plane by increasing pressure drop across the main valve and increasing flow across the main valve. For de-stroke ( $\dot{x}_m < 0$ ) the opposite is true. As may also be seen from the frequency response, the transfer

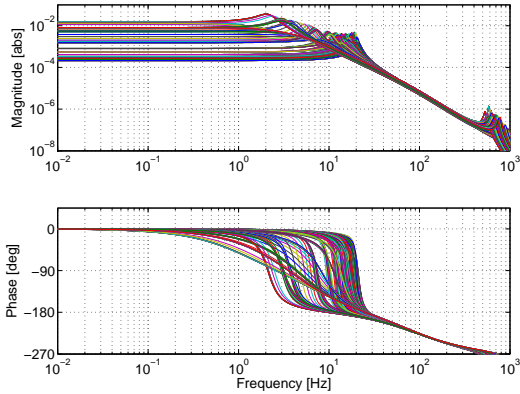


Figure 3.31: Frequency response associated with valve model.

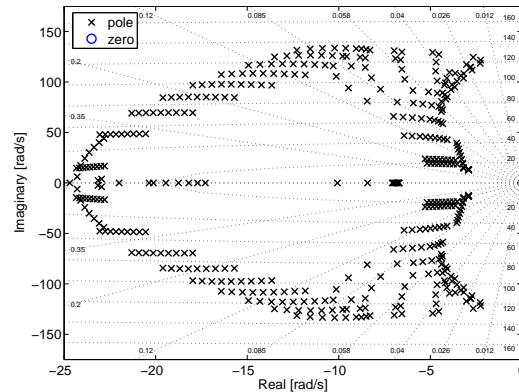


Figure 3.32: Pole-zero map associated with valve model.

function has a set of lightly damped complex poles due to the main spool with natural frequencies above  $2000 \left[ \frac{\text{rad}}{\text{s}} \right]$ . This large natural frequency is because the compressible oil in the pilot chambers acts as a spring, hereby raising the natural frequency of the main spool dynamics. Furthermore the transfer function has a real pole-zero set faster than  $4000 \left[ \frac{\text{rad}}{\text{s}} \right]$ , which approximately cancel each other. The latter is due to that the non-approximated version of the transfer function given by (3.60) and (3.63) have been used in the numerical computation, and that the approximations may be used instead.

It should be noted that the pole-zero plots are made for the case where the dynamic damping due to transient flow forces on the main spool is positive. If the net-damping force on the main spool becomes negative due to reversing flow direction, the fast poles

from the main spool dynamics may shift to the right half plane, and the valve may be difficult to stabilise by feedback when limited actuator force is present. It will be shown in chapter 4 that the stabilisation of a system with RHP-poles requires a bandwidth which is larger than the distance to the unstable pole from the origin. However, it should also be noted that only viscous damping is included in the linear model. Thus, even if the flow direction is reversed, Coulomb friction forces might keep the open loop dynamics stable, i.e. the net damping force on the main spool still may be positive. This is best investigated by a non-linear time domain simulation and preferably laboratory tests.

### 3.6.2 Valve with flow control pilot

The non-linear model of the valve with flow control pilot only differs from the model of the valve with pressure control pilot by the two equations (3.25) and (3.26). Therefore, the linear model of the valve with flow control pilot may be obtained by simply including a spring term in (3.50), and setting the pressure feedback gain,  $A_p$ , in figure 3.30 to zero. Thus the transfer function relating the force input to the pilot spool position is given by

$$G_1(s) = \frac{x_p}{f_a} = \frac{1}{m_p} \frac{1}{s^2 + 2\zeta_1\omega_1 s + \omega_1^2} \quad (3.69)$$

where  $2\zeta_1\omega_1$  is given by (3.49), and  $\omega_1^2$  is computed as

$$\omega_1^2 = \frac{1}{m_p} \left[ k_{sp} + \sum_{i=1}^4 k_{q_i} \sqrt{2\rho|\Delta p_i|} \cos(\theta_{Q_i}) \right] \quad (3.70)$$

The remaining transfer functions are the same as already presented for the valve design with pressure feedback. Combining the derived transfer functions into one, which models the dynamics between the force input to the pilot spool and the main spool position yields the following

$$G_p = \frac{x_m}{f_a} = \frac{G_1 G_2 G_5}{1 - s G_5 G_6} \quad (3.71)$$

The frequency response of this transfer function is plotted in figure 3.33 and the pole-zero locations are plotted in figure 3.34. The dominating dynamics of the valve with flow control pilot is represented by three real poles. The slowest of these poles is due to the time constant for pressure build up and the two faster ones are due to the over damped pilot spool dynamics of second order. This time constant associated with the pressure build up is inversely proportional to the pressure gain of the pilot orifice, which is small at steady state, e.g. see (3.60). For a valve with no leakage across the spools, the pressure gain would be zero and consequently there would be a pole at the origin. The same comments as already given on page 68 regarding higher order dynamics and possible negative damping force also apply to the valve with flow control pilot. That is, as these comments refer to the main spool dynamics, which is identical for the valves with pressure or flow control pilot.

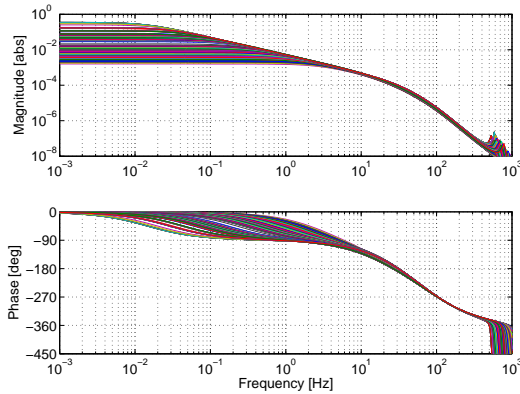


Figure 3.33: Frequency response associated with valve model.

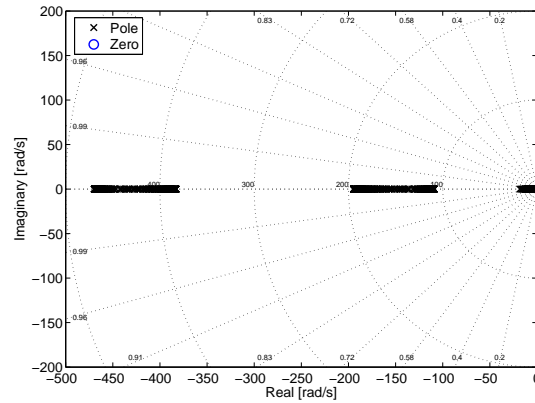


Figure 3.34: Pole-zero map associated with valve model.

### 3.6.3 Disturbance interaction between pilot circuit and main circuit

In this section a linear model of a potential disturbance interaction between the pilot spool and the main spool is derived. The modelled interaction may occur if the separate meter-in separate meter-out valve is connected to the drain through a long fluid line. The section is intended for pointing out the problem, and to establish a model which may be used to address the problem. The section itself is included due to some stability issues which were observed when carrying out experiments with the prototype valve during the model verification.

It is known from mobile hydraulic applications that if the drain line of the pilot circuit of a proportional valve is not isolated from the drain line of the main system, then, the dynamics of the connected drain line may yield instability. Occasionally, a separate drain connection for the pilot circuit is therefore used. However, a separate drain connection might not be desirable if the proportional valve is going to be actuator mounted. Instead, a damping orifice in the drain line of the pilot circuit may be used to limit the interaction between the main circuit and the pilot circuit. This may be implemented as shown in figure 3.35, where the pressure reduction valve in the pilot supply keeps the pilot supply pressure constant, relatively to the pressure in the pilot drain line.

The response time of the main spools may be limited by including the damping orifice in the pilot drain line, as the oil flow from the pilot circuit to the drain port is also restricted by the orifice. Another way of avoiding pressure peaks in the pilot drain line is to use a check valve instead of the damping orifice. Whichever solution is the best along with an analysis of potential performance limitations are not pursued further here and is left for further work.

Referring to figure 3.35, it is only the flow across the main spool connected to the drain line, carrying the pressure  $p_t$ , which may interact with the drain pressure,  $p_{pt}$ , of the pilot circuit. A simple linear model of this interaction between the main spool and the pressure in the pilot drain line is derived in the following. The flow and pressure

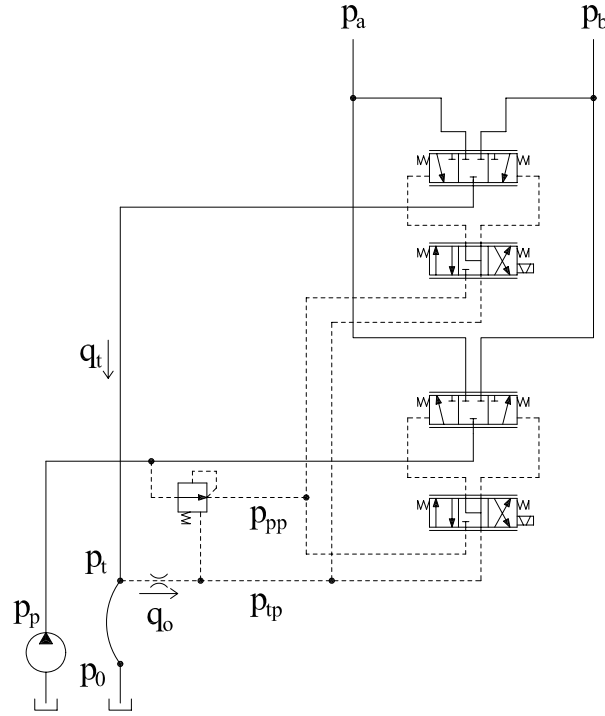


Figure 3.35: Implementation of damping orifice in pilot drain connection.

conditions at the ends of the modelled fluid line are denoted  $q_t$ ,  $p_t$  and  $q_0$ ,  $p_0$ , as shown in figure 3.35.

The flow and pressure conditions at the ends of a fluid line may be modelled in the frequency domain by a lumped model with  $n$  segments given by the transfer matrix below [105]

$$\begin{bmatrix} p_0 \\ q_0 \end{bmatrix} = \begin{bmatrix} \left(1 + \frac{\Gamma^2 L_h^2}{2n^2}\right) & \frac{-Z_c \Gamma L_h}{n} \\ \frac{-1}{Z_c} \left(\frac{\Gamma L_h}{n} + \frac{\Gamma^3 L_h^3}{4n^3}\right) & \left(1 + \frac{\Gamma^2 L_h^2}{2n^2}\right) \end{bmatrix}^n \begin{bmatrix} p_t \\ q_t \end{bmatrix} \quad (3.72)$$

where  $L_h$  is the length of the modelled fluid line, and the characteristic impedance,  $Z_c$ , and the propagation constant,  $\Gamma$ , may be chosen based on an average friction model as

$$Z_c = \sqrt{\frac{R^1 + sL^1}{sC^1}} \quad (3.73)$$

$$\Gamma = \sqrt{(R^1 + sL^1)sC^1} \quad (3.74)$$

Here,  $R^1$  is the resistance per unit length,  $L^1$  is the inductance per unit length and  $C^1$  is the capacitance per unit length.

Only the lowest modes of the fluid line is of interest as it is these that may be significant compared to the dominating dynamics of the valve. Thus we select  $n = 2$ , giving a 4th order linear model. Additionally, the pressure at the reservoir is assumed constant why



$p_0 = 0$ . By these conditions the transfer function relating the flow  $q_t$  into the fluid line to the pressure  $p_t$  at the damping orifice is given by

$$G_7(s) = \frac{p_t}{q_t} = \frac{4Z_c\Gamma L_h(\Gamma^2 L_h^2 + 8)}{\Gamma^4 L_h^4 + 16\Gamma^2 L_h^2 + 32} \quad (3.75)$$

As an example the frequency response of a 3 [m] long fluid line pressurised at 1 [bar] and having an inner diameter of 15.7 [mm] is shown in figure 3.36. The frequency response using a 1st order transfer function, i.e. pressure build up as traditionally used for lumped volumes, is also shown. The result may seem rather surprising due to the low dominating frequency compared to the length of the fluid line. The low frequency is because that at a pressure of 1 [bar] the effective bulk modulus of the oil is low due to the air content of the oil.

Watton remarks that the lumped model given by (3.72) give erroneous results for higher modes. Kruss et. al. obtained very good results with another lumped model in [55]. The model assumed distributed friction and for comparison a computation, however, using the exact expression (infinite order) from [55], is also plotted in figure 3.36. It shows that the two models agree regarding the frequency of the first mode, which is of interest here.

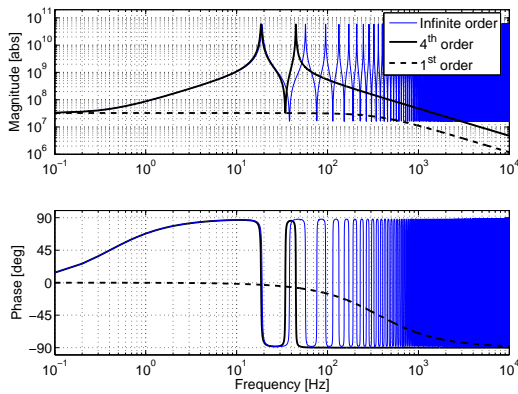


Figure 3.36: Frequency response of fluid line pressurised at 1 [bar].

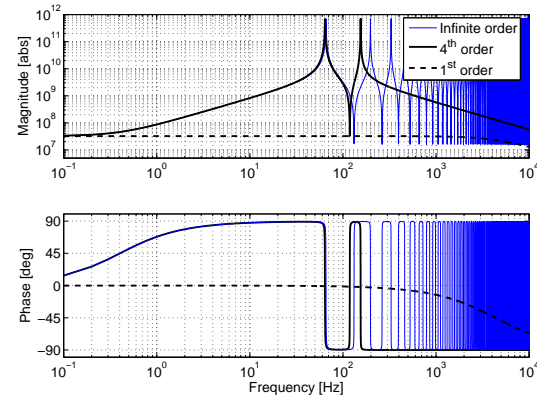


Figure 3.37: Frequency response of fluid line pressurised at 10 [bar].

It is clear that for the chosen example, using realistic fluid line dimensions, the dominant dynamics of the fluid line has natural frequencies in the same range as the dominant dynamics of the modelled spool valve. If no damping orifice or check valve is placed in the drain line of the pilot circuit, the fluid line may easily disturb the valve. The results from a similar computation assuming a fluid line average pressure of 10 [bar] is shown in figure 3.37. It is seen that at this pressure the frequency of the dominating dynamics of the fluid line is moved outside the range of interest regarding the dynamics of the valve.

Regarding the main spool which is connected to the drain line, e.g. see figure 3.35, the fluid line dynamics is part of a feedback loop and should be included in the plant

transfer function. By the linearised flow equation the flow from this main spool is given by

$$q_t = k_q x_m + k_p (p_{a,b} - p_t) \quad (3.76)$$

Substituting this into (3.75) and rearranging gives

$$\begin{aligned} G_8(s) &= \frac{p_t}{(k_q x_m + k_p p_{a,b})} \\ &= \frac{4(\Gamma^2 L_h^2 + 8) Z_c \Gamma L_h}{\Gamma^4 L_h^4 + 4Z_c \Gamma^3 L_h^3 k_p + 16\Gamma^2 L_h^2 + 32Z_c \Gamma L_h k_p + 32} \end{aligned} \quad (3.77)$$

If no damping orifice is used, the transfer function given by (3.77) may be inserted directly between the output and  $G_4(s)$  in figure 3.30. Doing this for the valve with flow control pilot yields the frequency responses in figure 3.38. The same fluid line dimensions as in the example above have been used. It is seen that the phase angle of the open loop dynamics becomes difficult to handle with regard to controller design. The frequency responses may be compared to those in figure 3.33, where the interaction is not included.

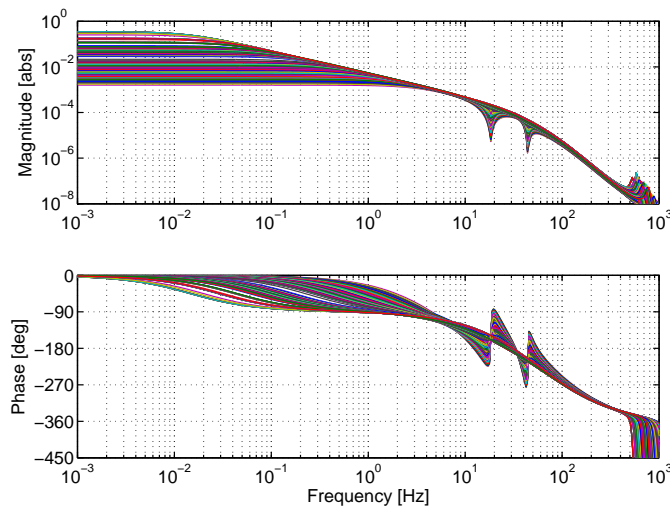


Figure 3.38: Frequency response of valve with flow control pilot including fluid line dynamics.

The effect of including a damping orifice is best investigated from time domain simulations, as the pressure gain across the orifice varies with pressure drop, and therefore so does the damping effect. An approximate effect of a damping orifice may be analysed in the frequency domain though. For a sharp edged orifice transition to turbulent flow may occur already at  $Re_t \approx 9$ , [70]. For simplicity we linearise the orifice equation at the pressure drop associated with transition to turbulent flow as sketched in figure 3.39.

Using a discharge coefficient equal to 0.6 and an orifice diameter equal to 0.6 [mm], the open loop frequency responses in figure 3.40 are obtained for the damped pilot drain

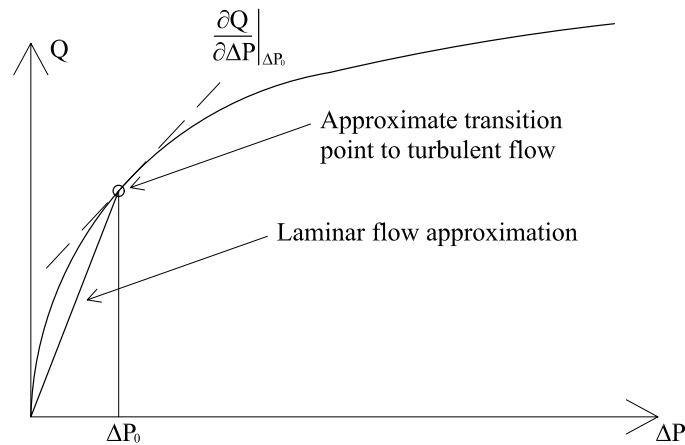


Figure 3.39: Linearisation point at transition to turbulent flow.

pressure. For the numerical computation it has been assumed that the fluid volume contained in the drain side of the pilot circuit is 20 [cm<sup>3</sup>] and does not change. By the latter assumption the effect of the damping orifice becomes equal to that of a first order low pass filter. It may be seen from the frequency responses that the phase properties of the plant have improved by using the damping orifice.

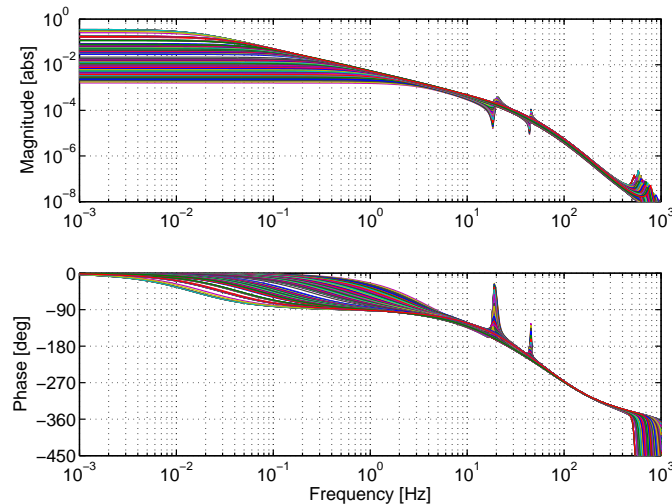


Figure 3.40: Frequency response of valve with flow control pilot including fluid line dynamics and effect of damping orifice.

Attention to the significance of the interaction between the main circuit and the pilot circuit of the considered spool valve has been drawn here. Two methods of limiting this interaction have been proposed. However, the subject is left for further work and in the following the interaction between the main circuit and the pilot circuit is ignored with regard to controller design. Experimentally, the interaction is dealt with using the separate drain connection for the pilot circuit which is available on the prototype.

## 3.7 Summary and conclusion

In this chapter a parametrised non-linear simulation model of the selected spool valve concept has been presented. The presented model includes Coulomb friction, leakage, spool overlap/underlap, viscous spool damping, fluid compliance and viscous damping associated with the voice coil, which is mounted on the pilot spool. The dynamics of the electrical system associated with the voice coil actuator has not been included, due to the voice coil actuator of the prototype being current controlled.

The experimental verification showed a good agreement between the measured and simulated responses, although issues of concern were pointed out. An appropriate limit for the minimum overlapped length used in the leakage model was found to be 10 times the radial clearance. The Coulomb friction on the pilot spool was found to be negligible when applying a dither signal with an amplitude larger than or equal to the size of the measured friction force. The verification of the flow force model showed that the flow forces on the main spool were smaller than expected from the simulation. The fluid jet angle was adjusted to compensate for this. As explained the error may equally well adhere from the discharge coefficient being used in the flow force calculation instead of the contraction coefficient.

The non-linear model was linearised with the purpose of being used for controller design in the subsequent chapter. The linear model was extended with a simple transmission line model, for checking how the main circuit and the pilot circuit interact if they share a common drain line. Due to the low bulk modulus of the fluid at low pressure, it was shown that low frequency interaction may occur between the pilot circuit and the main circuit. It was argued that a damping orifice or a check valve should be present in the drain line of the pilot circuit to limit this interaction. The study of the effectiveness of such a damping orifice was left for further work.



# Chapter 4

## Electrohydraulic pressure compensation

### Contents

---

4.1	Introduction to electrohydraulic pressure compensation . .	78
4.2	Requirements for flow controller . . . . .	79
4.3	Preliminary controller design for valve with pressure control pilot . . . . .	85
4.4	Preliminary controller design for valve with flow control pilot	98
4.5	Performance specification and analysis in the frequency domain . . . . .	102
4.6	Performance demands for closed loop position controller . .	106
4.7	Improved robust controller designs . . . . .	111
4.8	Robustness of controllers . . . . .	134
4.9	Experimental results . . . . .	141
4.10	Summary and conclusion . . . . .	145

---

This chapter is concerned with developing a flow controller by means of electrohydraulic pressure compensation of the separate meter-in separate meter-out prototype valve. The preliminaries for the electrohydraulic pressure compensation method which is used are that the pressure drop across the orifice, which is to be pressure compensated, is known, and that the flow gain of the orifice is known as a function of orifice opening. The idea is then to keep the flow through the orifice constant for a time varying pressure drop. This is done by controlling the opening of the orifice in response to the inverse flow gain as a function of a measured pressure drop and the desired flow rate.

For the separate meter-in separate meter-out prototype valve considered in this work, both spool positions and the pressure drop across the spools are measurable. Since the prototype valve consists of two identical pilot operated spools it is sufficient to consider only one of the spools when developing the flow controller.

## 4.1 Introduction to electrohydraulic pressure compensation

The flow through a spool valve may be described by the equation

$$q = k_v(x_m)\sqrt{\Delta p} \quad (4.1)$$

which is the same as equation (3.9), only the discharge coefficient, the mass density of the oil, as well as the orifice area as a function of spool position are contained in  $k_v(x_m)$ .  $k_v(x_m)$  is the valve gain at a 1 [bar] pressure drop.

Assume that an estimate,  $\hat{k}_v(x_m)$ , of  $k_v(x_m)$  is known and denote the measured pressure drop by  $\Delta p'$ . Then an estimate of the spool position, which is required for the reference flow  $q_r$  to occur through the valve, may be computed as

$$x_r = \hat{k}_v^{-1} \left( \frac{q_r}{\sqrt{\Delta p'}} \right) \quad (4.2)$$

By controlling the spool position such that  $x_m = x_r$  the flow through the valve is independent of pressure drop, whereby the valve is pressure compensated. This scheme of electrohydraulic pressure compensation is sketched in figure 4.1 where the valve (plant) dynamics is denoted by  $P$  and the spool position controller is denoted by  $C$ .

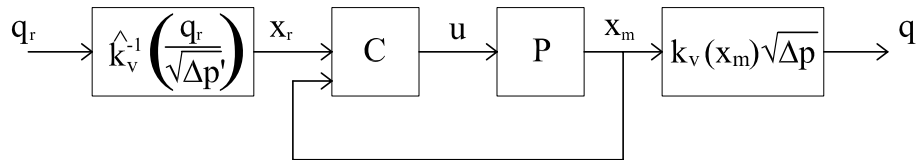


Figure 4.1: Flow control obtained by electrohydraulic pressure compensation.

If the valve is seen as an isolated system the compensation scheme may be considered as a feedforward compensation. This means that the method is sensitive to parameter errors of the estimate  $\hat{k}_v(x_m)$ . When the valve is coupled to a system, a feedback is introduced and the pressure compensation scheme is actually a static feedback linearisation. Thus, the feedback of  $\Delta p$  may also influence on the performance of the flow control.

Three non-trivial challenges follow by using the above method for electrohydraulic pressure compensation:

- The pressure drop must be measured sufficiently accurate to fulfil demands for maximum static flow rate error. If single pressure transducers should be used they should be paired. Ideally differential pressure transducers should be used. Commonly the maximum measurement error of a pressure transducer is rated according the maximum measurement range of the transducer. A plot of the worst case flow error due to a mismatched set of single pressure transducers is plotted in

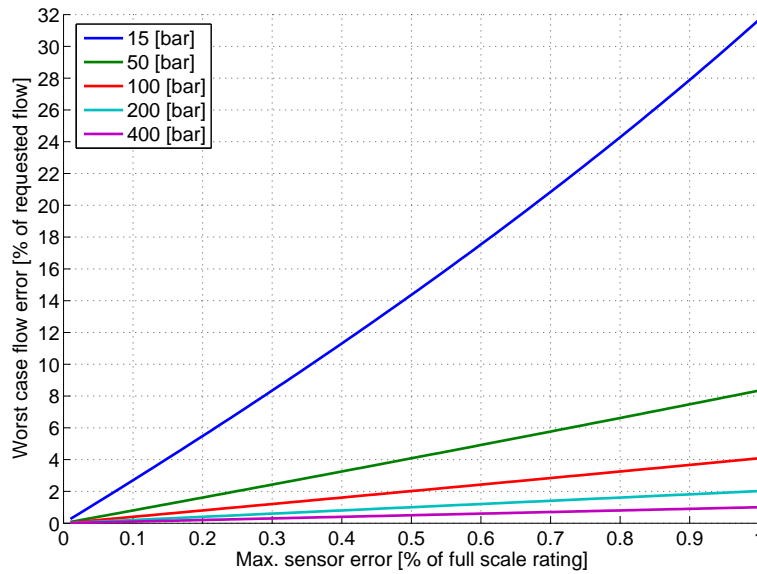


Figure 4.2: Flow error as a function of rated measurement error.

figure 4.2. The error is shown as a function of rated maximum measurement error relative to full range (400 [bar]).

- No feedback is used to correct for flow error. As mentioned the method is therefore sensitive to parameter error of the valve gain estimate  $\hat{k}_v(x_m)$ .
- A main spool position controller must be developed to control the opening of the orifice. The flow force on the main spool may result in large relative gain variations when the pressure drop and the flow rate across the spool varies. The flow force on the main spool approximately increases proportionally to the pressure drop and the flow across the main spool. The position controller must therefore be robust to gain variations.

In the following the focus will be on the last of these challenges, namely the development of spool controllers for the considered valve prototype.

## 4.2 Requirements for flow controller

In this section steady state accuracy requirements for the flow controller are established. It is also shown based on a linearised model that at frequencies where the pressure dynamics of the controlled application shall be decoupled, the magnitude of the closed loop frequency response of the main spool position controller must be unity.



### 4.2.1 Steady state accuracy

Proportional valves using pressure compensating spools currently represent state of the art of pressure compensated valves. The flow control accuracy of these valves is therefore used as a baseline for establishing requirements for the flow controller to be developed. A test using two PVG32 proportional valves from Sauer-Danfoss has been carried out to determine the necessary steady state accuracy of the flow controller. The hydraulic diagram of the test set-up is sketched in figure 4.3.

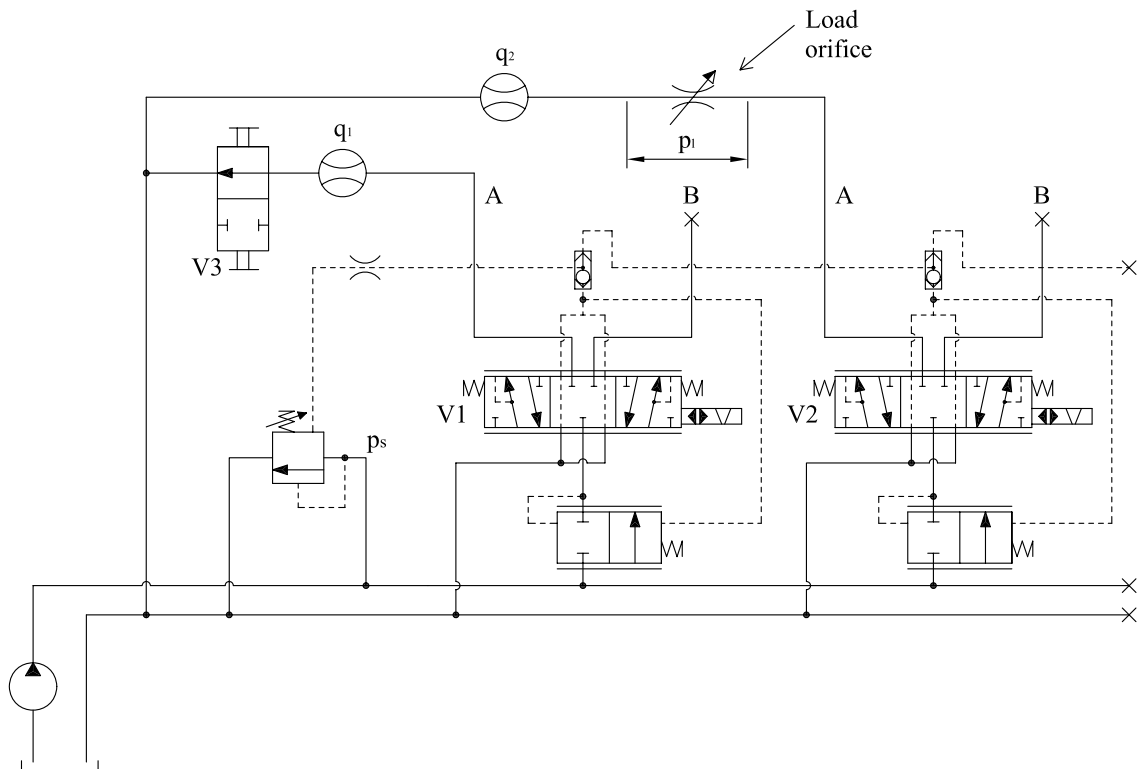


Figure 4.3: Hydraulic diagram of test set-up.

With reference to the hydraulic diagram the following test sequence was carried out:

1. Adjust the supply pressure of the pump to  $p_s$ .
2. Adjust the flow rate out of V1 to  $q_1$ .
3. Adjust the flow rate out of V2 to  $q_2$ .
4. Adjust the pressure drop across the load orifice to  $p_l$ .
5. Block valve V3.
6. Denote the new flow rate out of V2 by  $q'_2$  and compute the flow error relative to the rated flow rate of the valve,  $q_{2max}$ , as  $\frac{q'_2 - q_2}{q_{2max}}$ .

Step 5 raises the supply pressure to  $p'_s$  and therefore also raises the pressure drop across V2 (including the pressure compensator). Since the pressure compensation of the proportional valves are not ideal the flow rate out of V2 changes to  $q'_2$ . Table 4.1 presents the measured flow control accuracy found by applying different values of  $p_s, q_1, q_2$  and  $p_l$  in the test. The maximum flow rate of V2 in the test was  $q_{2max} = 100 \left[ \frac{1}{\text{min}} \right]$ . Two different work points of  $q_2$  was therefore selected for testing both at low and high flow rates relative to the maximum flow rate of the valve.

$p_s$ [bar]	$p'_s$ [bar]	$p_l$ [bar]	$q_1 \left[ \frac{1}{\text{min}} \right]$	$q_2 \left[ \frac{1}{\text{min}} \right]$	$\frac{q'_2 - q_2}{q_{2max}} [\%]$
43	289	20	31	10	<b>0.3</b>
117	292	103	31	10	<b>0.5</b>
52	286	21	30	82	<b>8.7</b>
133	286	103	32	82	<b>8.5</b>

Table 4.1: Measured flow control capability of Sauer-Danfoss PVG32.

It may be seen from the results that the maximum relative flow rate error, which was observed at  $\frac{q_2}{q_{2max}} = 82 [\%]$ , was 8.7 [%]. It may also be seen from the results that at  $\frac{q_2}{q_{2max}} = 10 [\%]$  the maximum flow rate error was 0.5 [%]. Therefore the pressure compensation is more accurate at low flow rates. This makes sense to have repeatability in the control of the valve around the opening point.

From the above test results it has been found that steady state maximum control error requirements may be specified in terms of an error band which depends on the flow rate across the valve. The suggested specification which will be used in this chapter is sketched in figure 4.4.

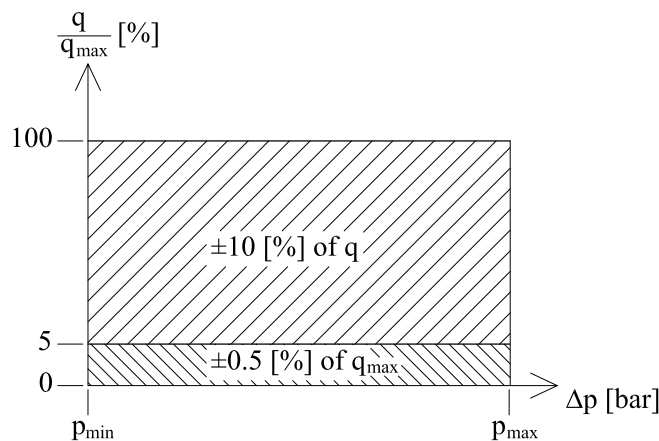


Figure 4.4: Suggested specification of flow control accuracy.

Normally, accurate control of a hydraulic actuator is required at low speed whereas at high speed control accuracy is less important. This matches the specification of flow

control accuracy in figure 4.4. The prototype valve is designed for a maximum flow rate of  $180 \left[ \frac{\text{l}}{\text{min}} \right]$ . According to the specification in figure 4.4, the flow controller for the prototype valve may then have a maximum allowed flow error as plotted in figure 4.5.

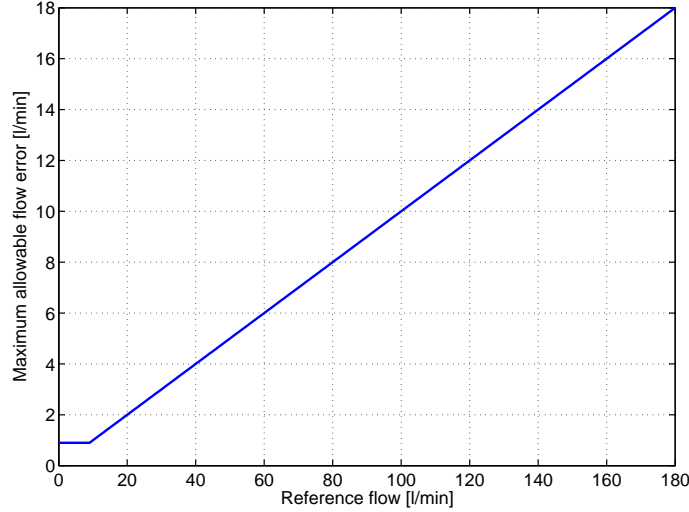


Figure 4.5: Allowed flow error of flow controller for prototype valve .

In this work it is assumed that the opening points of the individual valve is calibrated either at assembly or from a routine which may identify the opening point on-line. The above specification means that the maximum minimum flow rate which is to be metered through the valve is 0.5 [%] of full scale. In practice the opening point of a spool valve varies as a function of pressure drop due to leakage.

The flow rate resolution around the opening point must at least be as small as the maximum minimum flow rate which is to be metered through the valve. For a spool valve with a linear orifice opening area as a function of spool position, as the prototype valve, the minimum worst case position error around the opening point is found by rearranging the orifice equation. Provided that  $\hat{k}_v = k_v$  the maximum spool position error may be computed from

$$D_e = K_e \frac{q_{max}}{\pi d_m C_d \sqrt{\frac{2}{\rho} \Delta p_{max}}} \quad (4.3)$$

$K_e$  is a constant specifying the acceptable percentage flow control error with respect to full scale. For example, if a flow control error of 0.5 [%] of full scale is acceptable then  $K_e = \frac{5}{1000}$ . Therefore, with regard to the prototype valve with the nominal design parameters listed in appendix A, this means that the spool position control accuracy must be at least 1.52 [ $\mu\text{m}$ ] in the flow range from 0 – 5 [%] of rated flow, i.e. 0 – 9 [ $\frac{\text{l}}{\text{min}}$ ]. At 100 [%] of rated flow the position control accuracy for maximum pressure drop should be 30.4 [ $\mu\text{m}$ ]. Thus the difference between accuracy requirements at valve opening and maximum flow is a factor 20. The specification in figure 4.4 will always give this ratio of 20 independent of rated flow and pressure drop.

If the required accuracy at low flow rates cannot be met, then metering notches may be implemented in the main spool, or a chamfer of the metering edge of the spool may be used. This is a technique which is currently also used in state of the art proportional valves. A chamfer or metering notches may also be necessary, however, to limit flow peaks when the valve opens. This is explained in the following.

The main spool must necessarily have an overlap to limit the leakage across the spool. If the inverse flow gain estimate  $\widehat{k}_v(x_m)$  contains information about the overlap, then using the reference specification in (4.2) makes the main spool jump across its overlap region, when a non-zero flow reference is given. However, if the spool position controller is not to be too conservative it is likely that this may result in an overshoot of the spool position when jumping across the overlap. Therefore, to limit the flow peak due to a spool position overshoot, when the spool must jump to the point where the valve opens, the size of a chamfer or of metering notches should also be matched to the performance of the spool position controller. Thus the flow control performance at the valve opening point is made up of a complex connection between spool position controller performance and spool geometry. In practice it may be an iterative procedure during the design of a valve to find an appropriate match between position controller performance and spool geometry.

### 4.2.2 Dynamic flow control requirements

When possible it is convenient to specify the dynamic performance requirements in the frequency domain, as the interconnection of dynamical systems is then easy to analyse. A frequency domain approach is used for analysing dynamic flow control requirements in the following.

Assume for simplicity that the controlled spool valve feature rectangular fluid ports, as the prototype valve. Then the spool position enters linearly in equations (4.1) and (4.2), whereby they simplify to

$$q = k_v x_m \sqrt{\Delta p} \quad (4.4)$$

$$x_r = \frac{q_r}{\widehat{k}_v \sqrt{\Delta p'}} \quad (4.5)$$

Linearising these equations in the work points  $(x_{m_0}, \Delta p_0)$  and  $(q_{r_0}, \Delta p'_0)$  gives

$$\begin{aligned} q &= k_v \sqrt{\Delta p_0} x_m + \frac{k_v x_{m_0}}{2\sqrt{\Delta p_0}} \Delta p \\ &= k_q x_m + k_p \Delta p \end{aligned} \quad (4.6)$$

$$\begin{aligned} x_r &= \frac{1}{\widehat{k}_v \sqrt{\Delta p'_0}} q_r - \frac{q_{r_0}}{2\widehat{k}_v \Delta p'_0{}^{3/2}} \Delta p' \\ &= k_{qr} q_r - k_{pr} \Delta p' \end{aligned} \quad (4.7)$$

We denote the transfer function associated with the closed loop spool position control by  $G_v$ , the filter applied to the measured pressures by  $G_s$  and the transfer function

associated with the pressure dynamics of the controlled application by  $G_p$ . Then combined with the linearised equations (4.6) and (4.7) the suggested flow controller using electrohydraulic pressure compensation may be represented on block diagram form as shown in figure 4.6

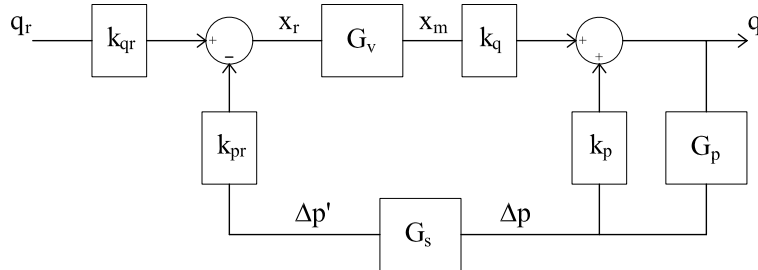


Figure 4.6: Flow controller on block diagram form.

The filter  $G_s$ , which is applied to the measured pressures, must have a unit gain at steady state. Otherwise a steady state flow error is encountered. Therefore we have that  $\Delta p_0 = \Delta p'_0$ . Using this and assuming that the valve gain is perfectly known, that is  $\hat{k}_v = k_v$ , then  $k_q k_{pr} = k_p$  and  $k_{qr} k_q = 1$ , hereby the block diagram simplifies to the one in figure 4.7

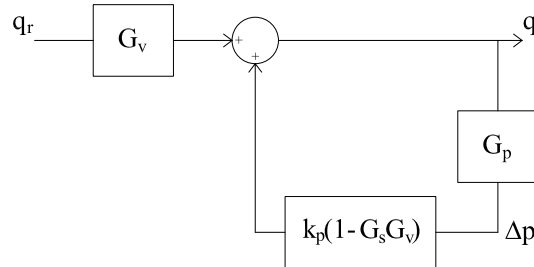


Figure 4.7: Flow controller if  $\hat{k}_v = k_v$ .

Assuming that  $\hat{k}_v = k_v$  is not realistic. However, the obtained block diagram demonstrates the point that at frequencies where the pressure dynamics  $G_p$  shall be decoupled  $G_s G_v = 1$  is required. Due to the product  $G_s G_v = 1$  a known phase lag of  $G_v$  may be compensated for by shaping the filter  $G_s$ . If  $G_s = 1$  this means that the bandwidth of the valve must be larger than the frequency up to which the pressure dynamics shall be decoupled. Thus one strategy is to select the bandwidth of the valve to be larger than any resonant frequencies of  $G_p$ .

Another strategy is to avoid exciting the modes of  $G_p$  by applying slow references. The advantage of this is that if the dynamics of  $G_p$  is not excited the bandwidth of  $G_v$  need not to be high to decouple the pressure dynamics. It should be noted that besides the pressure dynamics of the application itself, external disturbances may also put forward demands on the valve bandwidth.

From this discussion it should be clear that requirements for valve control bandwidth are specifically determined by the controlled application and external disturbances. Qualitatively the bandwidth of the valve should be selected higher than the dominating pressure dynamics of the controlled application.

## 4.3 Preliminary controller design for valve with pressure control pilot

Controller design for and stability analysis of the spool valve with pressure control pilot is considered in this section. Figure 3.1 may be consulted for a recapitulation of the topology of this valve. It is advantageous to check the stability of the internal pressure feedback loop of the pilot circuit before implementing an outer position control loop. Therefore, focus will be directed towards stability of the pressure feedback loop prior to considering controller design.

### 4.3.1 Absolute stability of pressure control pilot valve

The choice of pressure feedback gain (feedback pin diameter) is a compromise between the following issues:

1. Relative stability of the pressure feedback loop.
2. Ability of the feedback pins to provide enough force on the pilot spool to overcome Coulomb friction at power loss. This force is proportional to the pin diameter squared and proportional to the spring/flow force on the main spool.
3. Actuator force required to overcome feedback forces on the pilot spool.
4. The minimum feedback pin diameter which may be manufactured and still achieve an aimed for target cost of the valve.

Issue 4 is not straight forward to analyse without taking manufacturing processes into consideration, which is outside the scope of this work. Issues 2 and 3 may be dealt with from a static viewpoint. The bounds on the feasible feedback pin area due to these issues are given by

$$\frac{f_{f,max}}{p_{p0}} < A_p < \frac{f_{a,max} A_m}{p_{p0} A_m + q_{max} \sqrt{2\rho \Delta p_{max}} \cos(\theta_Q)} \quad (4.8)$$

where it has been assumed that the spring force from the main spool spring is negligible compared to the flow force at maximum flow and maximum pressure drop.

The lower and upper bounds on the diameter equivalent to the area bounds of (4.8) are shown in figure 4.8. The bounds are plotted as a function of minimum pressure



omitted when obtaining the linearised model previously in section 3.6. However, since the maximum feedback gain for which the pressure feedback loop is stable is to be determined, it will be useful to include the friction and analyse the effect of this friction in the frequency domain. To do this an approximate frequency domain interpretation of the non-linear friction feedback must be derived.

#### 4.3.1.1 Frequency domain interpretation of Coulomb friction

For frequency domain analysis the non-linearity of the feedback loop may be approximated by its DF (describing function). That is, provided

$$G(s) = \frac{1}{m_p} \frac{1}{s + 2\zeta_1\omega_1} \quad (4.9)$$

has sufficient low-pass filtering characteristics. This requirement is fulfilled here as in fact the transfer function has the structure of a first order low pass filter. Since steady state is considered no bias occurs at the input of the non-linearity, i.e. the pilot spool velocity is required to be zero at steady state. A SSDF (single sinusoid describing function) may therefore be used.

When approximating (3.18) by  $f_{cp} = f_{cp0} \text{sign}(\dot{x}_p)$  the corresponding SSDF is given by [42]

$$N_{cp}(a) = \frac{4f_{cp0}}{\pi a} \quad (4.10)$$

The signal input amplitude,  $a$ , is given by

$$a = |G(j\omega)| |f_a| \quad (4.11)$$

whereby the amplitude dependent frequency response function of the feedback interconnection becomes

$$G'(j\omega, |f_a|) = \frac{\frac{1}{m_p}}{j\omega + 2\zeta_1\omega_1 + \frac{N_{cp}(\omega, |f_a|)}{m_p}} \quad (4.12)$$

It may be seen that Coulomb friction approximately has the same effect as frequency and amplitude dependent viscous damping. The magnitude of  $G(j\omega)$  is given by

$$|G(j\omega)| = \left| \frac{1}{m_p} \frac{1}{j\omega + 2\zeta_1\omega_1} \right| = \frac{1}{m_p} \frac{1}{\sqrt{\omega^2 + (2\zeta_1\omega_1)^2}} \quad (4.13)$$

Hereby the extra damping associated with the DF may be quantified by

$$\frac{N_{cp}(\omega, |f_a|)}{m_p} = \frac{4f_{cp0}}{\pi |f_a|} \sqrt{\omega^2 + (2\zeta_1\omega_1)^2} \quad (4.14)$$

It may be expected that for small amplitudes the phase lag of  $G'(j\omega)$  is less than the phase lag of  $G(j\omega)$ , because the damping term associated with the SSDF increases with



frequency. Additionally, the magnitude of the SSDF decreases for increasing amplitude, or specifically

$$\lim_{|f_a| \rightarrow \infty} N_{cp}(\omega, |f_a|) \rightarrow 0 \Rightarrow \lim_{|f_a| \rightarrow \infty} G'(j\omega, |f_a|) \rightarrow G(j\omega) \quad (4.15)$$

The frequency response of  $G'(j\omega, |f_a|)$ , by which the above reasoning may be illustrated, is shown in figure 4.10 below. The plot is made with a friction force  $f_{cp0}$  of 0.3 [N], a pilot spool mass  $m_p$  of 68 [g], a viscous damping coefficient  $2m_p\zeta_1\omega_1 = 5 \left[\frac{\text{kg}}{\text{s}}\right]$  and input force magnitudes  $|F_a| = \{0.6, 1.3, 2.8, 5.3\}$  [N]. From the plot it is seen that  $G'(j\omega, |f_a|) \leq G(j\omega)$ . Thus, ignoring Coulomb friction gives an upper bound on the loop gain of the pressure feedback loop.

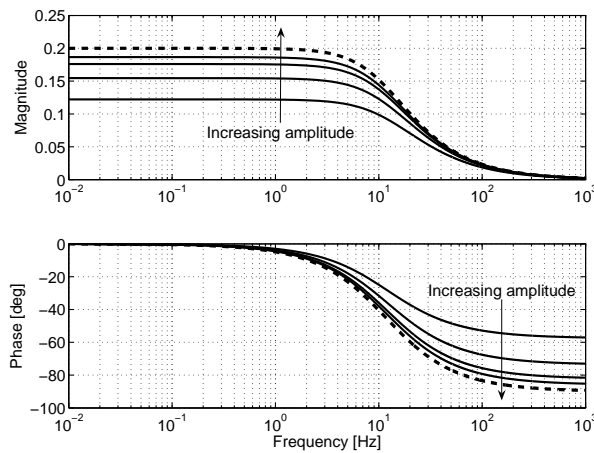


Figure 4.10: Frequency response of  $G(j\omega)$  (dashed) and  $G'(j\omega, |f_a|)$  (solid).

The accuracy of the results relies on the non-linear friction being approximated as a sign function with a gain. The assumption is justified by the fact that a piecewise SSDF description of a friction function including stiction and stiction effects has the same structure as that of the SSDF for a sign function. That is, including the stiction and stiction effects one obtains a sum of terms, like the one in (4.10). The accuracy also relies on that the input to the friction function is expected to be a single sinusoid, that is, with the frequency being that of the fundamental of the output from the friction function. Due to the low pass filtering properties of  $G(s)$  this approximation is expected to be good.

To verify these assumptions the results from a simulation are plotted in figure 4.11. A 10 [Hz] sine signal was used as input. For input amplitudes of  $f_a = 0.9$  [N] and  $f_a = 1.3$  [N], the amplitudes obtained using the SSDF are 14 [%] respectively 5.3 [%] too large. Compared to the linear frequency response function these numbers are 54 [%] respectively 30 [%]. At  $f_a = 1$  [N] the magnitude using the SSDF is approximately 10 [%] too large (not shown). This indicates that regarding gain the SSDF representation of the nonlinearity is slightly conservative. As may also be seen from the plot the simulations using the sign feedback and the SSDF feedback also show smaller phase lags than the simulation obtained with  $G(j\omega)$ .

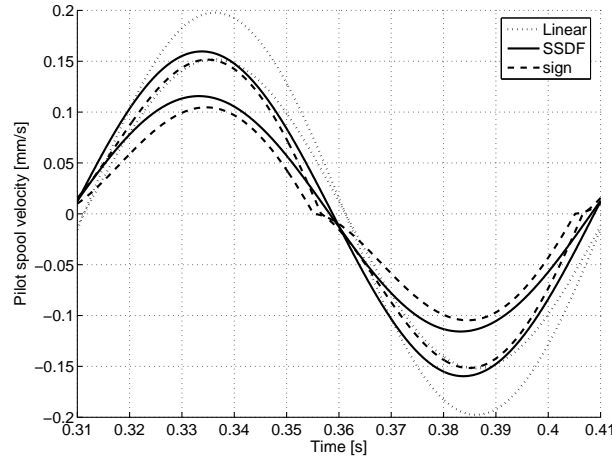


Figure 4.11: Time response of  $G(j20\pi)$ ,  $G'(j20\pi, |f_a|)$  and non-linear system.

It has been indicated that using the linear  $G(s)$  and ignoring the non-linear friction feedback loop in the stability analysis is conservative in terms of maximum loop gain. It should be noted that ignoring the Coulomb friction may be severe in terms of limit cycles. However, limit cycle analysis is a different discipline than maximum gain analysis. Thus, to identify the maximum gain of the pressure feedback loop yielding absolute stability, Coulomb friction will be ignored in the following, being aware that in a maximum gain sense results may be conservative. Using  $G(j\omega)$  instead of  $G'(j\omega, |f_a|)$  has the advantage that frequency domain analysis may be made without considering magnitudes of input signals.

#### 4.3.1.2 Absolute stability by Routh-Hurwitz criterion

Denoting the dead-zone in block diagram sketched in figure 4.9 by  $\Psi(u)$ , then the following inequality holds

$$\Psi(u)(\Psi(u) - u) \leq 0 \quad (4.16)$$

Due to this fact the dead-zone is said to belong to a sector  $[0,1]$  and for maximum gain analysis it may be replaced by a unity gain [51]. The dynamics in the forward path of the block diagram in figure 4.9 is hence given by

$$G_{ol}(s) = \frac{\Delta p_p}{f_a} = \frac{N_1(s)N_2(s)D_5(s)}{D_1(s)[D_5(s)D_6(s) - sN_5(s)N_6(s)]} \quad (4.17)$$

where the notation  $G_i = \frac{N_i}{D_i}$  has been used referring to the transfer functions derived in section 3.6. The frequency response of  $G_{ol}(j\omega)$  is plotted in figure 4.12. The plot is made looping through the operating points given in appendix D. A similar plot where  $G_5(s)$  is approximated by its steady state gain is shown in figure 4.13.

The plots show that, if containing no open loop RHP poles, the dynamics of  $G_5(s)$  may be omitted for stability analysis, as the frequency where  $\angle G_{ol}(j\omega) = -180$  [deg] is slightly lower when neglecting the dynamics of  $G_5(s)$ . Thus, approximating  $G_5(s)$

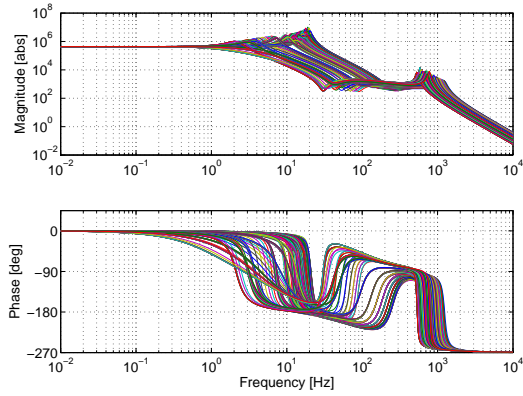


Figure 4.12: Frequency response of  $G_{ol}(j\omega)$  with second order  $G_5(s)$ .

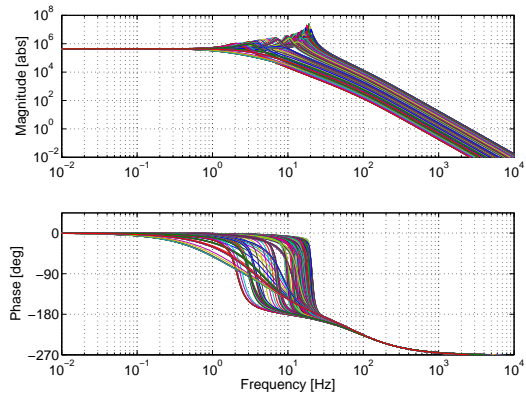


Figure 4.13: Frequency response of  $G_{ol}(j\omega)$  with  $G_5(s) = \frac{A_m}{m_m \omega_5^2}$ .

by its steady state gain is slightly conservative when analysing the loop gain yielding marginal stability. In the following  $G_5(s)$  is therefore approximated by its steady state gain, and it is assumed that the main valve design is such that no RHP poles are present in  $G_5(s)$ . That is, the damping associated with dynamic flow forces is positive; or not more negative than the total damping of the main spool is positive. By this assumption, the closed loop transfer function of the pressure feedback loop may be written as

$$G_{cl}(s) = \frac{\Delta p_p}{f_a} = \frac{s + b_0}{a_4 s^4 + a_3 s^3 + a_2 s^2 + (a_1 + A_p)s + a_0 + b_0 A_p} \quad (4.18)$$

where

$$\begin{aligned} b_0 &= \frac{c_{pa} c_{pb} (k_{qa} k_{pb} - k_{qb} k_{pa})}{c_0} & c_0 &= c_{pa} k_{qa} - c_{pb} k_{qb} \\ a_0 &= \frac{c_1 m_p \omega_1^2}{c_0} & c_1 &= c_{pa} c_{pb} k_{pa} k_{pb} \\ a_1 &= \frac{m_p}{c_0} \left[ \omega_1^2 c_2 + 2\zeta_1 \omega_1 c_1 + \frac{\omega_1^2 A_m^2 c_3}{m_m \omega_5^2} \right] & c_2 &= c_{pa} k_{pa} + c_{pb} k_{pb} \\ a_2 &= \frac{m_p}{c_0} \left[ \omega_1^2 + 2\zeta_1 \omega_1 c_2 + c_1 + \frac{A_m^2 [\omega_1^2 c_4 + 2\zeta_1 \omega_1 c_3]}{m_m \omega_5^2} \right] & c_3 &= c_{pa} c_{pb} (k_{pa} + k_{pb}) \\ a_3 &= \frac{m_p}{c_0} \left[ 2\zeta_1 \omega_1 + c_2 + \frac{A_m^2 [2\zeta_1 \omega_1 c_4 + c_3]}{m_m \omega_5^2} \right] & c_4 &= c_{pa} + c_{pb} \\ a_4 &= \frac{m_p}{c_0} \frac{\frac{1}{m_m} A_m^2 c_4 + \omega_5^2}{\omega_5^2} \end{aligned}$$

For the pressure feedback loop to be marginally stable, we have from the Routh-Hurwitz stability criterion that

$$a_2 a_3 - a_4 (a_1 + A_p) > 0 \quad (4.19)$$

$$-a_4 A_p^2 - [a_3 (a_2 - a_3 b_0) - 2a_1 a_4] A_p + a_1 (a_2 a_3 - a_1 a_4) - a_0 a_3^2 > 0 \quad (4.20)$$

By solving these equations the following absolute stability bounds may be derived<sup>1</sup>

$$0 < A_p < \min \left\{ \frac{\frac{a_2 a_3 - a_1 a_4}{a_4}}{-2a_1 a_4 + a_3 \left[ a_2 - a_3 b_0 + \sqrt{(a_2 - a_3 b_0)^2 + 4a_4 (a_1 b_0 - a_0)} \right]}{2a_4} \right\} \quad (4.21)$$

It turns out from numerical computations that the bound originating from the second order equation in (4.20) is the most restrictive. The bound have been used to compute the maximum feedback pin diameter as a function of flow and pressure drop across the main spool. The results are shown in figure 4.14 for  $\dot{x}_m > 0$  and in figure 4.15 for  $\dot{x}_m < 0$ . It may be seen from the plots that high pressure drop across the main spool yields worst case with regard to absolute stability for both  $\dot{x}_m > 0$  and  $\dot{x}_m < 0$ .

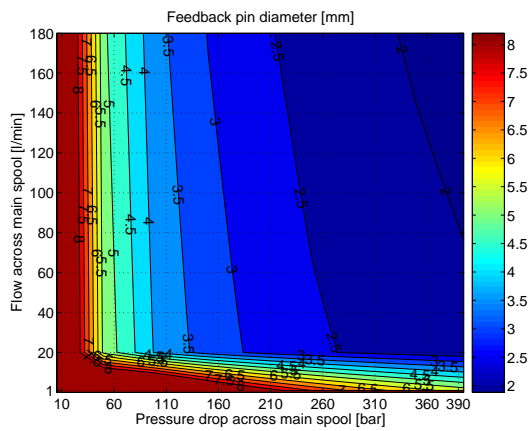


Figure 4.14: Maximum pressure feedback pin diameter ( $\dot{x}_m > 0$ ).

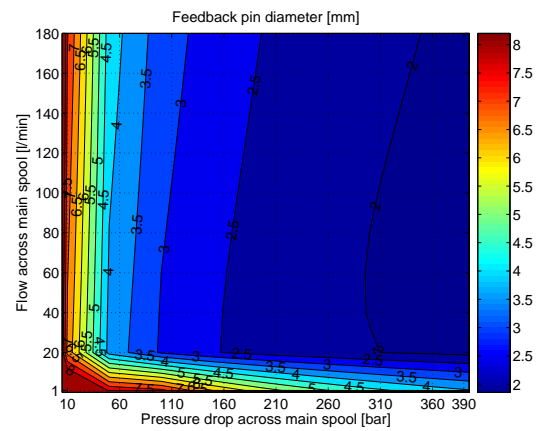


Figure 4.15: Maximum pressure feedback pin diameter ( $\dot{x}_m < 0$ ).

#### 4.3.1.3 Sensitivity analysis of pressure feedback loop stability

Sensitivity of the relative stability of the pressure feedback loop will be considered in the following. Due to the result in figures 4.14 and 4.15, the analysis of relative pressure feedback loop stability will be restricted to considering maximum pressure drop across the main spool. Results will be quantified in terms of gain and phase margins<sup>2</sup>.

The sensitivity to pilot spool + actuator mass is shown in figures 4.16 and 4.17 for respectively  $\dot{x}_m > 0$  and  $\dot{x}_m < 0$ . It is seen that decreasing the mass increases the relative stability. In a design problem the mass should thus be decreased as much as possible. Note that the results denoted 5th order is for the case where main spool

<sup>1</sup>Note, one of the solutions of (4.20) is not an upper bound for  $A_p$ . This may be seen by considering the case where the flow force gradient on the pilot spool is negligible whereby  $a_0 = 0$ . The coefficients of  $G_{cl}$  are positive why  $-2a_1 a_4 < 0$  and furthermore  $a_2 - a_3 b_0 - \sqrt{(a_2 - a_3 b_0)^2 + 4a_4 (a_1 b_0 - a_0)} < 0$  for  $0 \leq a_0 \leq a_1 b_0$ .

<sup>2</sup>A gain margin of 3 – 6 [dB] and a phase margin of 30 – 60 [deg] are commonly used as proper stability margins.

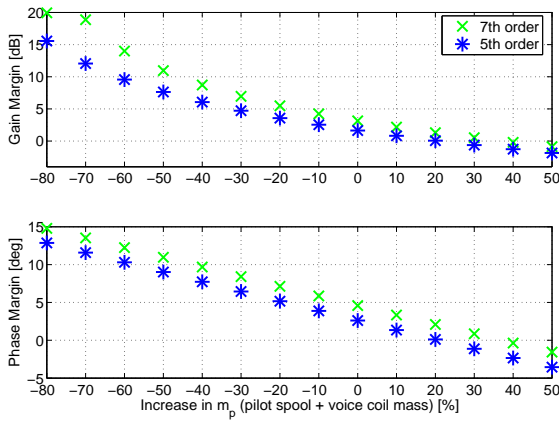


Figure 4.16: Gain and phase margins as a function of change in damping ( $\dot{x}_m > 0$ ).

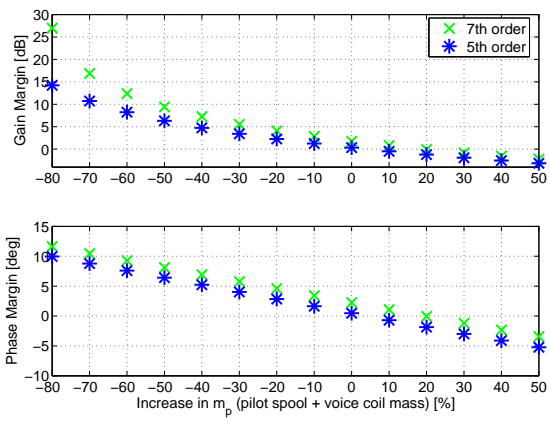


Figure 4.17: Gain and phase margins as a function of change in damping ( $\dot{x}_m < 0$ ).

dynamics is omitted. Results denoted 7th order is for included main spool dynamics (the order refers to the linear transfer function used in the analysis). A comparison shows that ignoring main spool dynamics with regard to stability is conservative as anticipated in section 4.3.1.2. The results are plotted as a function of relative change compared to the nominal design parameters listed in appendix A.

A lumped model of the viscous damping associated with the voice coil was included in the non-linear model. The model verification has indicated that this damping model may contain some uncertainty and it is appropriate to analyse the influence of the damping model on the relative stability. The sensitivity to the coil damping coefficient is plotted in figures 4.18 and 4.19. To increase the damping the clearance between

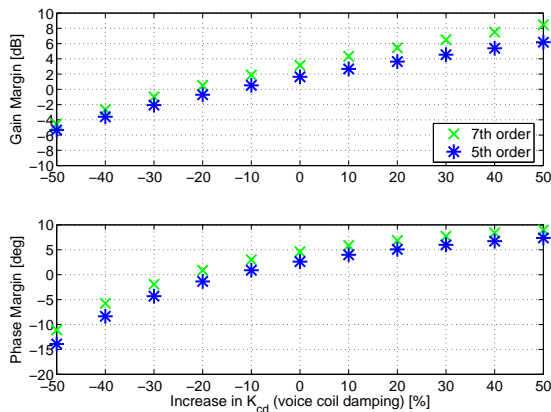


Figure 4.18: Gain and phase margins as a function of change in damping ( $\dot{x}_m > 0$ ).

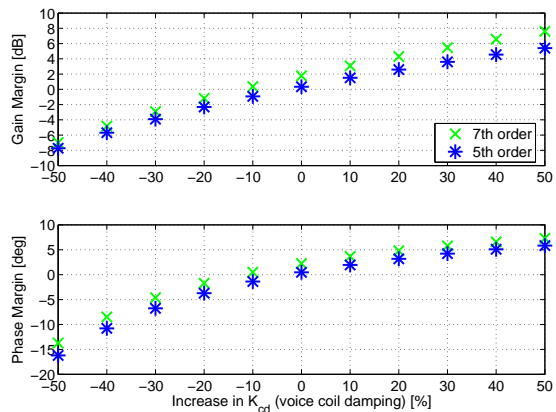


Figure 4.19: Gain and phase margins as a function of change in damping ( $\dot{x}_m < 0$ ).

the field assembly and the coil may be decreased which effectively also decreases the magnetic flux gap, e.g. see figure 3.6. It is seen from figures 4.18 and 4.19 that the relative stability of the pressure feedback loop increases with coil damping as expected.

Computations have shown that the volumes of the pilot chambers facing the ends of the main spool has a negligible influence on the relative stability margin. Because these pilot chamber volumes enter into the main spool dynamics, this should intuitively also be so, as the neglecting of main spool dynamics only has little effect on the relative stability. For a change in pilot chamber volume of  $\pm 90$  [%] the gain margin changed by approximately  $\pm 0.5$  [%] and the phase margin changed by approximately  $\pm 1.5$  [%] (plots are not shown).

For the design parameters considered in the following only a limited range of variation has been considered. Thus the results are presented better in a tabular form than by figure. To obtain the least conservative result, the main spool dynamics has been included in the computation of the relative stability. No distinction between on-stroke  $\dot{x}_m > 0$  and de-stroke  $\dot{x}_m < 0$  has been made.

Table 4.2 shows that the supply pressure used for the pilot circuit has very little influence on the relative stability of the pressure feedback loop.

$p_{pp}$ [bar]	Min. Gain Margin [dB]	Min. Phase Margin [deg]
15	1.76	2.24
20	1.70	2.17
25	1.70	2.18
30	1.70	2.20
35	1.71	2.23

Table 4.2: Gain and phase margins as a function of pilot supply pressure,  $p_{pp}$ .

Another result which is of the same category is a change of the main spool spring pre-stress force. An increase of the main spool spring pre-stress will increase the pressure drop across the active orifice of the pilot spool when  $\dot{x}_m < 0$ . Correspondingly, an increase of the main spool spring pre-stress will decrease the pressure drop of the active orifice when  $\dot{x}_m > 0$ . Thus for  $\dot{x}_m > 0$  it has the opposite effect of increasing the pilot supply pressure. The variation of the relative stability is listed in table 4.3 as a function of main spool spring pre-stress. To be consistent with figure 4.8 the varied variable is listed in [bar]. It is seen that the main spool spring pre-stress practically has no influence on relative stability.

$A_m f_{sm_0}$ [bar]	Min. Gain Margin [dB]	Min. Phase Margin [deg]
1	1.72	2.19
2	1.76	2.24
3	1.63	2.13
4	1.59	2.05
5	1.59	2.02

Table 4.3: Gain and phase margins as a function of main spool spring pre-stress,  $A_m f_{sm_0}$ .

The minimum relative stability margin for three different main spool diameters are

listed in table 4.4. It is seen that an increase in diameter increases the relative stability slightly.

$d_m$ [mm]	Min. Gain Margin [dB]	Min. Phase Margin [deg]
16	1.19	1.59
17	1.27	1.64
18	1.76	2.24

Table 4.4: Gain and phase margins as a function of main spool diameter,  $d_m$ .

Finally, the fluid viscosity has been varied. It is seen from table 4.5 that the stability of the pressure feedback loop is highly dependent on the fluid viscosity. This is not surprising as a decrease of the viscosity gives a decrease of the viscous damping of the pilot spool. It has already been shown by the results in figures 4.18 and 4.19 that stability of the pressure feedback loop is highly dependent on proper damping of the pilot valve.

$\nu$ [cSt]	Min. Gain Margin [dB]	Min. Phase Margin [deg]
2	-19.1	-60.7
5	-13.4	-36.0
10	-6.45	-13.3
20	1.76	2.24
50	14.1	9.25

Table 4.5: Gain and phase margins as a function of kinematic viscosity,  $\nu$ .

The findings by the analysis above have shown that to increase the relative stability of the pressure feedback loop one or both of the following may be done:

- Decrease the pilot spool + actuator mass.
- Increase the viscous damping associated with the pilot spool/actuator assembly.

The analysis also showed that the following parameters only have little influence on the relative stability:

- Pilot circuit supply pressure.
- Main spool spring pre-stress.
- Main spool diameter.

The relative stability as a function of fluid viscosity has also been analysed. It is clear that if the viscosity of the fluid becomes too low compared to the nominal viscosity

used in the computations, e.g. see table A.4, the pressure feedback loop may easily become unstable. In mobile fluid power systems this is critical as the same machine may operate under varying temperature using one type of oil. The conclusion is that to use the pressure control pilot for operating the main spools of the separate meter-in separate meter-out valve. The mix of fluid type, mass and damping of pilot valve should be chosen/ designed carefully.

It should be noted that even though the pressure feedback loop is found to be stable with regard to gain and phase margins computed using the linear model, this does not exclude the possible existence of limit cycles. This is due to the non-linearities, being Coulomb friction and pilot valve overlap, not considered in the linear model. From bifurcation analysis it is well known that a limit cycles cannot be represented by a linear model.

### 4.3.2 Controller design

The stability analysis in the previous subsection showed that the relative stability of the pressure feedback loop is low. It is therefore necessary to apply additional damping to the valve. This may for example be done by introducing fixed orifices between the work ports of the pilot valve and the drain, or by applying a control scheme which improves the relative stability of the valve. Unnecessary oil consumption of the pilot circuit is not desirable why the potential of the latter solution is investigated in the following.

By omitting the dynamics of the main spool and the flow forces on the pilot spool, the dynamical system associated with the valve with pressure control pilot may be represented by the block diagram in figure 4.20.

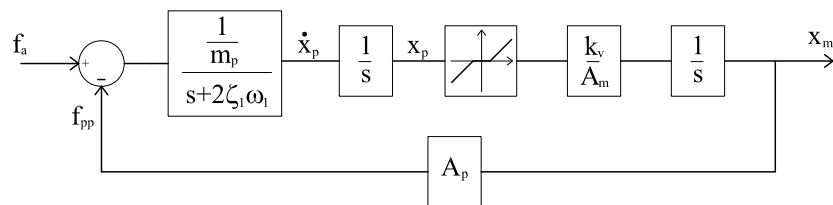


Figure 4.20: Block diagram of simplified dynamical valve model.

Since the main spool acts as an integrator, feeding back the main spool velocity corresponds to feeding back the pilot spool position. Main spool velocity feedback therefore has the effect of including a spring in the pilot stage, thus increasing the open loop phase angle of the system. By open loop in this context is meant the system with velocity feedback but without pressure feedback. Due to the pilot valve overlap, the spring feedback effect is only obtained when the pilot spool operates outside the dead-zone. Inside the dead-zone the gain of the feedforward loop is effectively zero. The damping feedback is sketched in the block diagram of figure 4.21, where a first order filter is placed in the feedback path to filter the main spool position; as it is not desirable to differentiate a potentially noisy signal.



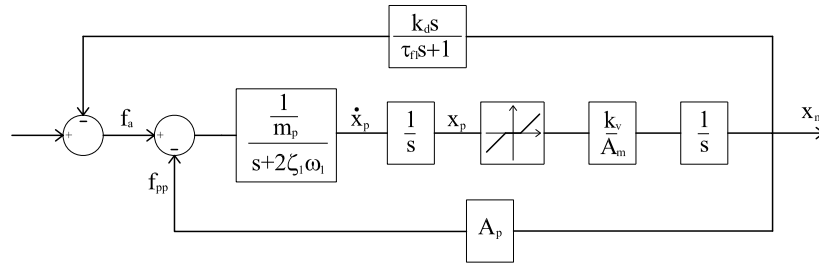


Figure 4.21: Simplified dynamical valve model with implemented damping.

The damping regulator may be extended with proportional and feedforward control action to improve the tracking of the valve. The proportional control action should be combined with a prefilter to increase the proportional gain as much as possible while damping resonant peaks. The purpose of the feedforward action should be to compensate for the prestress of the main spool spring. As the pilot valve generates pressure as a function of force, the feedforward may be included as a sign function with a gain. The proposed overall controller including the filtered velocity feedback is given by

$$f_a = \frac{k_p}{\tau_{f_2}s + 1} x_{mr} - \left( k_p + \frac{k_d s}{\tau_{f_1}s + 1} \right) x_m + \frac{f_{sm_0} A_p}{A_m} \text{sign}(x_{mr}) \quad (4.22)$$

For the set of considered work points listed in appendix D, the obtained frequency responses using this controller are plotted in figure 4.22.

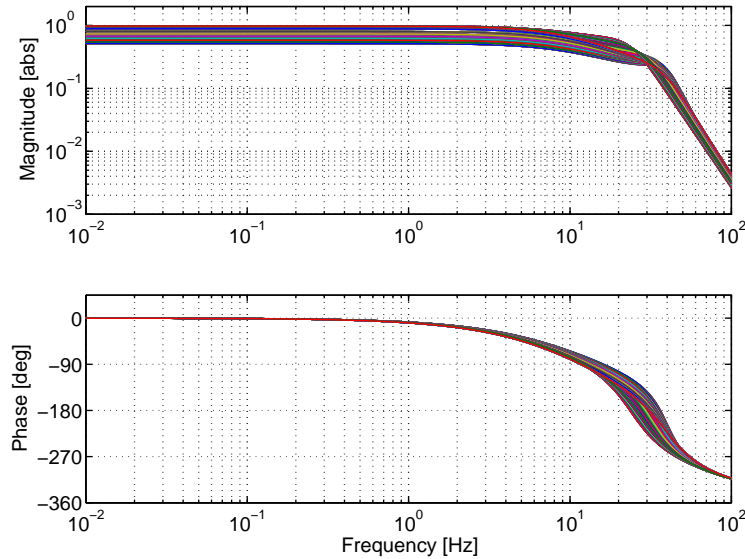


Figure 4.22: Closed loop frequency response of valve with controller in (4.22).

It may be seen that even though the loop is closed, the steady state gain variation is still large. The gain variation is due to the variation of pressure drop across the main spool. Specifically it turns out that the closed loop gain variation is approximately

inversely proportional to the pressure drop across the main spool, which is due to flow forces. Hence, it may be compensated for by scaling the flow reference proportionally to the pressure drop. Hereby the control scheme, including the electrohydraulic pressure compensation may be represented by the block diagram in figure 4.23. In the block diagram the proportional scaling of the flow reference is given by

$$k(\Delta p) = k_1 \Delta p + k_0 \quad (4.23)$$

Note, the flow reference is scaled instead of the spool position reference in order not to scale the compensation for the main spool overlap as a function of pressure drop.

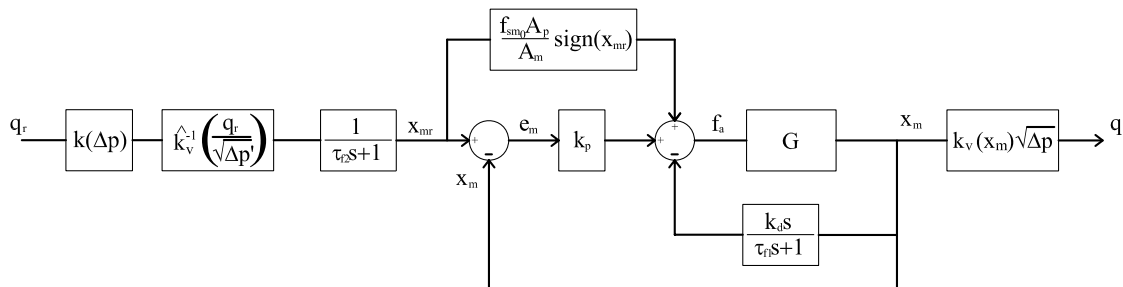


Figure 4.23: Overall control scheme including electrohydraulic pressure compensation.

The simulated flow tracking using the controller sketched in figure 4.23 is plotted in figure 4.24. The responses fulfil the requirements for steady state error set out in section 4.2.1. However, at large pressure drops the damping of the valve is still low as may be seen from the results. Additional damping is theoretically possible, however, the maximum force level obtained from the simulation data was 6.6 [N]. This maximum force will clearly increase if the damping gain  $k_d$  in (4.22) is increased.

The stability of the system is reliant on the stability of the internal loop closed by the pressure feedback. That is, the proposed controller does not stabilise the system if the pressure feedback loop introduces right half plane poles in the dynamical model of the valve. Another controller than that proposed might stabilise the system. However, due to safety of mobile fluid power applications in case of an electrical power loss, it is a requirement that the internal pressure feedback loop is stable by itself, because it is the pressure feedback loop that must bring the main spool back to the fail safe null position.

The conclusion is that if the stability of the internal pressure feedback loop may be guaranteed in addition to force limitations for the damping of the valve not being an issue, the potential of applying a pressure control pilot for the separate meter-in separate meter-out valve looks promising. However, due to the stability issues pointed out focus is directed to developing spool position controllers for the valve with flow control pilot.

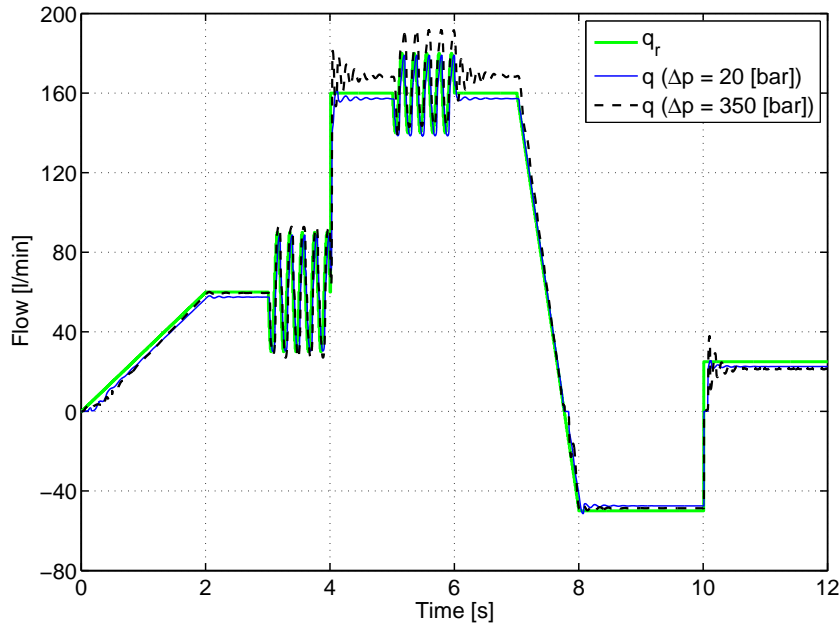


Figure 4.24: Simulated flow tracking.

#### 4.4 Preliminary controller design for valve with flow control pilot

In this section a spool position controller for the spool valve with flow control pilot is developed and evaluated. The controller design takes its basis in the linear model derived in section 3.6. Figure 3.2 may be consulted for a recapitulation of the topology of the spool valve with flow control pilot.

In terms of the transfer functions derived in section 3.6, the linearised open loop dynamics of the valve with flow control pilot is given by

$$G_p = \frac{x_m}{f_a} = \frac{G_1 G_2 G_5}{1 - s G_5 G_6} \quad (4.24)$$

Recall, that the pilot spool dynamics  $G_1$  is given by (3.48), the first order term for pilot chamber pressure build  $G_2$  up is given by the simplified version of (3.60), and the main spool dynamics  $G_5$  is given by (3.64). When linearising in the work points listed in appendix D a specific linear model  $G'_p$  is obtained for each work point. The collection of linear models for all the considered work points is a model set, which we will denote by  $G_{\Pi}$ . Mathematically we write that  $G'_p \in G_{\Pi}$ . The open loop plants in  $G_{\Pi}$  do not have RHP zeros and are thus minimum phase systems.

The frequency responses of the plants in  $G_{\Pi}$  are shown in figure 4.25. It may be seen that there is a large variation of the frequency response at both low and high frequencies as a function of the operating point. As the flow force on the main spool increases the differential pilot pressure available to drive the main spool decreases. This along

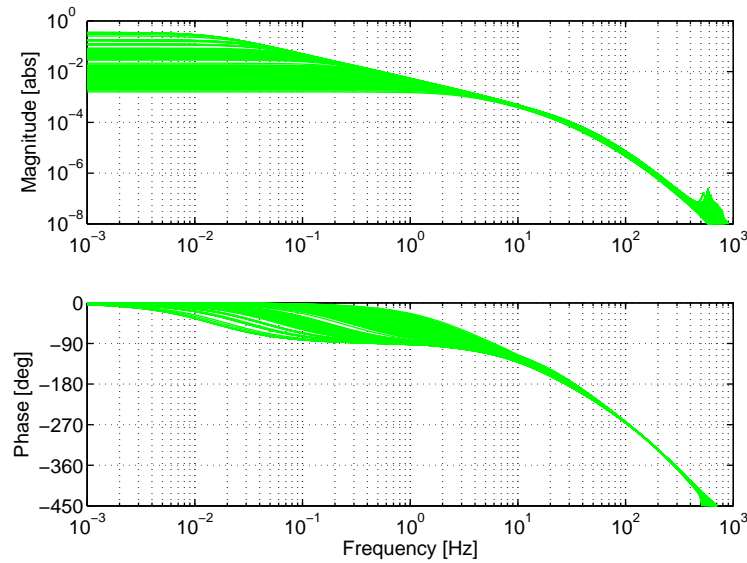


Figure 4.25: Open loop frequency response of the plants in  $G_{II}$ .

with the fact that leakage across the pilot spool lands occur gives the low frequency gain variation shown in figure 4.25. Flow forces acting on the main spool varies as a function of both pressure drop and spool position. Therefore the low frequency gain also varies as a function of these two variables. The high frequency variation between the frequency responses also originates from the flow force, as when the flow force increases, the pressure in the pilot chamber holding the main spool increases. Due to air in the oil this in turn increases the effective bulk modulus of the oil, which finally enter into the expression for the natural frequency of the main spool.

The second order first stage dynamics which is associated with the pilot valve has a lower roll of frequency than the second order main stage dynamics, which is associated with the main valve. The resonant peaks seen around 0.6 – 1 [kHz] in figure 4.25 are due to the resonance of the main spool. No resonance of the pilot spool is seen due to the fact that it is overdamped with a roll of frequency around 15 [Hz].

Due to the overdamped pilot valve, resonant peaks of the second order pilot valve dynamics is not a problem when closing the loop. Thus care must only be taken to keep the resonant peaks of the main spool dynamics below 1, i.e. the gain margin must be positive. Due to the resonance of the main spool being at high frequency it is possible to use a large loop gain at low frequency. At intermediate frequencies phase lead action may be applied to compensate for the phase lag of the pilot valve. A good controller for the linear plants in  $G_{II}$  is therefore a proportional-derivative controller. However, as the controller is to be implemented in a sampled date system, then, due to possible noise on the position transducer signal, the derivative action should preferably be implemented as a phase lead term. The following control law is suggested, in terms of the Laplace variable  $s$

$$f_a = \frac{\tau_d s + 1}{\tau_f s + 1} K_p e_m \quad (4.25)$$

where  $e_m = x_{mr} - x_m$ .

Implementing this controller for the model set  $G_{II}$  results in the frequency responses plotted in figure 4.26. The position tracking response obtained by simulation using the non-linear model is shown in figure 4.27. It is clear that the steady state gain expected

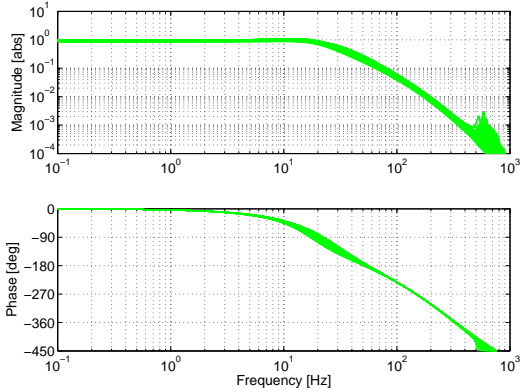


Figure 4.26: Frequency responses of plants in  $G_{II}$ .

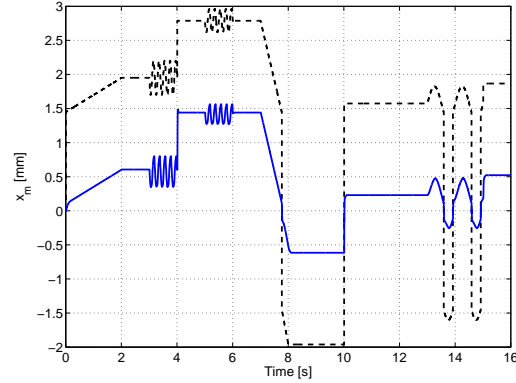


Figure 4.27: Time response,  $\Delta p = 50$  [bar]. Reference is shown dashed.

from the frequency responses and that observed from the simulation are divergent. This is because of the pre-stress of the spring in the pilot valve, and the fact that the pilot spool must be offset from neutral to hold the main spool in position. The latter offset hold position is due to the pilot valve dead-zone, e.g. see the description of the pilot and main spool interaction in section 3.2.

The spring prestress and the dead-zone are hard non-linearities which cannot be included in the linearised model. In fact the operating points where the frequency responses of the linear model set are valid, are at the limit of the dead-zone, where the active orifice of the pilot valve just opens, i.e. at null spool lap. Therefore, the plotted frequency responses may be seen as a representation of the dynamic performance if the dead-zone as well as the spring prestress of the pilot valve are absent.

Simulations have shown that the position where the pilot spool settles over time for a constant reference is approximately at the point where the drain port of the pilot spool opens. The pilot spool offset is therefore approximately equal to the drain port underlap of the pilot spool. This offset position is shown in figure 4.28 for the case where the main spool is moved to a positive position relative to the null position (the main spool is open to the A-port). Due to symmetry a corresponding hold position exists for negative main spool stroke.

It may be useful to implement a feedforward control action moving the pilot spool to either of the two hold positions. However, the exact drain port underlaps are unknown. Therefore only the spring prestress force,  $f_{sp0}$ , which is a design parameter, and the assumed hold position of the pilot spool may be compensated for.

The assumed hold position may be selected by choosing the maximum drain port underlap which can occur according to manufacturing tolerances. This is done here to move the pilot spool as close to the centre of the dead-zone of the pilot valve as possible.

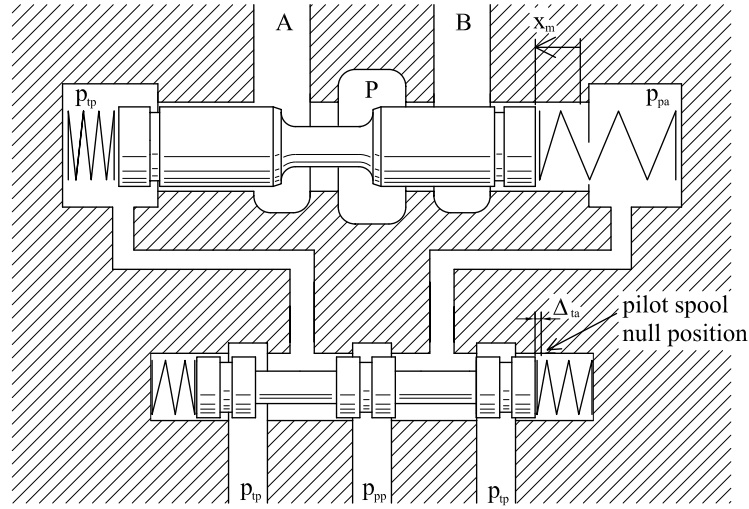


Figure 4.28: Pilot spool offset from null to hold main spool.

Recall that in the hold position, that is associated with a particular work port, the dead-zone of the pilot valve is computed by the difference of the absolute pilot spool overlap and the absolute pilot spool underlap, see equations (3.2) and (3.3). A feedforward force contribution moving the pilot spool to its assumed hold positions may therefore be computed as

$$f(x_{mr}) = \begin{cases} f_{sp0} + k_{sp}\Delta_{tmax} & x_{mr} > \epsilon_{x_m} \\ 0 & |x_{mr}| \leq \epsilon_{x_m} \\ -f_{sp0} - k_{sp}\Delta_{tmax} & x_{mr} < -\epsilon_{x_m} \end{cases} \quad (4.26)$$

where  $\epsilon_{x_m}$  is a small positive constant to limit sensitivity to a noisy reference signal.

We want to apply the feedforward contribution along with a proportional-lead controller. However, if applying a reference  $|x_{mr}| \geq \epsilon_{x_m}$  with  $x_m = 0$  being the initial main spool position, the feedforward control action will behave as a step input. Added to the proportional feedback control action of the proportional lead controller this corresponds to the control system having a large gain for this type of reference, i.e. a step input from the main spool null position. Consequently the plant may saturate or the spool position may overshoot. To avoid overshooting or plant saturation the feedforward contribution may be filtered or limited by a rate limit. In the following a first order feedforward filter is applied whereby the proportional-lead-feedforward (PLF) control law in terms of the Laplace variable  $s$  becomes

$$f_a = \frac{\tau_d s + 1}{\tau_f s + 1} K_p e_m + \frac{1}{\tau_{ff} s + 1} f(x_{mr}) \quad (4.27)$$

where the two inputs are the main spool position reference  $x_{mr}$  and the tracking error  $e_m$ .

Using this controller the simulated flow tracking response in figure 4.29 is obtained for the nominal size of the pilot spool dead-zone. The nominal dead-zone size corresponds to the pilot valve being manufactured such that the dimensions are in the centre of the

tolerance band. In the simulation perfect inversion of the valve gain has been used for the electrohydraulic pressure compensation. Therefore the error is due to position tracking error only. For a valve having the maximum dead-zone, which may be encountered by the selected manufacturing tolerances, the simulated flow tracking response is shown in figure 4.30.

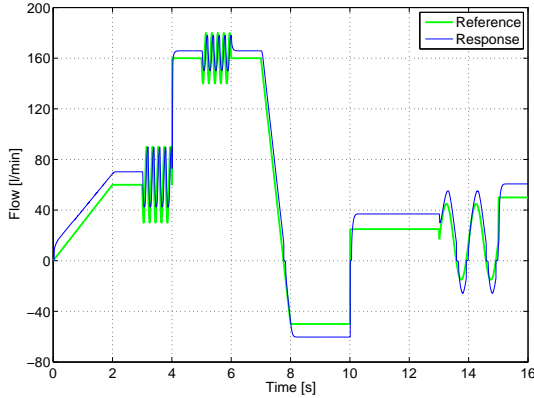


Figure 4.29: Flow tracking with nominal pilot spool overlap,  $\Delta p = 50$  [bar].

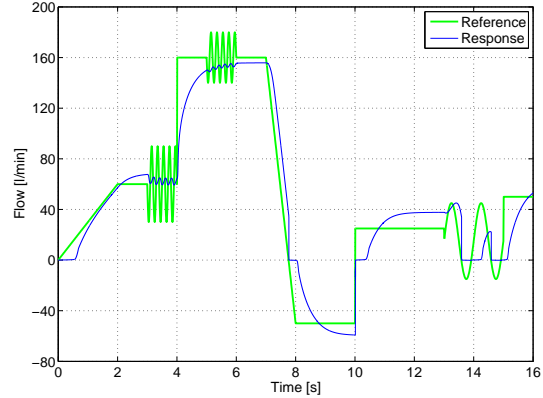


Figure 4.30: Flow tracking for maximum pilot spool overlap,  $\Delta p = 50$  [bar].

Note, the results in figures 4.29 and 4.30 showing flow cannot be directly compared to figure 4.27 showing spool position. However, the spool position in figure 4.27 is so far off the reference value that no flow would be metered out of the valve due to the main spool overlap. This is not the case with the responses in figures 4.29 and 4.30 why we may conclude that the feedforward improves the tracking performance. Neither of the responses fulfil the steady state error requirements according to figure 4.5 though. However, motivated by the seemingly good frequency responses of figure 4.26, in case the dead-zone may be compensated for, the next part of the chapter is concerned with making the PLF controller robust. That is, robust to both the dead-zone of the pilot valve and disturbances in general. Approximate performance demands due to the dead-zone and disturbances, and approximate methods for determining these are considered in the following.

## 4.5 Performance specification and analysis in the frequency domain

This section is meant as an introduction to readers not familiar with performance analysis and specifications in terms of the sensitivity function  $S$  and the complementary sensitivity function  $T$  of a closed loop control system. Readers familiar with this topic may skip directly to section 4.6. The introduction is useful to give a meaningful interpretation of the results in the following section. The content of the current section is

based on material from [89] which may be consulted for details beyond the scope of this small introduction.

Without loss of generality it is assumed that the plant model,  $G_p$ , and the disturbance model,  $G_d$ , are arranged as shown in figure 4.31<sup>3</sup>. Both models are transfer functions or transfer matrices. If the disturbance does not enter at the output of the physical plant

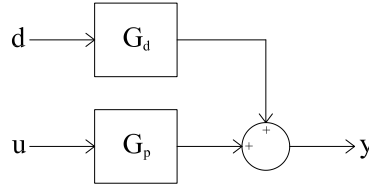


Figure 4.31: Generic model structure.

as sketched, a disturbance entering at the output is obtained by include some of the plant dynamics in the disturbance model.

The open loop model may be written as

$$y = D_e^{-1} \hat{G}_p D_u u + D_e^{-1} \hat{G}_d D_d d = G_p u + G_d d \quad (4.28)$$

where  $D_e$ ,  $D_u$  and  $D_d$  are scaling factors. The signals  $\{y, u, d\}$  are vectors for the MIMO case and scalars for the SISO case. The scaling factors are selected such that  $\{|y_i|, |u_i|, |d_i|\} \leq 1$ .  $\hat{G}$  denotes an unscaled transfer function or transfer matrix. A choice of scaling factors useful for our purpose is

- $D_e$ : Maximum control error
- $D_u$ : Maximum control input, e.g. actuator saturation level
- $D_d$ : Maximum expected disturbance input

For the SISO system (the valve model) considered in this chapter the scaling factors are scalar values.

A feedback controller may be implemented as  $u = K(r - y - n)$ , where  $r$  is the reference and  $n$  is measurement noise. Hereby the closed loop response is given by

$$y = Tr + SG_d d - Tn \quad (4.29)$$

where  $S$  and  $T$  are respectively the sensitivity function and the complementary sensitivity function. These are defined as

$$S = (I + G_p K)^{-1} \quad (4.30)$$

$$T = (I + G_p K)^{-1} G_p K = SG_p K \quad (4.31)$$

<sup>3</sup>Note, sensor dynamics which is not negligible should be included in  $G_p$ .



$$S + T = I \quad (4.32)$$

In terms of  $S$ , the input signal to the plant may be written as

$$u = K Sr - K S G_d d - K S n \quad (4.33)$$

where it may be seen, due to the scaling applied in (4.28), that  $|KS| < 1$  is the requirement to avoid control saturation due to reference changes or noise. The tracking error may be written as

$$e = y - r = -Sr + S G_d d - T n \quad (4.34)$$

From (4.29) it is seen that to have good tracking  $T$  should be large, which from (4.32) is equivalent to requiring  $S$  small. From (4.34) a small  $S$  gives good disturbance rejection. However, from (4.34) and (4.32) good tracking and good noise rejection cannot be obtained at the same frequencies. Fortunately, this is often not necessary. The control bandwidth is defined as where  $|S|$  crosses  $\frac{\sqrt{2}}{2}$  from below.

#### 4.5.1 Disturbance rejection of SISO plant

In the following it is assumed that measurement noise is insignificant in the frequency range where  $|S| < 1$ . Additionally it is assumed that a maximum disturbance and a maximum reference do not appear at the same time. By these assumptions and the fact that the plant inputs and outputs have been scaled it is seen from (4.34) that the performance requirement for disturbance rejection is

$$|S(j\omega)| < \frac{1}{|G_d(j\omega)|} \quad (4.35)$$

If one tries to make  $S$  small by increasing the controller gains then we obtain

$$\lim_{|K| \rightarrow \infty} |K S G_d| \rightarrow \frac{|G_d|}{|G_p|} \quad (4.36)$$

Due to actuator saturation this gives a performance limitation of a plant with regard to rejecting disturbances

$$|G_p(j\omega)| > |G_d(j\omega)| \quad \forall \omega \quad (4.37)$$

However, the magnitude of the scaled tracking error is allowed to be unity. Hence, a less strict magnitude bound on  $G_p$  is derived from (4.28). Since  $r = 0 \Rightarrow e = y$ , the minimum input required to keep  $|e| < 1$  is when the complex vectors given by  $G_p u$  and  $G_d d$  have opposite phase. Having  $|u| < 1$ , the magnitude of  $G_p$  to reject a disturbance should at least be

$$|G_p(j\omega)| > |G_d(j\omega)| - 1 \quad \forall \omega \text{ where } |G_d(j\omega)| > 1 \quad (4.38)$$

If (4.38) is fulfilled the plant does not have any fundamental limitations to controllability regarding disturbance rejection. However, even though this is the case, fulfilling (4.35)

may not be possible by a low order controller as the phase lead of such a controller is limited and an appropriate phase margin may then be a problem. Furthermore high frequency uncertainty of the plant model restricts the frequencies where  $|S|$  may be kept below  $1/|G_d|$ .

The disturbance  $d$  entering the plant in figure 4.31 should be thought of as being sinusoidal. Thus if performance requirements for other disturbances than sinusoidal ones are to be analysed, a scaling as a function of frequency should be applied to describe the disturbance in the frequency domain. If we are concerned with  $\mathcal{H}_\infty$  performance, the frequency weighted scaling must be chosen with some restrictions, namely that  $d$  must have a finite  $\mathcal{H}_2$  norm. This is due to the fact that the  $\mathcal{H}_\infty$  norm is induced by the  $\mathcal{H}_2$  norm. The  $\mathcal{H}_\infty$  norm corresponds to the  $\mathcal{L}_1$  norm in the time domain and therefore gives the worst case gain of the system. We require  $d$  to belong to the class of signals

$$V' = \left\{ v'(s) : \|v'\|_2 = \sqrt{\frac{1}{2\pi} \int_{-\infty}^{\infty} v'^*(j\omega)v'(j\omega)d\omega} \leq 1 \right\} \quad (4.39)$$

By introducing a weight, a new class of signals is obtained

$$V = \{v(s) = W(s)v'(s) : \|v'\|_2 \leq 1\} \quad (4.40)$$

A suitable performance objective for synthesizing a controller to reject a specific class of disturbance signals is therefore obtained by replacing  $G_d$  in (4.35) by

$$G'_d(s) = G_d(s)W(s) \quad (4.41)$$

If we are only interested in analysing or specifying performance for a specific disturbance signal (again other than a sinusoidal one)  $W(s)$  may simply be chosen as the Laplace transform of the disturbance signal. This is the approach which is used further below.

### 4.5.2 Minimum bandwidth due to RHP-poles

The transfer functions describing the main stage dynamics of the considered spool valves may have a set of complex RHP-poles. This is because the damping from the transient flow forces on the main spool may be negative, depending on the direction of flow through the valve. In the following a lower bound on the bandwidth of the complementary sensitivity function is derived for the case a plant has RHP-poles.

If  $\frac{1}{|w_T|}$  is an upper bound for  $|T(j\omega)|$  then

$$|T(j\omega)| < \frac{1}{|w_T(j\omega)|} \quad \forall \omega \quad (4.42)$$

Obviously, stability of  $T(s)$  is required whereby the poles of  $T(s)$  must be in the left complex half plane ( $T(s)$  is analytical in the complex right half plane). Hence, from the absolute maximum modulus principle (e.g. see theorem 16.28 in [13]) the maximum of

$T(s)$  in the RHP is attained on the  $j\omega -$  axis. From interpolation constraints  $T(p) = 1$ , where  $p$  is the location of the RHP pole. Therefore the following is obtained

$$\|w_T T\|_\infty \geq |w_T(p)| \quad (4.43)$$

From (4.42) and (4.43)

$$|w_T(p)| < 1 \quad (4.44)$$

An upper bound  $\frac{1}{|w_T|}$  on  $|T(j\omega)|$  may be chosen as

$$w_T = \frac{s}{\omega_{bT}} + \frac{1}{M_T} \quad (4.45)$$

where  $M_T$  is the low frequency gain and  $|w_T| = 1$  at  $\omega = \omega_{bT} \sqrt{1 - \frac{1}{M_T^2}} < \omega_{bT}$ . If  $p = \alpha + j\beta$ , then by using (4.45), (4.44) is equivalent to

$$\omega_{bT} > \frac{\frac{\alpha}{M_T} + \sqrt{\frac{\alpha^2}{M_T^2} + (1 - \frac{1}{M_T^2})(\alpha^2 + \beta^2)}}{1 - \frac{1}{M_T^2}} \quad (4.46)$$

For the case where the system has real or complex RHP poles this result may be used to compute a minimum control bandwidth  $\omega_c$  by letting  $\omega_c \approx \omega_{bT}$ . One may think of the bound as saying that for stability of the closed loop system the bandwidth of  $T$  must be larger than the distance from the origin to the unstable pole in the complex right half plane. Therefore actuator saturation may be a significant problem when trying to stabilise an unstable system.

## 4.6 Performance demands for closed loop position controller

In this subsection the impact on controller bandwidth requirements from the pilot valve dead-zone and from a pressure disturbance in the drain of the pilot circuit are analysed. The tools presented in the previous subsection are used for this. As explained in the previous subsection the first step is to scale the plant transfer function. The maximum position control error is obtained by combining the specification in figure 4.4 with equation (4.3). This scaling is used for the analysis presented subsequently.

It should be noted that the performance requirements specified in the following is mainly due to the fundamental valve design and the chosen design parameters of the valve. Although this research is focused around a prototype build of available of the shelf components, the analysis will anyway show some of the trade-offs of the particular type of valve design. Other design dimensions may give other numbers for the controller bandwidth requirements.

### 4.6.1 Decoupling of dead-zone in pilot valve

The methods given in section 4.5 regarding the ability of given feedback controller to decouple a disturbance, and the fundamental ability of a plant to decouple a disturbance are based on sinusoidal signals. Thus systems with hard non-linearities such as a dead-zone cannot be directly handled by the method. However, a plant with a dead-zone, such as the valve considered in this work, may be reformulated to a plant with a saturation instead as shown in figure 4.32. In the figure the two upper block diagrams are equivalent.

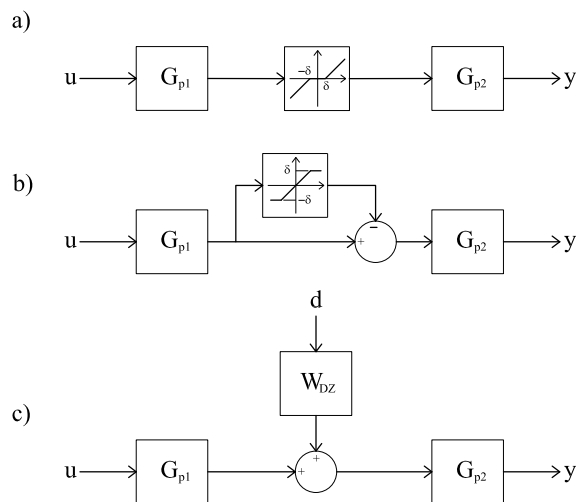


Figure 4.32: a) System with dead-zone. b) Equivalent system with saturation. c) Approximate system with disturbance weight.

As the dead-zone is a single valued non-linearity, it may be shown by describing function analysis that the feedforward path with the saturation may be opened without removing phase lag from the loop. That is, if the amplitude of a sinusoidal signal which is input to the saturation is sufficiently large compared to the saturation level. Additionally, the gain of the loop is not lowered by opening the loop, as the output from the saturation has opposite phase compared to the output of  $G_{p1}$ , see also the comment below equation (4.16) on page 89 regarding the maximum gain of the dead-zone because it is sector bounded. The approximation in the lower block diagram of figure 4.32 may thus be made for large signals compared to the width of the dead-zone. Hereby, the dead-zone may be considered as a disturbance.

For large sinusoidal signals (and step references) the disturbance due to the dead-zone may be considered approximately as a step. An input weight for this case may be chosen as

$$W_{DZ}(s) = \frac{G_{p1}(s)}{G_{p1}(0)} \frac{1}{s} \delta \quad (4.47)$$

Using the linear transfer functions derived in section 3.6, the model of the step disturbance, which enters at the output of the plant as shown in figure 4.31, is written

as

$$G_{d_{DZ}}(s) = D_e^{-1} \frac{G_2(s)G_5(s)}{1 - sG_5(s)G_6(s)} W_{DZ}(s) \quad (4.48)$$

The frequency responses of the set of disturbance models are plotted in figures 4.33 and 4.34 for two different size of dead-zones,  $\delta = \pm 0.15$  [mm] for small signal response where the main spool does not have to cross its null position and  $\delta = \pm 0.45$  [mm] for large signals where the main spool must cross its null position, e.g. see the explanation in section 3.2. One disturbance model for each specific operating point is obtained. Therefore the frequency responses of a set of disturbance models are plotted when all the operating points listed in appendix D are considered.

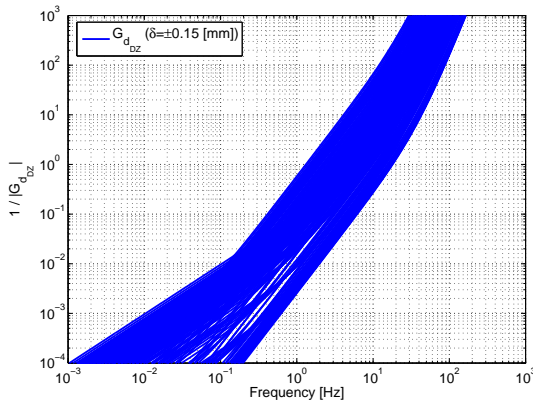


Figure 4.33: Frequency response of dead-zone disturbance for  $\pm 0.15$  [mm] dead-zone.

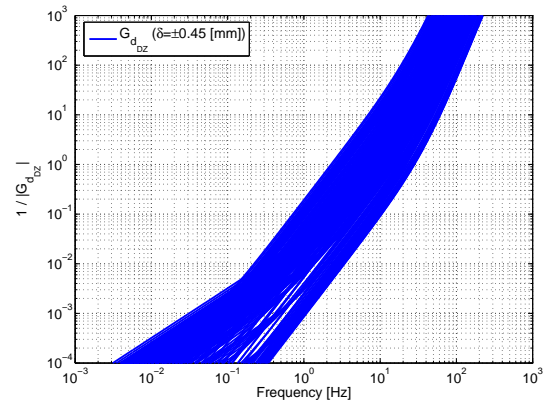


Figure 4.34: Frequency response of dead-zone disturbance for  $\pm 0.45$  [mm] dead-zone.

It may be seen by figure 4.33 that the control bandwidth should for best case operating point be  $> 1$  [Hz], and for worst case operating point the control bandwidth should be  $> 18$  [Hz] to approximately compensate for the dead-zone for small signals. This is seen as  $1/|G_{d_{DZ}}|$  crosses 1 from below at these frequencies. By figure 4.34 it may be seen that for large signals the best case work point gives a control bandwidth which should be  $> 2$  [Hz] and the worst case work point gives a control bandwidth which must be  $> 28$  [Hz]. The best case work point is for low pressure drop across the main spool and the worst case work point is obtained for high pressure drop across the main spool.

It should be noted that these approximate requirements are only valid provided the input signal does not saturate. To decouple the dead-zone both conditions in (4.35) and (4.37) must be fulfilled. The disturbance model derived in this section only gives requirements for (4.35), whereas fulfilling (4.37) may not be possible due the fundamental limitations of the plant. For example, due to pilot valve of the prototype being overdamped by the viscous damping applied on the voice coil, the roll off frequency of the pilot valve is only 15 [Hz]. Therefore, it is unlikely that a control bandwidth  $> 28$  [Hz] may be obtained. On the other hand, for the best case operating point the dead-zone should not pose a problem as this only requires a bandwidth  $> 2$  [Hz], approximately.

### 4.6.2 Decoupling of pilot drain pressure disturbances

Due to the low standby pressure in mobile applications the pilot circuit of proportional valves must be designed to operate with a minimum pressure differential between the pilot circuit's supply and drain. The supply pressure for the pilot circuit is commonly kept at a constant level relative to the drain side pressure. As described in section 3.6.3 a damping orifice is often placed in the drain line of the pilot circuit to damp pressure peaks. In the following the effect of a drain pressure disturbance on the required control bandwidth of the position controller is analysed. It is assumed that a damping orifice is not present in the drain port of the pilot circuit, i.e. worst case is considered.

A measurement of an extreme drain pressure disturbance is shown in figure 4.35. The measurement has been made on a system with a constant displacement pump and a 7 [m] long hose connected to the drain port of a state of the art proportional valve group. The pressure pulse develops as the hydraulic cylinder being moved encounters its end stop. Additional pump flow is then being dumped to the drain port of the valve group. This creates the plotted pressure disturbance on the drain port of the valve group. Obviously the pressure disturbance is not a problem for the valve section associated with the cylinder encountering the end stop. The pilot circuits of other valve sections in the group sharing the drain line will, however, be disturbed by the pressure pulse.

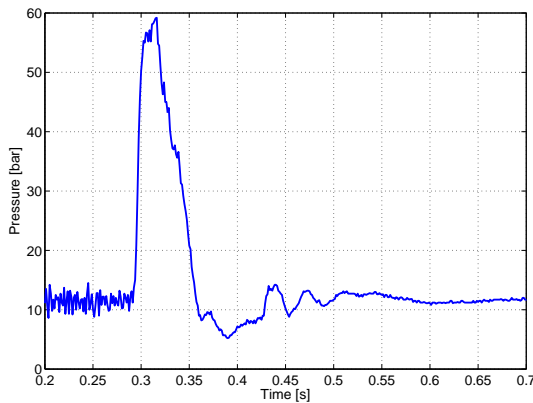


Figure 4.35: Measured drain pressure disturbance.

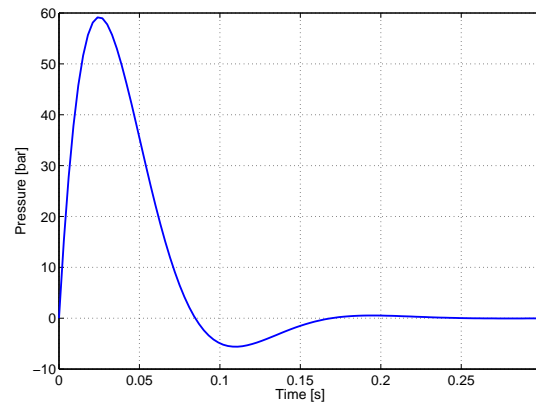


Figure 4.36: Simulated drain pressure disturbance.

The shown disturbance resembles the unit impulse response of a second order system. Thus a weight modelling the disturbance may be chosen as

$$W_{pt} = \frac{\omega_{pt}^2 K_{pt}}{s^2 + 2\zeta_{pt}\omega_{pt}s + \omega_{pt}^2} \quad (4.49)$$

where

$$\omega_{pt} = \frac{\tan^{-1} \left( \frac{\sqrt{1-\zeta_{pt}^2}}{\zeta_{pt}} \right)}{t_p \sqrt{1-\zeta_{pt}^2}} \quad (4.50)$$

$$K_{pt} = \frac{p_{t_{max}}}{\omega_{pt} \exp \left\{ -\frac{\zeta_{pt}}{\sqrt{1-\zeta_{pt}^2}} \tan^{-1} \left( \frac{\sqrt{1-\zeta_{pt}^2}}{\zeta_{pt}} \right) \right\}} \quad (4.51)$$

From the response in figure 4.35 the parameters describing the disturbance may be chosen as  $p_{t_{max}} = 60$  [bar],  $\zeta_{pt} = 0.6$  and  $t_p = 0.025$  [s] where the latter is the peak time. This gives the unit impulse response in figure 4.36.

Combined with the transfer functions derived in section 3.6 the model of the drain pressure disturbance is given by

$$G_{d_{pt}}(s) = D_e^{-1} \frac{(G_3(s) + G_4(s))G_5(s)}{1 - sG_5(s)G_6(s)} W_{pt}(s) \quad (4.52)$$

The frequency responses of the disturbance model are plotted in figure 4.37. However, as the dead-zone is always present in the pilot valve, the dead-zone disturbance should thus always be decoupled. A more realistic frequency response of the drain pressure disturbance is therefore obtained by superimposing the frequency response of the dead-zone disturbance onto the frequency response of the drain pressure disturbance. The result is shown in figure 4.38 whereby it may be seen that for best case a control bandwidth  $> 1$  [Hz] is required, whereas for worst case we at least require the control bandwidth to be  $> 34$  [Hz] to decouple the disturbance. Naturally the same comments regarding fundamental plant limitation as already given in the previous subsection apply here. It should be noted that the dynamics of a given pilot pressure controller have been omitted in the analysis.

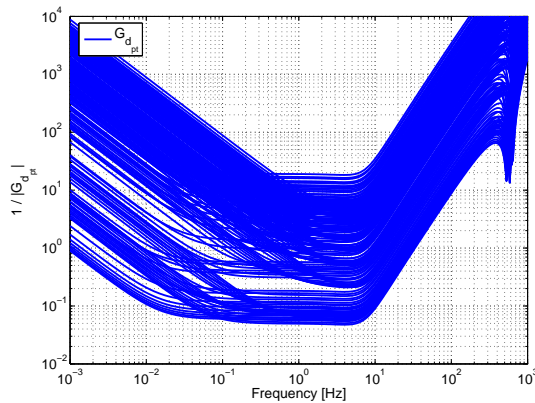


Figure 4.37: Frequency response of drain pressure disturbance.

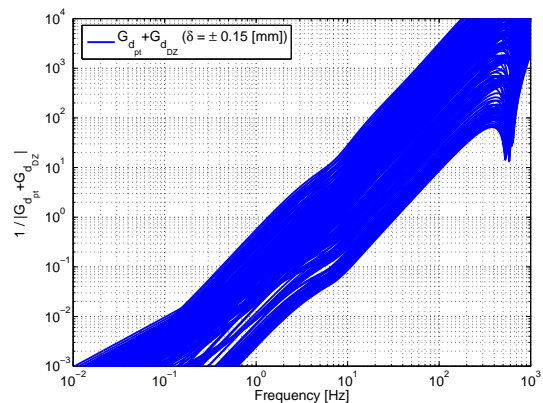


Figure 4.38: Frequency response of drain pressure + dead-zone disturbance.

### 4.6.3 Bandwidth requirements for negative damping of main spool

The chosen separate meter-in separate meter-out spool valve concept uses two identical spool valves. Because one of the spools is connected to the pump line and the other is connected to the drain line the, flow directions through the two valves are opposite to each other. Therefore the transient flow forces will apply as negative damping on one of the spools and as positive damping on the other. The associated dynamical system of the negatively damped spool may therefore have poles in the right complex half plane.

In the case where the transient flow forces on the main spool gives negative damping, the bound given by (4.46) may be used to compute an approximate bandwidth requirement for T that is necessary to stabilise the valve. By computing the pole locations associated with the open loop dynamics when transient flow forces are negative, it is found that there are right half plane pole locations around  $(288 \pm 7744i)$ . If a resonant peak size of  $M_T = 1.5$  is allowed for the closed loop frequency response, then by the computed pole location the control bandwidth must be larger 1700 [Hz] according to the bound in (4.46). Obviously this is impossible by the selected valve design. Therefore either one must rely on transient flow forces being negligible, or one must rely on Coulomb friction forces to damp the valve.

### 4.6.4 Summary of performance demands

It was found during the above analysis that the controller requirements in terms of control bandwidth to compensating for the dead-zone in the pilot valve, and to decoupling a pressure disturbance in the drain of the pilot circuit are highly dependent on the considered operating point. An approximate control bandwidth  $> 34$  [Hz] was computed for worst case.

Performance limitations of the prototype valve design was identified by the required control bandwidth to decouple the considered disturbances. For worst case this bandwidth is more than twice the roll off frequency of the pilot valve. It was argued that for a flow direction through the spool valve which gives negative transient flow forces, stabilisation relies on these transient flow forces being negligible, or the Coulomb friction acting on the main spool being sufficiently large to make the net damping of the spool positive.

## 4.7 Improved robust controller designs

In this section robust controllers are developed for the valve with flow control pilot. All simulation results presented in the remaining part of this chapter have been obtained with discrete implementations of the controllers to be developed. The interrupt/sample frequency which has been used in the simulations is 1 [kHz]. A bilinear approximation of the z-transform has been used to obtain discrete version of the used filters. Addi-



tionally, all controllers presented below expect the R2H controller uses a feedforward force contribution to compensate for the pilot valve dead-zone. In the controllers the feedforward is filtered by a 20 [Hz] first order low pass filter, to avoid overshoot of the main valve position. Finally, it is assumed that the underlap of the pilot spool, when it is in its null position, is known. The remaining overlap parameters are unmeasurable.

#### 4.7.1 State of the art and choice of controller types

The dynamical system describing the valve with flow control pilot resembles that of a 4-way servo valve controlling a hydraulic actuator with an external disturbance force. The external disturbance force being the flow and spring forces on the main spool in the present case. Much research has been made on control of this type of system. Edge gives a good overview of some of the research contributions in the review papers [32] and [33]. Other authors have given performance comparisons of specific implementations of different controller types [8, 21].

A controller design which is in its nature robust to uncertainties is preferable, for a system such as the considered valve, with an unknown sandwiched dead-zone and varying parameters due to the varying operating conditions. In the linear, non-linear and adaptive paradigms for controller design, the candidates  $\mathcal{H}_\infty$ ,  $\mu$ -iteration, sliding mode, and MRAC controller design methods are in their nature robust. Therefore this state of the art section is focused on these types of controllers. Specifically these controller types have their strengths with regard to the following types of uncertainties

- $\mathcal{H}_\infty$ : Unmodelled dynamics (unstructured uncertainty).
- $\mu$ -iteration: Unmodelled dynamics and parametric uncertainty (unstructured and structured uncertainty).
- Sliding mode: Fastly varying parametric uncertainty.
- MRAC: Constant unknown or slowly varying parametric uncertainty.

A structured approach to MRAC adaptive controller design of linear systems with an input or output dead-zone was given in [99]. Latter the work has been extended to linear systems with sandwiched dead-zones [100, 101]. To the authors knowledge no experimental implementations using the considered type of adaptive controllers have been made in hydraulic systems.

$\mathcal{H}_\infty$  control in hydraulic position servo systems was considered by Piché with co-workers in [80]. In another paper by the same authors a 2 d.o.f. controller was developed for the same system by using the  $\mu$ -iteration technique [81]. In [53] a 5th order discrete  $\mathcal{H}_\infty$  controller for a hydraulic position servo system was developed using a mixed sensitivity control formulation. The previous work on  $\mathcal{H}_\infty$  control for hydraulic position servo systems seems rather limited. Gain scheduling  $\mathcal{H}_\infty$  controllers have been applied to hydraulic force and velocity servo systems in [93, 94]. The non-linearities such as valve

overlap and varying operating conditions addressed in these references are similar to the ones encountered in the work of this dissertation.

Chern and Wu considered sliding mode with variable boundary layer control for a hydraulic position servo system in [28]. Their simulation results showed that the use of integral action in the switching surface gave superior tracking performance for varying parameters compared to a conventional selection of the sliding surface. Modification of the boundary layer control to avoid chattering of hydraulic position servos were considered by Chen et. al. in [26] and earlier by Hwang in [48]. Sliding mode control in connection to hydraulic position servo systems on manipulators was considered by Bonchis et. al. in [22] and Liu and Handroos for flexible load structures in [65, 66]. Other references on sliding model controllers for electrohydraulic position servos include [27, 40, 43]. Specifically with concern to fluid power valves Gamble successfully applied sliding mode control with a non-linear switching surface for a direct actuated solenoid valve in [41].

Of the above references only those concerned with adaptive control of systems with dead-zones have addressed dead-zone problems directly in the controller design. For the pilot operated valve considered in this work the size of the overlap of the pilot spool is constant but unknown, why, with regard to the controller types considered above, an MRAC controller for a sandwiched dead-zone system could be interesting. However, due to the slopes of the dead-zone function, or more specifically the gain of the pilot valve, being dependent on the operating conditions, which are not necessarily slowly varying, the stability proof of the parameter update law for the MRAC controller cannot be carried through.

Regarding the other robust controller design methods the following comments apply. When more real valued (parametric) uncertainties are lumped together the unstructured uncertainty representation assumed by the  $\mathcal{H}_\infty$  controller design method is likely to become less conservative. Due to the increased complexity of a controller design with  $\mu$ -iteration,  $\mu$ -iteration should usually not be the first choice, although tools are becoming increasingly more user friendly [17]. Parasitic actuator or sensor dynamics (unstructured uncertainty) may result in chattering of sliding model controllers [113]. However, by using fixed or varying boundary layers this problem may be circumvented, as have been addressed by several of the references listed above.

In this work focus is first directed towards gain-scheduling linear control, as one is obliged to try linear controllers first due to their simplicity. Secondly, controllers based on  $\mathcal{H}_\infty$  control and sliding mode control are designed.

#### 4.7.2 Gain scheduling Proportional-Integral-Lead-Feedforward (G-PILF) controller

The variation of the open loop dynamics of the considered valve is partly due to variation of the pressure drop across the valve. As the pressure drop across the main spool is measured, an obvious choice is to apply gain scheduling to the PLF controller in

section 4.4. Additionally, in linear control the way of cancelling steady state error for a constant reference is to include integral action in the controller. Thus augmenting the PLF controller with gain scheduling and integral action is considered in this subsection. The suggested controller is

$$f_a = \left[ K_p(\Delta p) \frac{\tau_d s + 1}{\tau_f s + 1} + \frac{1}{T_i s} \right] e_m + \frac{1}{\tau_{ff} s + 1} f(x_{mr}) \tag{4.53}$$

where

$$f(x_{mr}) = \text{(4.26)}$$

$$k_p(\Delta p) = \begin{cases} k_{p_{min}} & |\Delta p| < \Delta p_{min} \\ k_{p_{min}} + \delta k_p |\Delta p| & \Delta p_{min} \leq |\Delta p| \leq \Delta p_{max} \\ k_{p_{max}} & \Delta p_{max} < |\Delta p| \end{cases}$$

$$\delta k_p = \frac{k_{p_{max}} - k_{p_{min}}}{\Delta p_{max} - \Delta p_{min}}$$

The controller may be represented by the block digram in figure 4.39 where antiwindup has been included.

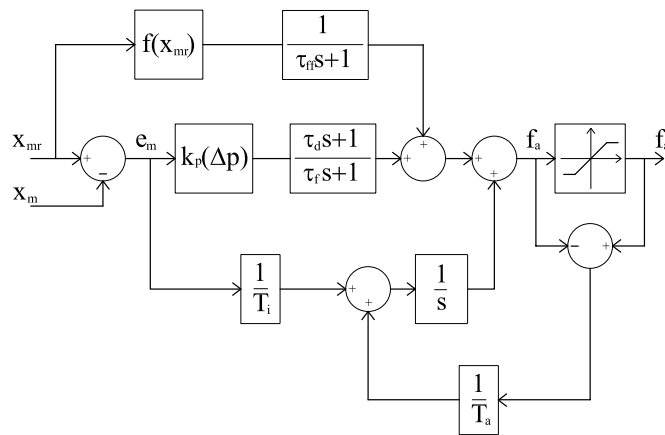


Figure 4.39: G-PILF controller.

The frequency responses of the sensitivity function and the complementary sensitivity function, which are obtained by implementing the G-PILF controller on the discrete model set  $G_{\Pi}$ , are plotted in figure 4.40. Recall that to decouple the dead-zone the requirement on  $S$  is  $|S| < |1/G_{d_{DZ}}|$ . Then from figures 4.33 and 4.34 it appears that the dead-zone cannot be decoupled for all operating points. This also holds for the dead-zone + drain pressure disturbance.

Simulated flow tracking using the G-PILF controller is shown in figure 4.41. Perfect inversion of the main spool flow gain has been used in the simulation. Therefore, flow tracking error is due to main spool position tracking error only. A positive flow corresponds to flow metered out of the A-port of the main spool and a negative flow corresponds to flow metered out of the B-port of the main spool.

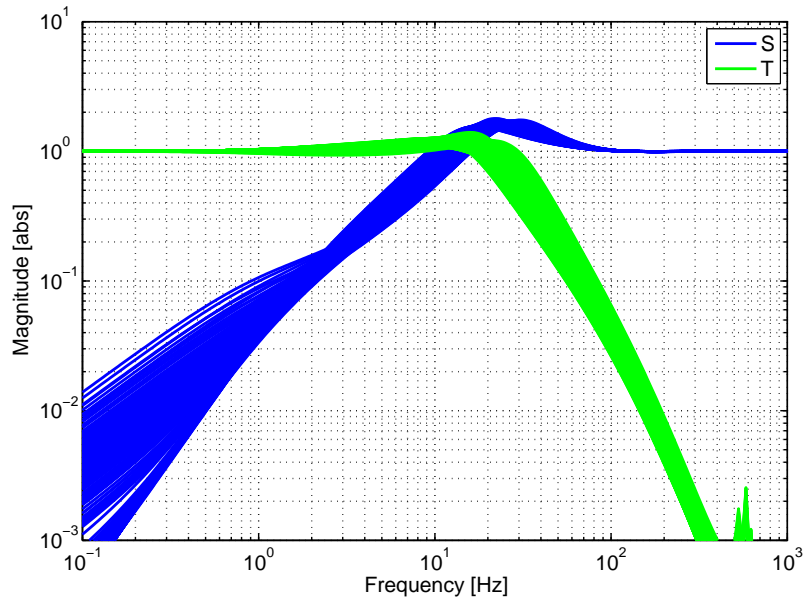


Figure 4.40: Frequency response of S and T with G-PILF controller

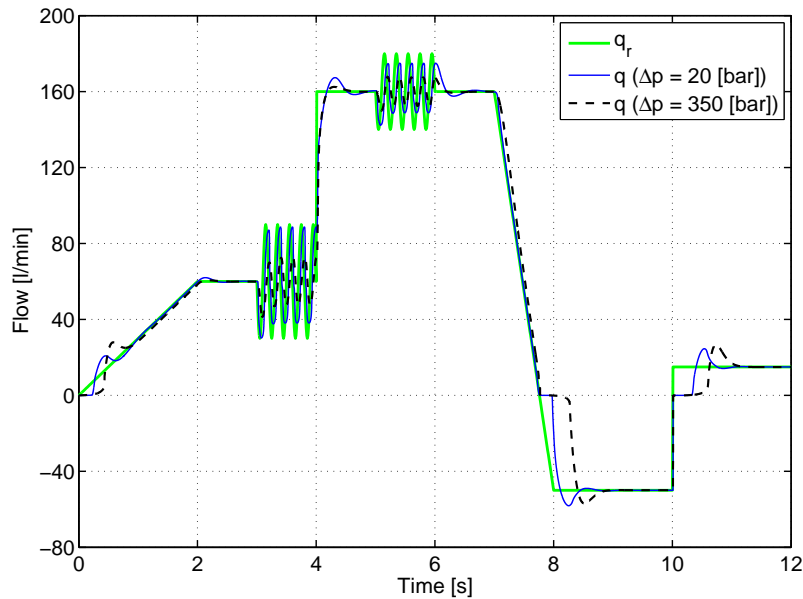


Figure 4.41: Simulated flow tracking using G-PILF controller.

The sinusoidal tracking is not as good as could be expected from frequency responses of the linear systems in figure 4.40. This is due to the dead-zone deteriorating the response. It is also seen that when the main spool shall cross the null position, i.e. when the flow reference changes sign, there is a delay in the flow response. This is due to that both the pilot spool and the main spool must cross their null positions, thus jump across their respective overlaps. The performance of the controller is summarised in table 4.6.

Performance criterion	Value	Unit
Steady state flow error, $\Delta p = 20$ [bar], $q_r = 160$ [l/min]	0	[%]
Steady state flow error, $\Delta p = 350$ [bar], $q_r = 160$ [l/min]	0	[%]
Control bandwidth for small signals $ S(j\omega)  \leq \frac{\sqrt{2}}{2}$	7.5 – 13.5	[Hz]
Maximum actuator force	7	[N]

Table 4.6: Performance of G-PILF controller.

### 4.7.3 Robust 2 d.o.f. $\mathcal{H}_\infty$ (R2H) controller

In this subsection we pursue the idea of using a 2 d.o.f. fixed controller where an inner proportional-lead control loop is first applied to linearise the varying dynamics of the plant. Secondly, an auxiliary controller is designed by formulating the design problem as a mixed sensitivity  $\mathcal{H}_\infty$  control problem. The considered controller structure is shown in figure 4.42.

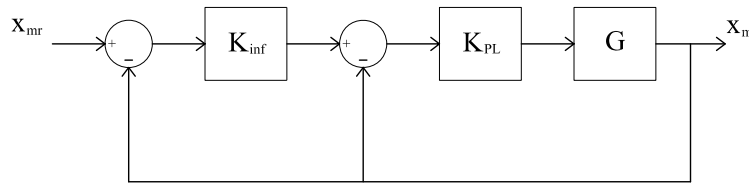


Figure 4.42: R2H controller structure.

It may be argued that the problem should be considered directly as an  $\mathcal{H}_\infty$  control problem. However, due to the variation between the frequency responses of the plants in  $G_\Pi$ , see figure 4.25, an uncertainty formulation for a single nominal plant may easily become conservative. For example, low frequency unstructured uncertainty is commonly modelled by an inverse multiplicative uncertainty, and high frequency unstructured uncertainty is commonly modelled by a multiplicative uncertainty. It is known that for a combined multiplicative and inverse multiplicative uncertainty description, which is a candidate for describing the uncertainty at both low and high frequency, the nominal performance condition is the same as the robust performance condition for a single multiplicative uncertainty [30].

The varying low frequency dynamics of the open loop plants in  $G_\Pi$  is reduced by implementing a proportional-lead controller as

$$K_{PL} = \frac{\tau_d s + 1}{\tau_f s + 1} e_m \quad (4.54)$$

By closing the loop we obtain a new plant set as

$$G_{\Pi_c} = \frac{G_\Pi K_{PL}}{1 + G_\Pi K_{PL}} \quad (4.55)$$

The frequency responses of the plants in  $G_{\Pi_c}$  are plotted in figure 4.43. Compared to

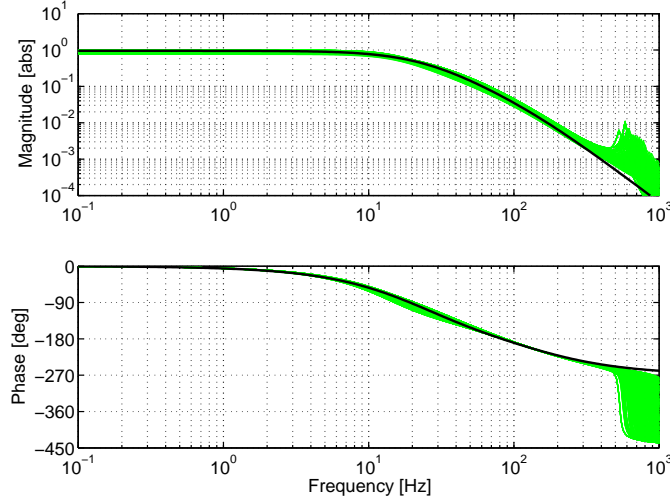


Figure 4.43: Frequency responses of  $G_{\Pi_c}$  and  $G_0$ .

the frequency responses in figure 4.25, it may be seen that the plants in  $G_{\Pi_c}$  have less low frequency variation. Therefore  $G_{\Pi_c}$  may be modelled by a fixed nominal plant and a single perturbation bounding the unmodelled dynamics. A fourth order nominal model is selected as

$$G_0 = \frac{K_0(s + b_1)}{(s + a_1)(s + a_2)(s^2 + a_3s + a_4)} \quad (4.56)$$

where  $K_0 = \frac{a_1 a_2 a_3 a_4}{b_1}$ . The parameters for the nominal model is chosen by inspection such that  $G_0$  and the plants in  $G_{\pi_c}$  "approximately" have common pole locations. The frequency response of the nominal model is also shown in figure 4.43.

Due to the unmodelled high frequency dynamics a multiplicative perturbation is suitable to represent the uncertainty. The perturbed plants are given in terms of the nominal plant as

$$G_{\Delta} = G_0(1 + \Delta W_m), \quad |\Delta(j\omega)| \leq 1, \quad \left| \frac{G_{\Delta}(j\omega)}{G_0(j\omega)} - 1 \right| \leq |W_m(j\omega)|, \quad \forall \omega \quad (4.57)$$

where  $G_{\Pi_c} \subseteq G_{\Delta}$ . An uncertainty bound is selected as

$$W_m = \frac{(s + \omega_{\Delta}^* A^{\frac{1}{n}})^n}{(s/M^{\frac{1}{n}} + \omega_{\Delta}^*)^n} \quad (4.58)$$

The magnitude of the weight is plotted in figure 4.44 along with  $\left| \frac{G_{\Pi_c}(j\omega)}{G_0(j\omega)} - 1 \right|$ .

Having found an appropriate uncertainty model the auxiliary controller may be designed considering the control configuration in figure 4.45. In the figure  $G_0$  is the nominal plant,  $K_{inf}$  is the auxiliary controller to be designed.  $W_m$  together with  $\|\Delta\|_{\infty} < 1$  bounds the unmodelled dynamics as shown in figure 4.44.  $W_p$  is a performance weight by which bandwidth requirements may be specified.  $W_u$  bounds the magnitude of the control

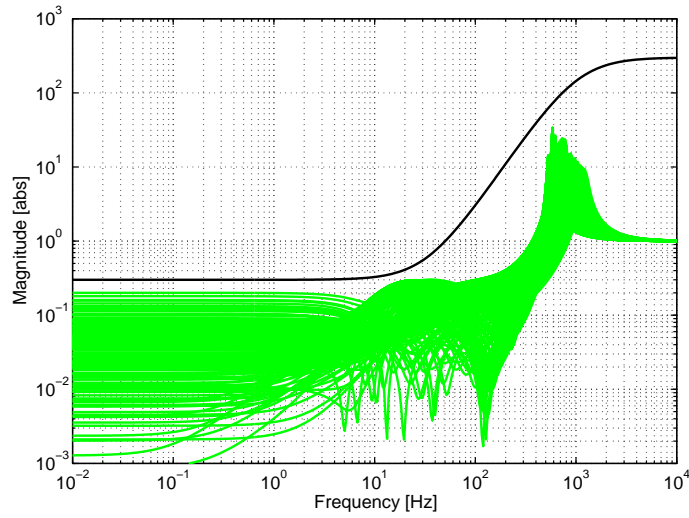


Figure 4.44: Frequency responses of  $W_m$  and  $\left| \frac{G_{\Pi c}(j\omega)}{G_0(j\omega)} - 1 \right|$ .

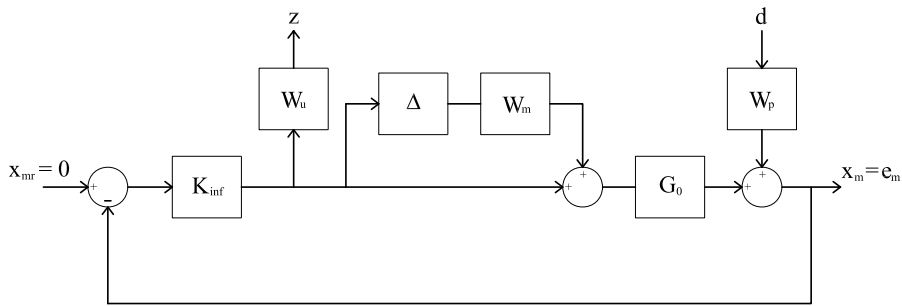


Figure 4.45: Considered control structure.

signals. In terms of these weights and the sensitivity and complementary sensitivity functions, the auxiliary controller is selected by solving the mixed sensitivity control problem

$$K_{inf} = \arg \min_{K \in \mathcal{K}} \|N(K)\|_{\infty}, \quad N = \begin{bmatrix} W_u K S \\ W_m T \\ W_p S \end{bmatrix} \quad (4.59)$$

where  $\mathcal{K}$  is the set of all stabilising controllers for  $G_{\Delta}$ .

The performance bound on  $S$  is selected as

$$W_p = \frac{(s/M^{\frac{1}{n}} + \omega_{\Delta}^*)^n}{(s + \omega_{\Delta}^* A^{\frac{1}{n}})^n} \quad (4.60)$$

The parameters of the weight may be given the following interpretation. A decrease of  $A$  gives a decrease of the steady state control error. The parameter  $A$  may therefore be chosen iteratively by trial and error to fulfil steady state position error requirements.  $n$  controls the slope of the roll-off of  $1/W_p$ , and  $\omega_{\Delta}^*$  specifies the control bandwidth where

$S$  crosses 1 from below. Hence  $n$  and  $\omega_\Delta^*$  may be selected as a compromise between high control bandwidth, and the fact that a reasonable frequency range between the cross over frequencies of  $W_m$  and  $W_p$  is necessary to fulfil the robust performance condition, see also [83]. Finally,  $M$  may be selected to secure a proper phase margin of  $G_0K_{inf}$ . The following connection between the phase margin, PM, and the sensitivity function  $\|S\|_\infty$  may be used to evaluate the relative stability of a specific plant controller combination, e.g. see [89]

$$\text{PM} \geq 2 \arcsin \left( \frac{1}{2\|S\|_\infty} \right) \geq \frac{1}{\|S\|_\infty} \quad (4.61)$$

$W_u$  is only included in the mixed sensitivity problem above to make the controller gains roll off outside the desired bandwidth<sup>4</sup>. Hence,  $W_u$  is selected as

$$W_u = \frac{(s + \omega_\Delta^* A^{\frac{1}{n}})^n}{(s/M^{\frac{1}{n}} + \omega_\Delta^*)^n} \quad (4.62)$$

It should be noted that the roll-off of  $W_u$  must be chosen considering both actuator bandwidth of the plant, and sample frequency of the control system.

Robust performance is analysed by connecting  $e_m$  and  $d$  in figure 4.45 through a performance perturbation block,  $\Delta_p$ . Omitting  $W_u$ , as it is not a part of the feedback loop, the block diagram in figure 4.45 may be redrawn in the general control configuration in figure 4.46.

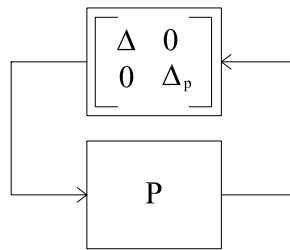


Figure 4.46: General control structure for analysis of robust performance.

The interconnection matrix is given by

$$P = \begin{bmatrix} -W_m T & -W_m K S W_p \\ G_0 S & W_p S \end{bmatrix} \quad (4.63)$$

Suppose the four transfer functions of  $P$  are all internally stable, then robust performance for all possible plants in  $G_\Delta$  is satisfied if and only if (a proof is found in [89])

$$\mu_{\tilde{\Delta}} = |W_m T| + |W_p S| < 1, \quad \forall \omega \quad (4.64)$$

<sup>4</sup>For minimum phase systems as the one considered the  $\mathcal{H}_\infty$  optimisation algorithm returns a controller with infinite gains unless they are penalised.



where  $\mu_{\tilde{\Delta}}$  is the structured singular value computed with respect to the diagonal perturbation block  $\tilde{\Delta} = \text{diag}[\Delta, \Delta_p]$ . For  $W_u = 0$ , in the mixed sensitivity problem, the minimised cost function is  $J = \sqrt{(W_m T)^2 + (W_p S)^2}$ . However, it may be shown that for this case  $J \leq \mu_{\Delta}(P) \leq \sqrt{2}J, \forall \omega$ .

An eight order controller has been derived numerically, using the solution to the standard  $\mathcal{H}_{\infty}$  control problem obtained by solving 2 Riccati equations as described in [31]. The controller order adheres from the four states of the nominal plant and four states of the performance weights. Controllers of high order are usually not desirable, therefore two reduced order controllers of respectively third and fourth order have been computed using balanced model reduction. All three controllers fulfil the robustness stability and robust performance criteria equally well. The obtained results are listed in table 4.7.

Criterion		3rd, 4th and 8th order $K_{inf}$
Nominal performance:	$\ W_p S\ _{\infty}$	0.94
Robust stability:	$\ W_m T\ _{\infty}$	0.30
Robust performance:	$\mu_{\tilde{\Delta}}(P)$	1.21
Mixed performance:	$\ N(K_{inf})\ _{\infty}$	0.96

Table 4.7: Summarised performance of controllers.

It is seen that robust performance is not obtained with any of the controllers. This is due to input constraints as the robust stability requirement is more than fulfilled, i.e. there is room for increased loop gain if allowed by the controller gain constraint. As a consequence of bode's sensitivity integral a larger control bandwidth may be obtained by relaxing the constraint on  $S$  by increasing  $M$  in (4.60), but this will jeopardize the relative stability. An alternative is to increase the frequency where the controller gains roll off if allowed by the actuator and the chosen sample frequency.

The frequency response of  $S$  and  $T$  which is obtained by closing the loop around the plants in the model set  $G_{\Pi_c}$  are plotted in figure 4.47. From the plots it is seen that the variations of  $S$  and  $T$  at low frequency are smaller with the R2H controller than with the G-PILF controller, see figure 4.41.

To facilitate implementation in a sampled control system, a discretisation by a bilinear approximation of the z-transform has been made for the two reduced order controllers. The bilinear approximation of the z-transform has been used as this gave the best match of the frequency response compared to other discretisation methods. The frequency responses of the eight order continuous controller and the 3rd order discrete one are shown in figure 4.48.

Implementations in the non-linear simulation model have shown equally good performance of the continuous controller and the reduced order discrete controller. Simulation results obtained using the 3rd order discrete controller are plotted in figure 4.49. Comparing with figure 4.41, it may be seen that the controller gives a poorer sinusoidal tracking than the G-PILF controller. The overlap is crossed faster than with the G-PILF controller, however, at the cost of a larger overshoot.

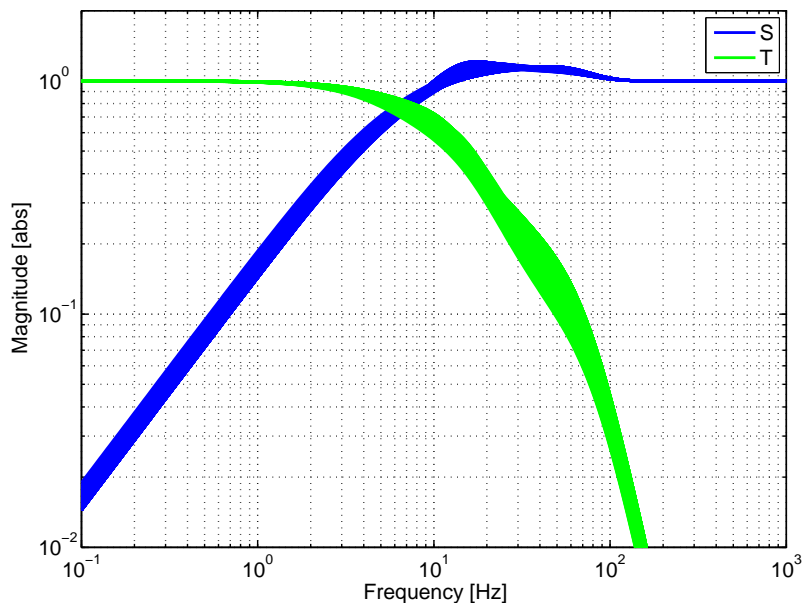


Figure 4.47: Frequency response of S and T with R2H controller

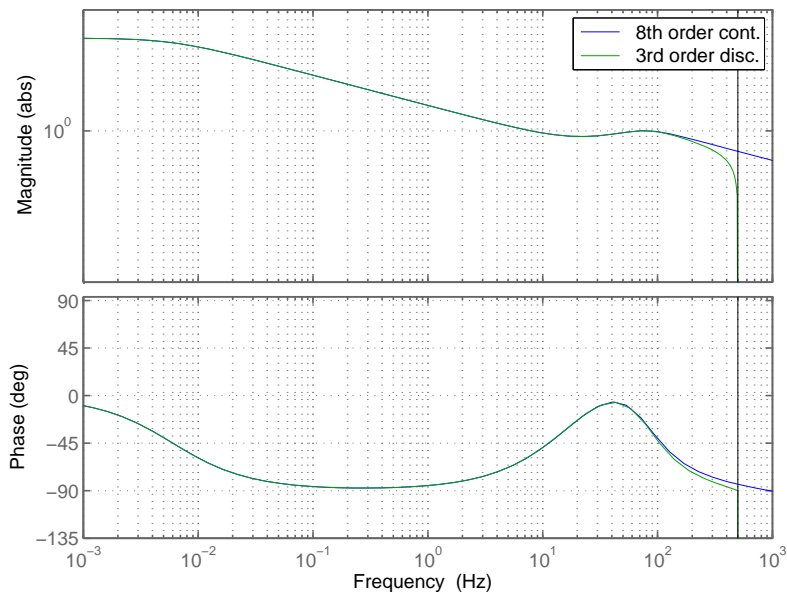


Figure 4.48: Frequency response of controllers.

It should be noted that the R2H controller uses no feedforward to compensate for the overlap of the pilot spool. Using feedforward has shown to improve the response at low pressure drops but it deteriorates the response at high pressure drops. Therefore feedforward has not been implemented. The performance of the R2H controller is summarised in table 4.8. The force has been limited to 8 [N] in the simulation to give a realistic level of maximum force input. This did not deteriorate the response.

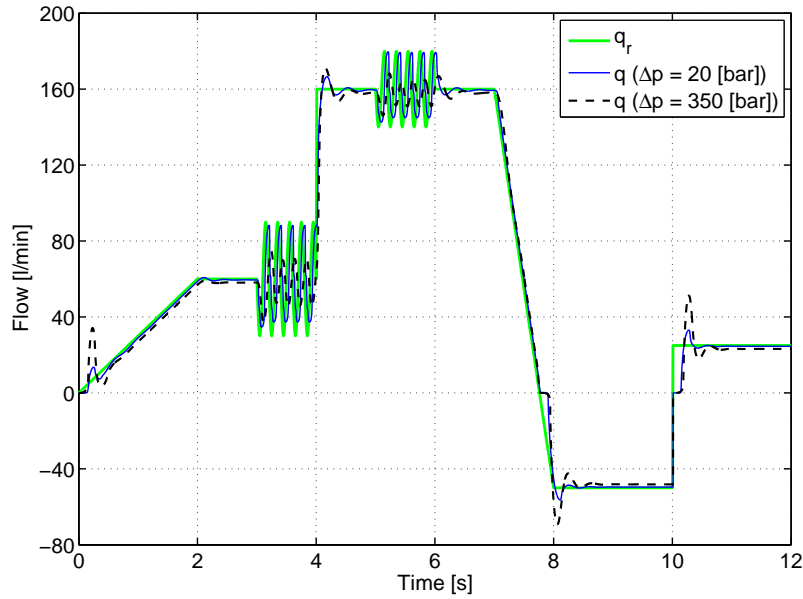


Figure 4.49: Simulated flow tracking using R2H controller.

Performance criterion	Value	Unit
Steady state flow error, $\Delta p = 20$ [bar], $q_r = 160$ [l/min]	0.94	[%]
Steady state flow error, $\Delta p = 350$ [bar], $q_r = 160$ [l/min]	1.25	[%]
Control bandwidth for small signals $ S(j\omega)  \leq \frac{\sqrt{2}}{2}$	5 – 6	[Hz]
Maximum actuator force	8	[N]

Table 4.8: Performance of R2H controller.

It should be noted that different parameters for the performance weights in (4.58) and (4.62), see tables A.15 and A.16, may be selected which give better simulation results. However, these parameters did not give a satisfactory performance when tested on the real system.

#### 4.7.4 Frequency shaping Sliding Mode (F-SM) controller

In this section the idea is pursued that the proportional lead controller may be extended with a non-linear feedback to make the controller robust to uncertainty. The idea is to augment a frequency shaping post filter to the output of the plant and choose a feedback control stabilising the nominal plant. Hereafter a sliding mode controller is designed by using the post filter as a switching operator. The approach is introduced in [112].

It should be noted that a frequency shaping sliding model controller can be obtained without first designing a feedback stabilising the nominal plant. In fact the equivalent control which is to be derived will counteract the stabilising feedback for the nominal plant. However, as will be shown in subsection 4.7.5, an intuitive and simple modification to the controller can be made when the nominal feedback is included.

A simpler plant model than those considered so far is needed to carry the approach through. Such a plant model is presented in the following.

#### 4.7.4.1 First order plant model

The main spool position is the integral of the flow from the pilot valve. Therefore, the pilot operated main spool may be modelled as an integrating plant governed by the equations

$$\dot{x}_m = \frac{q_p}{A_m} \quad (4.65)$$

$$q_p = k_v(t)[x_p - x_{p0}\text{sign}(x_{mr}) - g(x_p - x_{p0}\text{sign}(x_{mr}))] \quad (4.66)$$

$$g(x) = \begin{cases} -\Delta_{(t_1,p_2)} & , & x < -\Delta_{(t_1,p_2)} \\ x & , & -\Delta_{(t_1,p_2)} \leq x \leq \Delta_{(p_1,t_2)} \\ \Delta_{(p_1,t_2)} & , & \Delta_{(p_1,t_2)} < x \end{cases} \quad (4.67)$$

where  $x_m$  is the output and  $x_p$  is the input. Note, the two local dead-zones of the pilot valve is modelled by the expression within the squared brackets of (4.66), because a unit gain minus a saturation function gives a dead-zone function, see also figure 4.32b. The saturation function  $g(x)$  models the four metering edges in the pilot valve relative to the hold positions  $\pm x_{p0}$ , which are unknown. Recall that the pilot spool is underlapped in the null position. Thus the pilot spool must be offset to  $+x_{p0}$  ( $-x_{p0}$ ), to hold the main spool at a positive (negative) position relative to the main spool null position. The expression within the squared brackets giving the two local dead-zones is illustrated graphically in figure 4.50

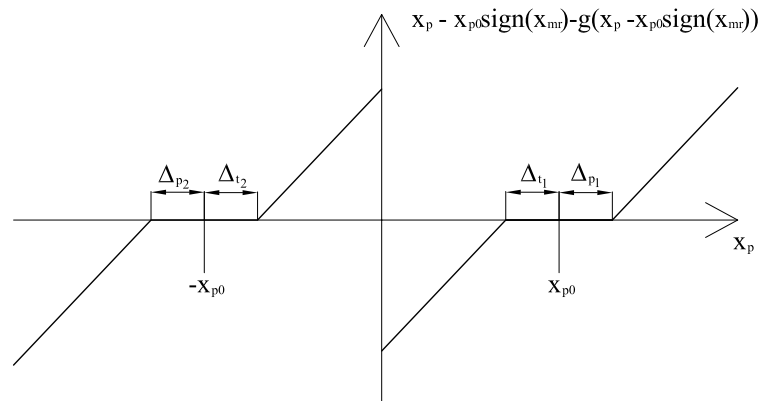


Figure 4.50: Illustration of local dead-zones.

The  $\Delta_{(\cdot,\cdot)}$ s in (4.67) are the local positions of the metering edges of the pilot spool relative to the hold positions  $\pm x_{p0}$ . The first subscript of  $\Delta_{(\cdot,\cdot)}$  refers to  $x_p > 0$  and the second subscript refers to  $x_p < 0$ . Thus,  $\Delta_{p_1}$  and  $\Delta_{t_1}$  are the limits of the dead-zone relative to  $x_p = x_{p0}$ , and  $\Delta_{p_2}$  and  $\Delta_{t_2}$  are the limits of the dead-zone relative to  $x_p = -x_{p0}$ . These

lengths relates to the absolute spool overlap/underlap lengths shown in figure 3.2 as

$$\begin{aligned}\Delta_{p1} &= \Delta_{pa} - x_{p0} \\ \Delta_{p2} &= \Delta_{pb} - x_{p0} \\ \Delta_{t1} &= x_{p0} - \Delta_{ta} \\ \Delta_{t2} &= x_{p0} - \Delta_{tb}\end{aligned}$$

The second order differential equation describing the pilot spool dynamics may be written as

$$x_p = \frac{f_a - f_{sp0}\text{sign}(x_{mr})}{k_{sp}} + d(t) \quad (4.68)$$

where  $f_{sp0}$  is the pilot spool spring pre-stress force and

$$d(t) = -\frac{m_p}{k_{sp}}\ddot{x}_p - \frac{c_p}{k_{sp}}\dot{x}_p$$

To compensate for the spring pre-stress force, which is known, and to make the pilot spool jump as close to the hold positions  $\pm x_{p0}$  as possible, a feedforward force input is chosen as

$$f_a = k_{sp}u + f_{sp0}\text{sign}(x_{mr}) + \Delta_0 k_{sp}\text{sign}(x_{mr}) \quad (4.69)$$

$\pm\Delta_0$  are the assume hold position taken as a position inside the dead-zone, which may be computed from manufacturing tolerances. Inserting this into (4.68) gives

$$x_p = u + \Delta_0\text{sign}(x_{mr}) + d(t) \quad (4.70)$$

By inserting (4.70) into (4.66), the model given by (4.65) to (4.66) may be written as

$$\dot{x}_m = \frac{k_v(t)}{A_m}u + \nu(t) \quad (4.71)$$

where

$$\nu(t) = \frac{k_v(t)}{A_m} [\alpha(t) - g(u - \alpha(t))] \quad (4.72)$$

$$\alpha(t) = (\Delta_0 - x_{p0})\text{sign}(x_{mr}) + d(t) \quad (4.73)$$

Due to the system being of first order,  $\nu(t)$  appears in the input channel and thus satisfies a matching condition.

#### 4.7.4.2 Nominal feedback

The following post filter, which gives a phase lead over a limited frequency range, is augmented to the output of plant in (4.71)

$$\dot{z} = -\frac{1}{\tau_f}z + x_m \quad (4.74)$$

$$y = \frac{1}{\tau_f} \left(1 - \frac{\tau_d}{\tau_f}\right) z + \frac{\tau_d}{\tau_f} x_m \quad (4.75)$$

The post filter corresponds to the lead filter used for the PLF controller in section 4.4. The plant with post filter is given by

$$\begin{aligned} \begin{bmatrix} \dot{z} \\ \dot{x}_m \end{bmatrix} &= \underbrace{\begin{bmatrix} -\frac{1}{\tau_f} & 1 \\ 0 & 0 \end{bmatrix} \begin{bmatrix} z \\ x_m \end{bmatrix}}_{\text{Nominal plant}} + \underbrace{\begin{bmatrix} 0 \\ \frac{k_v}{A_m} \end{bmatrix} u}_{\text{Matched uncertainty}} + \underbrace{\begin{bmatrix} 0 \\ \frac{k_v}{A_m} \end{bmatrix} \nu(t)}_{\text{Matched uncertainty}} \\ y &= \underbrace{\frac{1}{\tau_f} \left( 1 - \frac{\tau_d}{\tau_f} \right) z + \frac{\tau_d}{\tau_f} x_m}_{\text{Output equation}} \end{aligned} \quad (4.76)$$

We select the feedback control law  $u = \xi + v$  where  $\xi$  is a controller stabilising the nominal plant and  $v$  is a non-linear feedback making the system robust to uncertainties. Choosing  $\xi = -k_p y$  corresponds to the proportional lead feedforward controller suggested in section 4.4. Note, the feedforward is included by using (4.69). The following closed loop plant is obtained

$$\begin{bmatrix} \dot{z} \\ \dot{x}_m \end{bmatrix} = \begin{bmatrix} -\frac{1}{\tau_f} & 1 \\ -\frac{k_p k_v}{A_m} \frac{1}{\tau_f} \left( 1 - \frac{\tau_d}{\tau_f} \right) & -\frac{k_p k_v}{A_m} \frac{\tau_d}{\tau_f} \end{bmatrix} \begin{bmatrix} z \\ x_m \end{bmatrix} + \begin{bmatrix} 0 \\ \frac{k_v}{A_m} \end{bmatrix} (v + \nu(t)) \quad (4.77)$$

To simplify the writing in the following the above closed loop plant may be written as

$$\begin{bmatrix} \dot{z} \\ \dot{x}_m \end{bmatrix} = A \begin{bmatrix} z \\ x_m \end{bmatrix} + \begin{bmatrix} 0 \\ B \end{bmatrix} (v + \nu(t)) \quad (4.78)$$

#### 4.7.4.3 Equivalent control

A frequency shaping sliding mode control law is designed by choosing a time varying surface defined on the extended state space, including the state of the post filter introduced in (4.74) and (4.75) above. When the system is in sliding mode the dynamics is prescribed by selection of the post filter. The following switching operator is selected

$$\mathcal{S} = y - x_{mr} = Gx_m - x_{mr}, \quad G = \frac{\tau_d s + 1}{\tau_f s + 1} \quad (4.79)$$

where  $G$  is the transfer function associated with the lead filter in (4.74) and (4.75). When  $\mathcal{S} = 0$  the system is in sliding mode and the states are constrained to this operator. The closed loop dynamics is then given by

$$x_m = \frac{\tau_f s + 1}{\tau_d s + 1} x_{mr} \quad (4.80)$$

A frequency interpretation of the system dynamics when the system is in sliding mode is that the dynamic response rolls off at frequencies above  $\frac{1}{\tau_d}$ . The effect of the numerator

in (4.80) is negligible when  $\tau_f \ll \tau_d$ . However, an appropriate value of  $\tau_f < \tau_d$  makes the system less sensitive to sensor noise. Equation (4.79) may be written as

$$\mathcal{S} = [ H \quad L ] \begin{bmatrix} z \\ x_m \end{bmatrix} - x_{mr} \quad (4.81)$$

which is the output equation of the post filter subtracted the spool position reference  $x_{mr}$ .

To compute the equivalent control which makes  $\mathcal{S}$  an invariant set, whereby the sliding condition  $\dot{\mathcal{S}} = 0$  is satisfied, (4.81) is differentiated once where after the state derivatives given by (4.78) are substituted into the result. The equivalent control is the computed by setting  $v = v_{eq}$  and rearranging. The following expression is obtained for the equivalent control

$$v_{eq} = (LB)^{-1} \left( \dot{x}_{mr} - [ H \quad L ] A \begin{bmatrix} z \\ x_m \end{bmatrix} \right) - \nu(t) \quad (4.82)$$

The exact equivalent control may not be computed, however, as only estimates  $\hat{A}$  and  $\hat{B}$  for  $A$  and  $B$  are known, and additionally  $\nu(t)$  is unknown. The best guess for the equivalent control is then

$$v_{eq} = (L\hat{B})^{-1} \left( \dot{x}_{mr} - [ H \quad L ] \hat{A} \begin{bmatrix} z \\ x_m \end{bmatrix} \right) \quad (4.83)$$

To satisfy the reaching condition  $\mathcal{S}\dot{\mathcal{S}} < 0$  and point the state trajectories towards the sliding surface despite uncertainties and unmodelled dynamics a switching term is added to the equivalent control as

$$v = v_{eq} - k(t)\text{sign}(\mathcal{S}) \quad (4.84)$$

A lower bound for the function  $k(t)$  is derived in the following.

#### 4.7.4.4 Stability analysis

Consider the Lyapunov like function  $V(\mathcal{S}) = \frac{1}{2}\mathcal{S}^2$ . Then a sufficient condition to secure the stability of the control law (4.84) is

$$\frac{d}{dt}V(\mathcal{S}) = \mathcal{S}\dot{\mathcal{S}} \leq -\eta|\mathcal{S}| \quad (4.85)$$

where  $\eta$  is a strictly positive constant.

An expression for  $\dot{\mathcal{S}}$  is derived from (4.81) and (4.78). Doing this and inserting the result into (4.85) yields

$$\mathcal{S} \left\{ [ H \quad L ] \left( A \begin{bmatrix} z \\ x_m \end{bmatrix} + \begin{bmatrix} 0 \\ B \end{bmatrix} (v + \nu(t)) \right) - \dot{x}_{mr} \right\} \leq -\eta|\mathcal{S}| \quad (4.86)$$

Substituting (4.84) into (4.86) and using  $|\mathcal{S}| = \mathcal{S}\text{sign}(\mathcal{S})$  yields

$$\begin{bmatrix} H & L \end{bmatrix} \left( A \begin{bmatrix} z \\ x_m \end{bmatrix} + \begin{bmatrix} 0 \\ B \end{bmatrix} (v_{eq} - k(t)\text{sign}(\mathcal{S}) + \nu(t)) \right) - \dot{x}_{mr} \leq -\eta \text{sign}(\mathcal{S}) \quad (4.87)$$

Inserting (4.83) into (4.87), then after a little algebra the following is obtained

$$\begin{aligned} (LB)^{-1} \left( (B\hat{B}^{-1} - 1)\dot{x}_{mr} + \begin{bmatrix} H & L \end{bmatrix} \tilde{A} \begin{bmatrix} z \\ x_m \end{bmatrix} \right) + \nu(t) + (LB)^{-1}\eta \text{sign}(\mathcal{S}) \\ \leq k(t)\text{sign}(\mathcal{S}) \end{aligned} \quad (4.88)$$

where

$$\tilde{A} = A - B\hat{B}^{-1}\hat{A} \quad (4.89)$$

Since  $(LB)^{-1} > 0$  the sign functions may be removed by taking the absolute value as

$$\left| (LB)^{-1} \left\{ (B\hat{B}^{-1} - 1)\dot{x}_{mr} + \begin{bmatrix} H & L \end{bmatrix} \tilde{A} \begin{bmatrix} z \\ x_m \end{bmatrix} \right\} + \nu(t) \right| + (LB)^{-1}\eta \leq k(t) \quad (4.90)$$

Now rewrite  $\tilde{A}$  by using that

$$A = \begin{bmatrix} 1 & 0 \\ 0 & B \end{bmatrix} A' \quad \hat{A} = \begin{bmatrix} 1 & 0 \\ 0 & \hat{B} \end{bmatrix} A' \quad A' = \begin{bmatrix} -\frac{1}{\tau_f} & 1 \\ -\frac{k_p}{\tau_f} \left(1 - \frac{\tau_d}{\tau_f}\right) & -k_p \frac{\tau_d}{\tau_f} \end{bmatrix}$$

The following is obtained

$$\begin{aligned} \tilde{A} &= A - B\hat{B}^{-1}\hat{A} \\ &= \left( \begin{bmatrix} 1 & 0 \\ 0 & B \end{bmatrix} - B\hat{B}^{-1} \begin{bmatrix} 1 & 0 \\ 0 & \hat{B} \end{bmatrix} \right) A' \\ &= \left( \begin{bmatrix} 1 & 0 \\ 0 & B \end{bmatrix} - \begin{bmatrix} B\hat{B}^{-1} & 0 \\ 0 & B \end{bmatrix} \right) A' \\ &= \begin{bmatrix} 1 - B\hat{B}^{-1} & 0 \\ 0 & 0 \end{bmatrix} A' \\ &= \begin{bmatrix} -\frac{1}{\tau_f}(1 - B\hat{B}^{-1}) & 1 - B\hat{B}^{-1} \\ 0 & 0 \end{bmatrix} \end{aligned}$$

By using this result we get that

$$(LB)^{-1} \begin{bmatrix} H & L \end{bmatrix} \tilde{A} \begin{bmatrix} z \\ x_m \end{bmatrix} = (LB)^{-1} H (1 - B\hat{B}^{-1}) \begin{bmatrix} -\frac{1}{\tau_f} & 1 \end{bmatrix} \begin{bmatrix} z \\ x_m \end{bmatrix} \quad (4.91)$$

Inserting (4.91) into (4.90) yields

$$\left| (LB)^{-1} (B\hat{B}^{-1} - 1) \left( \dot{x}_{mr} + H \begin{bmatrix} \frac{1}{\tau_f} & -1 \end{bmatrix} \begin{bmatrix} z \\ x_m \end{bmatrix} \right) + \nu(t) \right| + (LB)^{-1}\eta \leq k(t) \quad (4.92)$$



Take  $\widehat{B}$  as the geometric mean  $\widehat{B} = \sqrt{B_{min}B_{max}}$ , where  $B_{min} \leq B \leq B_{max}$ . Then by choosing  $\beta = \sqrt{\frac{B_{max}}{B_{min}}}$  the following holds

$$\beta^{-1} \leq B\widehat{B}^{-1} \leq \beta \quad (4.93)$$

Hereby

$$(LB)^{-1}(B\widehat{B}^{-1} - 1) \leq \frac{\beta - 1}{LB_{min}} \quad (4.94)$$

Using this bound and  $(LB)^{-1} \leq (LB_{min})^{-1}$  in (4.92) yields

$$\frac{1}{LB_{min}} \left( (\beta - 1) \left| \dot{x}_{mr} + H \left[ \frac{1}{\tau_f} \quad -1 \right] \begin{bmatrix} z \\ x_m \end{bmatrix} + \nu(t) \right| + \eta \right) \leq k(t) \quad (4.95)$$

In the expression on the left hand side of this inequality  $z$ ,  $x_m$  and  $\dot{x}_{mr}$  are available for control. The remaining terms are constants except  $\nu(t)$ . An upper bound for  $\nu(t)$  is derived in the following.

First a bound for  $\alpha(t)$  in (4.73) is found. The positions  $\pm x_{p0}$  are inside the overlap of the pilot spool as shown in figure 4.50. Therefore an upper bound for  $|\Delta_0 - x_{p0}|$  is found from manufacturing tolerances as

$$|\Delta_0 - x_{p0}| \leq \max(|\Delta_0 - \Delta_{t_{min}}|, |\Delta_0 - \Delta_{p_{max}}|)$$

The additive perturbation  $d(t)$ , which is a part of  $\alpha(t)$ , describes the unmodelled pilot spool dynamics.  $d(t)$  is related to the acceleration and velocity of the pilot spool and is therefore dependent on the force applied onto the pilot spool. The following transfer function, written in terms of the Laplace operator  $s$ , describes the effect of  $f_a$  on  $d$

$$\begin{aligned} x_p(s) &= \frac{1}{k_{sp}} f_a(s) + d(s) = \frac{1}{m_p s^2 + c_p s + k_{sp}} f_a(s) \Rightarrow \\ d(s) &= \frac{x_p(s)}{f_a(s)} = -\frac{m_p s^2 + c_p s}{k_{sp}(m_p s^2 + c_p s + k_{sp})} \end{aligned} \quad (4.96)$$

This is a stable linear system which may be represented in state space form. For such a system it is possible to show BIBO stability (Bounded Input Bounded Output), as one can always find a Lyapunov function for a stable linear system in state space form<sup>5</sup>. Here it is assumed that  $|d(t)| \leq d_0$ ,  $d_0$  being a positive constant. The bound for  $\alpha(t)$  then becomes

$$\alpha(t) \leq \max(|\Delta_0 - \Delta_{t_{min}}|, |\Delta_0 - \Delta_{p_{max}}|) + d_0 = \alpha_0 \quad (4.97)$$

---

<sup>5</sup>Corollary 5.2 in [51] gives the result. However, this corollary gives a much too conservative result for the  $\mathcal{L}_\infty$  gain of the system in (4.96), in the sense that the lower bound for  $k(t)$  in (4.84), which also depends on the maximum force, becomes so large that the switching control action of (4.84) will destabilise the system.

It is easy to calculate a bound for  $g(x)$  as it is a saturation function. The maximum of the function is given relative to the two positions  $\pm x_{p0}$ . Again the two positions  $\pm x_{p0}$  are within the overlap of the spool, and a bound is computed from manufacturing tolerances as

$$g(x) \leq |\Delta_{p_{max}} - \Delta_{t_{min}}| = g_0 \quad (4.98)$$

By (4.97) and (4.98) an upper bound for  $\nu(t)$  is given by

$$\nu(t) \leq B_{max}(\alpha_0 + g_0) \quad (4.99)$$

Using this in (4.95) gives

$$\underbrace{\frac{\beta - 1}{LB_{min}} \left| \dot{x}_{mr} + H \begin{bmatrix} \frac{1}{\tau_f} & -1 \end{bmatrix} \begin{bmatrix} z \\ x_m \end{bmatrix} \right|}_{\text{State dependent}} + \underbrace{\frac{B_{max}(\alpha_0 + g_0) + \eta}{LB_{min}}}_{\text{Constant}} \leq k(t) \quad (4.100)$$

Using the left hand side of (4.100) in (4.84) stabilises the perturbed plant in (4.78), under the assumption that the unmodelled pilot spool dynamics,  $d(t)$ , in (4.68) is bounded by a constant.

Sliding mode control laws where the switching is done by a signum function often suffers from chattering, due to imperfect switching of the actuator. This has also shown to be the case for the control law in (4.84). It is therefore replaced by the following continuous boundary layer control

$$v = v_{eq} - k(t) \tanh(k_S \mathcal{S}) \quad (4.101)$$

where  $k_S$  is a strictly positive constant used for reducing chattering.  $k_S$  may be chosen freely, but if it is chosen too small the response may deteriorate. As  $k_S$  increases the boundary layer control approaches the discontinuous control in (4.84).

#### 4.7.4.5 Simulation results

The simulated flow tracking using the derived control law is plotted in figure 4.51. It may be seen by the response that the steady state load stiffness is reduced compared to that of the controllers presented previously. However, the controller fulfils requirements for maximum steady state flow control error. Dynamically the controller is robust to changing operating conditions as the sinusoidal tracking shows. The performance of the F-SM controller is summarised in table 4.9.

Performance criterion	Value	Unit
Steady state flow error, $\Delta p = 20$ [bar], $q_r = 160$ [l/min]	0.1	[%]
Steady state flow error, $\Delta p = 350$ [bar], $q_r = 160$ [l/min]	6.4	[%]
Maximum actuator force	5.7	[N]

Table 4.9: Performance of F-SM controller.

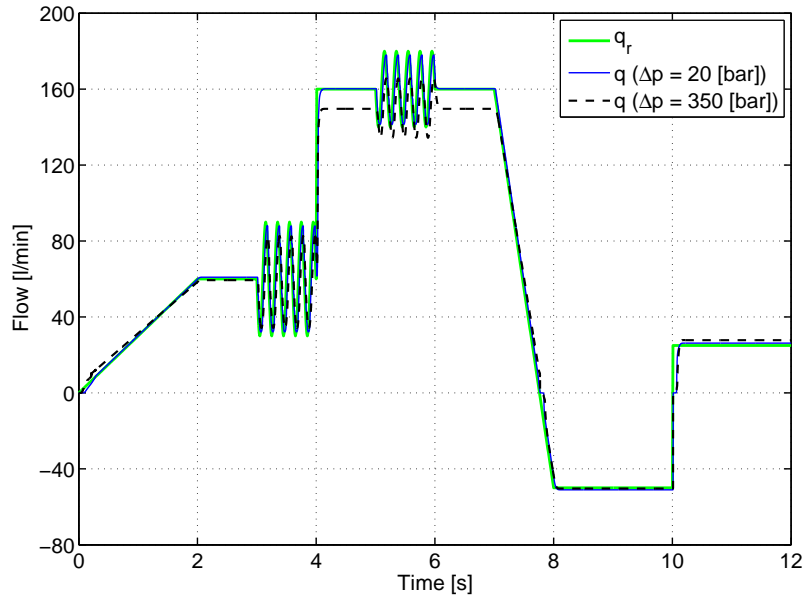


Figure 4.51: Simulated flow tracking using F-SM controller.

#### 4.7.5 Modified Frequency shaping Sliding Mode (MF-SM) controller

In this subsection an intuitive simplification is made to the F-SM controller derived above. The dynamic sliding surface in (4.79) is equal to the control error. As already explained the idea of the equivalent control is to keep  $\dot{\mathcal{S}} = 0$ . This is equivalent to keeping the gradient of the control error constant.

Above a feedback stabilising the nominal plant was introduced as  $\xi = -k_p y$ . If instead  $\xi = -k_p(y - x_{mr})$  is used, then one may expect that by this control  $y - x_{mr} \approx 0 \Rightarrow \mathcal{S} \approx 0 \Rightarrow \dot{\mathcal{S}} \approx 0$ . Hence intuitively  $v_{eq} = k_p x_{mr}$  may be used instead of (4.83). Additionally, simulations using the F-SM controller have shown that the state dependent part of (4.100) may be omitted without having significant effect on controller performance. Using these simplifications a much simpler controller implementation is obtained instead of (4.101), namely

$$v = k_p x_{mr} - k \tanh(k_S \mathcal{S}) \quad (4.102)$$

where  $k$  is a strictly positive constant.

The flow tracking response using this control law is plotted in figure 4.52. Compared to the F-SM controller the MF-SM controller gives noticeable poorer sinusoidal tracking at high pressure drops. Crossing of the main spool null position, where both the pilot spool and the main spool must jump across their dead-zones, is improved slightly. The steady state controller performance is within the required limits. The controller performance is listed in table 4.10. What is worth to notice is that the peak force is increased compared to the F-SM controller. In fact the force saturation of 8 [N] is reached.

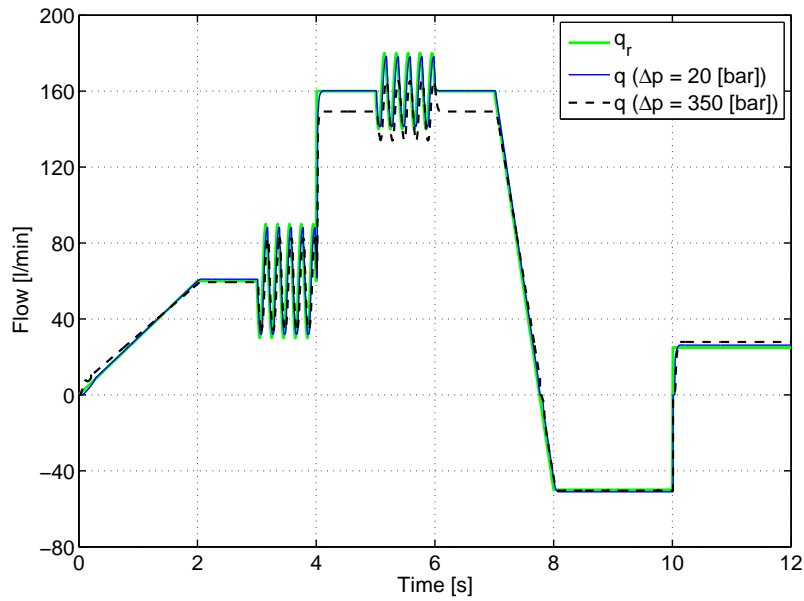


Figure 4.52: Simulated flow tracking using MF-SM controller.

Performance criterion	Value	Unit
Steady state flow error, $\Delta p = 20$ [bar], $q_r = 160$ [l/min]	0.1	[%]
Steady state flow error, $\Delta p = 350$ [bar], $q_r = 160$ [l/min]	6.8	[%]
Maximum actuator force	8	[N]

Table 4.10: Performance of MF-SM controller.

### 4.7.6 Sliding Mode controller with Prefilter (SM-P)

In the above the a dynamic sliding surface was chosen to avoid exiting unmodelled dynamics. In this subsection a sliding mode controller is developed where the pilot valve dynamics is considered directly in the design. The approach is motivated by work presented in [113], where sliding mode control of an integrating plant with parasitic second order actuator dynamics is considered.

#### 4.7.6.1 Plant model

The plant model given by (4.65) to (4.67) is augmented with the governing equation for the pilot valve dynamics. The result is

$$\dot{x}_m = \frac{k_v(t)}{A_m} [x_p - h(x_p, x_{mr})] \quad (4.103)$$

$$m_p \ddot{x}_p + c_p \dot{x}_p + k_{sp} x_p = f_a - f_{sp0} \text{sign}(x_{mr}) \quad (4.104)$$

$$h(x_p, x_{mr}) = x_{p0} \text{sign}(x_{mr}) + g(x_p - x_{p0} \text{sign}(x_{mr})) \quad (4.105)$$

where the function  $g(x)$  is the same as (4.67).

Suppose that when the pilot valve opens, which theoretically happens at the pilot spool position giving zero lap, this does not give a discontinuous flow out of the pilot valve as a function of pilot spool position<sup>6</sup>. Then the saturation function given by  $h(x_p, x_{mr})$  may be replaced by one having continuous gradients. Mathematically one may easily construct a saturation function which is  $C^\infty$ . We shall leave out the details but in the following it is assumed that  $h(x_p, x_{mr})$  may be replaced by its differentiable counterpart being at least  $C^2$ . In the following the  $C^2$  counterpart of  $h(x_p, x_{mr})$  is simply denoted by  $h$ .

#### 4.7.6.2 Equivalent control

The plan in (4.103) to (4.105) is of third order. We therefore chose the following second order sliding surface

$$s(t) = c_1 e_m + c_2 \dot{x}_m + \ddot{x}_m = 0 \quad (4.106)$$

where  $e_m = x_m - x_{mr}$ .

The sliding condition  $\dot{s}(t) = 0$  which constrain the states to the surface yields

$$\dot{s}(t) = c_1 \dot{e}_m + c_2 \ddot{x}_m + \dddot{x}_m = 0 \quad (4.107)$$

Assume that the variation of the valve gain is negligible and may be approximated by a constant such that  $k_v(t) = k_{v_0}$ . Then from (4.103), (4.104) and (4.106) the following coordinate transformations are obtained

$$\ddot{x}_m = -c_1 e_m - c_2 \dot{x}_m \quad (4.108)$$

$$\ddot{x}_m = \frac{k_{v_0}}{A_m} (\ddot{x}_p - \ddot{h}) \quad (4.109)$$

$$x_p = \frac{A_m}{k_{v_0}} \dot{x}_m + h \quad (4.110)$$

$$\dot{x}_p = \frac{A_m}{k_{v_0}} \ddot{x}_m + \dot{h} \quad (4.111)$$

$$\ddot{x}_p = \frac{1}{m_p} (f_a - f_{sp_0} \text{sign}(x_{mr}) - c_p \dot{x}_p - k_{sp} x_p) \quad (4.112)$$

By using these transformations (4.107) may be written as

$$\begin{aligned} \dot{s}(t) = & \frac{k_{v_0}}{A_m m_p} (f_a - f_{sp_0} \text{sign}(x_{mr})) - \frac{c_1 (c_2 m_p - c_p)}{m_p} e_m + c_1 \dot{e}_m \\ & - \frac{c_2^2 m_p - c_2 c_p + k_{sp}}{m_p} \dot{x}_m - \frac{(m_p \ddot{h} + c_p \dot{h} + k_{sp} h) k_{v_0}}{A_m m_p} = 0 \end{aligned} \quad (4.113)$$

---

<sup>6</sup>In practice this will be the case due to leakage.

By rearranging the equivalent control is obtained as

$$f_{a_{eq}} = \underbrace{\frac{A_m m_p}{k_{v0}} \left[ \frac{c_1(c_2 m_p - c_p)}{m_p} e_m - c_1 \dot{e}_m + \frac{c_2^2 m_p - c_2 c_p + k_{sp}}{m_p} \dot{x}_m \right]}_{\text{Known part}} + f_{sp0} \text{sign}(x_{mr}) + \underbrace{m_p \ddot{h} + c_p \dot{h} + k_{sp} h}_{\text{Unknown part}} \quad (4.114)$$

The part of (4.114) which is known may be used in the equivalent control, whereas it is assumed that the unknown part is upper bounded. If also assuming that  $m_p \ddot{h} + c_p \dot{h} + k_{sp} h < h_0$  the control in (4.84) only with  $k_v(t)$  replaced by  $h_0$  satisfies the reaching condition  $s\dot{s} < 0$ . To avoid chattering the following is used instead

$$f_a = f_{a_{eq}} - h_0 \tanh(k_s s) \quad (4.115)$$

An increase of  $h_0$  in the above improves the reaching performance of the controller whereby the states tend faster towards the sliding mode. Once in sliding mode the dynamics of the closed loop system is given by

$$\ddot{x}_m + c_2 \dot{x}_m + c_1 x_m = c_1 x_{mr} \quad (4.116)$$

$$\ddot{x}_p = \frac{A_m}{k_{v0}} (c_1 c_2 e_m - c_1 \dot{e}_m + c_2^2 \dot{x}_m) + \ddot{h} \quad (4.117)$$

The second order response of the main spool may therefore be prescribed by selecting appropriate values of  $c_1$  and  $c_2$ . A desired closed loop bandwidth  $\omega_b$  and a desired damping ratio  $\zeta$  of the dynamics given by (4.116) gives the following coefficients for  $c_1$  and  $c_2$

$$c_1 = \omega_b^2 \quad (4.118)$$

$$c_2 = 2\zeta\sqrt{c_1} \quad (4.119)$$

Equation (4.117) shows that  $h$  has to have bounded second order derivatives in order that the acceleration of the pilot spool is bounded. It has already been argued in section 4.7.6.1 that in practice  $\ddot{h}$  will be bounded.

A disadvantage of the above control scheme is that the main spool acceleration and velocity are used in the controller. As these are not directly available for control, the position has to be differentiated twice to implement the switching part of the controller.

### 4.7.6.3 Simulation results

The simulated flow tracking using the SM-P controller is plotted in figure 4.53. Although the difference may be difficult to notice from the figures, the SM-P controller gives slightly better transient response than the controllers presented previously. As may be seen from table 4.11 the demands for steady state performance is fulfilled.

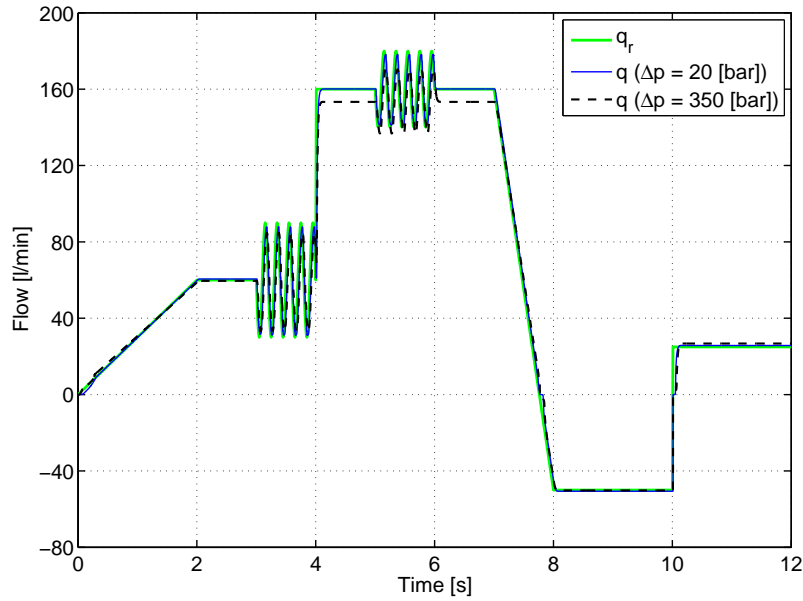


Figure 4.53: Simulated flow tracking using SM-P controller.

Performance criterion	Value	Unit
Steady state flow error, $\Delta p = 20$ [bar], $q_r = 160$ [l/min]	0.1	[%]
Steady state flow error, $\Delta p = 350$ [bar], $q_r = 160$ [l/min]	4.1	[%]
Maximum actuator force	8	[N]

Table 4.11: Performance of SM-P controller.

In the discrete time implementation of the SM-P controller used for simulation, the main spool position signal and the reference position signal were each filtered by 1st order filters with a crossover frequency of 60 [Hz] before differentiation.

## 4.8 Robustness of controllers

In this section the robustness of the developed controllers with respect to disturbances and variation of parameters is analysed by carrying through a simulation study. The varied parameters are the radial clearance and the dead-zone associated with the pilot valve, see table A.7 in appendix A regarding the parameter ranges. The flow reference which is used for evaluating the tracking response is shown in figure 4.54. In the figure a positive flow is equivalent to metering flow out of the A port and a negative flow is equivalent to metering flow out of the B port of the valve. For all simulations perfect inversion of the main spool flow gain has been used, whereby a flow error is due to position tracking error only.

For disturbances that are time limited the simulation results are presented directly. For disturbances which are not time limited or parameters which are constant but uncertain,

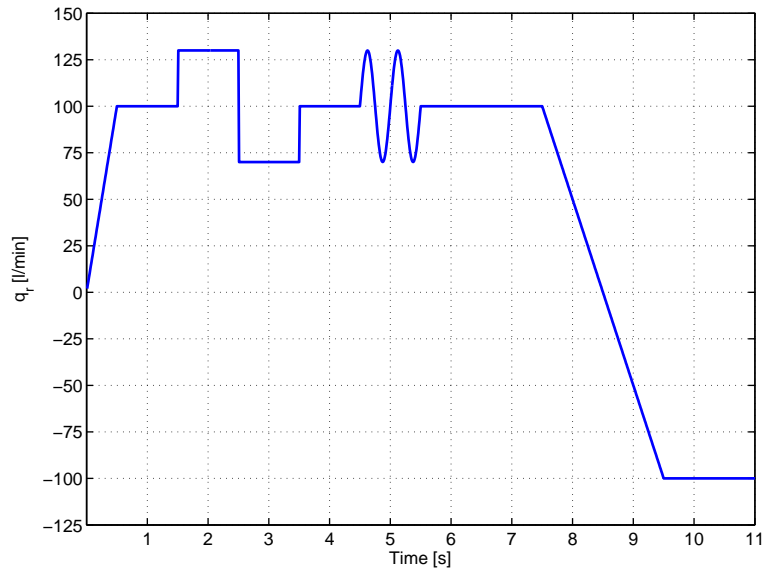


Figure 4.54: Flow reference.

the following performance measures are used for the evaluation of robustness

- Steady State (SS) flow error in % at 100  $\left[\frac{1}{\text{min}}\right]$ .
- Root Mean Square (RMS) flow tracking error in  $\left[\frac{1}{\text{min}}\right]$ .
- Time for flow response to reach and stay inside a  $\pm 10\%$  band of requested flow for a 100  $\left[\frac{1}{\text{min}}\right]$  step response.

A larger difference between the absolute steady state error and the RMS tracking error is equivalent to slower tracking or a more oscillatory response.

## 4.8.1 Robustness to disturbances

### 4.8.1.1 Coulomb friction on spools

Simulations where a 0.5 [N] Coulomb friction force was applied to the pilot spool has been made. Numerical values for the performance measures are listed in tables 4.12 and 4.13. In addition to the friction force, a 100 [Hz] sinusoidal dither signal with a 1 [N] amplitude was superimposed on the control signal in the simulation. For the entries of the tables marked with \*, a 2 [N] amplitude was used for the dither signal. This has shown to be necessary to avoid limit cycling when using the G-PILF and R2H controllers. Hence these controllers are more sensitive to Coulomb friction on the pilot spool than the sliding mode controllers. This is not surprising as the Coulomb friction force satisfies a matching condition, and the sliding mode controllers are in their nature robust to this type of uncertainty.



Pressure	No friction				Friction			
	20 [bar]		350 [bar]		20 [bar]		350 [bar]	
	SS	RMS	SS	RMS	SS	RMS	SS	RMS
G-PILF	0	6.5	0	10.9	0*	10.3*	0*	14.2*
R2H	-0.5	5.1	-2.0	8.9	-0.5*	9.5*	-2.0*	13.2*
F-SM	0.6	3.5	-4.5	6.2	0.5	5.2	-4.5	8.8
MF-SM	0.6	3.1	-4.7	6.2	0.5	4.0	-3.0	8.3
SM-P	0.4	2.7	-2.9	4.4	0.5	3.3	-3.0	5.8

Table 4.12: SS and RMS performance.

Pressure	No friction		Friction	
	20 [bar]	350 [bar]	20 [bar]	350 [bar]
G-PILF	253	474	254*	475*
R2H	260	507	250*	579*
F-SM	71	92	128	361
MF-SM	35	60	28	270
SM-P	49	70	46	55

Table 4.13: Flow settling time [ms].

Among the controllers the SM-P controller is the one most robust to Coulomb friction on the pilot spool. Simulations have also been made where the controller robustness to a 10 [N] Coulomb friction force on the main spool was evaluated. All the controllers showed to be robust to this disturbance.

#### 4.8.1.2 Drain pressure disturbance and step response

In this subsection the controller robustness with respect to the drain pressure disturbance plotted in figure 4.36 is analysed. In the simulation the pressure disturbance has been applied to the common drain line of the main circuit and the pilot circuit of the valve. No damping orifice in the pilot drain line has been used and an ideal controller for the pilot supply pressure has been assumed. The responses to the disturbance are plotted in figures 4.55 to 4.59. The first parts of the plotted responses are the responses to a flow reference step from 0 to 100  $\left[\frac{1}{\text{min}}\right]$ . Notice the scales of the figures.

It may be seen that the sliding mode controllers have approximately equal and superior performance compared to the linear controllers. The R2H controller has a slightly faster transient response than the G-PILF controller, otherwise they perform similarly. Again the SM-P controller is the most robust among the controllers.

#### 4.8.1.3 Pump pressure disturbance

The rejection of a pump pressure disturbance is considered in this subsection. Contrary to the pressure disturbance considered in the previous subsection, the pump pressure disturbance does not affect the pilot circuit directly. Again perfect control of the pilot

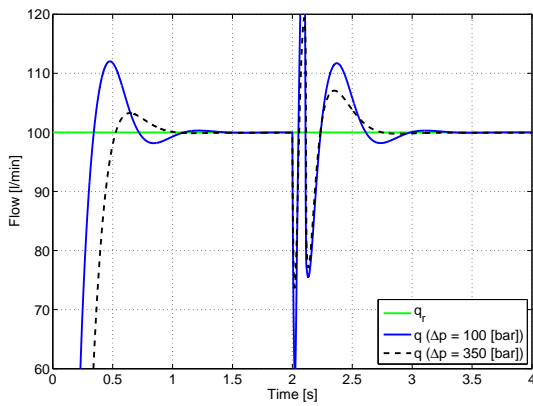


Figure 4.55: Drain pressure disturbance response G-PILF controller.

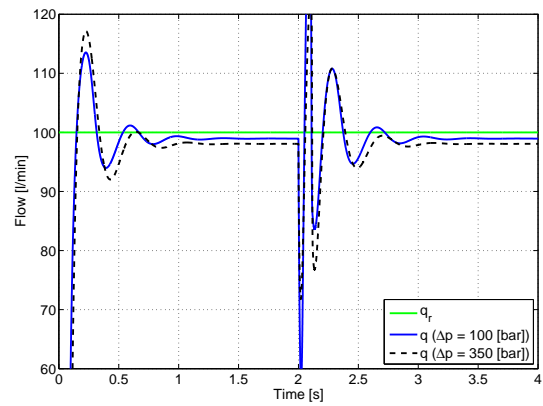


Figure 4.56: Drain pressure disturbance response R2H controller.

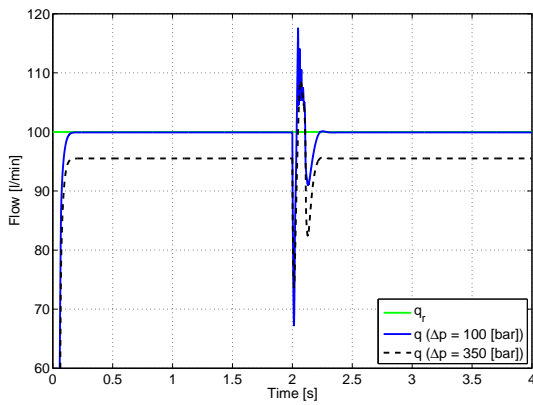


Figure 4.57: Drain pressure disturbance response F-SM controller.

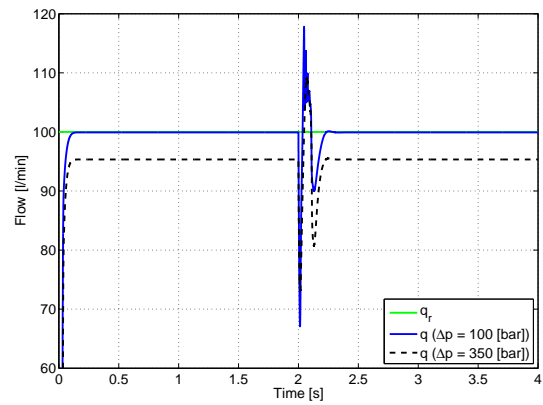


Figure 4.58: Drain pressure disturbance response MF-SM controller.

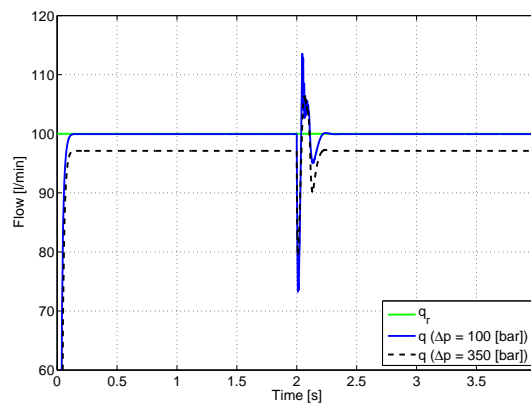


Figure 4.59: Drain pressure disturbance response SM-P controller.

pressure has been assumed in the simulation. The differential pressure which has been applied across the main spool is plotted in figure 4.60. The rise time of the plotted pressure disturbance is 40 [ms], which is fast compared to what is obtainable by conven-

tional load sensing pumps. A flow reference step from 0 to 100  $\left[\frac{1}{\text{min}}\right]$  has been applied initially. The obtained responses are plotted in figures 4.61 to 4.65.

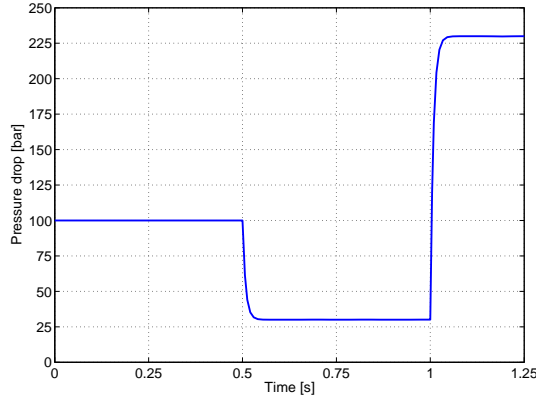


Figure 4.60: Applied differential pressure.

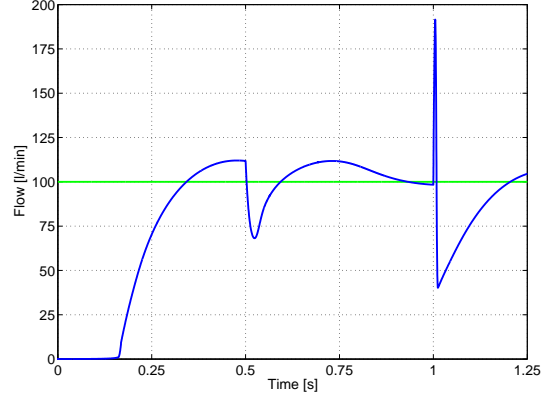


Figure 4.61: Supply pressure disturbance response G-PILF controller.

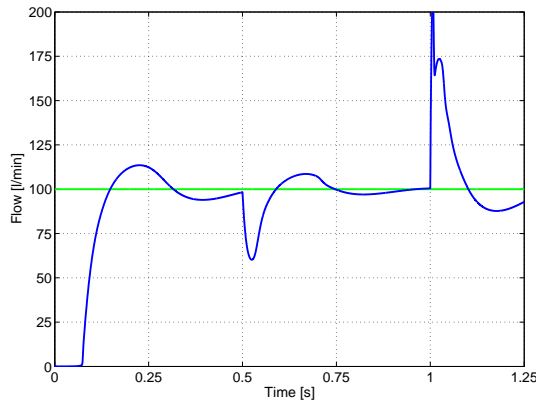


Figure 4.62: Supply pressure disturbance response R2H controller.

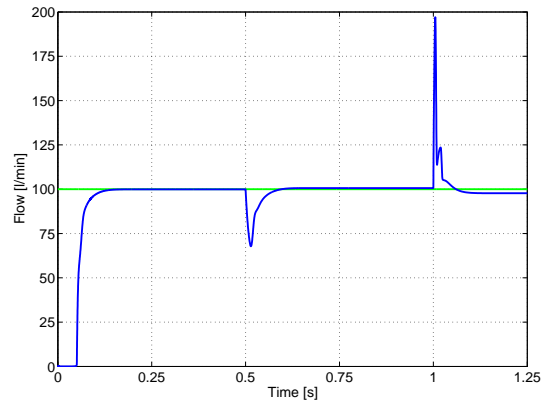


Figure 4.63: Supply pressure disturbance response F-SM controller.

It may be seen that the linear controllers give a poor decoupling of the disturbance, whereas the sliding mode controllers perform equally well as previously. The peak of the responses around 1 [s] is not assumed to be a problem due to the short duration of the peak. However, the best way to investigate whether the obtained pressure decoupling is sufficient, is by testing the pressure compensation on a real life application. By taking the fast disturbance into consideration, the results obtained using the sliding mode controllers look promising however.

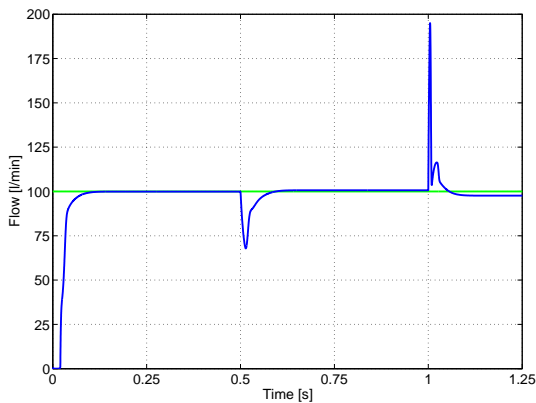


Figure 4.64: Supply pressure disturbance response MF-SM controller.

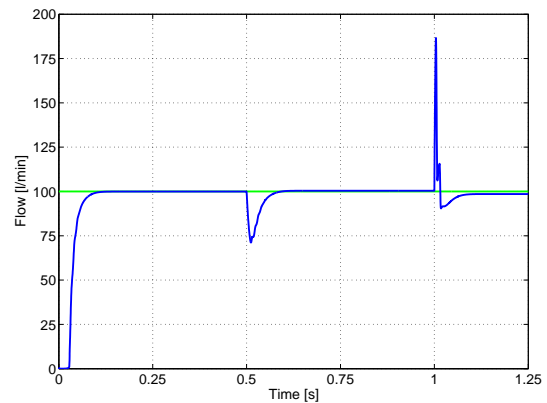


Figure 4.65: Supply pressure disturbance response SM-P controller.

## 4.8.2 Robustness to parameter variations

### 4.8.2.1 Robustness to variation in pilot spool dead-zone

When varying the dead-zone of the pilot valve, then to give a reasonable controller performance, it was found necessary to adjust the feedforward of the controllers based on the underlap of the pilot spool when in its null position. Therefore, the controller performance listed in tables below assumes that the underlap of the pilot spool is known for example due to calibration during assembly.

The controller robustness when varying the pilot spool dead-zone is summarised in tables 4.14 and 4.15. It may be seen that the sliding mode controllers are more robust to variation of the dead-zone than the linear controllers. Worst case is obtained when the dead-zone of the pilot valve is large. For this case the transient tracking of the G-PILF and the R2H controllers is poor and the responses become oscillatory. This may be seen by the fact that the time for the responses to settle within 10 % of the reference value are 943 [ms] respectively 758 [ms] for a 350 [bar] bar pressure drop. At the same time the difference between the SS and RMS performance measures for these operating conditions is large.

Pressure	Min. overlap				Nom. overlap				Max. overlap			
	20 [bar]		350 [bar]		20 [bar]		350 [bar]		20 [bar]		350 [bar]	
	SS	RMS	SS	RMS	SS	RMS	SS	RMS	SS	RMS	SS	RMS
G-PILF	0	3.9	0	9.9	0	6.5	0	10.9	0	9.7	0	13.9
R2H	-0.6	3.8	-2.0	4.9	-0.5	5.1	-2.0	8.9	-0.5	7.1	-2.0	14.3
F-SM	2.2	3.0	8.0	8.1	0.6	3.5	-4.5	6.2	-1.22	8.3	-15.5	18.1
MF-SM	2.3	2.9	8.4	8.4	0.6	3.1	-4.7	6.2	-1.3	6.3	-16.0	17.7
SM-P	1.0	1.9	5.0	4.8	0.4	2.7	-2.9	4.4	-0.8	4.4	-10.1	11.6

Table 4.14: Steady state tracking error and RMS performance measures for pilot spool dead-zone variation.

At a 350 [bar] pressure drop the sliding mode controllers do not have sufficient steady state gain to settle within a tracking error of 10 % of the reference when the dead-zone is large. However, because the difference between the SS and RMS performance measures is small the response is smooth. The trade off in this connection is that if the switching gain is increased, the tracking for large dead-zones is improved, but at the same time chattering is experienced when the dead-zone is small.

Pressure	Min. overlap		Nom. overlap		Max. overlap	
	20 [bar]	350 [bar]	20 [bar]	350 [bar]	20 [bar]	350 [bar]
G-PILF	265	590	253	474	673	943
R2H	130	171	260	507	342	758
F-SM	48	48	71	92	263	-
MF-SM	30	44	35	60	72	-
SM-P	38	43	49	70	60	-

Table 4.15: Flow settling time for pilot spool dead-zone variation (time in [ms]).

#### 4.8.2.2 Robustness to variation in pilot spool radial clearance

The robustness to variation of the radial clearance between the pilot spool and the housing is summarised in tables 4.16 and 4.17. The effect of decreasing the radial clearance is approximately the same as increasing the dead-zone because the leakage across pilot spool lands decreases. It may be seen from the tables that the response times and tracking are affected significantly by the radial clearance. Hence, combined with the findings in the previous subsection it may be concluded that worst case is obtained for a large dead-zone of the pilot spool and a small radial clearance between the pilot spool and the housing. Therefore the manufacturing tolerances for these parameters should be considered carefully in the design.

Pressure	Min. clearance				Nom. clearance				Max. clearance			
	20 [bar]		350 [bar]		20 [bar]		350 [bar]		20 [bar]		350 [bar]	
	SS	RMS	SS	RMS	SS	RMS	SS	RMS	SS	RMS	SS	RMS
G-PILF	0	8.0	0	14.3	0	6.5	0	10.9	0	4.3	0	10.0
R2H	-0.5	5.8	-2.0	12.4	-0.5	5.1	-2.0	8.9	-0.5	4.0	-1.9	5.8
F-SM	0.5	4.3	-5.5	10.1	0.6	3.5	-4.5	6.2	0.6	2.7	-4.3	5.1
MF-SM	0.5	4.1	-5.7	10.4	0.6	3.1	-4.7	6.2	0.7	2.3	-4.4	5.0
SM-P	0.5	3.3	-3.5	6.9	0.4	2.7	-2.9	4.4	0.4	2.1	2.8	3.5

Table 4.16: Steady state tracking error and RMS performance measures for variation of pilot spool radial clearance.

Pressure	Min. clearance		Nom. clearance		Max. clearance	
	20 [bar]	350 [bar]	20 [bar]	350 [bar]	20 [bar]	350 [bar]
G-PILF	272	1057	253	474	234	616
R2H	350	1646	260	507	118	139
F-SM	78	216	71	92	62	66
MF-SM	36	191	35	60	33	40
SM-P	49	102	49	70	45	57

Table 4.17: Flow settling time for variation of pilot spool radial clearance (time in [ms]).

## 4.9 Experimental results

The controllers developed above, except from the F-SM controller, have been tested experimentally on the prototype valve, which was presented in section 3.4, using the PV-B pilot valve with round fluid ports. It should be noted that the radial clearance of this pilot valve is at the minimum of the manufacturing tolerance. This is worst case with regard to performance as may be seen from tables 4.16 and 4.17 in the previous section. Additionally, the dead-zone is 0.08 [mm] larger for negative spool stroke than for positive spool stroke, see section 3.5.1 for details about the pilot valve design. Negative spool stroke corresponds to negative flow in the responses to be presented.

Due to limitations of the test bench, the tested operating range was limited to a maximum flow of 100 [ $\frac{1}{\text{min}}$ ] and a maximum supply pressure of 250 [bar]. A real time xPC rapid prototyping system from The Mathworks was used for the controller implementation and data collection.

Unfortunately the peak to peak measurement noise of the main spool position signal was approximately 50 [ $\mu\text{m}$ ] which should be seen in comparison with the required minimum control resolution of 1.52 [ $\mu\text{m}$ ], e.g. see section 4.2.1. A third order 300 [Hz] Butterworth filter was therefore implemented digitally in the xPC system. However, still the sliding mode controllers, which are more sensitive to noise than the linear ones, had to be detuned slightly. In a valve with integrated LVDT sensor signal conditioning circuit, better performance than that presented in this section may therefore be expected, due to less noise. As for all the simulations, the controllers were implemented with an interrupt frequency of 1 [kHz]. The 3rd order filters for the position signal were run at a 10 [kHz] interrupt frequency.

The flow responses presented in the following have been computed from the measured main spool position and the pressure drop measured across the main spool. That is, using the same look-up tables as were used for implementing the electrohydraulic pressure compensation. This means that tracking error of a presented response is due to main spool position error only. The results are therefore comparable to those presented above in this chapter. The data for the lookup tables were found from measurements, hereby calibrating each orifice of the main spools separately. A plot of the inverse  $k_v$  characteristics for the two main spools of the prototype is shown in figure 4.66. At small values of  $k_v$ , where flow control has to be more accurate than at large values of  $k_v$ , a fair agreement between the curves are seen. Recall that the  $k_v$  value for a given

flow rate and a given pressure drop is computed as  $k_v = q/\sqrt{\Delta p}$ . The p-spool of the prototype was used for the testing of controllers, and responses at respectively 50 [bar] and 250 [bar] pressure drops were measured.

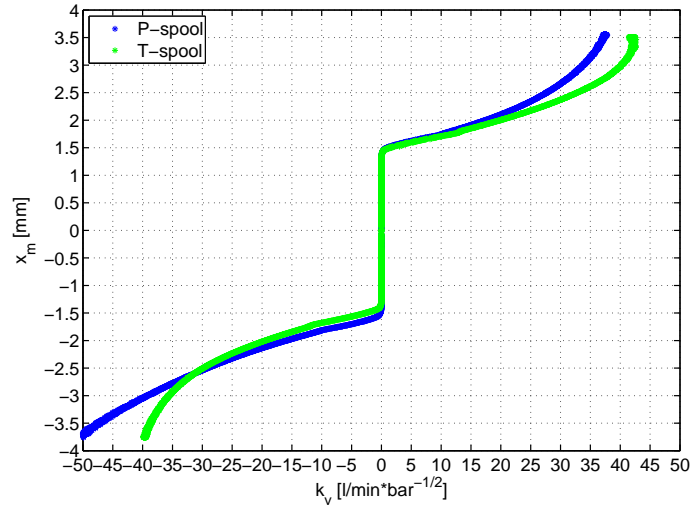


Figure 4.66: Inverse  $k_v$  characteristic of main spools of prototype.

The measured flow tracking of the G-PILF controller is plotted in figures 4.67 and 4.68 for the two different pressure drops. The test results show both a larger overshoot and a poorer tracking of sinusoids than the simulation, see figure 4.41. This is attributed to the smaller radial clearance of the tested pilot valve, compared to the nominal parameters used for the simulation, e.g. compare tables 3.3 and A.1. As mentioned, the smaller clearance gives less leakage and therefore has the same effect as a larger overlap. The tracking is poorer for a negative flow. This is attributed to the larger pilot spool dead-zone associated with negative spool stroke.

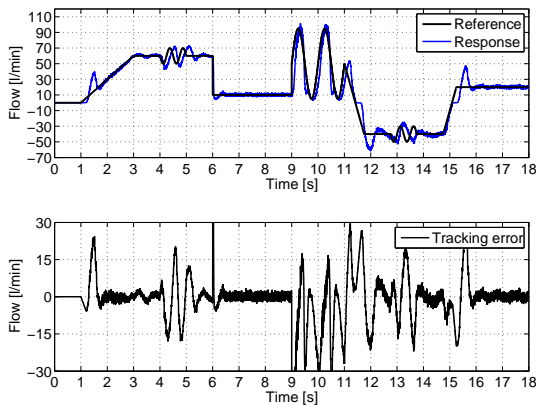


Figure 4.67: Flow tracking response of G-PILF controller at 50 [bar].

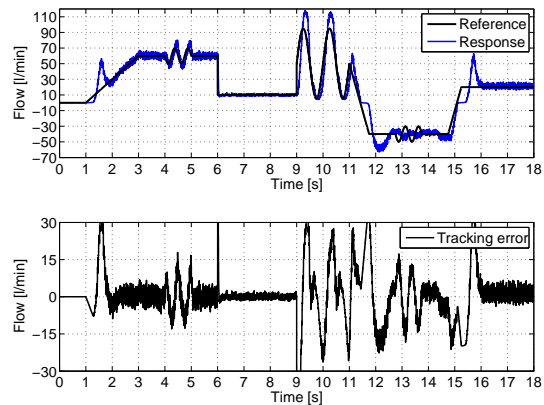


Figure 4.68: Flow tracking response of G-PILF controller at 250 [bar].

The test results obtained with the third order R2H controller are plotted in figures

4.69 and 4.70. For positive spool stroke these responses are in fair agreement with the simulation results in figure 4.49, except that small oscillations are seen at steady state. One may think that this is due to Coulomb friction on the pilot spool, since limit cycling with the R2H controller was also observed by applying Coulomb friction in a simulation, if at the same time insufficient dither was applied. During the experiments the limit cycling could not be removed by increasing the dither however. The exact reason for the oscillations was not found but a fourth order implementation of the controller with a larger high frequency gain solved the problem. This may be seen by figures 4.71 and 4.72.

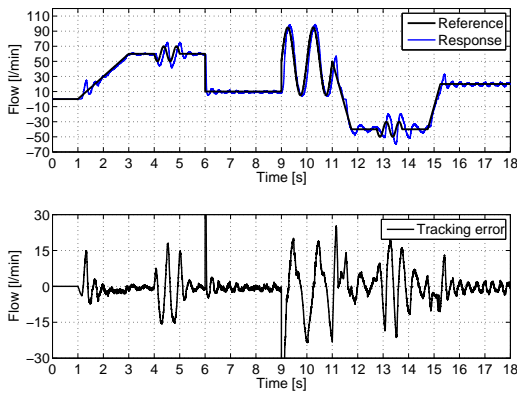


Figure 4.69: Flow tracking response of R2H third order controller at 50 [bar].

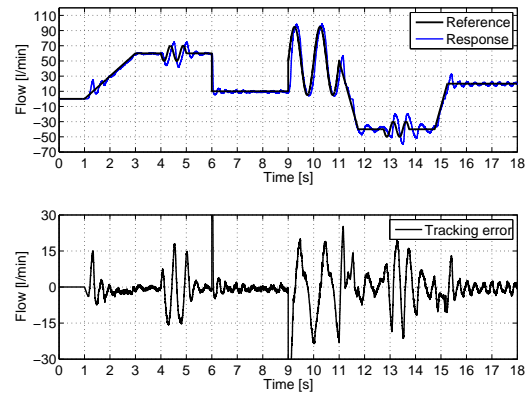


Figure 4.70: Flow tracking response of R2H third order controller at 250 [bar].

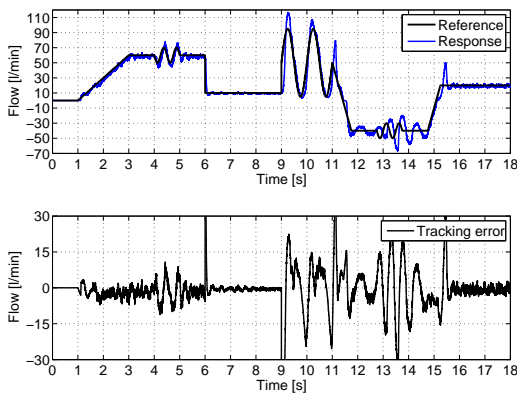


Figure 4.71: Flow tracking response of R2H fourth order controller at 50 [bar].

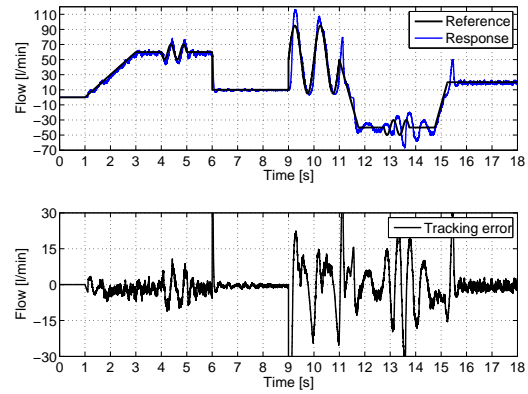


Figure 4.72: Flow tracking response of R2H fourth order controller at 250 [bar].

As may be seen from the tracking error of the fourth order R2H controller, the larger high frequency gain made the controller more sensitive to noise. The responses obtained using the R2H controllers in general are insensitive to pressure drop. The R2H controller



is sensitive to the larger pilot spool dead-zone for negative flows, which is in agreement with the robustness analysis of the previous chapter.

The responses obtained using the MF-SM controller are shown in figures 4.73 and 4.74. The controller provides a better tracking than G-PILF and R2H controllers. This was expected from the simulation results presented previously. As may be seen from the high pressure results the controller is rather noise sensitive, but the tracking is in general fairly robust to operating conditions. The larger pilot spool overlap associated with the negative main spool stroke side is clearly noticeable in the response.

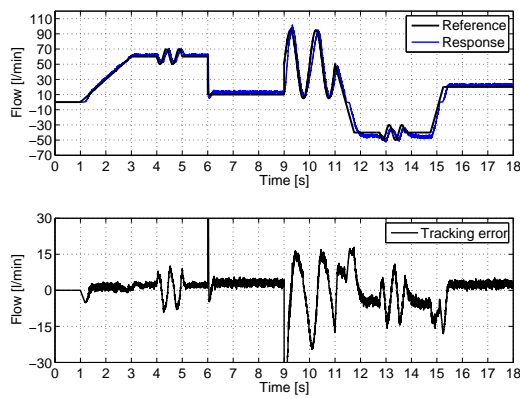


Figure 4.73: Flow tracking response of MF-SM controller at 50 [bar].

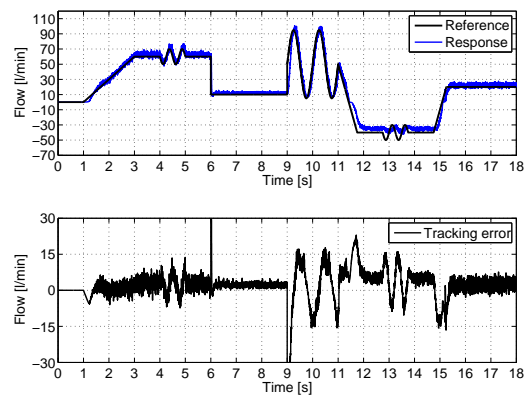


Figure 4.74: Flow tracking response of MF-SM controller at 250 [bar].

The SM-P controller test results are plotted in figures 4.75 and 4.76. The controller performs similar to the MF-SM controller but is slightly less noise sensitive. This is quite interesting as second order derivatives of the filtered main spool position was used in the controller implementation. It should be noted that before the two differentiations, the spool position was filtered by a first order digitally implemented filter, having a crossover frequency of 50 [Hz]. That is, besides the third order filtering of the main spool position.

From the experiments it is clear that the sliding mode controllers gives the best performance compared to the linear ones. This is in agreement with the findings from the simulations. All the controllers showed more or less sensitivity to pilot spool overlap, therefore as also expected from the simulations the tolerances determining this overlap should be carefully considered in the design. It could be interesting to test another pilot valve having a larger radial clearance to verify whether this gives a performance increase as expected. This is left for further work. A test set-up with better shielding of signals to remove some of the measurement noise is also left as a future exercise.

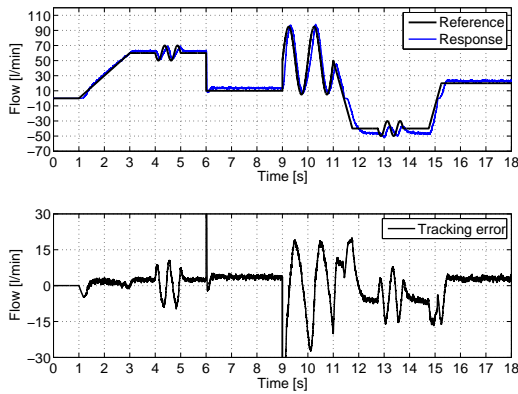


Figure 4.75: Flow tracking response of SM-P controller at 50 [bar].

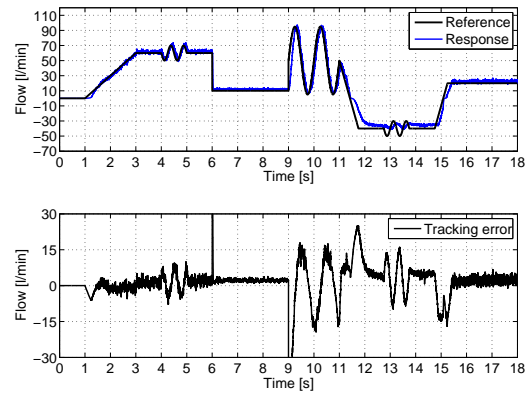


Figure 4.76: Flow tracking response of SM-P controller at 250 [bar].

## 4.10 Summary and conclusion

This chapter has been concerned with the development of a flow controller for the selected separate meter-in separate meter-out valve. The developed flow controller is based on electrohydraulic pressure compensation. The method comprises the development of a spool position controller and this has been the primary subject of the chapter.

Steady state accuracy requirements for the flow controller have been established by taking basis in the steady state performance of state of the art proportional valves. To dynamically decouple the pressure dynamics of a given application, it has been shown that qualitatively the bandwidth of the spool position controller must be above the frequencies of dominating dynamics of the controlled application.

Two different pilot actuation methods were considered for the actuation of the spool valve. One using a pilot stage generating pressure as a function of force input (pressure control pilot), and one using a pilot stage generating flow as a function of force input (flow control pilot). Preliminary controller designs were considered for both pilot actuation methods. Although the simulation results for the valve with the pressure control pilot looked promising for nominal parameters, a stability analysis of the internal pressure feedback loop of the valve showed a low relative stability. The following factors increasing the relative stability were identified:

- Lowering the movable mass of the pilot valve.
- Increasing the viscous damping associated with the pilot spool.

Due to the low relative stability of the spool valve with pressure control pilot, it was disqualified for further study and the valve with flow control pilot was selected. The remaining comments in this summary and conclusion therefore refers to the valve with flow control pilot.

The controller performance requirements in terms of bandwidth necessary to decouple the dead-zone of the pilot valve, and to decouple a pressure disturbance in the drain line of the pilot circuit, have been analysed. The analysis showed that requirements are largely dependent on the pressure drop across the main spool, with high pressure drop being worst case. A control bandwidth larger than 28 [Hz] was found necessary for decoupling of the dead-zone, and a control bandwidth larger than 34 [Hz] was found necessary for decoupling the dead-zone + drain pressure disturbance. These numbers are approximate due to the used disturbance model of the dead-zone being an approximate one.

Controllers showing robustness to varying operating conditions were designed. The best transient performance was obtained by non-linear sliding model controllers, whereas the best steady state accuracy, at a high pressure drop across the main spool, was obtained by a gain scheduling controller with integral control action, and a controller based on linear  $\mathcal{H}_\infty$  control.

The disturbance robustness of the controllers was analysed by simulations. A drain pressure disturbance and a pump pressure disturbance were considered. The used disturbances were selected as worst case both due to their size and short rise time. The sliding mode controllers showed the best disturbance rejection, however, all controllers yielded quite large flow peaks for an increase in pump pressure. Whether the dynamical decoupling of pressure disturbances is sufficient is best tested by a real life application, but due to the selected extreme disturbances, the results obtained with the sliding mode controllers were found to be promising. By the presence of Coulomb friction on the pilot spool, it was found that the valve may limit cycle, if using the G-PILF or the R2H controllers with an insufficient dither amplitude. The limit cycling was to some extent reproduced with the R2H controller by experiments.

The robustness of the controllers to a varying pilot spool dead-zone and a varying radial clearance was analysed. It was found that the radial clearance between the pilot spool and the housing as well as the size of the pilot spool dead-zone had a large influence on control performance. The worst case was obtained when the radial clearance was small and the overlap of the pilot spool was large. Thus a trade-off when specifying the manufacturing tolerances for these parameters is recommendable.

Finally, results from experimental tests of the controllers have been presented. Due to measurement noise the sliding mode controllers had to be detuned slightly. Still they showed the best performance of the tested controllers. Within the operating range of the test bench, being 0 – 250 [bar] and 0 – 100 [ $\frac{1}{\text{min}}$ ], the controllers fulfilled the demands for steady state performance. However, as expected from simulations, they showed a clear performance decrease for an increase of the pilot spool overlap. The radial clearance of the tested pilot valve was at the minimum of the manufacturing tolerance. It was left for further work to carry out tests with a pilot valve having a larger radial clearance, thus verifying that the radial clearance has the expected effect on the controller performance.

# Chapter 5

## Generic model of hydraulic application with flexible load structure

### Contents

---

5.1	Presentation of selected application . . . . .	147
5.2	Models of main lift axis and base rotational axis . . . . .	149
5.3	Summary and conclusion . . . . .	155

---

In this chapter a generic model structure of a hydraulic actuator system is developed. The model is generic in the sense that, by an appropriate choice of equivalent parameters, it models a hydraulic cylinder connected to an inertia load through a flexible mechanical structure. This is a configuration commonly encountered in mobile applications. The purpose of developing the model is to establish a realistic simulation model for testing separate meter-in separate meter-out control strategies developed in the subsequent chapter. Although the model is generic, basis is taken in a real life application, namely a loader crane.

### 5.1 Presentation of selected application

A loader crane has been selected as the studied application because general load cases which are characteristic for many hydraulic working functions are also encountered by a loader crane. The considered loader crane is shown in figure 5.1. The loads on the hydraulic actuators associated with the four degrees of freedom of the crane are:

- **Main lift:** Non-linear unidirectional inertia load with flexible load structure.
- **Jib rotation:** Non-linear bidirectional inertia load with flexible load structure.
- **Jib extension:** Bidirectional load controlled by fluid regeneration. For some loader cranes the hydraulic system associated with this degree of freedom contains long fluid lines.

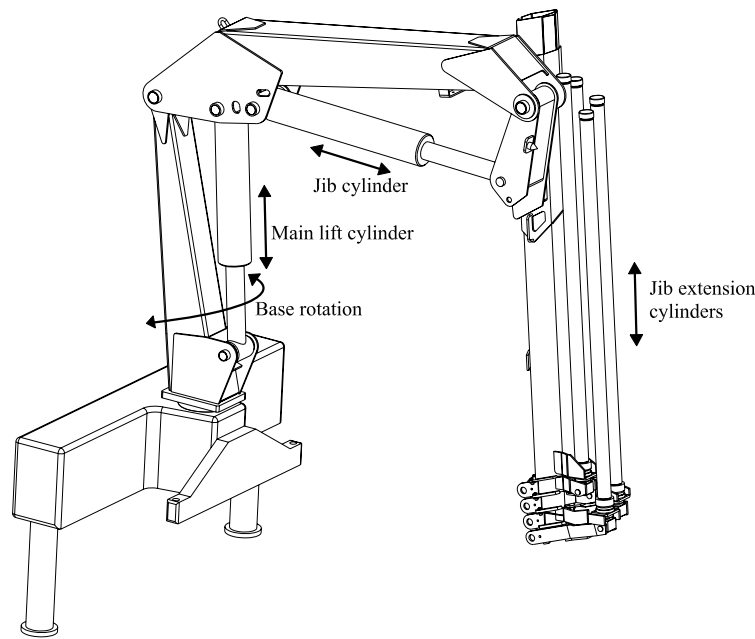


Figure 5.1: Loader Crane.

- **Base rotation:** Bidirectional inertia load with flexible load structure.

The mechanical structure of the jib of the loader crane gets more flexible as the jib is extended. For loader cranes, the natural frequencies of the coupled hydraulic and mechanical subsystems are in the approximate range of  $0.25 - 5$  [Hz], depending on the kinematic configuration and the carried payload. The lowest natural frequency is commonly associated with the base rotational axis. Due to the low natural frequency structural modes are easily excited. This shall preferably be avoided as it makes it difficult for the operator to deliver the payload at a desired position, and stresses the mechanical structure of the crane.

In this dissertation work is focussed around controlling the main lift and the base rotation. Therefore the generic model presented in this chapter takes its basis in the dynamical systems associated with these two axes. The hydraulic actuator that is associated with the base rotation is a cylinder which is connected to the base column by a rack and pinion construction. The main difficulty about operating the base rotation is that the load applied to the hydraulic cylinder is bidirectional and that the natural frequency of the system associated with the base rotation is very low as mentioned above. Therefore the control of the base rotation has been chosen for further study.

The main lift is also a challenge to control due to the highly non-linear load on the actuator, and again due to the low natural frequency of the system. This makes it relevant to also choose the main lift for further study.

An over-centre-valve is mounted on the main lift cylinder of loader cranes manufactured for the European market. The functionality of the over-centre-valve is to control the meter-out of the main lift cylinder when lowering loads, and to hold the load in position

in case of hose bursts. In the following an over-centre-valve is not included in the model of the hydraulic system associated with the main lift cylinder. This is done as the meter-out functionality is already present in a separate meter-in separate meter-out valve. An over-centre-valve on the main lift is associated with additional cost of the system and will therefore be an undesirable solution. A load holding valve without the meter-out functionality but which it is either fully open or fully closed could be used instead.

## 5.2 Models of main lift axis and base rotational axis

It is desirable to obtain a model with as few states as possible, both due to the implementation and to ease the controller design. As illustrated by figure 5.1 the considered loader crane has 4 controllable axes. These are distributed over 7 mechanical degrees of freedom, that is by the movement of 7 hydraulic cylinders, see appendix E for details<sup>1</sup>. Therefore, a complete loader crane model is complex to use for separate meter-in separate meter-out controller design for a single hydraulic cylinder.

A single degree of freedom of the loader crane may instead be represented by the generic system sketched in figure 5.2. It is shown by the results in appendix E that the structural flexibility may be modelled accurately by including only two structural modes.

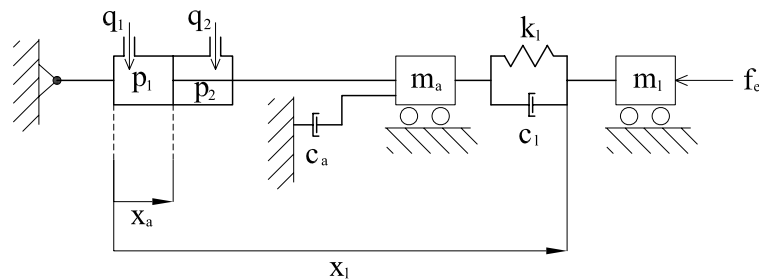


Figure 5.2: Equivalent system in linear coordinates.

Seen from a single degree of freedom point of view, the structure in figure 5.2 is different from the one presented in appendix E, in that the masses are lumped. For the model in the appendix the mass is distributed along the bodies making up the mechanical structure of the crane. This primarily affects the way the vibration energy is distributed in the structure. Only a single structural vibration mode is represented by the system in figure 5.2, whereas a mechanical system may have several vibration modes.

For loader cranes the lowest mode is dominating, whereby it is assumed that the model associated with the structure in figure 5.2 captures the dominating dynamics of the crane. The governing equations of this model are given by

$$f_l = k_l(x_a)(x_a - x_l) + c_l(x_a)(\dot{x}_a - \dot{x}_l) \quad (5.1)$$

<sup>1</sup>The appendix has been included to show that the dynamics of a loader crane may be modelled using only the lowest modes of the mechanical structure.

$$\dot{p}_1 = \frac{\beta_e(p_1)}{V_{1s} + Ax_a}(q_1 - A\dot{x}_a) \quad (5.2)$$

$$\dot{p}_2 = \frac{\beta_e(p_2)}{V_{2s} - \alpha Ax_a}(q_2 + \alpha A\dot{x}_a) \quad (5.3)$$

$$\ddot{x}_a = \frac{1}{m_a}(p_1 A - p_2 \alpha A - c_a \dot{x}_a - f_l) \quad (5.4)$$

$$\ddot{x}_l = \frac{1}{m_l(x_a)}(f_l - f_e) \quad (5.5)$$

Note, Coulomb friction associated with the cylinder has been neglected to obtain a system which is linearisable. The equations shows the structural spring stiffness and the equivalent mass as being functions of the cylinder position. This is the case for the main lift axis, due to the non-linear transmission ratio of the mechanical structure between the hydraulic cylinder and the load mass.

### 5.2.1 Equivalent parameters for main lift axis

The case where the jib actuator is fully extended is considered. For this case the structure associated with the main lift axis may be represented by the sketch in figure 5.3. In

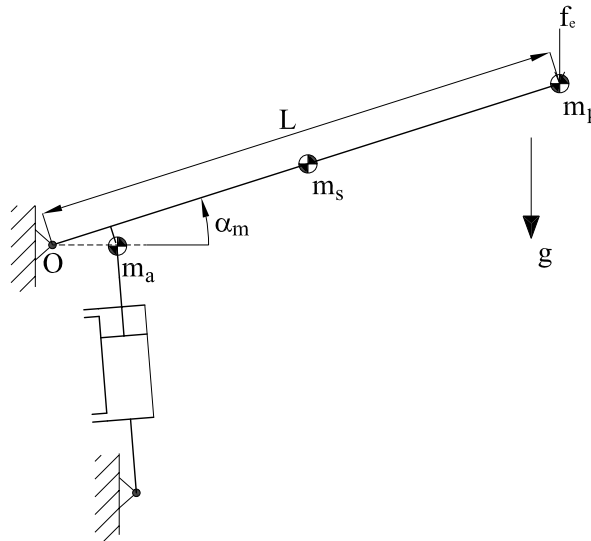


Figure 5.3: Equivalent mechanical structure.

the figure  $m_p$  is the lumped mass of the payload,  $m_s$  is the lumped mass associated with the jib,  $m_a$  is the lumped mass associated with the main lift cylinder, and  $f_e$  is an external force modelling unknown forces due to payload dynamics, e.g. due to angular acceleration of the payload inertia itself which is neglected in the model.

It is assumed that the centre of gravity of the jib (excluding the payload) is at  $L/2$ . Due to the movement of bodies in the jib arm, the centre of gravity moves as the length of

the jib changes. For some cases the centre of gravity is slightly nearer to the base of the crane than at  $L/2$ . Due to the mass of the payload the error is assumed to be negligible when computing the mass moment of inertia around point  $O$ . The mass moment of inertia about point  $O$  is computed by

$$J_O = \left( m_p + \frac{m_s}{3} \right) L^2 \quad (5.6)$$

The mass moment of inertia may be converted to the equivalent mass  $m_l$  on the main lift actuator. Due to the transmission ratio of the structure this equivalent mass depends on the position of the main lift cylinder. It may be shown from conservation of energy that the equivalent mass is related to  $J_O$  through a coordinate transformation as

$$m_l = \frac{J_O}{\left( \frac{\partial x_a}{\partial \alpha_m} \right)^2}, \quad \dot{x}_a = \frac{\partial x_a}{\partial \alpha_m} \dot{\alpha}_m \quad (5.7)$$

The equivalent mass load on the main actuator for a 400 [kg] payload<sup>2</sup> is plotted in figure 5.4, as a function of the length of the main boom + jib, and the position of the main lift cylinder. It may be seen that the mass load on the main lift cylinder is non-linear.

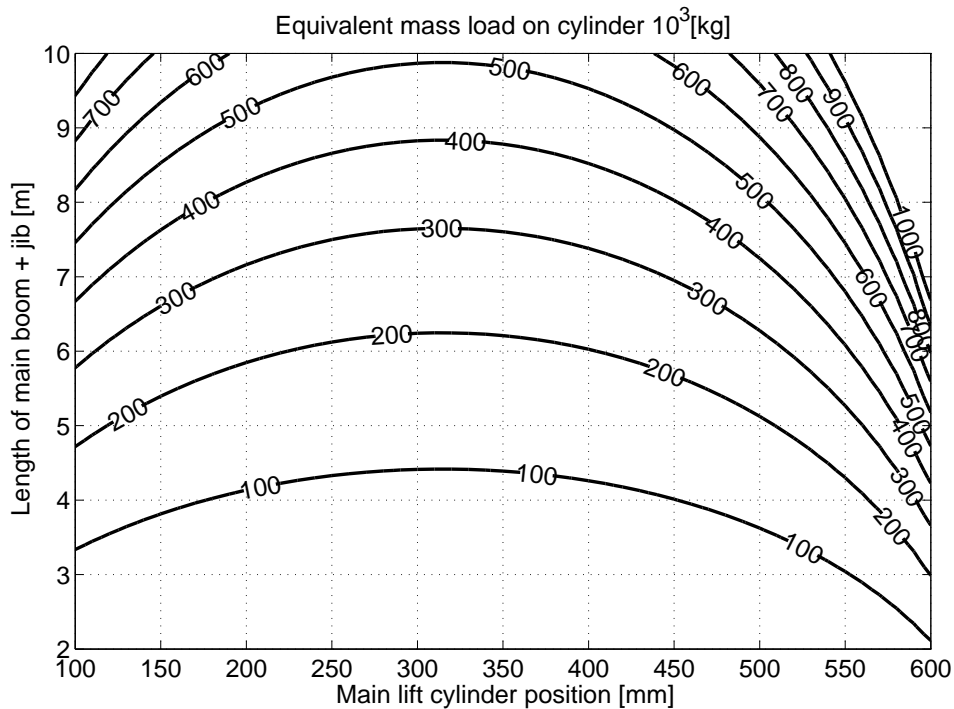


Figure 5.4: Equivalent mass of system in linear coordinates.

Münzer presented experimental measurements in [73] showing that the torsional rigidity of the mechanical structure, of the exact same loader crane which is considered here, is

<sup>2</sup>This is the maximum payload which may be carried by the loader crane in the full operating range.



inversely proportional to the length of the jib. Münzer's results included the mechanical stiffness of the crane but excluded the stiffness of the hydraulic system. Here the concern is directed towards the equivalent parameters for the main lift axis. Therefore the stiffness of the fluid in the jib cylinder must also be considered, as the jib cylinder is coupled in mechanical series with the main lift cylinder and mounted between the main lift cylinder and the payload, see figure 5.1.

For the position where the jib actuator is fully extended the effective moment arm of the jib cylinder with respect to the jib rotation is given by  $L_\tau$ . A series coupling of the equivalent spring stiffness of the fluid in the jib actuator and the torsional rigidity gives the following expression for the equivalent spring stiffness of the main lift axis

$$k_\tau = \left( \frac{1}{k_{\tau_1} L^{-1}} + \frac{V_j}{A_j^2 L_\tau^2 \beta_e} \right)^{-1} \quad (5.8)$$

where the left term is the inverse structural spring stiffness, and the right term is the inverse spring stiffness of the fluid in the jib actuator.

Due to the effective bulk modulus of the fluid in the jib actuator being dependent on the actuator loading, the right hand term within the brackets of (5.8) depends on the gravitational load on the mass of the jib and on the carried payload. It therefore also depends on the rotation angle  $\alpha_j$  of the jib. Furthermore, the loading of the jib actuator depends on the length of the jib. The details are left out, but, the pressure describing the loading of the jib cylinder is plotted in figure 5.5 again assuming a 400 [kg] payload.

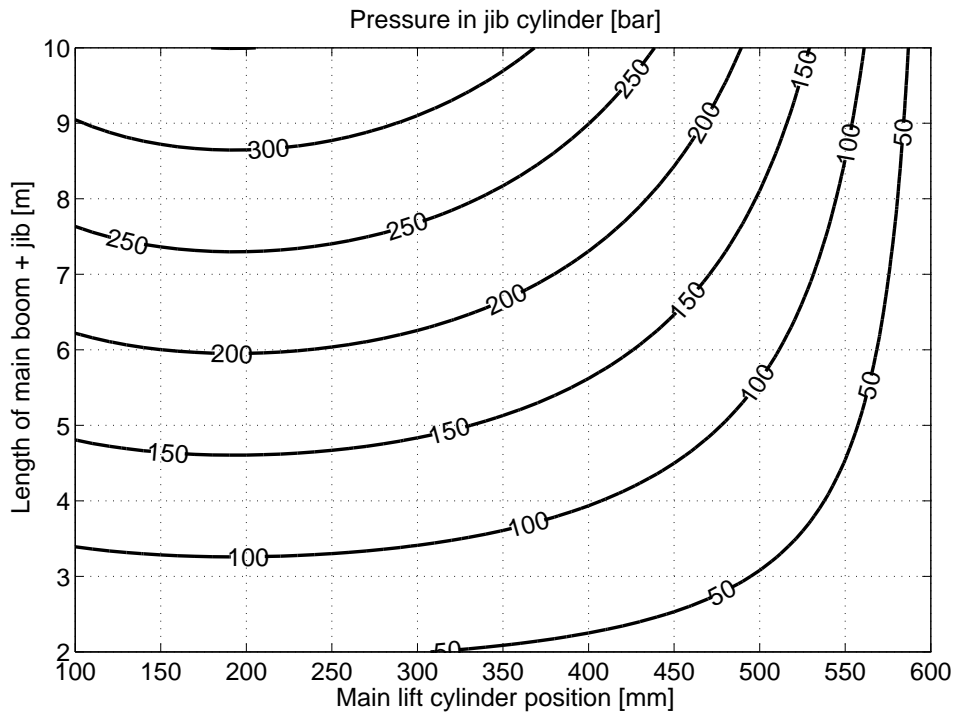


Figure 5.5: Pressure in jib cylinder.

By matching undamped natural frequencies, the torsional spring stiffness in equation (5.8) is transformed to a spring stiffness in linear coordinates of the main lift cylinder as

$$k_l = \frac{k_\tau}{J_O} m_l = \frac{k_\tau}{\left(\frac{\partial x_l}{\partial \alpha_m}\right)^2} \quad (5.9)$$

A plot of  $k_l$  is shown in figure 5.6, again as a function of the main lift cylinder position and the length of the main boom + jib.

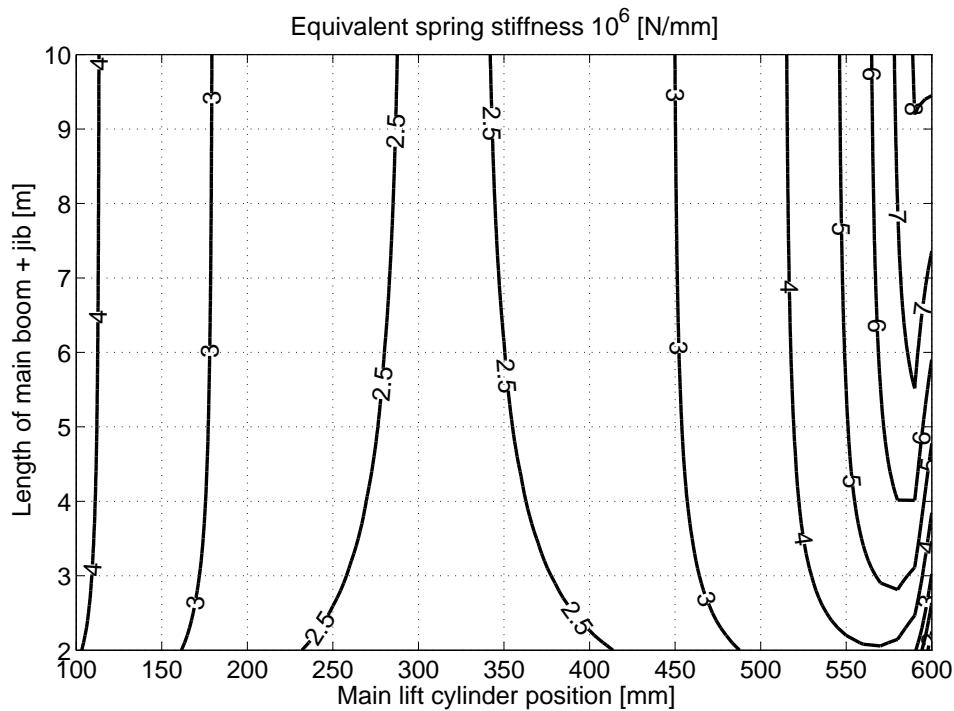


Figure 5.6: Equivalent spring stiffness of system in linear coordinates.

The undamped natural frequency in Hz of the main lift axis is computed from the equivalent spring stiffness and the equivalent mass as  $\sqrt{\frac{k_l}{m_l}} \frac{1}{2\pi}$ . The result is plotted in figure 5.7

The low natural frequency for the fully extended main lift actuator is due to the jib being in a nearly vertical position, why the load on the jib actuator is small. In practice this gives a configuration of the crane which will seldom (if ever) be used in practice. If disregarding the case where the main lift cylinder is nearly fully extended, then the natural frequency of the main lift axis is approximately proportional to the length of the jib.

The only parameter which needs to be found to complete the model of the main lift is the structural damping of the system. Generally the damping in mechanical structures is low. In the more complex simulation model of appendix E all damping was attributed to the hydraulic cylinders. However, to avoid pure imaginary poles in a linearisation of

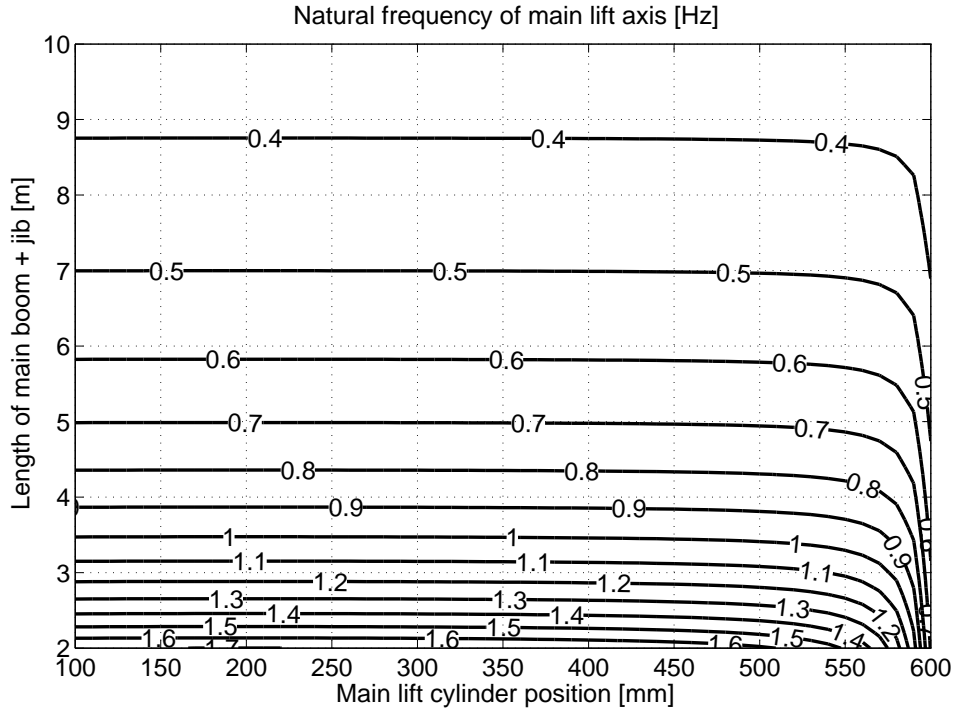


Figure 5.7: Natural frequency of main lift axis.

the equations (5.1) to (5.5), constant structural damping ratio of  $\zeta_l$  is assumed. This gives the following expression for  $c_l$

$$c_l = 2\sqrt{\frac{k_l}{m_l}}\zeta_l \quad (5.10)$$

### 5.2.2 Equivalent parameters for base rotational axis

The base rotational axis may be represented by the mechanical system in figure 5.8. Due to the constant transmission ration of the rack and pinion, a model of the base rotational axis may be seen as a simplified case of that already presented above for the main lift axis. The base rotation of the crane makes a rotation of  $\alpha_b$  [rad] for an end to end stroke of the cylinder. The same expression for computing the mass moment of inertia around point  $O$  as above may be used hereby the equivalent mass load on the cylinder rod becomes

$$m_l = \frac{J_O\alpha_b^2}{L_c^2} = \frac{\alpha_b^2}{L_c^2} \left( m_p + \frac{1}{3}m_s \right) L^2 \quad (5.11)$$

The mechanical stiffness around the base rotational axis of the considered crane has not been measured. Commonly the jib is less rigid around this axis than the main rotational axis, because it is not designed for carrying as large a load around the base rotational

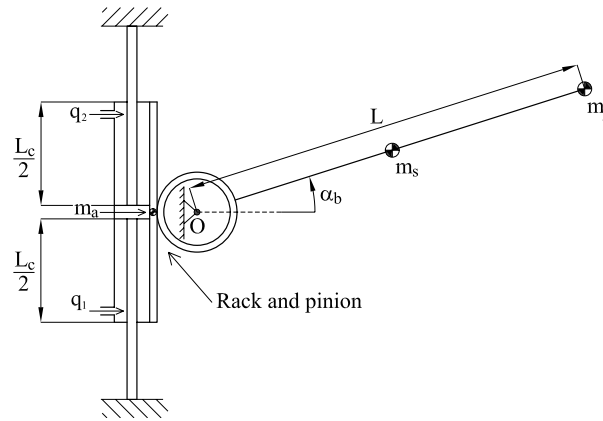


Figure 5.8: Equivalent mechanical structure.

axis. For want of a better estimate, of the structural stiffness around the base rotational axis, the same stiffness of the jib as around the main lift axis is assumed. Hereby the stiffness around the base rotational axis is computed by

$$k_l = \frac{k_\tau \alpha_b^2}{L_c^2} \quad (5.12)$$

### 5.3 Summary and conclusion

In this chapter a generic model of a single degree of freedom hydraulic application with structural flexibility has been presented. Equivalent parameters for the model have been computed by taking basis in the main lift axis and the base rotational axis of a loader crane. The generic model has not been verified but results presented in appendix E have shown that it is sufficient to include only the lowest modes of the structure in the model. However, the generic model uses a simpler representation of the structural flexibility than the verified model presented in appendix E. The parameters for the simplified structural flexibility representation have been verified though, due to work presented in [73].



# Chapter 6

## Multivariable pressure/velocity control

### Contents

---

<b>6.1</b>	<b>State of the art - Separate metering control . . . . .</b>	<b>157</b>
<b>6.2</b>	<b>Introduction to the multivariable control problem . . . . .</b>	<b>158</b>
<b>6.3</b>	<b>Tools for decentralised controller design . . . . .</b>	<b>162</b>
<b>6.4</b>	<b>Linear models for controller development . . . . .</b>	<b>164</b>
<b>6.5</b>	<b>Decentralised pressure/velocity control structures . . . . .</b>	<b>166</b>
<b>6.6</b>	<b>Summary and conclusion . . . . .</b>	<b>190</b>

---

This chapter is concerned with multivariable control of hydraulic actuators by separate meter-in separate meter-out. Two controllers for controlling inertia loads with flexible load structures are developed. The developed controller structures are based on meter-in respectively meter-out and may both control bidirectional loads. The parameters from the loader crane presented in the previous chapter are used in the numerical computations. Algorithms using regenerative features are not considered, as stated in the demarcation of research.

### 6.1 State of the art - Separate metering control

Within research institutions, work regarding separation of metering orifices in valves targeted for mobile applications is found in [11]. In his dissertation Andersson considered the design of a seat valve for integration in a Wheatstone configuration. Although the Wheatstone valve configuration featured the separate metering elements, the four seat valves were controlled by a single input from the operator.

Lantto et. al. were the first to consider separate meter-in separate meter-out for decoupled control of actuator velocity and pressure using combined pump and valve control [57]. Further considerations regarding functionality when separating the metering orifices were given by Jansson and Palmberg in [50]. Jansson et. al. authored another interesting paper on a control structure, decoupling the velocity and pressure level of

a hydraulic actuator [49]. As pointed out by Jansson et. al. implementation of velocity feedback along with the proposed control scheme was necessary to obtain statically good control of the actuator velocity. The results in the particular paper showed that dynamically the velocity and pressure were decoupled.

An LQG controller decoupling the actuator pressures was developed in [38]. Elfving et. al. considered a feedforward control scheme for decoupling the actuator pressures [34]. The downside of this scheme with respect to mobile fluid power systems was that the actuator velocity had to be measured. In [36] the control scheme was extended with closed loop pressure controllers and closed loop velocity control. In [35] these closed loop controllers were further improved by adding electrohydraulic load sensing.

In [84] a control scheme based on switching between different control strategies as a function of the measured actuator velocity error was considered. The purpose was to provide smooth accelerating and decelerating of large inertia loads. Research on separate metering control of hydraulic manipulators has also been made by a number of authors [9, 18, 59, 69]. A control scheme for decoupling of the interference between two separate meter-in separate meter-out valves sharing the same load and drain pressures was proposed in [64]. Adaptive control using separate meter-in separate meter-out valves was considered by researches in [23, 109, 110]. Finally, basic hydraulic functionality of a valve topology with five 2-way valves was tested in [24] and control schemes with a similar valve topology was considered in [47].

The above summarises the work that has been made at universities regarding control with separate meter-in separate meter-out valves. Recently the industry has also begun to show interest in this field [4, 54]. Due to this, several methods for establishing hydraulic functionality in software, have been patented or sought patented [60, 67, 82, 95, 96, 97, 98]. Common for these patents and patent applications are that they are not concerned with the dynamic properties of a separate meter-in separate meter-out control system but describe overall separate meter-in separate meter-out control functionality and set-point manipulation.

## 6.2 Introduction to the multivariable control problem

The operator may control the actuator velocity either by controlling the meter-out flow rate from the actuator or by controlling the meter-in flow rate to the actuator. The operator will thus occupy one of the two control variable available in a separate meter-in separate meter-out valve. Only one additional control variable is therefore left for controlling one of the work port pressures of the actuator. In this way combined control of a work port pressure and the velocity is a multivariable control problem with two inputs and two outputs. Around a specific operating point the controlled plant may be represented as the  $2 \times 2$  linear transfer matrix

$$G = \begin{bmatrix} G_{11} & G_{12} \\ G_{21} & G_{22} \end{bmatrix} \quad (6.1)$$

If the operator, who controls the velocity, and the pressure controller, which controls one of the work port pressures, are exclusively in control of each their control variable the suggested controller structure is a decentralised control structure. In a decentralised control structure the controller is diagonal. If we assume that the velocity may be controlled by controlling the flow rate  $q_1$ . Then a decentralised control structure may look like the one in figure 6.1. In this control structure the operator is in control of  $q_1$  and the pressure controller is in control of  $q_2$ . In the figure the velocity reference  $\dot{x}_{ar}$  is created in the brain of the operator and the reference pressure  $p_r$  may for example be a constant pre-set back pressure.  $G_{v1}$  and  $G_{v2}$  symbolises the closed loop dynamics of the controllable orifices.

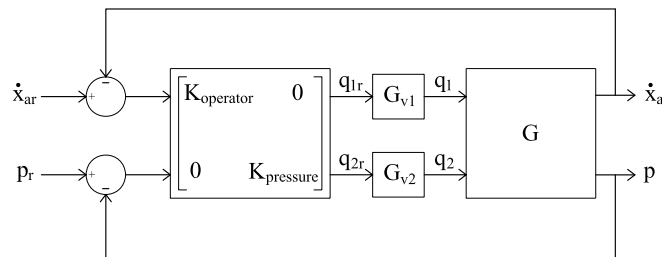


Figure 6.1: decentralised control structure with operator in loop.

If the off diagonal elements,  $G_{12}$  and  $G_{21}$ , of (6.1) are non-zero, the pressure controller may affect the controlled velocity, and the control input from the human operator may affect the controlled pressure. However, the pressure controller cannot influence "too much" on the velocity controlled by the operator, as this makes it difficult for the operator to control the velocity. In other words the velocity and the pressure level should be decoupled. If a multivariable plant is diagonally dominant, meaning that the off-diagonal elements of (6.1) are small compared to the elements on the diagonal, the plant is in its nature decoupled. In this case the pressure and velocity control loops may be designed by separate SISO controller design problems, whereby a diagonal (decentral) controller structure is obtained.

In this chapter concerned is directed towards the actuator set-up sketched in figure 6.2<sup>1</sup>. The set-up is generic for hydraulic applications, but the actuators are assumed to be the ones associated with the main lift and the base rotation of the loader crane modelled in the previous chapter. Without loss of generality, it is assumed that the load sensing pump is connected to  $v_1$  and  $v'_1$ , and therefore that the velocities of the actuators are in the positive directions, that is  $\dot{x}_a > 0$  and  $\dot{x}'_a > 0$ .  $q_1$ ,  $q_2$ ,  $q'_1$  and  $q'_2$  are shown with arrows marking their positive directions. In the following we concentrate on control of the actuator to the left in the figure.

For meter-in the flow rate through  $v_1$  controls the velocity, and the pressure level of the actuator is controlled by controlling the fluid flow through  $v_2$ . For meter-out the flow rate through  $v_2$  controls the velocity, and the pressure level of the actuator is controlled by

<sup>1</sup>The reader is requested to mark the page with this figure with a note, as reference to the figure is made several times in the sequel.



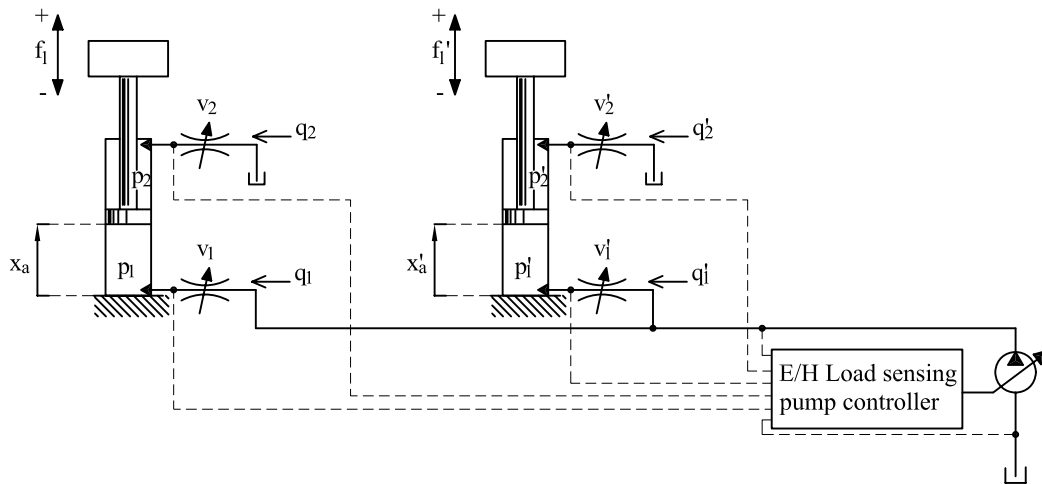


Figure 6.2: Separate meter-in separate meter-out controlled actuators.

controlling the fluid flow through  $v_1$ . When choosing a decentralised controller structure, one may choose between two overall control strategies:

1. Choose meter-in or meter-out depending on the direction of the actuator velocity. Hereby the pressure control scheme will depend on the load direction, and the orifice which is controlled by the operator will only change when the sign of the velocity changes.
2. Choose meter-in or meter-out depending on the load direction. Hereby the orifice which controls the velocity changes when the direction of the load changes.

It is assumed that the controlled actuators are supplied from a pressure controlled load sensing pump, two main objectives may therefore be stated for the pressure control scheme:

1. Prevent bidirectional loads in overrunning, i.e. keep  $p_1 > 0$  and  $p_2 > 0$ .
2. Keep the necessary pump pressure as low as possible to save energy.

It is assumed in the following that a sufficient pump pressure is always present. For an actuator controlled by meter-in, this means that a sufficient pressure drop to drive the desired flow rate across the meter-in orifice must be present. Otherwise the electrohydraulic pressure compensation, developed in chapter 4, will not work. For an actuator controlled by meter-out this means that a sufficient pressure drop to drive the desired flow rate across the meter-out orifice must be present. For the particular system in figure 6.2 the E/H load sensing pump controller must therefore know whether a particular actuator is controlled by meter-out or by meter-in. That is, to select the appropriate actuator pressure for generating the reference for the pump.

A decentralised control structure where  $\dot{x}_a$  is controlled by  $v_1$  (meter-in) is sketched in figure 6.3. In the figure  $K_H$  symbolises the human operator and  $K_P(t, p_1, p_2)$  is the pressure controller. For the control structure in figure 6.3 and  $\dot{x}_a > 0$  the objectives for

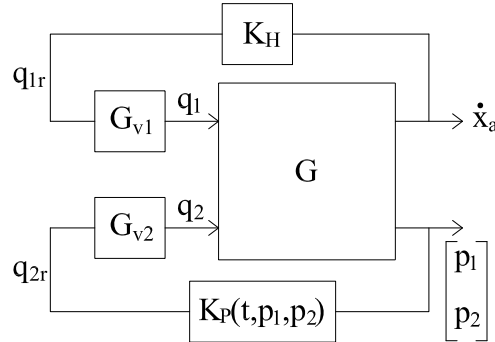


Figure 6.3: Decentralised control structure for meter-in.

the pressure controller may be specified as:

- For  $f_l > 0$ : Avoid cavitation of the pressure chamber associated with  $v_1$  and keep pump pressure low. This may be done by controlling  $p_1$  such that  $0 < p_1 < p_0$ , where  $p_0$  is the standby pressure of the pump.
- For  $f_l < 0$ : Avoid unnecessary waste of energy such that the pump pressure supplying  $v_1$  is kept as low as possible. This may be done by keeping  $p_2$  as low as possible.

Now referring to figure 6.2, in the case that the actuator to the right is in charge of the pump pressure, for example because  $p_1 < p'_1$ . Then the pressure level of the actuator to the left may be raised without causing additional power consumption of the total system as long as  $p_1 < p'_1$  holds. Therefore, with regard to the outline above, keeping  $p_1 < p_0$  (first bullet point) and  $p_2$  as low as possible (second bullet point) are sufficient conditions to secure the lowest possible power consumption of the considered system, but the conditions are not always necessary.

A decentralised control structure where  $\dot{x}_a$  is controlled by  $v_2$  (meter-out) is sketched in figure 6.4.

For this meter-out control structure the objectives outlined for the pressure controller may be specified as:

- For  $f_l > 0$ : Avoid cavitation of the pressure chamber associated with  $v_1$  by keeping  $p_1 > 0$ . Also keep  $p_2 \geq \Delta p_{min} + p_t$ , where  $\Delta p_{min}$  is the minimum rated pressure drop of  $v_2$ . The lower limit for  $p_2$  secure that there is a sufficient pressure drop for the desired flow rate to occur through  $v_2$ .
- For  $f_l < 0$ : Keep  $p_2 = p_t + \Delta p_{min}$  to secure sufficient pressure drop for the desired flow rate across  $v_2$  to occur.

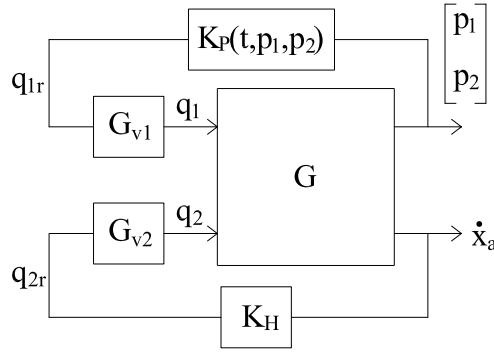


Figure 6.4: Decentralised control structure for meter-out.

Before approaching the design of multivariable controllers for the pressure and velocity, some tools for decentralised controller design and analysis are described.

## 6.3 Tools for decentralised controller design

The relative gain array will be used to get insight into how the load direction and the cylinder piston position influence on the interactions between the control loops of a separate meter-in separate meter-out controlled hydraulic cylinder. Furthermore, the structured singular value interaction measure will be used for computing a bound on the complementary sensitivity function, which is sufficient for a decentralised controller to stabilise a multivariable plant. The relative gain array and the structured singular value interaction measure are introduced in the following. Readers familiar with these may skip to section 6.4.

### 6.3.1 Relative gain array

The relative gain array (RGA) of a matrix is defined as

$$\text{RGA}(G) = \Lambda(G) \triangleq G \times (G^{-1})^T \quad (6.2)$$

where  $\times$  denotes an element by element multiplication. The  $ij$ 'th element of the RGA may be written as [89]

$$\lambda_{ij} \triangleq \frac{g_{ij}}{\widehat{g}_{ij}} \quad (6.3)$$

$$\left. \frac{\partial y_i}{\partial u_j} \right|_{u_k=0, k \neq j} = g_{ij} = [G]_{ij} \quad \text{Other control loops are open}$$

$$\left. \frac{\partial y_i}{\partial u_j} \right|_{y_k=0, k \neq i} \triangleq \widehat{g}_{ij} = 1/[G^{-1}]_{ji} \quad \text{Other control loops are closed}$$

Thus,  $g_{ij}$  is the gain from input  $i$  to output  $j$  if all other control loops are open, and  $\hat{g}_{ij}$  is the gain from input  $i$  to output  $j$  if all other control loops are closed. Their ratio as given by (6.3) is a measure of the interactions between control loops, and may thus be used to analyse whether a plant is decoupled or not. If  $g_{ij} = \hat{g}_{ij}$  the plant remains unaffected by closing other control loops and is said to be decoupled. Therefore, if a plant is completely decoupled the RGA is the identity matrix. The RGA has a number of useful properties, e.g. see [89]. We will use the following two

1. The RGA of a square matrix is independent of the scaling of the matrix
2. The row sum and the column sum are both unity

### 6.3.2 Structured singular value interaction measure

The idea of the Structured Singular Value Interaction Measure (SSVIM) is to treat the interactions of a plant as a perturbation, and then use the structured singular value to compute bounds on the loop gain to assure stability of the system. Let  $\tilde{G} \triangleq \text{diag}\{g_{ii}\}$ , then the off-diagonal elements of  $G$  relative to  $\tilde{G}$  may be written as

$$E \triangleq (G - \tilde{G})\tilde{G}^{-1} \quad (6.4)$$

Let  $GK$  be the loop transfer function of a closed loop control system, then write

$$\begin{aligned} I + GK &= I + (I + E)\tilde{G}K = I + \tilde{G}K + E\tilde{G}K \\ &= I + \tilde{G}K + E\tilde{G}K(I + \tilde{G}K)^{-1}(I + \tilde{G}K) \\ &= (I + E\tilde{T})(I + \tilde{G}K) \end{aligned} \quad (6.5)$$

If the negative feedback closed loop system with loop transfer function  $GK$  shall be stable, then from the generalised Nyquist criterion, the Nyquist plot of  $\det(I + GK)$  must encircle the origin  $p_{ol} = \mathcal{N}(\det(I + GK))$  times in the counter clockwise direction and cannot pass through the origin.  $p_{ol}$  is the number of open loop unstable poles of  $GK$ .

For assertion of the stability of the factorisation in (6.5), it may be used that the number of encirclements of  $\mathcal{N}(f_1 f_2) = \mathcal{N}(f_1) + \mathcal{N}(f_2)$ . Therefore, if each loop of  $\tilde{G}K$  is stable, then stability of the negative feedback connection of  $GK$  is equal to the condition that  $\mathcal{N}(\det(I + E\tilde{T})) = 0$ . From the small gain theorem a sufficient condition for stability is

$$\rho(E(j\omega)\tilde{T}(j\omega)) < 1 \quad \forall \omega \quad (6.6)$$

where  $\rho(L(j\omega)) \triangleq \max_i |\lambda_i(L(j\omega))|$  and  $\lambda_i(L(j\omega))$  is the  $i$ 'th eigenvalue of the complex matrix  $L(j\omega)$ . A proof of (6.6) is found on page 150 in [89]. It should be noted that because phase information is not included (6.6) is conservative.

$\rho(E\tilde{T})$  may be split up as [88]

$$\rho(E\tilde{T}) \leq \mu_{\tilde{T}}(E)\bar{\sigma}(\tilde{T}) \quad (6.7)$$

where  $\bar{\sigma}(\tilde{T})$  is the maximum singular value of  $\tilde{T}$ .

Hereby an upper bound on the complementary sensitivity function of the  $i$ 'th loop which assures stability is

$$\bar{\sigma}(\tilde{T}(j\omega)) = \max_i(\tilde{t}_i) < \frac{1}{\mu_{\tilde{T}}(E(j\omega))} \quad \forall \omega \quad (6.8)$$

The structured singular value interaction measure,  $\mu_{\tilde{T}}(E)$ , is computed with respect to  $\tilde{T}$  corresponding to a diagonal complex perturbation. The bound in (6.8) will be used in the following.

## 6.4 Linear models for controller development

A linear model description is necessary to apply the frequency domain tools presented in the previous section. Thus, a local linearisation of the generic non-linear model developed in chapter 5 is made in the following, and a linear representation of the valve dynamics is given.

### 6.4.1 Linear model representation of hydraulic actuator system

A linear model representation of the system governed by equations (5.1) to (5.5) is derived in the following. The specific operating point ( $p_1 = p_{10}, p_2 = p_{20}, x_a = x_{a0}$ ) is considered whereby the following coefficients are introduced

$$\begin{aligned} \beta_{10} &= \beta_e(p_{10}) & m_l &= m_l(x_{a0}) \\ \beta_{20} &= \beta_e(p_{20}) & k_l &= k_l(x_{a0}) \\ V_{10} &= V_{1s} + Ax_{a0} & c_l &= c_l(x_{a0}) \\ V_{20} &= V_{2s} - \alpha Ax_{a0} \end{aligned}$$

Using these coefficients a linear model representing the system in equations (5.1) to (5.5) is sketched in figure 6.5. In the figure the transfer function  $G_l$  modelling the load dynamics is given by

$$G_l = \frac{m_l(c_l s^2 + k_l s)}{m_l s^2 + c_l s + k_l} \quad (6.9)$$

By choosing

$$P = \begin{bmatrix} P_{11} & P_{12} \\ P_{21} & P_{22} \end{bmatrix} = \left[ \begin{array}{c|cc} -\frac{A^2}{s} \left( \frac{\beta_{10}}{V_{10}} + \alpha^2 \frac{\beta_{20}}{V_{20}} \right) & \frac{\beta_{10}}{V_{10}} \frac{A}{s} & -\frac{\beta_{20}}{V_{20}} \frac{\alpha A}{s} \\ \hline 1 & 0 & 0 \\ -\frac{\beta_{10}}{V_{10}} \frac{A}{s} & \frac{\beta_{10}}{V_{10}} \frac{1}{s} & 0 \\ \frac{\beta_{20}}{V_{20}} \frac{\alpha A}{s} & 0 & \frac{\beta_{20}}{V_{20}} \frac{1}{s} \end{array} \right] \quad (6.10)$$

and

$$L = \frac{1}{m_a s + c_a + G_l} \quad (6.11)$$

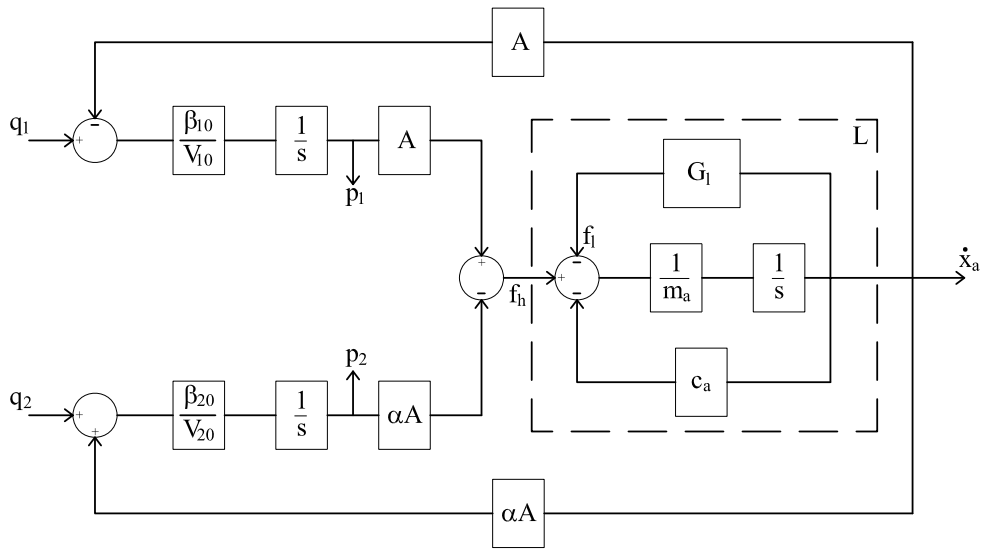


Figure 6.5: Linear block diagram of hydraulic actuator system with load.

a linear transfer matrix may be obtained by computing an upper Linear Fractional Transformation (LFT) as shown in figure 6.6. Note that if one wants to model a system where the flexibility of the mechanical structure may be omitted, this corresponds to choosing  $G_l = 0$  in (6.11).

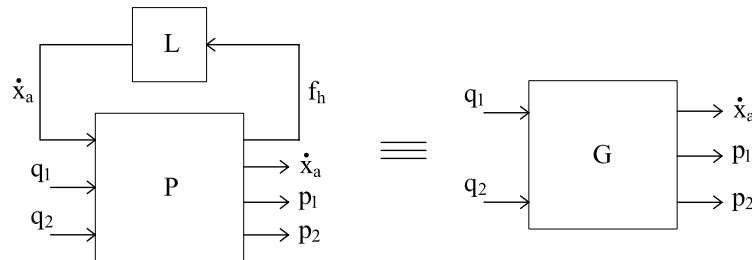


Figure 6.6: Hydraulic actuator system with load represented by an upper LFT.

The upper LFT is computed as

$$G = \mathcal{F}_u(P, L) = P_{22} + P_{21}L(1 - P_{11}L)^{-1}P_{12} \quad (6.12)$$

The velocity output,  $\dot{x}_a$ , of the linear plant is the velocity of the actuator itself. For most cases it is the velocity of the load,  $\dot{x}_l$ , which is of interest. These two are related as

$$\dot{x}_l = \frac{G_l}{m_l s} \dot{x}_a \quad (6.13)$$

Depending on the purpose, either  $\dot{x}_a$  or  $\dot{x}_l$  is used in the following.

### 6.4.2 Linear valve dynamics

The inputs for the above linear model are the flows  $q_1$  and  $q_2$ . Therefore we may use the output from the flow controllers developed in chapter 4 as inputs for the this model. However, from the results in section 4.2.2 it should be clear that the valve dynamics may influence on both the control performance and the stability of the system in general. The non-linear ones of the flow controllers developed in chapter 4 showed the best performance. But, due to these being non-linear, they do not fit into use with the linear controller design tools presented above. The following linear valve dynamics is therefore used instead.

$$G_v = \frac{900\pi^2}{[s^2 + 30\pi s + 900\pi^2][(60\pi)^{-1}s + 1]^2} \quad (6.14)$$

The model gives a  $-480$  [deg] phase at high frequency, to include a realistic limitation of the size of controller feedback gains at high frequency.

## 6.5 Decentralised pressure/velocity control structures

In this section different pressure/velocity control structures are developed. The control structures are characterised by that first either pre-filters or inner feedback loops are implemented to diagonalise (decouple) the plant. After decoupling one control variable may exclusively be used to control the velocity of the actuator as described above. As the next step a SISO pressure controller is designed for controlling the actuator pressure level.

In the section we will refer to the actuator to the left in figure 6.2 several times. Without loss of generality  $\dot{x}_a > 0$  is assumed. No flexible load dynamics is attached to the actuator in the figure. However, regarding closed loop response, concern is directed towards controlling the load velocity,  $\dot{x}_l$ , of the equivalent systems related to the base rotational axis and the main lift axis of the loader crane. Due to the fact that the base rotation axis and the main lift axis have comparable dynamics, the controller designs are demonstrated using numerical data for the base rotational axis only. Simulation results are given for both axes however.

Regarding computation of interaction measures, such as the RGA or the SSVIM, these are most meaningful with regard to  $\dot{x}_a$ , as  $\dot{x}_l$  may not be used for feedback in the considered systems. This should be understood in the way that although in this work it is assumed that the operator closes the velocity loop, then for example the SSVIM may be used to obtain bounds on the complementary sensitivity function, which are sufficient for stability of any of the control loops in a decentralised controller. When the SSVIM is computed for a plant having  $\dot{x}_a$  as the output instead of  $\dot{x}_l$ , the bounds are also sufficient for a velocity control loop, which is closed by using sensor feedback of  $\dot{x}_a$  instead of being closed by the operator.

Insight into interactions of the linear plant derived in section 6.4.1 above is gained by

using the RGA in the following.

### 6.5.1 Plant interactions

It may be seen from figure 6.6 that  $G$  has three outputs and only two inputs. Only as many outputs as there are inputs may be controlled independently. In this section it is investigated whether the two most intuitive input/output pairings for combined pressure/velocity control yield decoupled plants. For simplicity the valve dynamics is ignored and the following two plants are considered

$$P_{MI} = \begin{bmatrix} 1 & 0 & 0 \\ 0 & 1 & 0 \end{bmatrix} G \Rightarrow \begin{bmatrix} \dot{x}_a \\ p_1 \end{bmatrix} = P_{MI} \begin{bmatrix} q_1 \\ q_2 \end{bmatrix} \quad (6.15)$$

$$P_{MO} = \begin{bmatrix} 0 & 0 & 1 \\ 1 & 0 & 0 \end{bmatrix} G \Rightarrow \begin{bmatrix} p_2 \\ \dot{x}_a \end{bmatrix} = P_{MO} \begin{bmatrix} q_1 \\ q_2 \end{bmatrix} \quad (6.16)$$

If considering figure 6.2, then for the case where  $\dot{x}_a > 0$  the plant  $P_{MI}$  corresponds to controlling a cylinder by meter-in and the plant  $P_{MO}$  corresponds to controlling a cylinder by meter-out. In the following, the RGAs of these plants are analysed as a function of frequency, actuator position and load force to search for a conclusion whether one should select meter-in or meter-out for a given load condition. To limit the parameter space the main boom + jib length is set equal to 5 [m]. The following notation is used

$$\Lambda(P_{MI}) = \begin{bmatrix} \lambda_{MI11} & \lambda_{MI12} \\ \lambda_{MI21} & \lambda_{MI22} \end{bmatrix} \quad (6.17)$$

$$\Lambda(P_{MO}) = \begin{bmatrix} \lambda_{MO11} & \lambda_{MO12} \\ \lambda_{MO21} & \lambda_{MO22} \end{bmatrix} \quad (6.18)$$

Recall that the RGA of a square plant is symmetric, thus for the  $2 \times 2$  plants only two of the RGA elements needs attention, to decide whether the plant is diagonally dominant or not. Consider first the RGA as a function of frequency, then figures 6.7 and 6.8 show that the RGA elements are approximately constant up to resonance. The plots have been made for the case where the load force is negative, with pressure levels  $p_1 = 110$  [bar] and  $p_2 = 10$  [bar], see figure 6.2. The actuator stroke has been chosen as half of the full stroke whereby the volumes on each side of the piston are equal.

Figure 6.7 shows that the meter-in plant,  $P_{MI}$ , have the largest elements along the diagonal and is "decoupled" for the considered load direction. Figure 6.8 shows that if trying to control the velocity with the valve connected to the low pressure side yields a plant with interactions, as the off-diagonal elements are larger than the diagonal elements. This suggests that we should always control the velocity by the valve associated with the high pressure side. For reversing load directions and use with a diagonal control structure, this requires a controller shift while the controlled actuator/load is in motion. Such a shift is undesirable as it may induce oscillations in the system. Further insight into the variation of the RGA elements are gained by considering the steady state RGA.



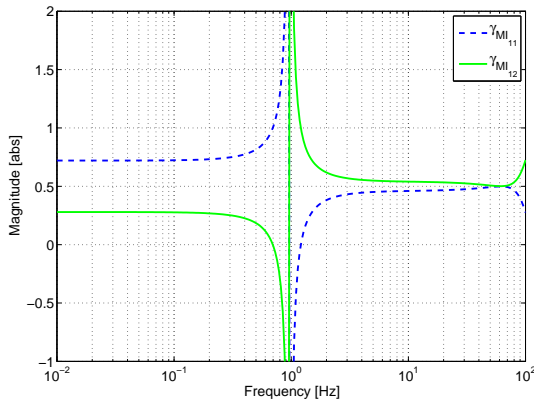


Figure 6.7: RGA elements of  $P_{MI}$ .

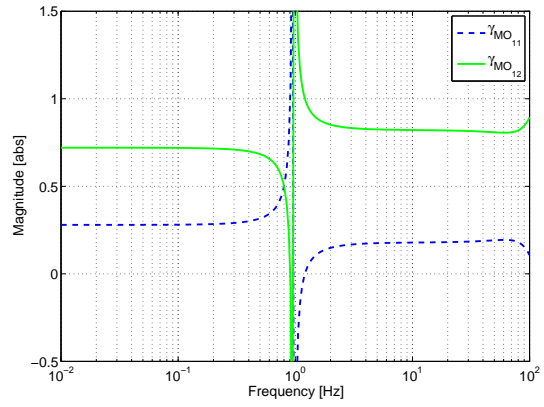


Figure 6.8: RGA elements of  $P_{MO}$ .

For the two considered plants these are given by

$$\Lambda(P_{MI}(j0)) = \frac{1}{\beta_{10}V_{20} + \alpha^2\beta_{20}V_{10}} \begin{bmatrix} \beta_{10}V_{20} & \alpha^2\beta_{20}V_{10} \\ \alpha^2\beta_{20}V_{10} & \beta_{10}V_{20} \end{bmatrix} \quad (6.19)$$

$$\Lambda(P_{MO}(j0)) = \frac{1}{\beta_{10}V_{20} + \alpha^2\beta_{20}V_{10}} \begin{bmatrix} \alpha^2\beta_{20}V_{10} & \beta_{10}V_{20} \\ \beta_{10}V_{20} & \alpha^2\beta_{20}V_{10} \end{bmatrix} \quad (6.20)$$

Since  $\beta_{10} > \beta_{20}$  for  $p_{10} > p_{20}$  and  $\beta_{10} < \beta_{20}$  for  $p_{10} < p_{20}$ , and since the effective bulk modulus is a function pressure level, it may be seen that the steady state RGA elements depend on the direction and size of the load force. The steady state RGA elements also depend on cylinder position due to the volumes  $V_{10}$  and  $V_{20}$ . The variation is illustrated by figures 6.9 and 6.10. The plots are made for a 10 [bar] back pressure and a variable load force giving a pressure from 10 [bar] to 110 [bar] in the opposite pressure chamber.

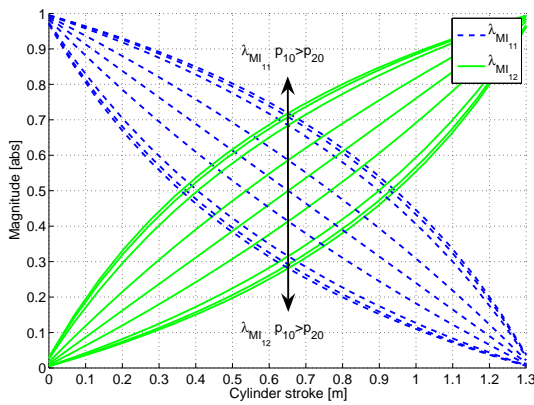


Figure 6.9: Steady state RGA elements of  $P_{MI}$ .

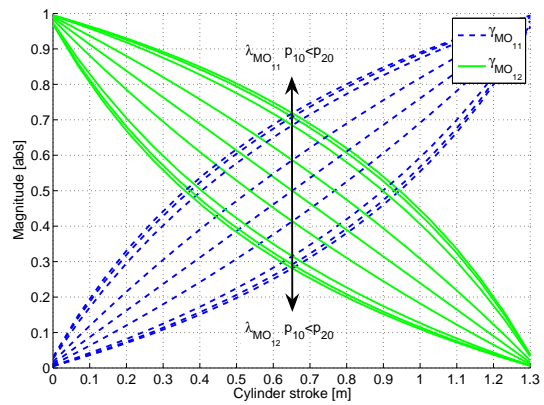


Figure 6.10: Steady state RGA elements of  $P_{MO}$ .

The figures should read in the way that the closer  $\lambda_{MI11}$  is to 1, the closer is the plant  $P_{MI}$  to being decoupled at steady state. The closer  $\lambda_{MO11}$  is to 1, the closer is the plant

$P_{MO}$  to being decoupled at steady state. The arrows mark the directions in which the steady state RGA elements increase or decrease. For example, with reference to figure 6.9,  $\lambda_{MI11}$  increases when  $p_{10}$  increases compared to  $p_{20}$ .

What is learned from the above is that due to changing cylinder volumes and changing load direction, the hydraulic actuator system is not decoupled, and interestingly, decoupling is not necessarily obtained by always controlling the velocity with the valve associated with the high pressure side of the actuator, although it is the preferred option as it gives the least interaction. Therefore, other means of decoupling may be necessary to apply decentralised controllers. Regarding whether meter-in or meter-out should be applied for a given load direction cannot be concluded as it depends on the volumes associated with a specific actuator.

As may be seen from the steady state RGAs in (6.19) and (6.20), the main reason for the off diagonal interaction is that the hydraulic capacitances vary. To apply effective decoupling, this motivates the use of a sensor for measuring the piston rod position of the actuator. The position measurement in combination with pressure measurements gives the ability to estimate the hydraulic capacitances, when cylinder parameters are known. For a rotational hydraulic motor the pressurised volumes associated with the work ports do not change, and position measurements are thus not necessary to establish an estimate of the hydraulic capacitances. Fortunately, there are other means than piston rod position measurement to decoupling of the hydraulic actuator system, as will be shown in the following.

### 6.5.2 Pseudo SISO control strategy for meter-in

A decentralised pressure control structure for meter-in may be written on block diagram form as shown in figure 6.3. A pressure control strategy for this decentralised control structure may be chosen as

$$q_{2r} = \text{sat}_q(K_P(t)(p_{min} - p_1)) \quad (6.21)$$

where

$$\text{sat}_q(u) = \begin{cases} 0 & , u > 0 \\ u & , -q_{max} \leq u \leq 0 \\ -q_{max} & , u < -q_{max} \end{cases}$$

This pressure control strategy on block diagram form is sketched in figure 6.11

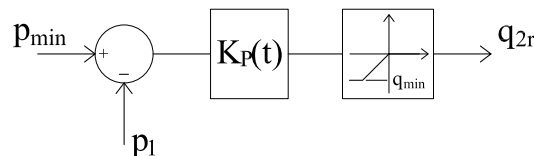


Figure 6.11: Pseudo SISO control strategy for meter-in.

Referring to figure 6.2, we first consider the case where  $f_l < 0$ . Then, the pressure control strategy works in the way that when  $p_1$  increases, the error for the pressure controller decreases and for  $p_1 > p_{min}$  the reference for the pressure controller is negative. However, as negative pressures cannot occur, the pressure controller will saturate the control valve  $v_2$ , when the negative reference for the the pressure controller becomes small enough. Thus,  $v_2$  will open up fully the connection between the chamber carrying the pressure  $p_2$  and the drain line. When  $v_2$  is saturated only the control variable for  $v_1$  is active and the control system becomes a SISO meter-in control system. The pressure level which will saturate  $v_2$  depends on the chosen pressure controller.

If  $f_l > 0$ , then the error for the pressure controller is zero when  $p_1 = p_{min}$ . The pressure controller will therefore try to maintain  $p_1 = p_{min}$ , whereby overrunning of the load is avoided. For this case the control strategy is multivariable.

**6.5.2.1 Controller design for  $f_l < 0$**

Consider again the case where  $f_l < 0$  and where  $v_2$  is saturated. This corresponds to omitting the lower branch of the block diagram in figure 6.5, which is associated with  $p_2$ . Doing this and multiplying the input by the actuator area and the valve dynamics, and multiplying the output with the load dynamics gives the block diagram in figure 6.12.

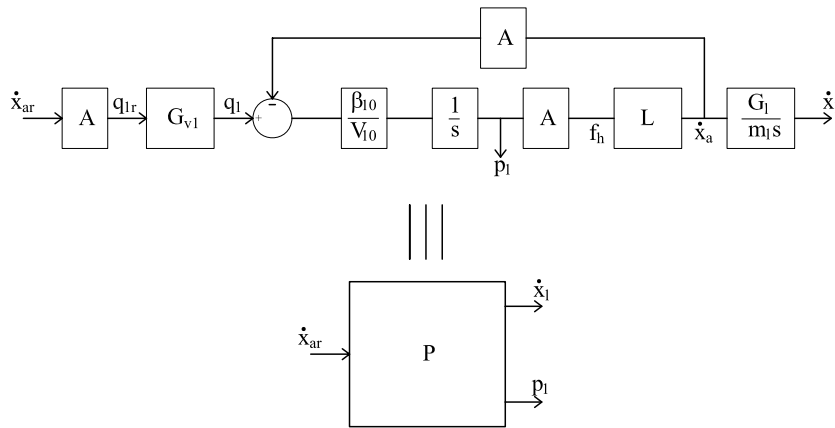


Figure 6.12: Linear block diagram of hydraulic actuator system with load when  $v_2$  in figure 6.2 is saturated.

The plant  $P$  may be obtained from the transfer matrix  $G$  in equation (6.12), by setting  $\alpha = 0$  and selecting weights as

$$P = \begin{bmatrix} p_{11} \\ p_{21} \end{bmatrix} = W_O G W_I \quad W_I = \begin{bmatrix} A G_{v1} & 0 \\ 0 & 0 \end{bmatrix} \quad W_O = \begin{bmatrix} \frac{G_l}{m_l s} & 0 & 0 \\ 0 & 1 & 0 \end{bmatrix} \quad (6.22)$$

The transfer function  $p_{11}$  relates the operator velocity reference to the load velocity. The frequency response of  $p_{11}$  associated with base rotation axis of the loader crane

depends on the jib length and the cylinder position. For different jib lengths and cylinder positions, a set of frequency responses are obtained. These are shown in figure 6.13. The lowest resonance frequency for the base rotation axis is  $0.27 \text{ [Hz]}^2$ .

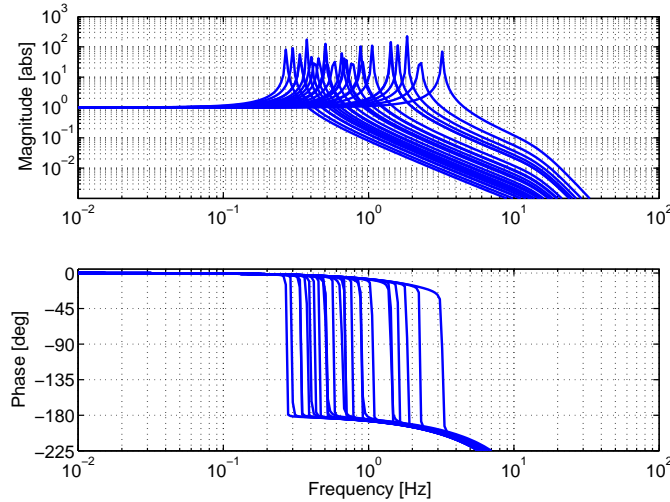


Figure 6.13: Frequency response of  $p_{11}$  associated with base rotation axis.

It may be seen from the figure that the damping of the system is low, and a simulation will verify that the resulting time response is not satisfactory. To improve the response, a phase lead compensator may be inserted in the feedforward path of the block diagram in figure 6.12.

The block diagram in figure 6.14a shows how a lead compensator is implemented by feeding back the actuator pressure through a high pass filter. It may be easier to see that this is a lead filter from the mathematically equivalent implementation in figure 6.14b<sup>3</sup>.

The lead compensator is described by the parameters  $\tau_{fd_1}$  and  $k_{pd_1}$ . Assuming that the valve dynamics  $G_{v_1} \approx 1$  at frequencies of interest, the feedforward dynamics inside the loop of figure 6.14a becomes

$$g_{ol} = \frac{s + \frac{1}{\tau_{fd_1}}}{s + \frac{1+k_{pd_1} \frac{\beta_{10}}{V_{10}}}{\tau_{fd_1}}} \frac{\beta_{10} AL}{V_{10} s} \quad (6.23)$$

To improve the response, the phase lead must be effective from below the frequency where  $\omega_{180} = \angle \left( \frac{\beta_{10} AL}{V_{10} j \omega_{180}} \right) = -180^\circ$ , hence  $\frac{1}{\tau_{fd_1}} < \omega_{180}$ , which is below the lowest resonance frequency of the system. The gain  $k_{pd_1}$  determines the frequency up to which the phase lead is effective. This frequency should be chosen above the resonance frequencies of the system.

<sup>2</sup>For the main lift axis the lowest resonance frequency is  $0.32 \text{ [Hz]}$ .

<sup>3</sup>The block diagram in figure 6.14b has no physical meaning, as the signal used for feedback cannot be measured.

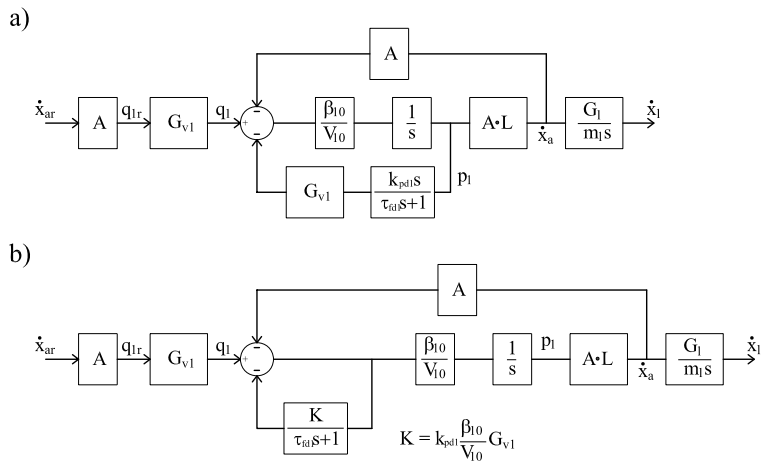


Figure 6.14: Implementations of lead compensator.

The frequency response of the system in figure 6.14a for the base rotation axis of the loader crane is shown in figure 6.15. It may be seen from the figure that the lead compensation has reduced the resonant peaks. Hence a better response may be expected. Simulation result are presented further below.

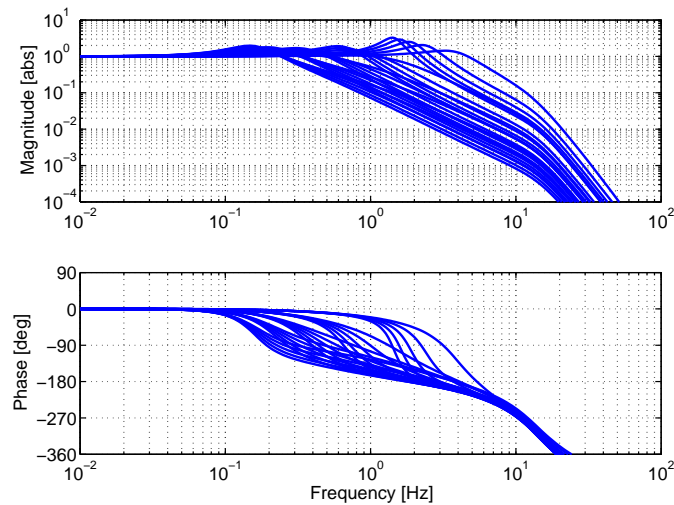


Figure 6.15: Frequency response function from  $\dot{x}_{ar}$  to  $\dot{x}_l$ .

### 6.5.2.2 Controller design for $f_l > 0$

It is desirable not to have a shift of the controller while controlling the plant if the sign of  $f_l$  changes. Therefore, in this section, where a pressure controller is designed for the pseudo SISO control strategy in case  $f_l > 0$ , the plant is considered with the lead compensator in the branch associated with pressure  $p_1$  implemented. The considered plant is sketched in figure 6.16.

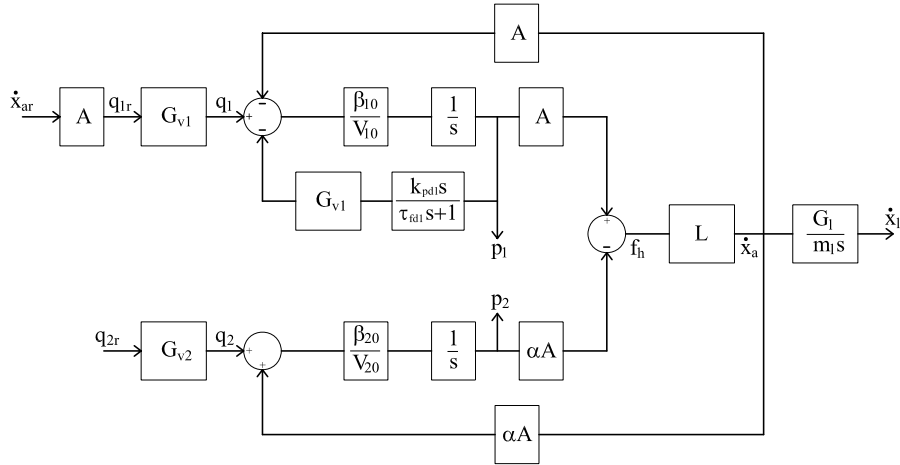


Figure 6.16: Linear block diagram of hydraulic actuator system with lead compensation of the meter-in feedforward path.

In terms of the SSVIM, recall from section 6.3 that a sufficient condition for the stability of a multivariable plant,  $P$ , with a diagonal controller is

$$\bar{\sigma}(\tilde{T}(j\omega)) = \max_i(\tilde{t}_i) < \frac{1}{\mu_{\tilde{T}}(E(j\omega))} \quad \forall \omega \quad E \triangleq (P - \tilde{P})\tilde{P}^{-1} \quad (6.24)$$

Since the plant in figure 6.16 is multivariable, the SSVIM may be used to compute a sufficient upper bound on the complementary sensitivity function, which is associated with the pressure control loop obtained when closing the loop between  $p_1$  and  $q_{2r}$ . To compute the SSVIM, we select the outputs  $p_1$  and  $\dot{x}_a$ . Hereby the following plant is equivalent to that in figure 6.16, when omitting the outputs  $\dot{x}_l$  and  $p_2$

$$\begin{bmatrix} \dot{x}_a \\ p_1 \end{bmatrix} = P \begin{bmatrix} \dot{x}_{ar} \\ q_{2r} \end{bmatrix} \quad P = \mathcal{F}_l(W_O G W_I, K_{d_1}) \quad (6.25)$$

$G$  is the linear plant given by (6.12) and

$$W_I = \begin{bmatrix} A G_{v1} & 0 & -1 \\ 0 & G_{v2} & 0 \end{bmatrix} \quad W_O = \begin{bmatrix} 1 & 0 & 0 \\ 0 & 1 & 0 \\ 0 & 1 & 0 \end{bmatrix} \quad K_{d_1} = G_{v1} \frac{k_{pd1}s}{\tau_{d1}s + 1}$$

Having selected the velocity output as  $\dot{x}_a$ , the upper bound on  $\tilde{T}$  in (6.24) also applies to a velocity control loop, in case the pseudo SISO control strategy is to be extended with closed loop velocity control between  $\dot{x}_a$  and  $\dot{x}_{ar}$ . At low frequencies we require  $|\tilde{t}_i(j\omega)| = 1$  to have good reference tracking. Hence,  $\mu_{\tilde{T}}(E(j\omega)) \leq 1$  to fulfil the sufficient condition in (6.24). The plot of the inverse structured singular value in figure 6.17 shows that this does not hold for all considered operating points. Again the varied variables are the jib length and actuator position. However, implementing a lead compensator in the feedforward path associated with  $p_2$  of the block diagram in figure 6.16 decouples

the plant at low frequencies. This may be done in terms of the linear plant  $G$  in equation (6.12) as

$$\begin{bmatrix} \dot{x}_a \\ p_1 \end{bmatrix} = P \begin{bmatrix} \dot{x}_{ar} \\ q_{2r} \end{bmatrix} \quad P = \mathcal{F}_l(W_O G W_I, K_d) \quad (6.26)$$

where

$$W_I = \begin{bmatrix} A G_{v1} & 0 & -1 & 0 \\ 0 & G_{v2} & 0 & -1 \end{bmatrix} \quad W_O = \begin{bmatrix} 1 & 0 & 0 \\ 0 & 1 & 0 \\ 0 & 1 & 0 \\ 0 & 0 & 1 \end{bmatrix}$$

and

$$K_d = \begin{bmatrix} K_{d1} & 0 \\ 0 & K_{d2} \end{bmatrix} \quad K_{d_i} = G_{vi} \frac{k_{pd_i} s}{\tau_{d_i} s + 1}, \quad i \in \{1, 2\}$$

The inverse structured singular value of the new plant in (6.26) is plotted in figure 6.18, whereby  $\mu_{\tilde{T}}(E(j\omega)) < 1$  at low frequencies. This means that implementing lead compensation for both both work port pressures decouples the multivariable plant, such that the of diagonal interactions are small at low frequencies.

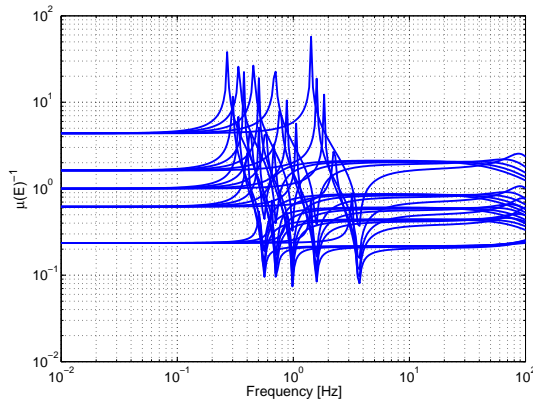


Figure 6.17:  $\mu_{\tilde{T}}(E(j\omega))^{-1}$  for the plant in (6.25).

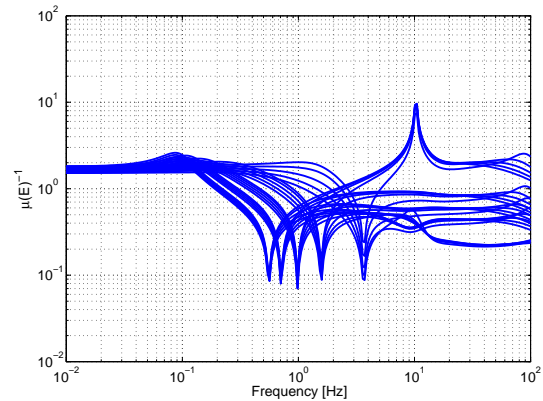
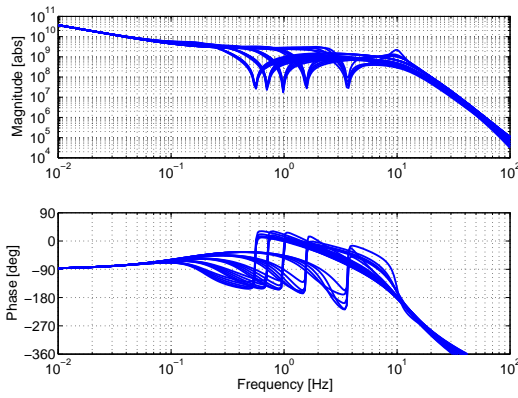
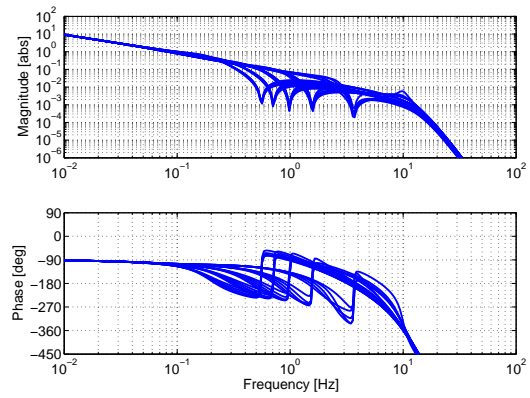
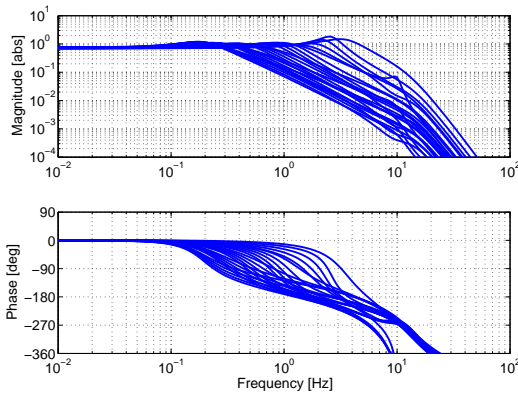
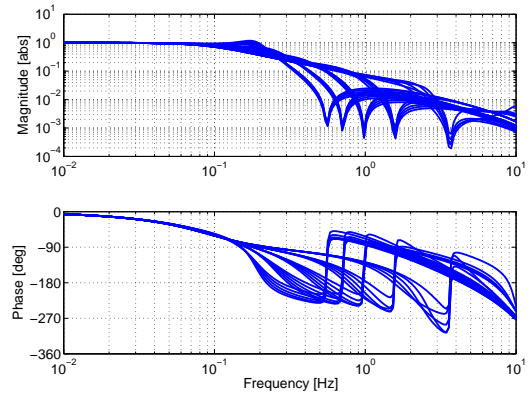


Figure 6.18:  $\mu_{\tilde{T}}(E(j\omega))^{-1}$  for the plant in (6.26).

Having decoupled the system, the pressure controller for  $p_1$  may be designed as a SISO controller. The frequency response of transfer function relating  $q_{2r}$  to  $p_1$  of the plant in (6.26) is plotted in figure 6.19. The dynamics may be considered as made up of an integrator with unmodelled dynamics due to the structural dynamics of the mechanical system. To obtain a loop shape with a roll off rate of -1 at crossover, the following controller is selected

$$K_p = \frac{q_{2r}}{p_{1r} - p_1} = \frac{k_{p1}}{\tau_{p1} s + 1} \quad (6.27)$$

The obtained loop shape is shown in figure 6.20. By closing the pressure control loop, the frequency responses for respectively the velocity control  $\frac{\dot{x}_1}{\dot{x}_{ar}}$  and the pressure control  $\frac{p_1}{p_{1r}}$  may be computed. These are shown in respectively figure 6.21 and figure 6.22.

Figure 6.19: Open loop frequency response function from  $q_{2r}$  to  $p_1$ .Figure 6.20: Open loop frequency response function from  $p_{1r}$  to  $p_1$ .Figure 6.21: Frequency response function from  $\dot{x}_{ar}$  to  $\dot{x}_l$ .Figure 6.22: Closed loop frequency response function from  $p_{1r}$  to  $p_1$ .

The stability of the pressure control loop may be checked using the sufficient condition in (6.24). Which is equivalent to

$$\mu_{\tilde{T}}(E(j\omega))\bar{\sigma}(\tilde{T}(j\omega)) < 1 \quad \forall \omega \quad (6.28)$$

By looping through discrete points in the operating space, it may be seen from figure 6.23 that this is not fulfilled for all operating points. Specifically, the condition is violated as the jib of the loader crane is nearing its full extension, whereby the equivalent inertia load becomes large. By lowering either the gain or the filter frequency of the pressure controller in (6.27) by 25 %, the stability condition may be fulfilled at all the considered operating points. However, the pressure control performance will then be reduced, and as the used stability condition is only sufficient and not necessary, the system may anyway be stable even though the condition is not fulfilled. This is confirmed by the simulation results, which will be presented in section 6.5.5.

The overall control strategy is shown implemented on block diagram form in figure 6.24, where  $G$ ,  $G_{v1}$ ,  $G_{v2}$  and  $\frac{G_l}{m_l s}$  is the plant model derived in section 6.4. It should be noted



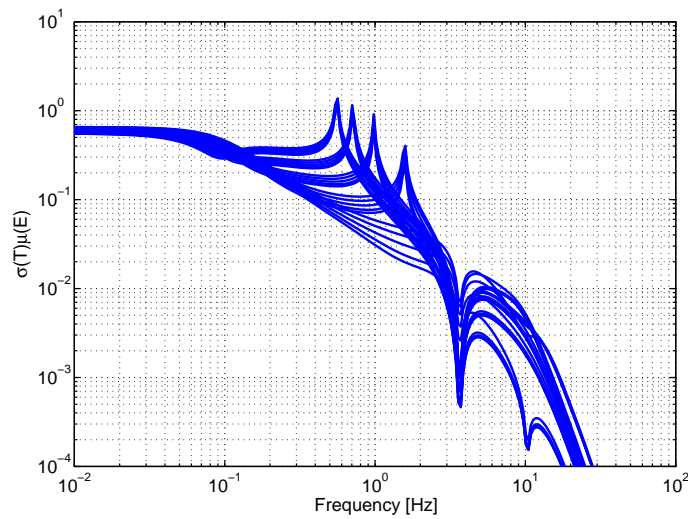


Figure 6.23:  $\mu_{\tilde{T}}(E(j\omega))\bar{\sigma}(\tilde{T})$  for the pseudo SISO control strategy.

that the shown implementation is valid for  $\dot{x}_a > 0$ . For  $\dot{x}_a < 0$ ,  $q_{1r}$  and  $q_{2r}$  as well as  $p_1$  and  $p_2$  must be exchanged.

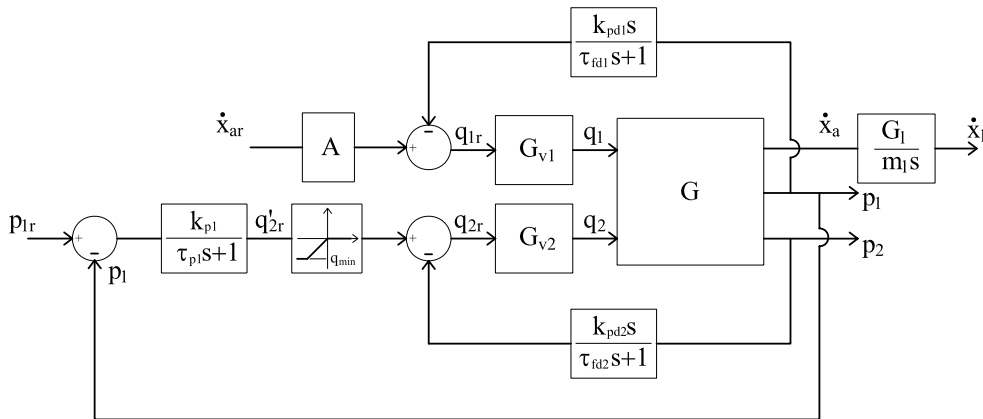


Figure 6.24: Overall pseudo SISO meter-in control strategy implementation with valve and plant dynamics.

### 6.5.3 Pseudo SISO control strategy for meter-out

For a controller structure based on meter-out a sufficient pressure drop across the meter-out orifice must be present to drive the desired flow rate through the orifice. For loads in the same direction as the velocity,  $f_l > 0$  in figure 6.2, the load itself may generate a sufficient pressure drop. If this is not the case, e.g. because  $f_l < 0$ , then the pump must generate the required pressure drop. The E/H load sensing pump controller in figure 6.2 automatically matches the pump pressure to the required load pressure, due to the

electrohydraulic load sensing. Because of this,  $v_1$  may be opened fully while controlling the velocity with  $v_2$ .

Suppose the actuator to the right in figure 6.2 is in control of the pump through the E/H load sensing pump controller. Then controlling the velocity of the left actuator by controlling  $v_2$  will function as a SISO meter-out control scheme. Suppose instead that the left actuator is the highest loaded and therefore is in control of the pump. Then controlling the velocity of the left actuator by controlling  $v_2$ , will, seen from the valve, still be a SISO control problem. However, the true control problem is multivariable. The pressure control loop has just been moved to the E/H load sensing pump controller. Referring to figure 6.4, this corresponds to the pressure controller  $K_P(t, p_1, p_2)$  being integrated in the E/H load sensing pump controller, and to replacing the valve dynamics  $G_{v1}$  by the pump dynamics. The multivariable control structure is therefore the same, whether the pressure control loop is closed with the pump or with the valve<sup>4</sup>.

Consider again the case where the right actuator of figure 6.2 is in control of the pump, and the velocity of the left actuator shall be controlled by  $v_2$ . Then as mentioned the control problem is a SISO control problem. However, a disadvantage is that in case  $f_l > 0$  and the pump pressure is high, for example because  $f_l' < 0$ , then both the pump pressure,  $p_p$ , and the load pressure,  $f_l$ , contribute to raising the pressure drop across  $v_2$ . Therefore, if using this control strategy one must take care that the rated pressure levels of hoses and fittings, as well as the rated pressure drop across  $v_2$  are not exceeded. To circumvent this potential problem a refined meter-out control strategy is considered in the following.

#### 6.5.4 Output selecting pressure control strategy for meter-out

A pressure control strategy for meter-out which circumvents the problem of high pressure drops across the meter-out orifice is sketched by the block diagram in figure 6.25.

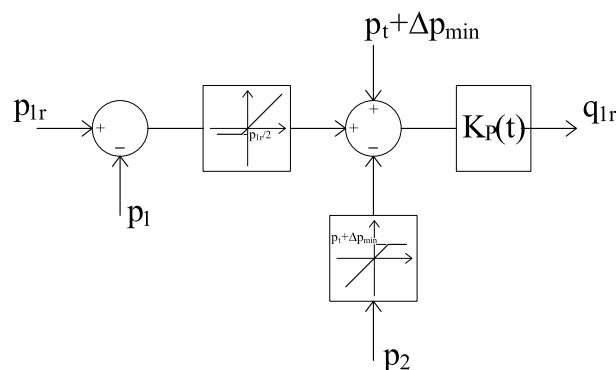


Figure 6.25: Output selecting pressure control strategy for meter-out.

<sup>4</sup>If the pump may operate in flow control mode, such as suggested in section 1.3.1, will simplify the control problem since no pressure control using the pump will then be necessary.

Referring again to figure 6.2, then first the case where  $f_l > 0$  is considered. In this case the pressure  $p_2$  may carry a load such that  $p_2 > p_t + \Delta p_{min}$ . Then the contributions from  $p_t + \Delta p_{min}$  and the measured value of  $p_2$  entering the summation to the right in figure 6.25 outbalance each other due to the saturation in the feedback path of  $p_2$ . A non-zero reference for the pressure controller  $K_P(t)$  will be generated if  $p_1 \neq p_{1r}$  whereby cavitation of the chamber associated with  $p_1$  is avoided.

The lower bounded saturation in the feedforward path of the block diagram only allows values larger than  $-p_{1r}/2$  to pass. Another value for the lower bound may be used as long as its absolute value is smaller than  $\Delta p_{min}$ . If  $f_l < 0$  and the load generates a pressure of  $p_1 > p_{1r}$ , the output of the non-linearity is saturated at  $-p_{1r}/2$ . If at the same time  $p_2 < p_t + \Delta p_{min} - p_{1r}/2$  the error for the pressure controller will be positive due to the right summation. Thus cavitation of the chamber associated with  $p_2$  is avoided.

It should be noted that if  $p_t + \Delta p_{min} - p_{1r}/2 < p_2 < p_t + \Delta p_{min}$ , the reference for the pressure controller is negative, and theoretically the load may drop for  $f_l < 0$ . However, this may be handled by not allowing negative flows for the valve  $v_1$  in figure 6.2, whereby flow may only be metered into the chamber associated with  $p_1$ .

On equation form the pressure control strategy is given by

$$q_{1r} = \begin{cases} K_P(t)(p_{1r} - p_1) & , p_1 \leq \frac{3}{2}p_{1r} \wedge p_2 \geq p_t + \Delta p_{min} \\ K_P(t)(p_t + \Delta p_{min} - p_2 - \frac{1}{2}p_{1r}) & , p_1 \geq \frac{3}{2}p_{1r} \wedge p_2 \leq p_t + \Delta p_{min} \\ 0 & , p_1 > \frac{3}{2}p_{1r} \wedge p_2 > p_t + \Delta p_{min} \\ K_P(t)(p_{min} + p_t + \Delta p_{min} - p_1 - p_2) & , p_1 < \frac{1}{2}p_{1r} \wedge p_2 < p_t + \Delta p_{min} \end{cases} \quad (6.29)$$

#### 6.5.4.1 Controller design

Referring to figure 6.2, then by the described output selecting control strategy for meter-out,  $q_2$  will be in control of  $\dot{x}_a$  and  $q_1$  will be in control of  $p_2$ , when  $f_l < 0$  and  $\dot{x}_a > 0$ . However, this is equivalent to the input/output pairing of the plant  $P_{MO}$  in section 6.5.1. It has therefore already been shown that this input/output pairing does not yield a plant which is decoupled. When  $f_l > 0$  and  $\dot{x}_a > 0$ ,  $q_2$  will still be in control of the velocity, as meter-out is considered, and  $q_1$  will be in control of  $p_1$ . The two considered plants may be written as

$$\begin{bmatrix} p_2 \\ \dot{x}_a \end{bmatrix} = P \begin{bmatrix} q_{1r} \\ \dot{x}_{ar} \end{bmatrix} \quad P = W_O G W_G W_I \quad W_O = \begin{bmatrix} 0 & 0 & 1 \\ 1 & 0 & 0 \end{bmatrix} \quad \text{for } f_l < 0 \quad (6.30)$$

$$\begin{bmatrix} p_1 \\ \dot{x}_a \end{bmatrix} = P \begin{bmatrix} q_{1r} \\ \dot{x}_{ar} \end{bmatrix} \quad P = W_O G W_G W_I \quad W_O = \begin{bmatrix} 0 & 1 & 0 \\ 1 & 0 & 0 \end{bmatrix} \quad \text{for } f_l > 0 \quad (6.31)$$

where

$$W_I = \begin{bmatrix} 1 & 0 \\ 0 & \alpha A \end{bmatrix} \quad W_G = \begin{bmatrix} G_{v1} & 0 \\ 0 & G_{v2} \end{bmatrix}$$

The SSVIM for these two plants are plotted in figures 6.26 and 6.27. In the figures

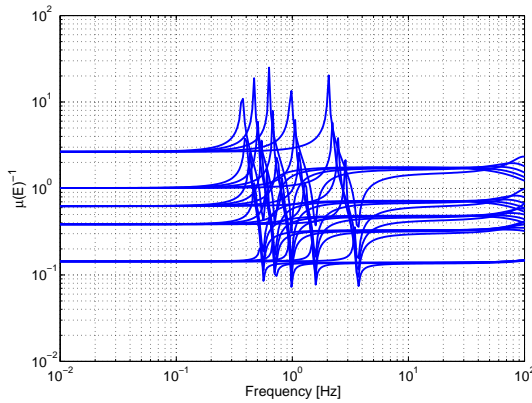


Figure 6.26:  $\mu_{\tilde{T}}(E)^{-1}$  for plant in (6.30)  $p_{10} = 100$  [bar] and  $p_{20} = 10$  [bar] whereby  $f_l < 0$ .

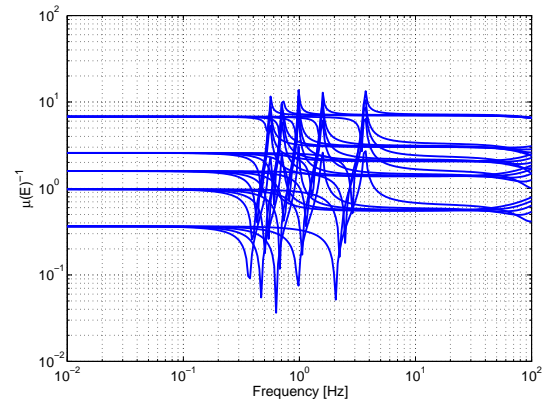


Figure 6.27:  $\mu_{\tilde{T}}(E)^{-1}$  for plant in (6.31)  $p_{10} = 10$  [bar] and  $p_{20} = 100$  [bar] whereby  $f_l > 0$ .

the variation of the peak frequency is primarily due to a variation of the jib length of the loader crane. A variation along the gain axis is primarily due to a variation of the cylinder position. It may be seen from the figures that without decoupling, for some of the cylinder positions, meter-out yields a plant with interactions irrespective of load directions. It may be seen from figure 6.27 that the SSVIM is above 1 at low frequencies for most of the considered work points. Thus the hydraulic actuator system has less interactions, when controlling the velocity by the valve associated with the high pressure side of the actuator, but still decoupling is necessary. These conclusions are the same as derived by the RGA analysis in section 6.5.1.

The same decoupling method by lead compensation as was used for the meter-in pressure control strategy does, however, not work for meter-out. Another method is therefore considered. In steady state the flows through the meter-in and the meter-out valves should intuitively be inverse proportional to each other, by a proportionality factor equal to the area ratio of the actuator. This may be used to obtain a decoupled plant. By exchanging the input weight in equations (6.30) and (6.31) by the following

$$W_I = \begin{bmatrix} 1 & -\frac{1}{\alpha} \\ 0 & \alpha A \end{bmatrix} \quad (6.32)$$

By using this weight the plants are decoupled at low frequencies as may be seen by the plots in figures 6.28 and 6.29.

The frequency response functions of the decoupled plants relating  $\dot{x}_{ar}$  to  $\dot{x}_l$  are undamped, having frequency responses similar to the ones plotted in figure 6.13 for the meter-in strategy. Additional damping of the resonant peaks is therefore necessary to obtain a satisfactory response. Similar to the damping implemented in the previous subsection, this may be done by feeding back the measured pressure through a high pass filter. The first step in doing this is to augment additional inputs and outputs to

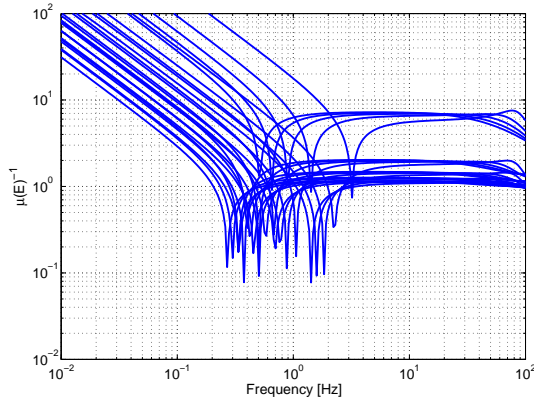


Figure 6.28:  $\mu_{\tilde{T}}(E)^{-1}$  for decoupled plant in (6.30)  $p_{10} = 100$  [bar] and  $p_{20} = 10$  [bar] whereby  $f_l < 0$ .

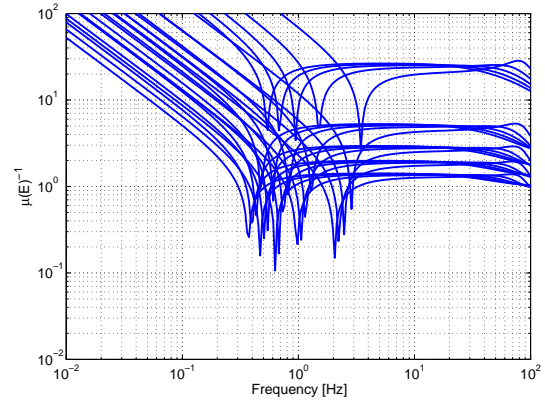


Figure 6.29:  $\mu_{\tilde{T}}(E)^{-1}$  for decoupled plant in (6.31)  $p_{10} = 10$  [bar] and  $p_{20} = 100$  [bar] whereby  $f_l > 0$ .

the plants in (6.30) and (6.31) as

$$\begin{bmatrix} \dot{x}_a \\ p_2 \\ p_1 \\ p_2 \end{bmatrix} = P \begin{bmatrix} \dot{x}_{ar} \\ q_{1r} \\ q_{1d} \\ q_{2d} \end{bmatrix} \quad P = W_O G W_G W_D W_I \quad W_O = \begin{bmatrix} 1 & 0 & 0 \\ 0 & 0 & 1 \\ 0 & 1 & 0 \\ 0 & 0 & 1 \end{bmatrix} \quad \text{for } f_l < 0 \quad (6.33)$$

$$\begin{bmatrix} \dot{x}_a \\ p_1 \\ p_1 \\ p_2 \end{bmatrix} = P \begin{bmatrix} \dot{x}_{ar} \\ q_{1r} \\ q_{1d} \\ q_{2d} \end{bmatrix} \quad P = W_O G W_G W_D W_I \quad W_O = \begin{bmatrix} 1 & 0 & 0 \\ 0 & 1 & 0 \\ 0 & 1 & 0 \\ 0 & 0 & 1 \end{bmatrix} \quad \text{for } f_l > 0 \quad (6.34)$$

where  $q_{1d}$  and  $q_{2d}$  are the extra inputs used for damping and

$$W_I = \begin{bmatrix} 0 & 1 & -1 & 0 \\ \alpha A & 0 & 0 & -1 \end{bmatrix} \quad W_D = \begin{bmatrix} 1 & -\frac{1}{\alpha} \\ 0 & 1 \end{bmatrix} \quad W_G = \begin{bmatrix} G_{v1} & 0 \\ 0 & G_{v2} \end{bmatrix}$$

A diagonal controller is chosen as

$$K_d = \begin{bmatrix} \frac{k_{pd1}s}{\tau_{fd1}s+1} & 0 \\ 0 & \frac{k_{pd2}s}{\tau_{fd2}s+1} \end{bmatrix} \quad (6.35)$$

Whereby the closed loop plant is obtained as

$$P_{cl} = \mathcal{F}_l(P, K_d) \quad \begin{bmatrix} \dot{x}_a \\ p_i \end{bmatrix} = P_{cl} \begin{bmatrix} \dot{x}_{ar} \\ q_{1r} \end{bmatrix} \quad i = \begin{cases} 2 & \text{for } f_l < 0 \\ 1 & \text{for } f_l > 0 \end{cases} \quad (6.36)$$

By multiplying the velocity output of this plant by the transfer function in (6.13), and looping through the operating space, the velocity frequency response functions in figure 6.30 are obtained<sup>5</sup>.

<sup>5</sup>The plot has been made without including the valve dynamics, due to numerical difficulties when computing high order frequency response functions.

Having both decoupled and damped the plant, the remaining step before the output selecting meter-out control strategy is complete, is to implement the pressure controller in  $K_P(t)$ , which is sketched in figure 6.25. The open loop frequency response functions from input  $q_{1r}$  to output  $p_i$  are plotted in figure 6.31 for both  $f_i > 0$  and  $f_i < 0$ .

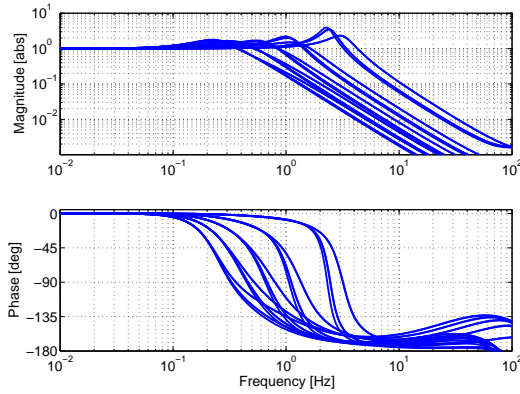


Figure 6.30: Frequency response function from  $\dot{x}_r$  to  $\dot{x}_l$  for  $P_{cl}$ .

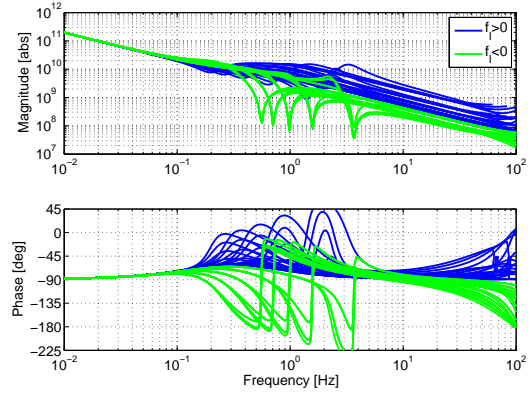


Figure 6.31: Open loop frequency response functions from  $q_{1r}$  to  $p_i$ ,  $i \in \{1,2\}$ .

It may be seen from the figure that the open loop pressure responses are very similar to those in figure 6.19 why the controller in (6.27) is also used for the meter-out control strategy. The closed loop frequency responses of the pressure loop are plotted in figure 6.32

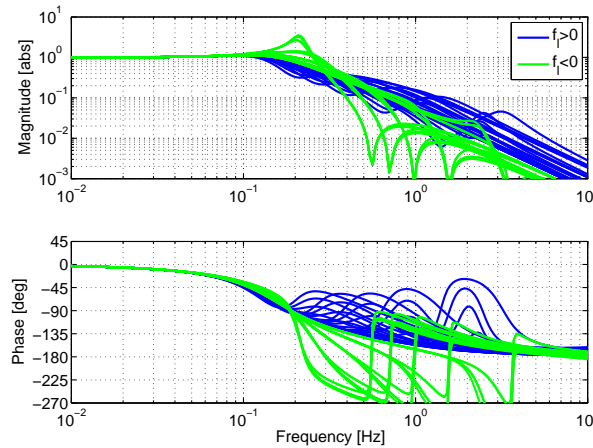


Figure 6.32: Closed loop frequency responses of pressure control loop.

Again the stability of the pressure control loop may be checked by (6.28). The result which is plotted in figures 6.33 and 6.34 shows that the control strategy is stable for both positive and negative loads.

The complete meter-out control strategy with output selection is sketched on block diagram form in figure 6.35, where the shown case corresponds to  $\dot{x}_a > 0$ . For  $\dot{x}_a < 0$

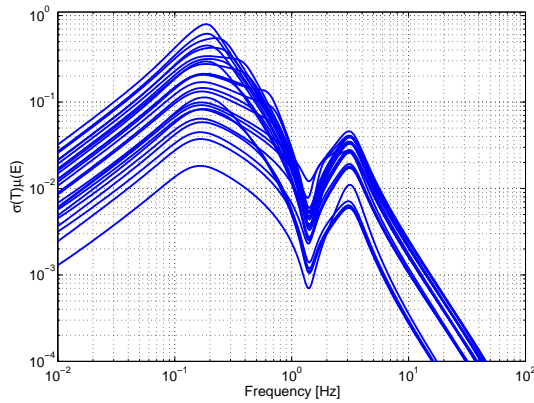


Figure 6.33:  $\mu_{\tilde{T}}(E(j\omega))\bar{\sigma}(\tilde{T}(j\omega))$  for  $f_l > 0$ .

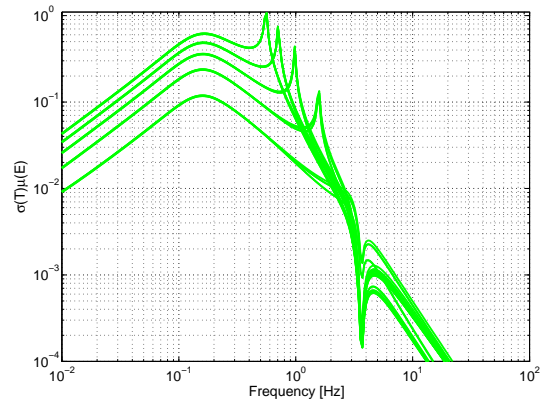


Figure 6.34:  $\mu_{\tilde{T}}(E(j\omega))\bar{\sigma}(\tilde{T}(j\omega))$  for  $f_l < 0$ .

the  $p_1$  and  $p_2$  as well as  $q_1$  and  $q_2$  must be exchanged. The one sided saturations at the output of the valves are included to circumvent the theoretical possibility of load drop as discussed in the introduction to the pressure control strategy in section 6.5.4. Already for the prototype valve the signs of  $q_1$  and  $q_2$  have to be opposite of each other for mechanical reasons.

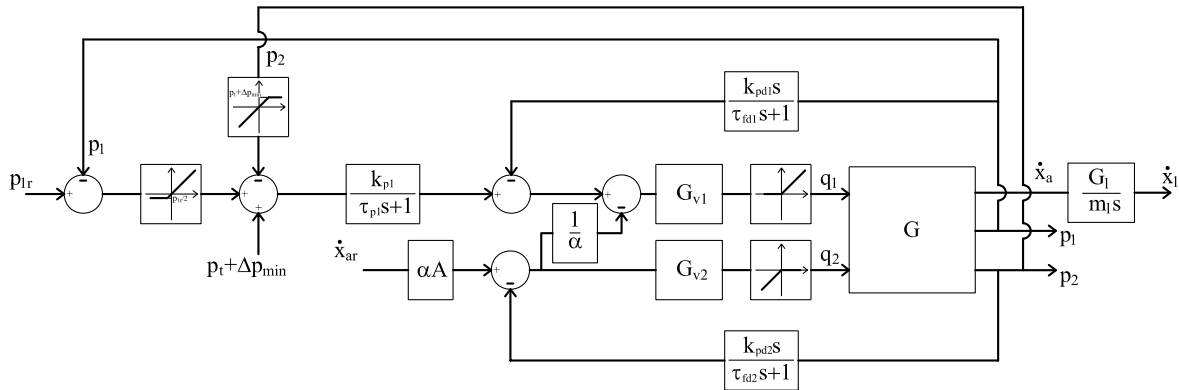


Figure 6.35: Output selecting pressure control strategy for meter-out.

### 6.5.5 Simulation results

The control strategies derived above have been implemented in the non-linear simulation model of the loader crane. Due to numerical efficiency, the linear valve dynamics given by (6.14) has been used for the implementation instead of the non-linear valve model with controllers. In the following, simulation results are presented for the base rotational axis for both meter-in and meter-out. Regarding the implementation of the meter-out scheme, it turned out that the parameters for the pressure controller could be set less conservative than anticipated from the above controller design. The controller

parameters used for obtaining the simulation results are listed in tables A.23 and A.24 of appendix A.

The simulation results obtained using the pseudo SISO meter-in control strategy are shown in figures 6.36 to 6.41. The results are shown pairwise with velocity responses and pressure responses. It should be noted that the load velocity is shown in terms of the equivalent parameters of the model in chapter 5. However, due to the constant transmission ration of the rack and pinion associated with the base rotation, the load velocity relates proportionally to the jib rotation angle. It may be seen from the responses that the control strategy is robust to varying payload and jib length. In the first part of the responses (from 1 to 13 [s]) the meter-in side is associated with the A-port (upper pressure graphs), and in the last part of the responses the meter-in side is associated with the B-port (lower pressure graphs). In the simulations the back pressure reference was set to 10 [bar].

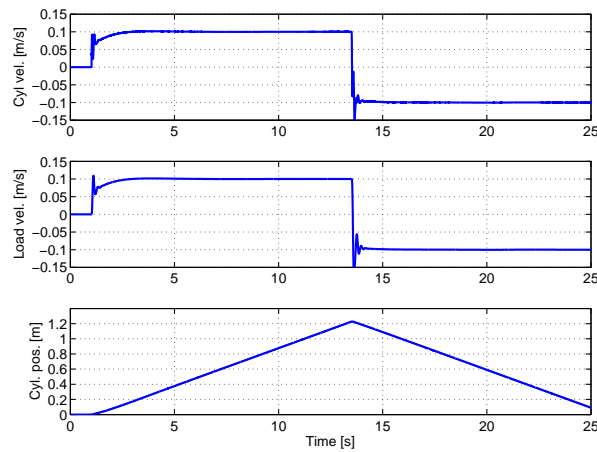


Figure 6.36: Base rotation velocity response, payload 200[kg], jib length 2 [m].

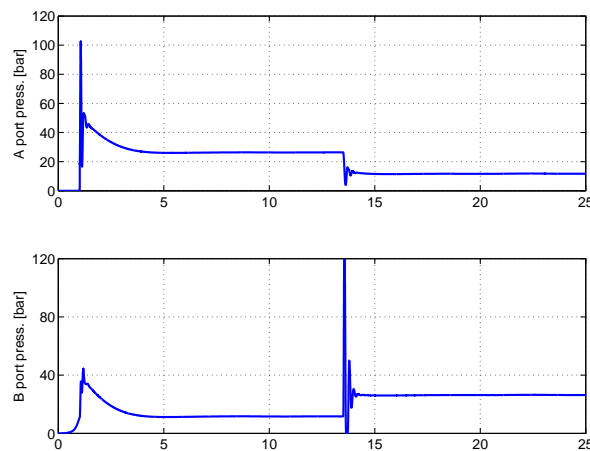


Figure 6.37: Base rotation pressure response, payload 200[kg], jib length 2 [m].



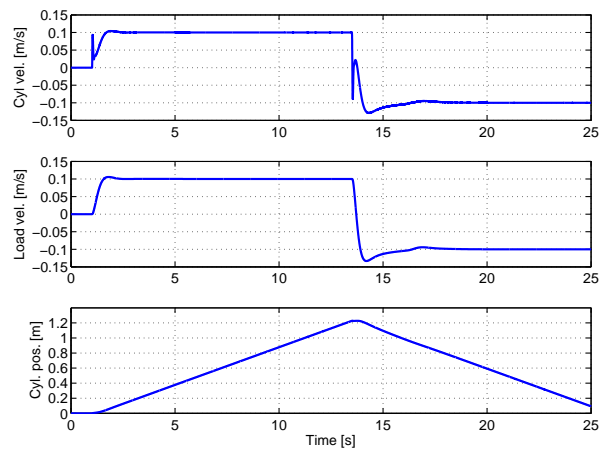


Figure 6.38: Base rotation velocity response, payload 400[kg], jib length 5 [m].

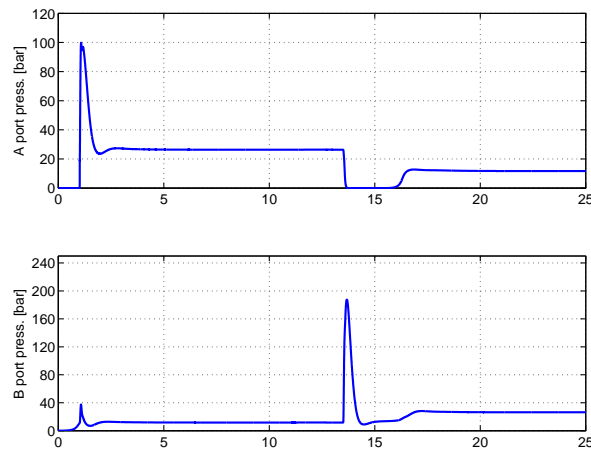


Figure 6.39: Base rotation pressure response, payload 400[kg], jib length 5 [m].

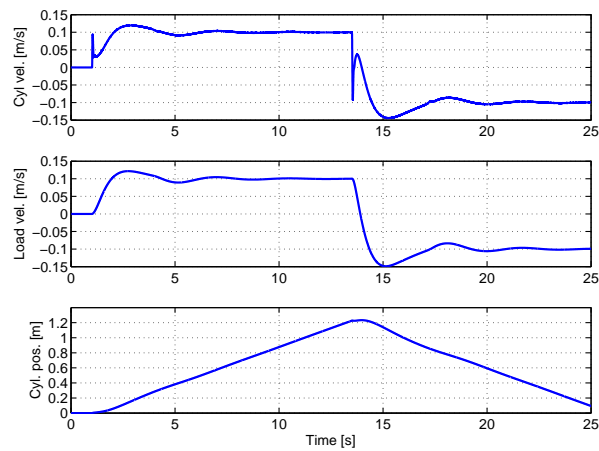


Figure 6.40: Base rotation velocity response, payload 400[kg], jib length 8 [m].

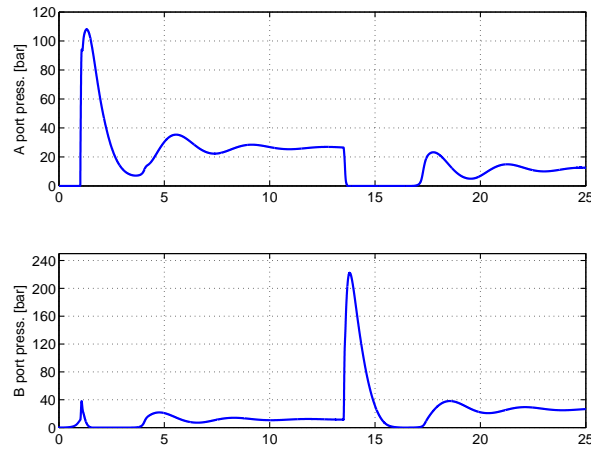


Figure 6.41: Base rotation pressure response, payload 400[kg], jib length 8 [m].

Simulation results obtained by using the meter-out control strategy for operating the base rotational axis are plotted in figures 6.42 to 6.47. In the simulations the meter-out pressure was set to 15 [bar], whereas the minimum pressure level of the non-load carrying side of the chamber was set to 5 [bar]. Since there is no static load on the cylinder associated with the base rotation, the output selecting control strategy simply selects the 15 [bar] reference pressure. This is because at least 15 [bar] must be present at both sides of the cylinder piston, when the piston carries no load. In the first part of the responses the meter-out side is associated with the B-port (lower pressure graph), and in the last part of the responses the meter-out side is associated with the A-port (upper pressure graph).

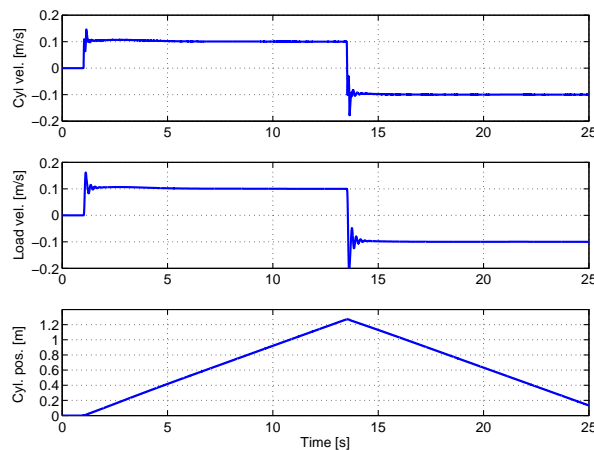


Figure 6.42: Base rotation velocity response, payload 200[kg], jib length 2 [m].

It may be seen that the pressure controller maintains 15 [bar] in the meter-out side at steady state. However, it should be noticed that by accelerating the load at the 1 [s] mark of the responses, the meter-out pressure is low. The electrohydraulic pressure compensation scheme developed in chapter 4 will not work below a certain threshold

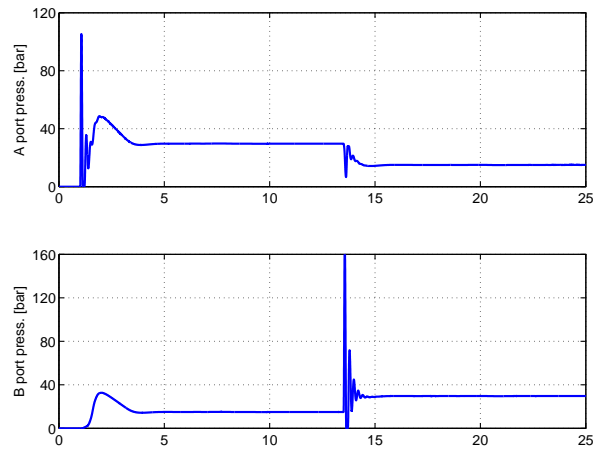


Figure 6.43: Base rotation pressure response, payload 200[kg], jib length 2 [m].

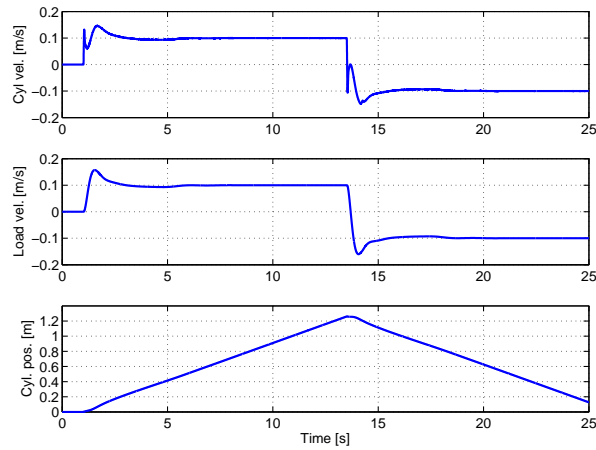


Figure 6.44: Base rotation velocity response, payload 400[kg], jib length 5 [m].

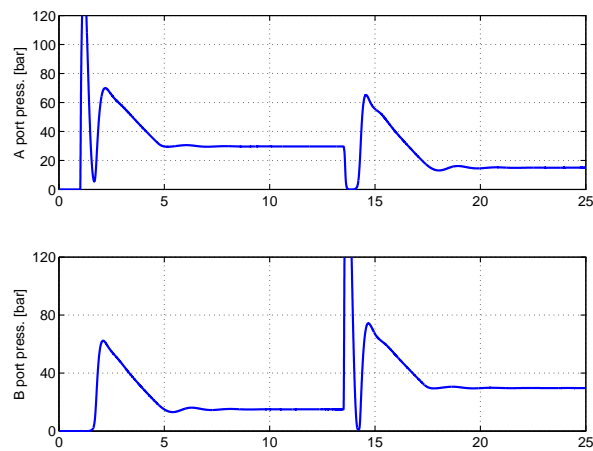


Figure 6.45: Base rotation pressure response, payload 400[kg], jib length 5 [m].

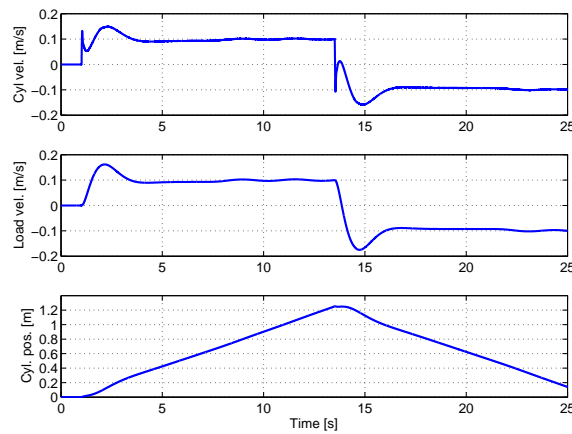


Figure 6.46: Base rotation velocity response, payload 400[kg], jib length 8 [m].

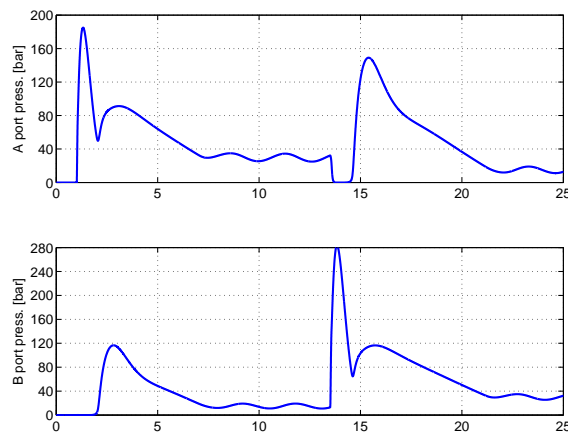


Figure 6.47: Base rotation pressure response, payload 400[kg], jib length 8 [m].

pressure, thus velocity cannot be controlled by meter-out. Due to the decoupling weight given by (6.32) it is possible to accelerate the load by the meter-in flow. Therefore, the pump pressure controller should be implemented, such that the meter-in pressure is selected as reference for the pump if the meter-out pressure drops below the required threshold. Otherwise, there will not be sufficient pressure available to accelerate the load. In the shown simulation results insufficient pressure is not a problem because the linear valve dynamics is used instead of the non-linear valve model. The robustness of the meter-out control strategy to varying payload and jib length is equally good to that of the meter-in strategy. However, the pressure peaks as well as the static pressure level are larger for the meter-out strategy than for the meter-in strategy.

Due to the fact that the gravitational loads on the main lift cylinder of the loader crane is always in the same direction, it is most appropriate to use meter-in when lifting the jib and meter-out when lowering the jib. This is due to the fact that from section 6.5.1 it basically yields a better decoupling of the plant to control the velocity by the valve associated high pressure side of the cylinder. The two control strategies presented above may thus be combined, without risking undesired dynamic behaviour at controller shift.

The latter is because control structure shift is only necessary when the reference velocity is zero. Such a combined control strategy has been implemented in the simulation model of the main lift axis of the loader crane. Simulation results obtained by the combined control strategy are shown in figures 6.48 to 6.53. The non-linear transmission ratio between the cylinder stroke and the jib rotation may be seen by comparing the cylinder stroke to the angular velocity of the jib.

From the pressure responses it may be seen that the pseudo SISO control strategy saturates the valve associated with the non-load carrying side of the actuator as expected. This is because the load carried by the meter-in side of the cylinder gives a pressure which is larger than the threshold for minimum pressure, which for the given case was set to 5 [bar]. When reversing the velocity sufficient pressure to generate the flow across the meter-out valve is generated by the load. Therefore, the output selecting meter-out control strategy keeps the pressure in the non-load carrying side of the cylinder at the 5 [bar] threshold value as expected.

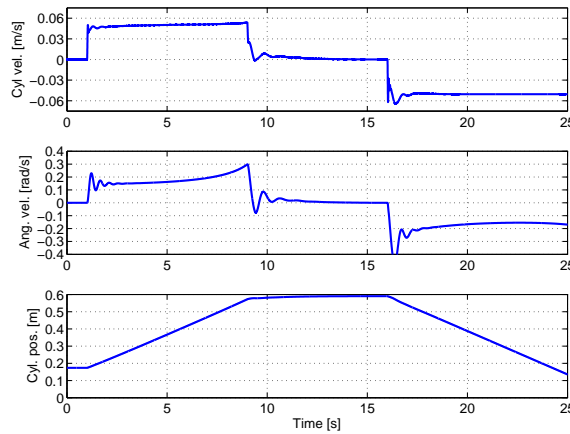


Figure 6.48: Main lift velocity response, payload 200[kg], jib length 2 [m].

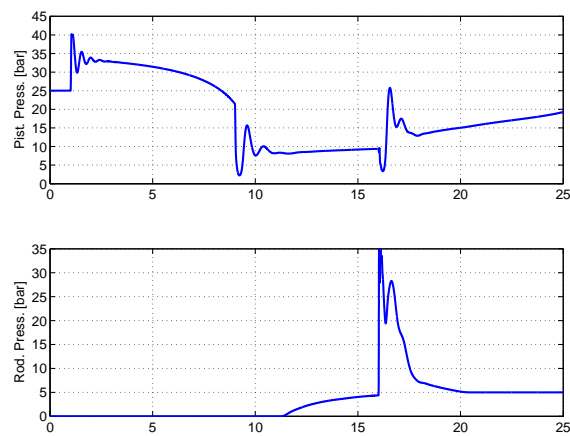


Figure 6.49: Main lift pressure response, payload 200[kg], jib length 2 [m].

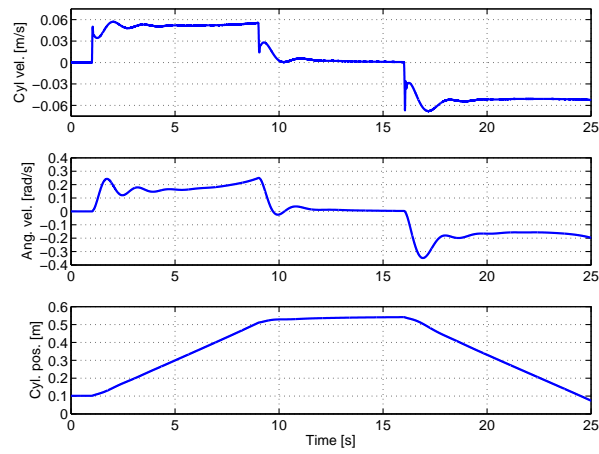


Figure 6.50: Main lift velocity response, payload 400[kg], jib length 5 [m].

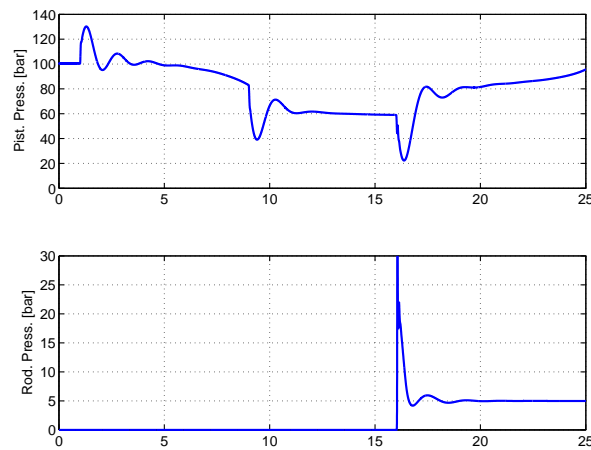


Figure 6.51: Main lift pressure response, payload 400[kg], jib length 5 [m].

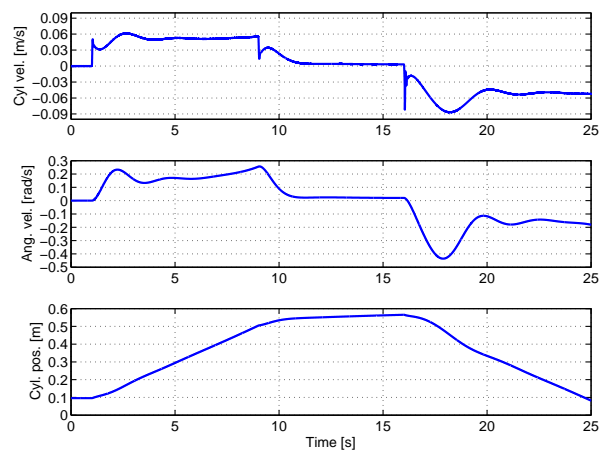


Figure 6.52: Main lift velocity response, payload 400[kg], jib length 8 [m].

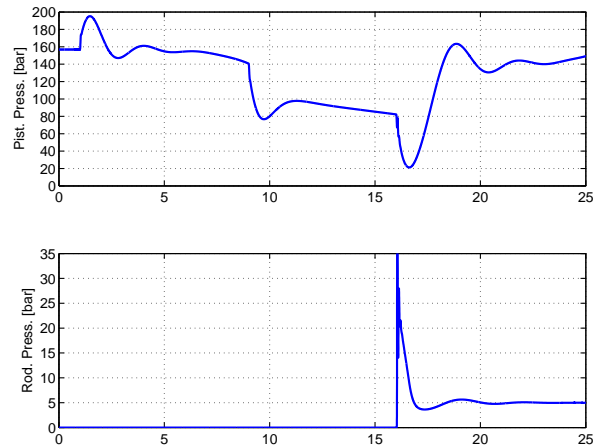


Figure 6.53: Main lift pressure response, payload 400[kg], jib length 8 [m].

## 6.6 Summary and conclusion

This chapter has been concerned with the development of two multivariable control strategies for combined pressure and velocity control, for the use with a conventional pressure controlled variable load sensing pump.

First the concept of decentralised control was introduced and the necessity of decoupling was explained. With the purpose of obtaining the best energy efficiency, qualitative objectives for the pressure control strategy were stated.

Next a linearised model of the generic actuator model developed in chapter 5 was derived. Instead of including input uncertainty in the model, a linear high order valve model was used as input weight. The main downside of doing this is that low frequency gain uncertainty is not captured by the model description. The Relative Gain Array (RGA) and the Structured Singular Value Interaction Measure (SSVIM) were introduced, and used in the remain part of the chapter for analysing plant interaction and controller stability.

It was found that it is advantageous to control the velocity of a hydraulic actuator by the valve associated with the high pressure side of an actuator, as basically a hydraulic actuator system is less interactive for this input output choice. For cylinders it was shown that even though this is done, one cannot always obtain a decoupled plant and additional decoupling is necessary.

Two different means of plant decoupling for respectively a meter-in and a meter-out control strategy was introduced, and controllers for the strategies were developed. Simulation results obtained by implementing the control strategies in the non-linear simulation model of the loader crane were presented. Regarding the base rotational axis, where no static load is carried, it was found that the meter-in and the meter-out control strategies were equally robust to variations of payload and jib length. The meter-in control strategy is the preferred one for the particular control problem (control of the base

rotation), because of the better pressure response and the potentially simpler implementation of the pump pressure control scheme. Regarding the main lift axis a combined meter-in/meter-out control strategy was found to be beneficial.

In general all presented simulation results look promising. However, a scientific dissertation should preferably contain experimental results to support what has been found from numerical simulations. Within the time frame of this Ph.D. project it has unfortunately not been possible to verify the multivariable control strategies presented in this chapter. In the authors opinion all major precautions regarding the dynamics considered in the controller design have been taken, and additionally, the suggested controllers are of low order. These facts increase the chance of an experimental test of the controllers to turn out positive. Obviously, a verification is the first choice for further work after finishing the writing of this dissertation.





# Chapter 7

## Conclusion and recommendations for further work

### Contents

---

7.1	Summary of work . . . . .	193
7.2	Contributions . . . . .	194
7.3	Recommendations for further work . . . . .	195

---

### 7.1 Summary of work

This dissertation has been concerned with concept development and control of a separate meter-in separate meter-out valve for mobile fluid power applications. In chapter 1 a motivation for the research was given by explaining some of the benefits that a programmable separate meter-in separate meter-out valve offers. Secondly the demarcation of the research was outlined.

Chapter 2 was concerned with the objectives that a valve manufacturer puts up for the evaluation of a separate meter-in separate meter-out valve on a conceptual level. Additionally, *The Company's* priorities regarding valve concept selection was explained. Taking the basis in these priorities and an internal confidential market analysis, existing state of the art separate meter-in separate meter-out concepts for a single valve section were evaluated. New ideas regarding other separate meter-in separate meter-out valve concepts were presented and compared to the existing state of the art concepts and ideas. A valve concept driven by voice coil actuators was selected for further study.

In chapter 3 a parametric non-linear simulation model of the selected valve concept was presented. The model included Coulomb friction, viscous damping associated with the spool and the voice coil actuator, leakage, spool overlap and pressure dynamics of the pilot circuit. The dynamics of the electrical system associated with the voice coil actuator was not included, due to the actuator being current controlled. The model was verified experimentally using a prototype of the selected separate meter-in separate

meter-out valve, and weak points of the model were discussed. Next a linearised model was derived with the purpose of being used for controller design of the subsequent chapter. Chapter 3 was closed by giving further insight into the interactions between the main valve and the pilot valve, which may occur when these valves share a common drain line.

Chapter 4 was concerned with the development of electrohydraulic pressure compensation for a single spool of the separate meter-in separate meter-out valve. The influence from pressure sensor inaccuracy on the flow control accuracy of the considered pressure compensation method was explained. With basis in the measured flow control accuracy of existing state of the art proportional valves, steady state flow control accuracy requirements were established. The trade-off between the valve bandwidth and the pressure dynamics of a controlled application was explained. Spool position controllers were designed for two different pilot operation principles, being a pilot valve generating pressure and a pilot valve generating flow. Additional robust controller design for the valve with the flow generating pilot valve was carried through. A parameter sensitivity analysis of the developed controllers was carried out. Experimental test results obtained by implementing the controllers on the prototype valve were presented.

Chapter 5 presented a simplified model of a loader crane for which separate meter-in separate meter-out controllers should be developed. The main assumption which was made to develop the model was that the structural flexibility could be modelled by a single structural vibration mode. This assumption was partly supported by experimental results presented in an accompanying appendix.

Chapter 6 addressed the design of two decoupling control strategies for combined pressure and velocity control. The necessity of plant decoupling when using decentralised controllers was explained. It was shown that interactions between the velocity control loop and the pressure control loop may occur as the volumes of the actuator changes relative to each other. On this basis it was argued that an actuator position measurement was desirable to decouple the two control loops. Due to the lack of actuator position measurements on the considered loader crane, other means for decoupling was used. From simulation studies the developed controllers proved to be robust to parameter variations.

## 7.2 Contributions

The main contributions of this work are outlined below. This work has:

- Established an overview of state of the art within separate meter-in separate meter-out control of hydraulic actuators.
- Provided several valve concepts which are suitable as a platform for future programmable proportional valves.
- Established and verified a comprehensive parametric model of a generic pilot op-

erated spool valve, which may be used for evaluating specific trade-offs in design work. The model includes all major types of uncertainties in spool valves.

- Contributed to the understanding of interaction between the pilot spool and the main spool of the generic pilot operated spool valve by the presence of long fluid lines.
- Analysed the stability of a spool valve with pressure control pilot and highlighted the major design parameters which affects the stability.
- Explained the influence of including a dead-zone in the pilot valve, of the generic spool valve concept, by using a simplified frequency domain approach.
- Developed and experimentally tested flow controllers for the considered valve and highlighted several performance limiting factors by a robustness analysis.
- Established a simple generic model representation of a loader crane, partly with basis in a more comprehensive model.
- Contributed significantly to the understanding of off-diagonal interactions of hydraulic actuators controlled by separate meter-in separate meter-out .
- Developed two new ways of obtaining decoupled pressure and velocity control of a hydraulic actuator controlled by separate meter-in separate meter-out, and which is connected to a flexible load structure.

### 7.3 Recommendations for further work

The present dissertation reflects the current state of the art on robust controller development for separate meter-in meter-out valves, although it is only a small step forward in this interesting field. Sources for further work includes:

- Development of variable displacement pumps with advanced controllability. This is an important area where further understanding must be gained to make use of the full potential of fluid power systems on mobile machinery.
- Investigation into coordinated control of the overall mobile machine incorporating programmable regenerative functions, for maximum energy efficiency.
- Further investigation into separate meter-in separate meter-out control of other types of applications than loader cranes, and in addition into force and torque control.
- Investigations into the feasibility of using separate meter-in separate meter-out valves along with advanced pump controls for low to medium duty hydraulic transmissions.
- Investigation into benefits of using actuator position measurement for actuator mounted separate meter-in separate meter-out valve solutions.

- Analyse the benefits of using other controllers than those developed. This refers both to the SISO controllers developed in chapter 4 and the MIMO controllers developed in chapter 6.

Naturally the work in this dissertation has also opened up a number of opportunities for laboratory experiments, to refine and test the validity of the developed models and the developed controllers further.

# Appendix A

## Parameter values

In this appendix numerical values for the various parameters used throughout the thesis are listed. Note, parameters are listed in units convenient for typesetting. Therefore parameters which are not in compliance with the SI unit system must be converted before used in the equations of the main thesis.

### A.1 Parameters associated with chapter 3

parameter	value	unit
$A_p$	0	[m <sup>2</sup> ]
$C_{rp}$	5	[ $\mu$ m]
$d_p$	8	[mm]
$f_{cp0}$	0	[N]
$f_{cp1}$	0	[N]
$f_{sp0}$	3	[N]
$k_{vc}$	2000	[m]
$k_{sp}$	3030	[ $\frac{N}{m}$ ]
$L_1$	2	[mm]
$L_2$	4	[mm]
$L_{d1} = L_{d2}$	-5	[mm]
$L_{d3} = L_{d4}$	4	[mm]
$m_p$	$63 \cdot 10^{-3}$	[kg]
$\delta_{x_{p0}}$	$10^{-6}$	[m]
$\Delta_{pa} = \Delta_{pb}$	0.6	[mm]
$\Delta_{ta} = \Delta_{tb}$	0.3	[mm]
$\epsilon_{rp}$	$C_{rp}$	[ $\mu$ m]

Table A.1: Nominal design parameter values for flow control pilot valve.

parameter	value	unit
$A_p$	$\frac{\pi}{4} \cdot 0.0017^2$	[m <sup>2</sup> ]
$C_{rp}$	5	[ $\mu\text{m}$ ]
$d_p$	8	[mm]
$f_{cp0}$	0	[N]
$f_{cp1}$	0	[N]
$f_{sp0}$	3	[N]
$k_{vc}$	2000	[m]
$k_{sp}$	0	[ $\frac{\text{N}}{\text{m}}$ ]
$L_1$	2	[mm]
$L_2$	4	[mm]
$L_{d1} = L_{d2}$	-5	[mm]
$L_{d3} = L_{d4}$	4	[mm]
$m_p$	$63 \cdot 10^{-3}$	[g]
$\delta_{x_{p0}}$	$10^{-6}$	[m]
$\Delta_{pa} = \Delta_{pb}$	0.6	[mm]
$\Delta_{ta} = \Delta_{tb}$	0.3	[mm]
$\epsilon_{rp}$	$C_{rp}$	[ $\mu\text{m}$ ]

Table A.2: Nominal design parameter values for pressure control pilot valve.

parameter	value	unit
$C_{rm}$	7	[ $\mu\text{m}$ ]
$d_m$	18	[mm]
$f_{cm0}$	8	[N]
$f_{cm1}$	4	[N]
$f_{sm0}$	0	[N]
$k_{sm}$	9475	[ $\frac{\text{N}}{\text{m}}$ ]
$m_m$	150	[g]
$L_3$	15	[mm]
$L_4$	4	[mm]
$L_5$	10	[mm]
$L_{d5} = L_{d6}$	15	[mm]
$V_{c0}$	1.5	[cm <sup>3</sup> ]
$\delta_{x_{m0}}$	$10^{-6}$	[m]
$\Delta_a = \Delta_b$	1	[mm]
$\epsilon_{rm}$	$C_{rm}$	[ $\mu\text{m}$ ]

Table A.3: Nominal design parameter values for main valve.

parameter	value	unit
$p_{a0}$	1	[bar]
$V_{a0}$	1	[%]
$\beta_f$	14e8	[Pa]
$\beta_h$	10.8e8	[Pa]
$\kappa$	1.4	[-]
$\nu$	20	[cSt = $10^{-6} \frac{\text{m}^2}{\text{s}}$ ]
$\rho$	870	[ $\frac{\text{kg}}{\text{m}^3}$ ]

Table A.4: Nominal fluid parameter values.

parameter	value	unit
$d_g$	4	[mm]
$h_g$	2	[mm]
$N_g$	2	[-]
$C_{d1} - C_{d4}$	0.54	[-]
$Re_{t1} - Re_{t4}$	1	[-]
$\theta_{q1} - \theta_{q4}$	70	[deg]

Table A.5: Parameters of a single orifice for pilot valve (Round fluid ports).

parameter	value	unit
$C_{d5} - C_{d6}$	0.6	[-]
$Re_{t5} - Re_{t6}$	260	[-]
$\theta_{q5} - \theta_{q6}$	79	[deg]

Table A.6: Orifice parameters for main valve (Rectangular fluid ports).

parameter	value	unit
$C_{rp}$	3-8	[ $\mu\text{m}$ ]
$\Delta_{pa}, \Delta_{pb}$	0.6-0.8	[mm]
$\Delta_{ta}, \Delta_{tb}$	0.3-0.5	[mm]

Table A.7: Ranges for selected parameters which vary due manufacturing tolerances.

parameter	value	unit
$\nu$	5-470	[cSt = $10^{-6} \frac{\text{m}^2}{\text{s}}$ ]

Table A.8: Ranges for selected parameters which vary due operating conditions.

## A.2 Parameters used in chapter 4

parameter	value	unit
$k_0$	1	[-]
$k_1$	1.125/400e5	[ $\frac{1}{\text{Pa}}$ ]
$k_d$	30	[ $\frac{\text{Ns}}{\text{m}}$ ]
$k_p$	5000	[ $\frac{\text{m}}{\text{s}}$ ]
$\tau_{f1}$	$\frac{1}{200\pi}$	[s]
$\tau_{f2}$	$\frac{1}{20\pi}$	[s]

Table A.9: Controller parameters (section 4.3.2).



parameter	value	unit
$k_p$	3000	$\left[\frac{\text{N}}{\text{m}}\right]$
$\Delta t_{max}$	$4 \cdot 10^{-4}$	[m]
$\epsilon_{x_m}$	$10^{-5}$	[m]
$\tau_d$	$\frac{1}{60\pi}$	[s]
$\tau_f$	$\frac{1}{250\pi}$	[s]
$\tau_{ff}$	$\frac{1}{10\pi}$	[s]

Table A.10: Parameters for PLF controller (section 4.4).

parameter	value	unit
$k_{p_{min}}$	2500	$\left[\frac{\text{N}}{\text{m}}\right]$
$k_{p_{max}}$	4000	$\left[\frac{\text{N}}{\text{m}}\right]$
$T_a$	$2 \cdot 10^{-3}$	[s]
$T_i$	$3 \cdot 10^{-5}$	[s]
$\Delta p_{min}$	0	[Pa]
$\Delta p_{max}$	400e5	[Pa]
$\Delta t_{max}$	$4 \cdot 10^{-4}$	[m]
$\epsilon_{x_m}$	$10^{-5}$	[m]
$\tau_d$	$\frac{1}{60\pi}$	[s]
$\tau_f$	$\frac{1}{160\pi}$	[s]
$\tau_{ff}$	$\frac{1}{400\pi}$	[s]

Table A.11: Parameters for G-PILF controller (section 4.7.2).

parameter	value	unit
$k_p$	2000	$\left[\frac{\text{N}}{\text{m}}\right]$
$\tau_d$	$\frac{1}{60\pi}$	[s]
$\tau_f$	$\frac{1}{250\pi}$	[s]

Table A.12: Parameters for  $K_{PL}$  controller (section 4.7.3).

parameter	value
$b_1$	190
$a_1$	100
$a_2$	950
$a_3$	352
$a_4$	34580

Table A.13: Nominal plant parameters for  $G_0$  (section 4.7.3).

parameter	value
$A$	0.30
$M$	300
$\omega_{\Delta}^*$	$120\pi$
$n$	2

Table A.14: Parameters for  $W_m$  (section 4.7.3).

parameter	value
$A$	$10^{-3}$
$M$	1.25
$\omega_{\Delta}^*$	$12\pi$
$n$	1

Table A.15: Parameters for  $W_p$  (section 4.7.3).

parameter	value
$A$	0.05
$M$	1000
$\omega_{\Delta}^*$	$400\pi$
$n$	1

Table A.16: Parameters for  $W_u$  (section 4.7.3).

parameter	value	
$B_{min}$	0.28	$\left[\frac{1}{s}\right]$
$B_{max}$	0.37	$\left[\frac{1}{s}\right]$
$g_0$	5e-6	[m]
$k_S$	1e4	[-]
$\alpha_0$	0	[m]
$\Delta_0$	$\Delta_{ta,b} + 1e - 4$	[m]
$\eta$	3.52	$\left[\frac{N}{s}\right]$
$\tau_d$	$\frac{1}{50\pi}$	[s]
$\tau_f$	$\frac{1}{500\pi}$	[s]

Table A.17: Parameters for plant and F-SM controller (section 4.7.4).

parameter	value	
$k$	1.5	$\left[\frac{N}{m}\right]$
$k_p$	2000	$\left[\frac{N}{m}\right]$
$k_S$	1e4	[-]
$\Delta_0$	$\Delta_{ta,b} + 1e - 4$	[m]
$\tau_d$	$\frac{1}{50\pi}$	[s]
$\tau_f$	$\frac{1}{500\pi}$	[s]

Table A.18: Parameters for plant and MF-SM controller (section 4.7.5).

parameter	value	
$h_0$	1.25	$\left[\frac{N}{m}\right]$
$k_{v_0}$	4	$\left[\frac{l}{min}\right]$
$\omega_b$ (see (4.118))	$50\pi$	$\left[\frac{rad}{s}\right]$
$\zeta$ (see (4.119))	0.8	[-]

Table A.19: Parameters for SM-P controller (section 4.7.6).

### A.3 Parameters used in chapter 5

parameter	value	unit
$\zeta_l$	0.05	[-]
$c_a$	1800	$\left[\frac{\text{kg}}{\text{s}}\right]$
$g$	9.81	$\left[\frac{\text{m}}{\text{s}^2}\right]$
$k_{\tau_0}$	520e3	$\left[\frac{\text{Nm}}{\text{rad}}\right]$
$k_{\tau_1}$	1154e3	$\left[\frac{\text{Nm}}{\text{rad}}\right]$
$m_a$	100	[kg]
$m_p$	400	[kg]
$m_s$	363	[kg]

Table A.20: Common parameters for main lift and base rotational axes.

parameter	value	unit
$\alpha$	1	[-]
$\alpha_b$	$\frac{19}{9}\pi$	[rad]
$A$	122.7	[cm <sup>2</sup> ]
$L_c$	1.3	[m]
$V_{1s}$	0.20	[litre]
$V_{2s}$	16.15	[litre]

Table A.21: Specific parameters for base rotational axis.

parameter	value	unit
$\alpha$	1	[-]
$\alpha_b$	$\frac{19}{9}\pi$	[rad]
$A$	122.7	[cm <sup>2</sup> ]
$L_c$	1.3	[m]
$V_{1s}$	0.20	[litre]
$V_{2s}$	16.15	[litre]

Table A.22: Specific parameters for base rotational axis.

### A.4 Parameters used in chapter 6

parameter	value	unit
$k_{pd1}$	1e-10	$\left[\frac{\text{m}^3}{\text{Pa}}\right]$
$k_{pd2}$	3e-10	$\left[\frac{\text{m}^3}{\text{Pa}}\right]$
$k_{p1}$	0.75e-9	$\left[\frac{\text{m}^3}{\text{Pa}}\right]$
$\tau_{d1}$	$\frac{1}{0.3\pi}$	[s]
$\tau_{d2}$	$\frac{1}{0.3\pi}$	[s]
$\tau_{p1}$	$\frac{1}{0.2\pi}$	[s]

Table A.23: Parameters for pseudo SISO control strategy for meter-in (section 6.5.2).

parameter	value	unit
$k_p d1$	0.5e-10	$\frac{\text{m}^3}{\text{Pa}}$
$k_p d2$	0.5e-10	$\frac{\text{m}^3}{\text{Pa}}$
$k_{p1}$	1e-10	$\frac{\text{m}^3}{\text{Pa}}$
$\tau_{d1}$	$\frac{1}{0.4\pi}$	[s]
$\tau_{d2}$	$\frac{1}{0.4\pi}$	[s]
$\tau_{p1}$	$\frac{1}{0.2\pi}$	[s]

Table A.24: Parameters for output selecting pressure control strategy for meter-out (section 6.5.4).



# Appendix B

## Orifice area equations

In this appendix equations describing the orifice area and the hydraulic diameter as a function of spool position are given, which may be used in the valve model of chapter 3. Equations for two different orifice geometries are given: a spool with a rectangular fluid port and a spool with circular metering notches. To compute the area of the circular metering notches it is assumed that the port geometry is flat.

### B.1 Rectangular fluid port

For a sharp metering land the area and hydraulic diameter as functions of the spool stroke are given by

$$\begin{aligned} A_o(x_l) &= \pi d x_l \\ d_h(x_l) &= \frac{4A_o(x_l)}{2\pi d} \approx 2x_l \end{aligned} \tag{B.1}$$

### B.2 Circular fluid port

For a spool with circular grooves the following area function may be used as approximation (e.g., see figure B.1)

$$A_o(x_l) = \begin{cases} N_g \left( \frac{\alpha_g}{4} d_g^2 - l_g \sqrt{\left(\frac{d_g}{2}\right)^2 - l_g^2} \right) & 0 < x_l \leq h_g \\ N_g \left( \frac{\alpha_{gm}}{4} d_g^2 - l_{gm} \sqrt{\left(\frac{d_g}{2}\right)^2 - l_{gm}^2} \right) + \pi d (x_l - h_g) & x_l > h_g \end{cases} \tag{B.2}$$

where  $\alpha_g = \cos^{-1} \left( \frac{2l_g}{d_g} \right)$ ;  $l_g = \left( \frac{d_g}{2} - x_l \right)$ ;  $\alpha_{gm} = \cos^{-1} \left( 1 - 2\frac{h_g}{d_g} \right)$  and  $l_{gm} = \left( \frac{d_g}{2} - h_g \right)$ .

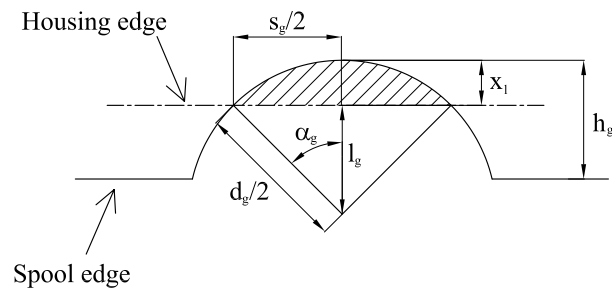


Figure B.1: Circular metering notch, the orifice opening is shown hatched.

The hydraulic diameter may be approximated by

$$d_h(x_l) = \begin{cases} \frac{4A_o(x_l)}{2\pi d + N_g(\alpha_g d_g - s_g)} & 0 < x_l \leq h_g \\ \frac{4A_o(x_l)}{2\pi d + N_g(\alpha_{gm} d_g - s_{gm})} & x_l > h_g \end{cases} \quad (\text{B.3})$$

where  $s_g = \sqrt{d_g^2 - 4l_g^2}$  and  $s_{gm} = \sqrt{d_g^2 - 4l_{gm}^2}$ .

# Appendix C

## Derivation of flow and pressure gains

In this appendix the flow and pressure gains are derived for the following equation describing the flow across a spool valve orifice.

$$q = \begin{cases} \left(1 + \frac{3}{2} \left(\frac{\epsilon_r}{C_r}\right)^2\right) \frac{\pi d_p C_r^3 \Delta p}{12 \mu L_1} & x_l \leq -L_1 \\ -\left(1 + \frac{3}{2} \left(\frac{\epsilon_r}{C_r}\right)^2\right) \frac{\pi d_p C_r^3 \Delta p}{12 \mu x_l} & -L_1 < x_l \leq -10C_r \\ \frac{2}{\mu} d_h(x_l + 10C_r) A_o(x_l + 10C_r) \delta_Q \Delta p + q_0(\Delta p) & Re < Re_t \wedge x_l > -10C_r \\ C_d A_o(x_l + 10C_r) \sqrt{\frac{2}{\rho} |\Delta p|} \text{sign}(\Delta p) + q_0(\Delta p) & Re \geq Re_t \wedge x_l > -10C_r \end{cases} \quad (\text{C.1})$$

Partial differentiation with respect to  $\Delta p$  gives the pressure gain

$$K_p = \frac{\partial Q}{\partial \Delta p} = \begin{cases} \left(1 + \frac{3}{2} \left(\frac{\epsilon_{rp}}{C_{rp}}\right)^2\right) \frac{\pi d_p C_{rp}^3}{12 \mu L_1} & x_l \leq -L_1 \\ -\left(1 + \frac{3}{2} \left(\frac{\epsilon_{rp}}{C_{rp}}\right)^2\right) \frac{\pi d_p C_{rp}^3}{12 \mu x_l} & -L_1 < x_l \leq -10C_{rp} \\ \frac{2}{\mu} d_h(x_l + 10C_r) A_o(x_l + 10C_r) \delta_Q + \frac{\partial q_0(\Delta p)}{\partial \Delta p} & Re < Re_t \wedge x_l > -10C_r \\ \frac{C_d A_o(x_l + 10C_r)}{\sqrt{2\rho |\Delta p|}} + \frac{\partial q_0(\Delta p)}{\partial \Delta p} & Re \geq Re_t \wedge x_l > -10C_r \end{cases} \quad (\text{C.2})$$

Partial differentiation with respect to  $x_l$  gives the flow gain

$$K_q = \frac{\partial Q}{\partial x_l} = \begin{cases} 0 & x_l \leq -L_1 \\ \left(1 + \frac{3}{2} \left(\frac{\epsilon_r}{C_r}\right)^2\right) \frac{\pi d_p C_r^3 \Delta p}{12 \mu x_l^2} & -L_1 < x_l \leq -10C_r \\ \frac{2\delta_Q \Delta p}{\mu} \left( A_o(x_l + 10C_r) \frac{\partial d_h(x_l + 10C_r)}{\partial x_l} + d_h(x_l + 10C_r) \frac{\partial A_o(x_l + 10C_r)}{\partial x_l} \right) & Re < Re_t \wedge x_l > -10C_r \\ C_d \sqrt{\frac{2}{\rho} |\Delta p|} \text{sign}(\Delta p) \frac{\partial A_o(x_l + 10C_r)}{\partial x_l} & Re \geq Re_t \wedge x_l > -10C_r \end{cases} \quad (\text{C.3})$$



The gradient of the orifice area and of the gradient of the hydraulic diameter are used in (C.3). These are computed in the following for two different orifice geometries. To simplify the writing we substitute  $x_l + 10C_r = y$ .

## C.1 Rectangular fluid port

For rectangular ports  $A_o(y) = \pi d y$ , hence

$$\frac{\partial A_o(y)}{\partial y} = \pi d \quad (\text{C.4})$$

and  $d_h(y) = 2y$ , hence

$$\frac{\partial d_h(y)}{\partial y} = 2 \quad (\text{C.5})$$

## C.2 Circular fluid port

For round ports the orifice area function is given by

$$A_o(y) = \begin{cases} N_g \left( \frac{\alpha_g}{4} d_g^2 - l_g \sqrt{\left(\frac{d_g}{2}\right)^2 - l_g^2} \right) & 0 < y \leq h_g \\ N_g \left( \frac{\alpha_{gm}}{4} d_g^2 - l_{gm} \sqrt{\left(\frac{d_g}{2}\right)^2 - l_{gm}^2} \right) + \pi d (y - h_g) & y > h_g \end{cases} \quad (\text{C.6})$$

where  $\alpha_g = \cos^{-1} \left( \frac{2l_g}{d_g} \right)$ ;  $l_g = \left( \frac{d_g}{2} - y \right)$ ;  $\alpha_{gm} = \cos^{-1} \left( 1 - 2\frac{h_g}{d_g} \right)$  and  $l_{gm} = \left( \frac{d_g}{2} - h_g \right)$ , and

$$\frac{\partial l_g}{\partial y} = -1 \quad (\text{C.7})$$

$$\frac{\partial \alpha_g}{\partial y} = \frac{2}{d_g \sqrt{1 - \frac{4l_g^2}{d_g^2}}} \quad (\text{C.8})$$

$$\frac{\partial \sqrt{\left(\frac{d_g}{2}\right)^2 - l_g^2}}{\partial y} = -\frac{l_g}{\sqrt{\left(\frac{d_g}{2}\right)^2 - l_g^2}} \frac{\partial l_g}{\partial y} = \frac{l_g}{\sqrt{\left(\frac{d_g}{2}\right)^2 - l_g^2}} \quad (\text{C.9})$$

Thus, the area gradient is given by

$$\begin{aligned}
\frac{\partial A_o(y)}{\partial y} &= \begin{cases} N_g \left[ \frac{d_g}{2\sqrt{1-\left(\frac{2l_g}{d_g}\right)^2}} - \frac{l_g^2}{\sqrt{\left(\frac{d_g}{2}\right)^2 - l_g^2}} + \sqrt{\left(\frac{d_g}{2}\right)^2 - l_g^2} \right] & y \leq h_g \\ \pi d & y > h_g \end{cases} \\
&= \begin{cases} \frac{N_g}{2} \left[ \frac{d_g^2 - 4l_g^2}{\sqrt{d_g^2 - 4l_g^2}} + \sqrt{d_g^2 - 4l_g^2} \right] & y \leq h_g \\ \pi d & y > h_g \end{cases} \\
&= \begin{cases} N_g \sqrt{d_g^2 - 4l_g^2} & y \leq h_g \\ \pi d & y > h_g \end{cases} \tag{C.10}
\end{aligned}$$

The hydraulic diameter is computed as

$$d_h(y) = \begin{cases} \frac{4A_o(y)}{2\pi d + N_g(\alpha_g d_g - s_g)} & y \leq h_g \\ \frac{4A_o(y)}{2\pi d + N_g(\alpha_{gm} d_g - s_{gm})} & y > h_g \end{cases} \tag{C.11}$$

where  $s_g = \sqrt{d_g^2 - 4l_g^2}$ , and

$$\frac{\partial s_g}{\partial y} = \frac{4l_g}{\sqrt{d_g^2 - 4l_g^2}} \tag{C.12}$$

From (C.8) and (C.12) we have

$$\frac{\partial N_g(\alpha_g d_g - s_g)}{\partial y} = 2N_g \frac{d_g - 2l_g}{\sqrt{d_g^2 - 4l_g^2}} \tag{C.13}$$

The hydraulic diameter gradient may now be computed by substituting (C.10) and (C.13) into the following equation

$$\frac{\partial d_h(y)}{\partial y} = \begin{cases} \frac{4}{2\pi d + N_g(\alpha_g d_g - s_g)} \frac{\partial A_o(y)}{\partial y} - \frac{4A_o(y)}{(2\pi d + N_g(\alpha_g d_g - s_g))^2} \frac{\partial N_g(\alpha_g d_g - s_g)}{\partial y} & y \leq h_g \\ \frac{4}{2\pi d + N_g(\alpha_{gm} d_g - s_{gm})} \frac{\partial A_o(y)}{\partial y} & y > h_g \end{cases} \tag{C.14}$$



# Appendix D

## Selected operating points for valve model linearisation

The operating points used to obtain the coefficients for the linear valve model are chosen as

$$\begin{aligned}\dot{x}_{m_0} &= \pm 5 \text{ [mm/s]} \\ x_{m_0} &= x_{l5}(q_{5_0}) + \Delta_a \\ q_{5_0} &= \{0, 1, 20, 40, 60, 80, 100, 120, 140, 160, 180\} \text{ [l/min]} \\ \Delta p_{5_0} &= \{5, 10, 50, 100, 150, 200, 250, 300, 350, 395\} \text{ [bar]} \\ p_{pp} &= 20 \text{ [bar]} \\ p_{pt} &= 0 \text{ [bar]} \\ p_t &= 0 \text{ [bar]}\end{aligned}$$

For steady state  $\dot{x}_{m_0} = 0$  should ideally be used. However, as time domain simulation is used to find steady state values, this would lead to a steady state linearisation point inside the dead-zone of the pilot spool. Therefore, the main spool velocity has been perturbed slightly by  $\pm 5$  [mm/s], to secure that coefficients are found in work points where the pilot spool is positioned such that the controlling orifice is (approximately) at its opening point, with regard to main spool on-stroke ( $\dot{x}_m \geq 0$ ) and de-stroke ( $\dot{x}_m \leq 0$ ).



# Appendix E

## Development and verification of loader crane model

This appendix contains the development and verification of comprehensive models of the mechanical and the hydraulic subsystems of a loader crane. The appendix is included to show that the dynamics of the crane may be captured by including only the lowest modes of the mechanical structure in the model.

In previous work on mobile flexible cranes low order models have been used [45, 61, 62, 63, 71, 72]. However, none of these references considered flexibility in concern to the telescopic arms, often encountered on loader cranes. The results in these references may therefore not be generalised to the considered loader crane.

The main parts of the appendix have with kind permission of Engineers Australia been reused from the paper<sup>1</sup>: B. Nielsen, H. C. Pedersen, T. O. Andersen, M. R. Hansen, Modelling and Simulation of Mobile Hydraulic Crane with Telescopic Arm, *Australian Journal of Mechanical Engineering*, 2(2):105-116, 2005

### Nomenclature

$\underline{A}_i^0$	Angular transformation matrix	$d_h$	Hydraulic diameter
$A_0$	Orifice area	$\underline{F}$	Viscous friction matrix
$A_m$	Effective area of spool	$\overline{F}_{\mu,act,i}$	Cylinder friction force
$A_{p,i}$	Piston side area of the $i$ 'th cylinder	$F_{\mu,j,i}$	Friction force of $i$ 'th prismatic joint
$A_{pilot}$	Area of pilot spool	$F_{\mu,ocv}$	Friction force in OCV
$A_{r,i}$	Rod side area of the $i$ 'th cylinder	$F_{act,i}$	Force developed by the $i$ 'th cylinder
$A(x_s)$	Orifice area of over centre valve	$F_{c,atm}$	Seal friction at atmospheric pressure
$C_d$	Orifice discharge coefficient	$F_{flow}$	Flow force
$C_v$	Velocity coefficient	$\underline{G}$	Gravitational terms
$d$	Seat diameter of over centre valve	$g$	Gravitational acceleration

---

<sup>1</sup>The modelling and experimental work which is basis for the appendix has been made in collaboration with Ph.D. student Henrik C. Pedersen.

$\underline{K}$	Stiffness vector	$\underline{u}_{i,P}$	Local vector to point $P$
$K_L$	Geometry dependent loss coefficient	$V$	Total volume (hose+air+oil)
$k_s$	Spring constant	$V_{\%,air}$	Volume percentage of air in the oil
$l$	length of duct	$V_{hose}$	Volume of hose
$l_s$	Length between the clamping supports	$V_{p,i}$	Piston side volume of the $i$ 'th cylinder
$\underline{M}$	Mass matrix	$V_{r,i}$	Rod side volume of the $i$ 'th cylinder
$m_{eq,j}$	Equivalent mass of the $j$ 'th boom	$v$	Flow velocity through duct
$m_l$	Mass of payload	$v_1$	Flow velocity through diffuser area ( $A_1$ )
$m_s$	Mass of over centre valve spool	$w(x,t)$	Deflection of beam
$\underline{O}_i$	Global position vector to the $i$ 'th origo	$\dot{x}_i$	Velocity of the $i$ 'th cylinder piston
$\Delta p$	Pressure drop	$\dot{x}_{\eta a}$	Friction normalisation velocity
$p_b$	Back Pressure	$x_i$	Length of the $i$ 'th cylinder
$p_c$	Crack pressure	$x_s$	Over centre valve spool travel
$p_{pilot}$	Pilot pressure	$\alpha$	Angle of pipe bend in radians
$\dot{p}_{p,i}$	Piston side pressure of the $i$ 'th cylinder	$\alpha_s$	Half cone angle of valve poppet
$\dot{p}_{r,i}$	Rod side pressure of the $i$ 'th cylinder	$\beta_e$	Effective bulk modulus of volume $V$
$\underline{Q}$	Generalised force vector	$\beta_{air}$	Bulk modulus of air
$\underline{q}$	System vector	$\beta_{hose}$	Bulk modulus of hose material
$\underline{Q}$	Flow through flow restriction	$\beta_{oil}$	Bulk modulus of pure oil
$Q_{p,i}$	Flow into the $i$ 'th piston chamber	$\Delta$	Actual seal displacement
$Q_{r,i}$	Flow into the $i$ 'th rod chamber	$\Delta_{cr}$	Critical seal displacement
$q_{a,i}$	The $i$ 'th rotational coordinate	$\underline{\Phi}_d$	Drive Jacobian
$q_{f,j}(t)$	The $j$ 'th flexible coordinate	$\eta_a$	Cylinder efficiency
$q_{l,i}$	Length of the $i$ 'th extension boom	$\lambda$	Flow coefficient
$q_l$	Total length of jib	$\mu_d$	Dynamic friction coefficient
$Re_t$	Reynolds transition number	$\mu_s$	Static friction coefficient
$\underline{r}_P$	Global position vector to point $P$	$\rho$	Mass density of oil
$\underline{s}_{f,i,P}$	Position vector to point $P$ , flexible part	$\psi_j(x)$	the $j$ 'th mode shape
$\underline{s}_{i,P}$	Position vector to point $P$ , rigid part	$\zeta$	Pressure drop coefficient

## E.1 Introduction to the modelled system

The considered loader crane is sketched in figure E.1. The crane has 4 controllable axes for manoeuvring. These are the main lift axis, the jib rotational axis, the jib extension axis and the base rotation. All axes are operated by hydraulic cylinders. To simplify the modelling problem only two dimensional manoeuvring of the crane is considered. The plane crane configuration and the associated hydraulic system is sketched in figure E.2. In the two dimensional plane, the loader crane has six degrees of freedom, two associated with the main and jib rotational joints, and four prismatic joints associated with the jib extension.

The parallel connection of the hydraulic cylinders of the jib is sketched in figure E.3. The area ratios of these cylinders are not alike. This means that the rate of change of the jib length (the local velocity) does not depend on the applied flow alone, but also on the movement of cylinders. Furthermore, the operating sequence of the mechanical links of the jib is not controllable, but a function of the joint friction. The relative lengths of the mechanical links also affect the rigidity of the jib. Hence, to obtain the correct rigidity of the jib the local positions should be correctly estimated by the simulation model.

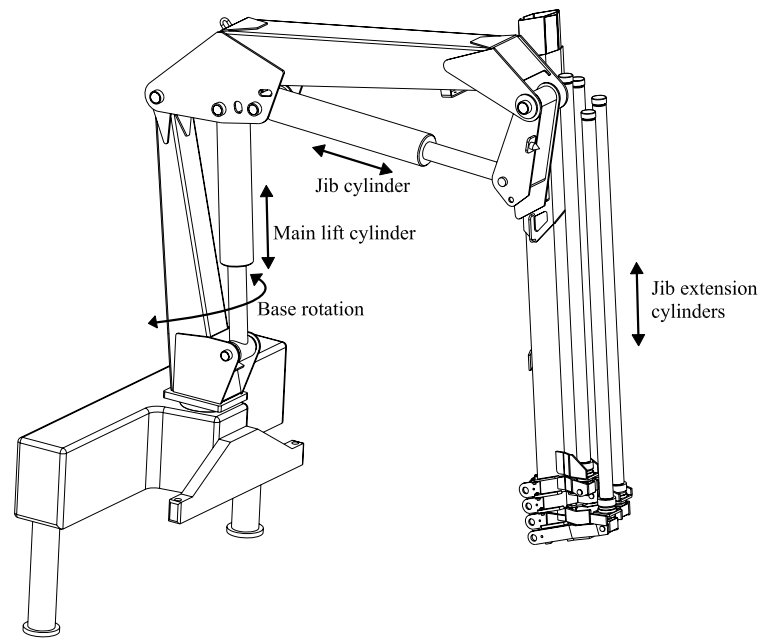


Figure E.1: The considered loader Crane.

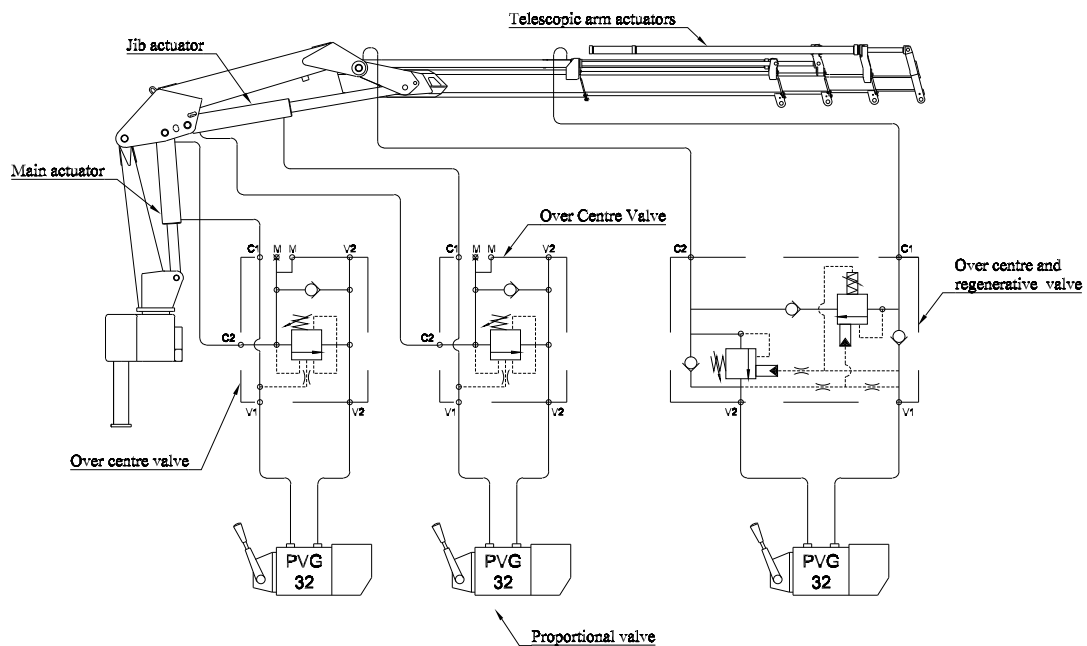


Figure E.2: Sketch of the test crane.

As shown in figure E.2, over centre valves are included on all three controllable axes. This is due to European safety regulations. The over centre valve associated with the jib extension axis is of a special type including a regenerative function. The three over centre valves are also considered in the model presented below. The flows to the cylinders are measured as part of the data sets used for model verification. Therefore the flows are used as inputs in the verification of the simulation model, instead of modelling the



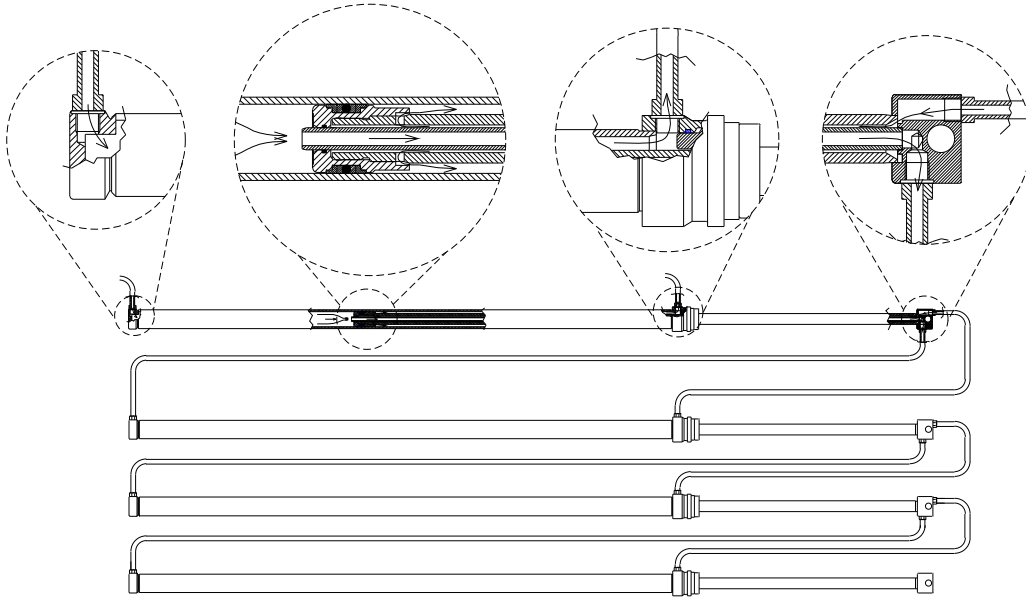


Figure E.3: Sketch showing the parallel connection of cylinders and the areas where the largest pressure drops are expected.

proportional valves and using pressure signals as inputs.

## E.2 Model of hydraulic subsystem

### E.2.1 Hydraulic cylinder model

As explained above the system has six degrees of freedom, and hence six corresponding cylinders. Three of the degrees of freedom are controllable, due to the parallel arrangement of the jib extension cylinders. We define positive velocity for an extending cylinder, hence the pressure derivative in the piston and rod side chamber of the  $i$ 'th cylinder is found by

$$\dot{p}_{p,i} = \frac{\beta_e}{V_{p,i}(x_i)}(Q_{p,i} - A_{p,i} \cdot \dot{x}_i - Q_{p,i+1}) \quad (\text{E.1})$$

$$\dot{p}_{r,i} = \frac{\beta_e}{v_{r,i}}(Q_{r,i} + A_{r,i} \cdot \dot{x}_i - Q_{r,i+1}) \quad (\text{E.2})$$

where  $Q_{p,i+1}$  and  $Q_{r,i+1}$  corresponds to the flow to the subsequent cylinder. For the main lift cylinder, the jib cylinder and last jib extension cylinder, these terms simply vanish.  $\beta_e$  is the effective bulk modulus of the oil. Accounting for air contained in the oil and flexibility of the hoses, the effective bulk modulus may for each volume be calculated by

$$\beta_e = \frac{1}{\frac{1}{\beta_{oil}} + \frac{V_{hose}}{V \cdot \beta_{hose}} + \frac{V_{\%,air}}{\beta_{air}}} \quad (\text{E.3})$$

Once the percentage of air in the hydraulic oil at atmospheric pressure is known, the percentage of air at the pressure associated with a given volume may be calculated from Boyle/Mariottes law assuming an adiabatic compression. From experimental results, the percentage of air at atmospheric pressure was estimated to 5%. This number may, however, contain some uncertainty. The bulk modulus of the hose is assumed to be pressure dependent, with  $\beta_{hose} = 100.000\sqrt{p}$ , as used by [71].

The force balance of the  $i$ 'th cylinder piston is given by

$$F_{act,i} = p_{p,i} \cdot A_{p,i} - p_{r,i} \cdot A_{r,i} - F_{\mu,act,i} \quad (\text{E.4})$$

Note that the mass of the cylinder piston has been neglected in (E.4) as the equivalent mass on the piston from the mechanical structure is far greater than the piston mass itself. The inertia of the oil in the pipes and hoses connecting the cylinders may be included as an equivalent piston mass by the method used in [62]. However, this has shown to have a negligible effect for the given system.

The friction force,  $F_{\mu,act,i}$ , in (E.4) is calculated from (E.5), where a mechanical cylinder efficiency  $\eta_a = 92\%$  is assumed.  $\dot{x}_{\eta_a}$  is a normalisation value controlling the steepness of the friction function around zero velocity. It was found that an appropriate value for the normalisation factor was  $\dot{x}_{\eta_a} = 0.02[\frac{m}{s}]$ .

$$F_{\mu,act,i} = \tanh\left(\frac{\dot{x}_i}{\dot{x}_{\eta_a}}\right) \cdot |p_{p,i} \cdot A_{p,i} - p_{r,i} \cdot A_{r,i}| \cdot (1 - \eta_a) \quad (\text{E.5})$$

Other friction models including stiction, stribeck and hysteresis effects have been tried out. However, for the particular application more accurate results than those presented later in this appendix have not been gained by using these more advanced friction models. The latter should also be seen in combination with the necessity of determining the friction parameters of the more advanced models accurately, which is not a straight forward task.

The cylinder model presented by (E.1) to (E.5) is used for all six cylinders on the crane. The flow resistances between the jib extension cylinders are modelled next.

## E.2.2 Model of flow resistances in jib extension cylinders

By studying the section view of the cylinders in figure E.3, it is found that the pressure drops between the cylinders may be modelled as resulting from three flow situations. These are, flow through an orifice, flow through pipes and flow through a diffuser. Section views of the areas where the largest pressure drops occur are enlarged in figure E.3. By rewriting the orifice equation, the pressure drop over an orifice may be expressed as

$$\Delta p = \frac{Q^2 \rho}{2C_d^2 A_0^2} \quad (\text{E.6})$$

Similarly the pressure drop over a diffuser may be written as

$$\Delta p = \frac{1}{2} K_L \rho v_1^2 \quad (\text{E.7})$$

In (E.7) the loss coefficient is calculated by the two cross sectional areas of the diffuser as  $K_L = (1 - A_1/A_2)^2$  and the velocity in the channel before the diffuser is calculated by  $v_1 = Q/A_1$ . Equation (E.7) is valid for Bernoulli flow, i.e. stationary incompressible frictionless flow, none of which is completely fulfilled here. Therefore, the above is an approximation. The errors resulting from this approximation are however negligible. The third reason from which pressure drops arise are the flows in the channels connecting the volumes in the jib extension cylinders. For estimating these pressure drops the pressure drop across a duct may be used. For straight ducts we have

$$\Delta p = \frac{\lambda l \rho v^2}{2d_h} \quad (\text{E.8})$$

The dimensionless coefficient  $\lambda$  depends on whether the flow is turbulent or laminar. In the simulation model the flow is either regarded as turbulent or laminar, which of course is an approximation as transition exists between the two. For turbulent flow  $\lambda \approx \frac{0.316}{Re^{0.25}}$  and for laminar flow  $\lambda \approx \frac{64}{Re}$ , with an expected transition occurring at a Reynolds number of  $Re = 2300$ . For bend ducts the corresponding pressure drop is described by

$$\Delta p = \frac{\zeta \rho v^2 \alpha}{2 \cdot \frac{\pi}{2}} \quad (\text{E.9})$$

where  $\zeta$  is a dimensionless pressure drop coefficient determined by the bend radius of the pipes as  $\zeta = 0.3 / \left(\frac{r_b}{d_h}\right)^{0.6}$ .

Having expressions for the pressure drops through the channels, the total pressure drop from one cylinder to the next may be written as a summation over all the pressure drops

$$\Delta p = \sum_{i=1}^{no} \frac{Q^2 \rho}{2C_{D,i}^2 A_i^2} + \sum_{i=1}^{nd} \frac{1}{2} K_{L,i} \rho \frac{Q^2}{A_i^2} + \sum_{i=1}^{nc} \frac{Q^2 \rho \lambda_i}{2d_{h,i} A_i^2} + \sum_{i=1}^{nb} \frac{\zeta \rho Q^2 \alpha}{\pi A_i^2} \quad (\text{E.10})$$

Notice in (E.10) that the flow is inserted instead of the velocities, since  $v_i = Q/A_i$ . The same flow amount is flowing through all the critical areas as the flow is assumed incompressible. The flow is obtained by rearranging (E.10) as

$$Q = \sqrt{\frac{\Delta p}{\rho \left( \sum_{i=1}^{no} \frac{1}{2C_{D,i}^2 A_i^2} + \sum_{i=1}^{nd} \frac{1}{2A_i^2} K_{L,i} + \sum_{i=1}^{nc} \frac{\lambda_i}{2d_{h,i} A_i^2} + \sum_{i=1}^{nb} \frac{\zeta \rho \alpha}{\pi A_i^2} \right)}} \quad (\text{E.11})$$

Hereby the flow between the jib extension cylinders may be found. As indicated a number of coefficients should be determined, including, area coefficients, lengths etc. The non directly measurable parameters have been estimated based on textbook values and afterwards been adjusted based on test results from measurements other than those used for model verification in section E.4.

### E.2.3 Over centre valve model

The over centre valves mounted on the crane are of similar type, with the exclusion that the over centre valve associated with the jib extension axis includes a regenerative function. The hydraulic diagram of the over centre valves is sketched in figure E.2. Due to similarities between the three over centre valves only equations for the main and jib type over centre valve are presented here.

For the flow direction where the main cylinder is extending the over centre valve simply works as a check valve and for this flow direction it is ignored in the simulation model. For the opposite flow direction, i.e. for a retracting cylinder, the flow through the valve is given by a modified orifice equation, compensated for laminar flow at low Reynolds numbers

$$Q = C_d(Re)A(x_s)\sqrt{\frac{2}{\rho}\Delta P} \quad (\text{E.12})$$

The transition number at which the flow pattern shifts may vary over a wide range. According to results presented in [91] a transition number at  $Re_t = 640$  was found for the particular geometry. The discharge coefficient may hereby be calculated as

$$C_d(Re) = \begin{cases} \frac{C_d\sqrt{Re}}{\sqrt{Re_t}} & , \quad Re \leq Re_t \\ C_d & , \quad > Re_t \end{cases} \quad (\text{E.13})$$

The opening area used in (E.12) is dependent on the spool position, which may be calculated from the force balance on the spool<sup>2</sup>

$$m_s\ddot{x}_s = p_p A_m + p_{pilot} A_{pilot} - p_c A_m - F_{flow} - k_s x_s - F_{\mu,ocv} \quad (\text{E.14})$$

In the above  $p_{pilot}$  may be found by pressure build up in the small volume behind the damping orifice in the pilot port of the over centre valve. A model including hysteresis is used for determining the friction force  $F_{\mu,ocv}$ . The model is based on deformation of the valve seal i.e. the seal deforms until stiction is overcome and then slips across the valve housing. This is described by the following equation

$$F_{\mu,ocv} = \begin{cases} \frac{F_{\mu}(p_p, p_r) + F_{c,atm}}{\Delta_{cr}} |\Delta| & , \quad |\Delta| < \Delta_{cr} \\ F_{\mu}(p_p, p_r) + F_{c,atm} & , \quad |\Delta| \geq \Delta_{cr} \end{cases} \quad (\text{E.15})$$

Both results from [44] and experimental verification of the model of the over centre valve itself have shown that it is appropriate to neglect the pressure dependent term of the friction force. Hence,  $F_{\mu}(p, p_r) \approx 0$ . Based on the experiments appropriate values for  $F_{c,atm}$  and  $\Delta_{cr}$  where found as  $F_{c,atm} = 20$  [N] and  $\Delta_{cr} = 4.5$  [ $\mu\text{m}$ ].

---

<sup>2</sup>Note, the back pressure does not appear in the force balance as the valve is back pressure compensated. This is not the case for the over centre valve for the jib extension axis, why a back pressure term appears in the force balance for this valve.

The flow force in (E.14) is given by

$$F_{flow} = \pi C_d C_v dx_s \sin(2\alpha_s) |p_p - p_b| \quad (\text{E.16})$$

Hereby the main equations governing the over centre valve model have been presented and the modelling of the hydraulics is completed. The modelling of the mechanical system is considered next.

### E.3 Model of mechanical subsystem

Common for modelling of most mechanical multibody systems are that they are modelled as rigid lumped bodies which interact. However for mobile cranes, telehandlers and the like, the flexibility of the mechanical structure plays an important role, both in regard to controlling the tool centre position, but as well to determine the correct dynamic behaviour of the system. For the test crane, the primary structural deflection is due to the jib, whereas the other booms as an approximation may be considered rigid. This imposes a number of difficulties, as describing the flexibility in a system with multiple prismatic joints is not a straightforward task.

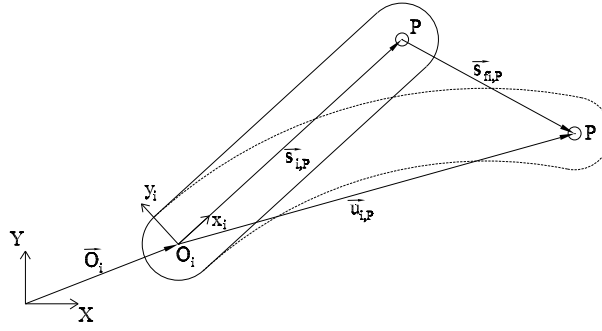
To describe the deflection of the jib, knowledge of the relative positions of the individual bodies is necessary, as the flexibility of the arm is influenced by both the length of the arm and the cross sectional area along it. Both length and cross sectional areas are time dependent as a function of the manoeuvring of the crane. Secondly, the information of position and velocity of the individual bodies is needed in order to couple the hydraulic and mechanical models of the system. Here a method is presented, where the jib is modelled as one beam for describing the flexibility, but where a rigid body model is used as an estimator in order to describe the relative movement of the individual bodies.

#### E.3.1 Model of structural flexibility

In order to model the behaviour of the mechanical system, the flexibility needs to be taken into consideration in the position equations from which the equations of motion are derived. To describe the deflection it is assumed that any point  $P$  on the deflecting body, see figure E.4, may be described as a function of the rigid body position of the point added a contribution from the deflection of the body

$$\underline{r}_P = \underline{Q}_i + \underline{A}_i^0 \cdot \underline{u}_{i,P} = \underline{Q}_i + \underline{A}_i^0 \cdot (\underline{s}_{i,P} + \underline{s}_{fi,P}) \quad (\text{E.17})$$

For small deflections the longitudinal length change is negligible, why  $\underline{s}_{fi,P} \approx w_i(x, t)$ , where  $w_i(x, t)$  is the transverse deflection of the  $i$ 'th body. To describe the deflection with a low number of modes the assumed modes method is used. The deflection curve is described using two modes, as this has yielded better results than using only the first

Figure E.4: Flexible body in the floating reference frame  $(x_i, y_i)$ .

mode. For both modes the deflection shape is assumed to be describable by part sine curves, resulting in the deflection expression:

$$w(x, t) = \sum_{j=1}^2 \psi_j(x) q_{f,j}(t) = \left( \sin\left(\frac{\pi x}{2q_l} + \frac{\pi}{2}\right) - 1 \right) q_{f,1} + \left( \sin\left(\frac{\pi x}{q_l} + \frac{\pi}{2}\right) - 1 \right) q_{f,2} \quad (\text{E.18})$$

The validity of the assumed modes method is only fulfilled as long as the deflection shape of the beam is time and space separable, which related to the Euler-Bernoulli beam theory is identical to the beam only having kinetic energy due to the transverse vibrations of the beam. For beams undergoing translational motion this property does not hold, as these also possess kinetic energy due to the translational motion. For small translational velocities the approximation of the deflection shape being time and space separable is however valid, as shown by Theodore and Ghosal [102]. They found that as long as the ratio between the translational velocity,  $U$  and the dispersive wave group propagation velocity,  $U_g$  is less than 0.03 the approximation is valid. For the crane the highest ratio is  $\max\{U/U_g\} = 6.8 \cdot 10^{-3}$ .

The equations of motion of the mechanical structure is derived using Lagrange's method. Lagrange's method is based on spatial integration of the structure to obtain the kinetic and potential energy. Hence, energy terms resulting from deflection and vibrations in the structure is included. The result in standard closed form is

$$\underline{\underline{M}}(\underline{q}) \cdot \underline{\ddot{q}} + \underline{\underline{B}}(\underline{q}, \underline{\dot{q}}) \cdot \underline{\dot{q}} + \underline{\underline{K}}(\underline{q}) + \underline{\underline{G}}(\underline{q}) + \underline{\underline{F}} \cdot \underline{\dot{q}} = \underline{\underline{Q}} \quad (\text{E.19})$$

where  $\underline{q} = [q_{a,1}, q_{a,2}, q_{a,8}, q_l, q_{f,1}, q_{f,2}]^T$  is the generalised coordinate vector. The payload is included in the model as the eighth body, the third to seventh bodies are the individual links on the jib.

To establish a link between the model of the hydraulic system and the model of the flexible mechanical system a rigid body model of the mechanical system is to be used. This is described further below. The rigid body model is derived in a similar manner as the flexible one, also using Lagrange's method, but where any deformation in the mechanical structure is disregarded, i.e. the term describing the deformation,  $w(x, t)$ , is left out. In the rigid body model each of the bodies on the jib is as well modelled as single bodies, resulting in the generalised coordinate vector  $\underline{q} = [q_{a,1}, q_{a,2}, q_{a,8}, q_{l,4}, q_{l,5}, q_{l,6}, q_{l,7}]^T$ . The dynamics of the rigid body model is also described in closed form, similar to (E.19).

### E.3.2 Coupling between flexible, rigid and hydraulic models

To combine the mechanical and the hydraulic model, the cylinder forces shall be converted to generalised forces. This is done through the drive Jacobian, which for the first two coordinates is

$$\underline{\underline{\Phi}}_d = \begin{bmatrix} \frac{\partial x_1}{\partial q_{a,1}} & \frac{\partial x_1}{\partial q_{a,2}} \\ \frac{\partial x_2}{\partial q_{a,1}} & \frac{\partial x_2}{\partial q_{a,2}} \end{bmatrix} \quad (\text{E.20})$$

A change in length of any of the four jib extension cylinders must result in a similar change in length of the jib. As described, the jib is modelled as one beam in the flexible body model. Whereas the model of the hydraulic system has a length coordinate associated with each individual cylinder. Therefore, it is not possible directly to combine the flexible mechanical model and the hydraulic system associated with the jib. The jib extension cylinders are not carrying the same load. Therefore, to relate the forces from each of the cylinders to a change in the length of the jib, the movement of the individual bodies on the jib needs to be considered. In the model this is dealt with using the rigid body model as an estimator to update the positions of the individual bodies on the jib, see figure E.5. These positions are fed to the flexible body model and used for computing the jib length, rigidity, and centre of mass etc. of the jib. To do this cross model update the rigid and the flexible body models are simulated simultaneously. The position coordinates, which are common for both the rigid body model and the flexible one, are fed from the flexible body model to the rigid body model to ensure a two way updating keeping both models on track.

For the rigid body model the including the jib extension cylinder forces is simple, as the movement of the individual cylinders in the extension boom system is identical to the movement of the individual bodies. The above drive Jacobian is therefore simply expanded with ones on the diagonal entries associated with the jib extension cylinders. Hence, the cylinder forces determined by (E.4) may in the rigid body model be converted to generalised forces as

$$\underline{Q} = \underline{\underline{\Phi}}_d^T \underline{F}_{act} \quad (\text{E.21})$$

In the flexible body model the one generalised force associated with the jib is included by adding an imaginary spring between the tool centre position of the rigid and the flexible body model. When the jib of the rigid body model moves it simply drags/pushes the jib of the flexible body model due to the spring force. The generalised force associated with the jib in the flexible body model, may mathematically be expressed by

$$Q_4 = k_s(s_3 + q_{l,4} + q_{l,5} + q_{l,6} + q_{l,7} - q_l) \quad (\text{E.22})$$

where  $k_s$  is the spring constant of the imaginary spring,  $s_3$  is the length of the stationary part of the jib, see Fig. E.5,  $q_{l,i}$  is the extended length of the  $i$ 'th body and  $q_l$  is the length of the jib in the flexible body model.

### E.3.3 Model of prismatic joint friction

In the derivation of the mechanical model, friction in the prismatic joints is not directly handled in the system equations. To include friction in the prismatic joints a simple method is utilised, where friction is included as a term in the generalised force vector of the rigid body model. The bodies of the jib are held in place by a force couple producing a torque on the "clamped" end as shown in figure E.5.

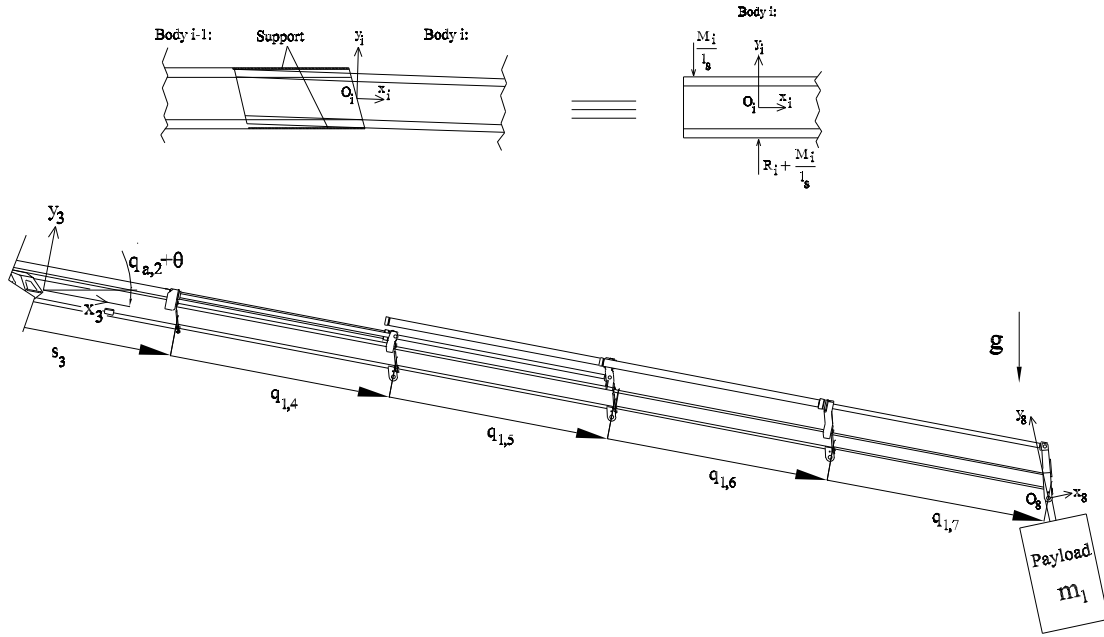


Figure E.5: Sketch in the top, showing how each body in the jib is held in place by a force couple. The lower part of the figure shows the jib and the generalised coordinates related to this.

The friction works in the direction opposite of the relative movement between two bodies and is expected to be primarily coulomb friction, as the sliding velocities between the bodies are relatively low. Hence, by considering the lower part of figure E.5, a Coulomb friction model based on gravitational forces may, for the rigid body model and for bodies  $i = 4..7$ , be modelled by

$$F_{\mu,j,i} = \mu_i \cdot g \cdot \cos(q_{a,2} + \theta) \left[ \sum_{j=i}^7 \left( m_{eq,j} \left( 1 + \frac{2 \sum_{k=i}^{j-1} q_{l,k} + q_{l,j}}{l_s} \right) \right) + m_l \left( 1 + \frac{2 \sum_{k=i}^7 q_{l,k}}{l_s} \right) \right] \quad (E.23)$$

The direction of the force is included in the friction coefficient which is described as

$$\mu_i = \begin{cases} \mu_s \cdot \text{sign}(F_{act,i}) & , \text{ for } \dot{q}_{l,i} = 0 \\ \mu_d \cdot \text{sign}(\dot{q}_{l,i}) & , \text{ elsewhere} \end{cases} \quad (E.24)$$

Notice that stiction is included in terms of a higher friction coefficient at zero velocity.



## E.4 Model verification

The stiffness and therefore the natural frequency of the loader crane including both hydraulic and mechanical subsystem changes when the configuration of the crane changes. Therefore, the relative positions of the bodies of the jib must be correctly estimated by the model, for the stiffness of the jib to be computed correctly. By a comparison of measurements recorded for an extending movement of the jib and the simulation results in figure E.6 it is found that there is a fairly good agreement for the first and second jib extension booms. For the third and fourth jib extension booms there is less good agreement. This is contributed to the friction between the third and fourth extension boom being overestimated by the model.

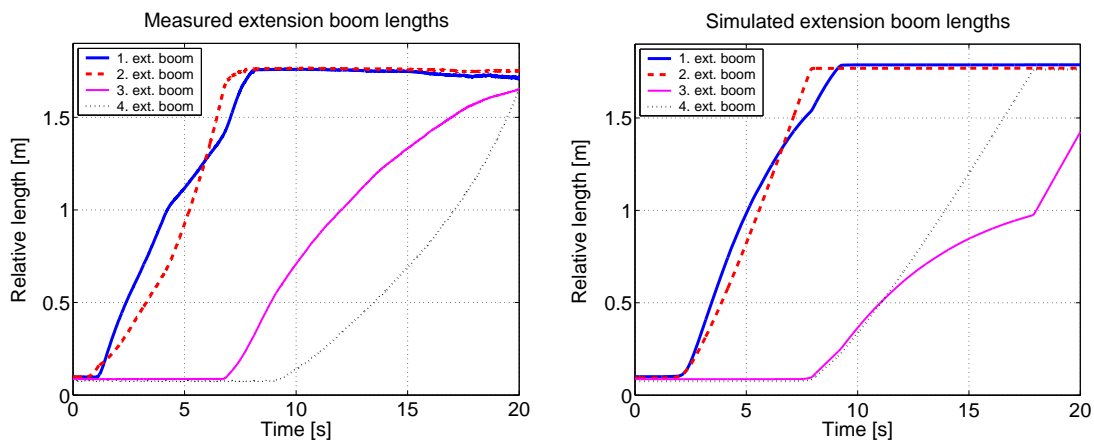


Figure E.6: Measured and simulated relative lengths of the individual bodies when the jib is extending.

The first and second jib extension booms move before the third and fourth jib extension booms. This is because the effective areas of the cylinders associated with the first and second jib extension booms are larger than those of the cylinders associated with the third and fourth jib extension booms. The measured and simulated pressures in the chamber of the jib extension actuator nearest to the over centre valve are plotted to the left in figure E.7.

To the right in this figure the measured and simulated tool centre positions are shown. In the response all axes are manoeuvred simultaneously. A good agreement is found between the measurement and the simulation. The horizontal tool centre position is estimated within  $\pm 100$  [mm]. This accuracy is found to be satisfactory, considered that the measurements were made with heavy oscillations of the crane. Under the measurements the total deflection approached 1 [m] with the jib being fully extended. For comparison, the total stationary deflection is approximately 0.5 [m] for the same payload and configuration of the crane.

The pressure levels in the main and jib cylinders for the manoeuvring of all axes are plotted in figure E.7. These results show that the simulated pressure levels in the jib cylinder are too low, but this is the case for both the piston and rod side pressure. Con-

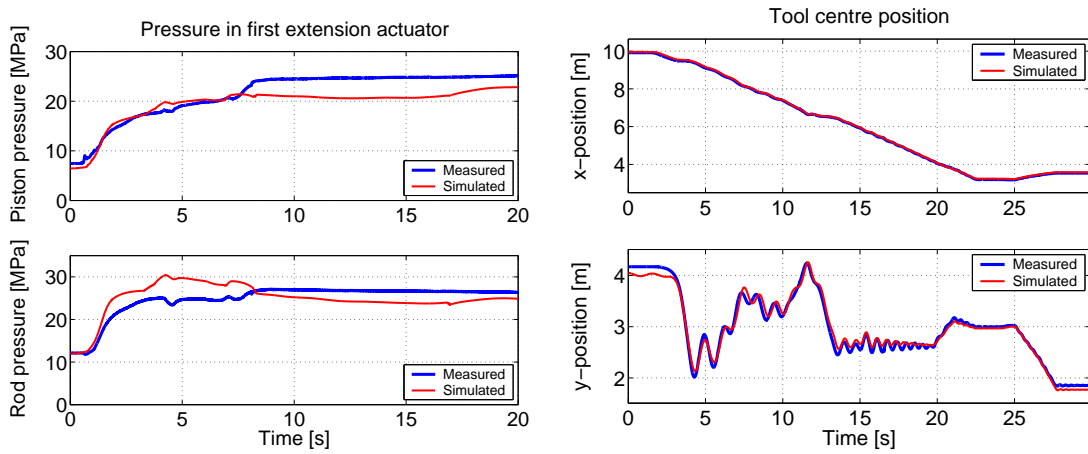


Figure E.7: To the left the pressure in the first extension cylinder, when the jib is extended. To the right the tool centre position when all the axes are moved simultaneously.

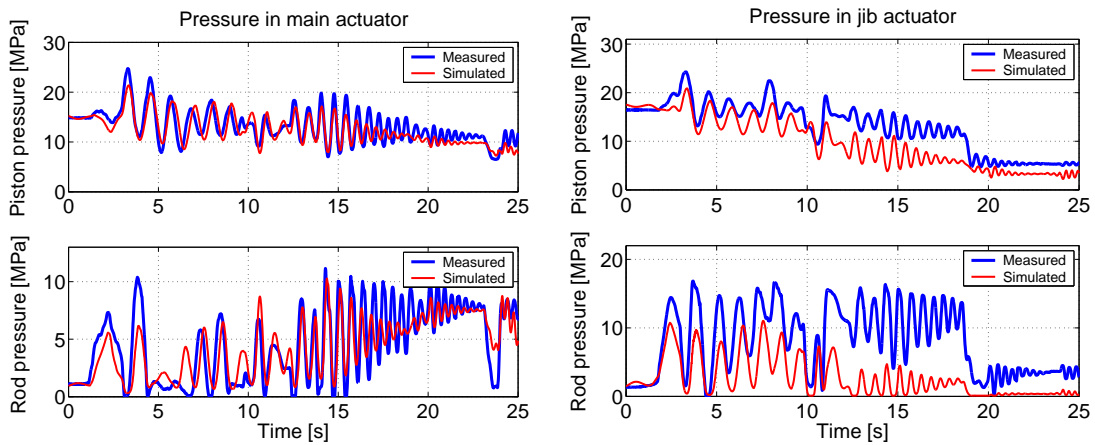


Figure E.8: Pressures in the main and jib cylinders when all cylinders are operated simultaneously.

Considering the area ratio of the jib cylinder, the resulting simulated force from the cylinder corresponds to the force that may be determined from the measured pressures. The dynamic content of the measurement is however captured fairly well by the simulation, although the damping of the simulation model is slightly too large.

The conclusion of this appendix is that even though only two structural modes are included in the model of the mechanical structure it captures the dynamics of the complex crane structure fairly well.



# Appendix F

## Publications

Publications by the author or to which the author has contributed during his Ph.D. study are listed below. The listed patent applications are direct results of the Ph.D. study, whereas the remaining publications reflect the broad technical interests of the author. Most recent publications are listed first.

### Pending patents:

1. B. Nielsen, Hydraulic Valve Arrangement, United States Patent Application Publication No.: US 2005/0072954 A1, 2005
2. B. Nielsen, P. E. Hansen, T. O. Andersen, Valve Arrangement and Hydraulic Drive, United States Patent Application Publication No.: US 2005/0051026 A1, 2005
3. B. Nielsen, P. E. Hansen, T. O. Andersen, Valve Arrangement and Hydraulic Drive, United States Patent Application Publication No.: US 2005/0051025 A1, 2005
4. B. Nielsen, P. E. Hansen, T. O. Andersen, Valve Arrangement and Hydraulic Drive, United States Patent Application Publication No.: US 2005/0051024 A1, 2005

### Journal papers:

- B. Nielsen, H. C. Pedersen, T. O. Andersen, M. R. Hansen, Modelling and Simulation of Mobile Hydraulic Crane with Telescopic Arm, *Australian Journal of Mechanical Engineering*, 2(2):105-116, 2005

### Conference papers:

1. T. O. Andersen, M. R. Hansen, B. Nielsen, An approach to specifying the dynamic performance of a hitch valve on an agricultural tractor, *Proceedings of IMECE'04 2004 ASME International Mechanical Engineering Congress and Exposition*, 2004

2. B. Nielsen, T. O. Andersen, L. B. Tandrup, M. R. Hansen, Design Optimisation and Control of a Pilot Operated Seat Valve, *4th International Fluid Power Conference*, Dresden, Germany, 2004
3. H. C. Pedersen, B. Nielsen, T. O. Andersen, M. R. Hansen , P. Pedersen, Resolved Motion Control of Hydraulic Loader Crane, *1st International Conference on Computational Methods in Fluid Power Technology*, Melbourne, Australia 26-28 November 2003
4. H. C. Pedersen, B. Nielsen, T. O. Andersen, M. R. Hansen , P. Pedersen, Robust and Adaptive Resolved Motion Control of a Hydraulic Loader Crane, *Proceedings of IMECE'03 2003 ASME International Mechanical Engineering Congress & Exposition*, Washington, D.C., November 16-21, 2003
5. M. R. Hansen, T. O. Andersen, B. Nielsen, F. Conrad, Electro Hydraulic Hitch Control, *The 18th International Conference on Hydraulics and Pneumatics*, Prague, September 30 - October 1, 2003
6. B. Nielsen, H. C. Pedersen, T. O. Andersen, M. R. Hansen, Algorithm for Solving the Inverse Kinematic Redundancy Problem of a Flexible Mobile Hydraulic Crane, *Eight Scandinavian International Conference on Fluid Power*, Tampere, Finland, 2003
7. T. O. Andersen, M. R. Hansen, H. C. Pedersen, B. Nielsen, Robust Adaptive Control of Hydraulic Actuator Systems, *Eight Scandinavian International Conference on Fluid Power*, Tampere, Finland, 2003

# Bibliography

- [1] <http://www.artemisip.com/>. (date accessed 20th September 2005).
- [2] Cmx sectional controls - application guide. Product catalogue, March 1995. Eaton Corporation.
- [3] Emv-611e electro-hydraulic mobile control valve, April 1996. Document No. 5024/EN/0496/A, Eaton Corporation.
- [4] Eaton ultronics™ management system - electro-hydraulic can bus control system. On: <http://hydraulics.eaton.com>, May 2005. Eaton Corporation. Document No. E-VLDI-MR003-E2.
- [5] J. A. Aardema. Hydraulic circuit having dual electrohydraulic control valves. US Patent US 5 568 759, October 1996. Caterpillar Inc.
- [6] J. A. Aardema and D. W. Koehler. System and method for controlling an independent metering valve. US Patent US 5 947 140, September 1999. Caterpillar Inc.
- [7] A. Akers and S. J. Lin. A comparison of the performance of single-spool and two-spool, two-stage flow control valves. In *Fluid Power - Proceedings of the 9th International Symposium*, pages 67–82, Oxford, UK, 1990. STI.
- [8] T. O. Andersen, M. R. Hansen, H. C. Pedersen, and F. Conrad. On the control of hydraulic servo system - evaluation of linear and non-linear control schemes. In *The Ninth Scandinavian International Conference on Fluid Power, SICFP05*, 2005.
- [9] T. O. Andersen, M. E. Münzer, and M. R. Hansen. Evaluations of control strategies for separate meter-in separate meter-out boom actuation in mobile applications. In *17th International Conference on Hydraulics and Pneumatics*, 2001.
- [10] R. T. Anderson and P. Y. Li. Mathematical modelling of a two spool flow control servovalve using a pressure control pilot. *Transactions of the ASME Journal of Dynamic Systems, Measurement, and Control*, 124:420–427, September 2002.
- [11] B. R. Andersson. *On The Valvistor a Proportionally Controlled Seat Valve*. PhD thesis, Linköping University, Division of Hydraulics and Pneumatics, S-581 83 Linköping Sweden, 1984.

- [12] B. R. Andersson and J. L. Ayres. Load sensing directional valves, current technology and future development. In *The Fifth International Conference on Fluid Power*, Linköping, Sweden, 1997.
- [13] T. M. Apostol. *Mathematical Analysis*. Adison Wesley Longman, Menlo Park, California, 1974.
- [14] J. Ayres. Aspects in the design of construction equipment load sensing fluid power systems. In *Ninth Bath International Fluid Power Work Shop*, Bath UK, September 9-11 1996.
- [15] W. Backé. Design systematics and performance of cartridge valve controls. In *International Conference on Fluid power*, Tampere, Finland, March 24-26 1987.
- [16] W. Backé. What are the prospects facing new ideas in fluid power? In *Proceedings of the Sixth International Conference on Fluid Power Transmission and Control*, Hangzhou, China, 2005. International Academic Publishers World Publishing Corporation.
- [17] G. J. Balas, A. K. Packard, M. G. Safonov, and R. Y. Chiang. Next generation of tools for robust control. In *Proceedings of the 2004 American Control Conference*, Boston, Massachusetts, June 30 - July 2 2004.
- [18] R. Bindel, R. Nitsche, R. Rothfuss, and M. Zeitz. Flatness based control of a two valve hydraulic joint of a large manipulator. *Automatisierungstechnik*, 48(3):124–131, 2000.
- [19] J. F. Blackburn, G. Reethof, and J. L. Shearer. *Fluid Power Control*. The M.I.T. Press, The Massachusetts Institute of Technology Cambridge, England, first edition, 1960.
- [20] C. Boes, W. Lenz, and J. Müller. Digital servo valves with fieldbus interface in closed loop applications. In *The Eight Scandinavian International Conference on Fluid Power*, pages 845–856, Tampere, Finland, May 7-9 2003. MOOG commercial paper.
- [21] A. Bonchis, P. I. Corke, and D. C. Rye. Experimental evaluation of position control methods for hydraulic systems. *IEEE Transactions on Control Systems Technology*, 10(6):876–882, 2002.
- [22] A. Bonchis, P. I. Corke, D. C. Rye, and Q. P. Ha. Variable structure methods in hydraulic servo systems control. *Automatica*, 37(4):589–595, 2001.
- [23] R. Book and C. Goering. MIMO adaptive control of a "smart" hydraulic system. *Smart Engineering System Design*, 3:15–27, 2001.
- [24] R. Book and C. E. Goering. Programmable electrohydraulic valve. In *SAE International Off-Highway and Powerplant Congress and Exposition*, 1999.

- [25] C. R. Burrows. Fluid power technology - progress or plateau? In *Proceedings of the Sixth International Conference on Fluid Power Transmission and Control*, Hangzhou, China, 2005. International Academic Publishers World Publishing Corporation.
- [26] H.-M. Chen, J.-C. Renn, and J.-P. Su. Sliding mode control with varying boundary layers for an electro-hydraulic position servo system. *International Journal of Advanced Manufacturing Technology*, 26(1-2):117–123, 2005.
- [27] H.-M. Chen, J.-P. Su, and J.-C. Renn. A novel sliding mode control of an electro-hydraulic position servo system. *IEICE Transactions on Fundamentals of Electronics, Communications and Computer Sciences*, Vol.E85-A Issue.8:1928–1936, 2002.
- [28] T.-L. Chern and Y.-C. Wu. An optimal variable structure control with integral compensation for electrohydraulic position servo systems. *IEEE Transactions on Industrial Electronics*, 39(5):460–463, 1992.
- [29] X. Dong and J. Whitaker. An innovative neutral valve for a light duty hydrostatic transmission. In *Proceedings of the 50th National Conference on Fluid Power*, pages 15–19, Las Vegas, March 16-18 2005.
- [30] J. Doyle, B. Francis, and A. Tannenbaum. *Feedback Control Theory*. Macmillan Publishing Co., 1990.
- [31] J. C. Doyle, K. Glover, P. P. Khargonekar, and B. A. Francis. State-space solutions to standard  $\mathcal{H}_2$  and  $\mathcal{H}_\infty$  control problems. *IEEE Transactions on Automatic Control*, 34(8):831–847, 1989.
- [32] K. A. Edge. The control of fluid power systems - responding to the challenges. *Proc. ImechE*, 211 part I:91–110, 1997.
- [33] K. A. Edge. On the control of electrohydraulic systems - some recent research contributions. In *The Eight Scadinavian international Conference on Fluid Power*, pages 31–59, Tampere Finland, May 7-9 2003.
- [34] M. Elfving and J.-O. Palmberg. Distributed control of fluid power actuators - decoupled chamber pressure controlled cylinder. In *Ninth Bath International Fluid Power Workshop*, Bath, UK, September 9-11 1996.
- [35] M. Elfving and J.-O. Palmberg. Distributed control of fluid power actuators - a load sensing application of a cylinder with decoupled chamber pressure control. In *Fifth Scandinavian International Conference on Fluid Power*, Linköping, Sweden, 1997.
- [36] M. Elfving, J.-O. Palmberg, and A. Jansson. Distributed control of fluid power actuators - experimental verification of a decoupled chamber pressure controlled cylinder. In *Fourth International Conference on Fluid Power Transmission and Control*, Hangzhou China, September 9-11 1997.



- [37] A. Ellman and R. Piché. A two regime flow formula for numerical simulation. *Transactions of the ASME, Journal of Dynamic Systems, Measurement, and Control*, 121(4):721–724, December 1999.
- [38] B. Eriksson and J. Wikander. Integrated linear hydraulic actuator - a force control approach. In *The Third Scandinavian International Conference on Fluid Power*, pages 71–90, Linköping Sweden, May 25-26 1993.
- [39] H.-J. Feigel. *Strömungskraftkompensation in direktgesteuerten elektrohydraulischen Stetigventile*. PhD thesis, RWTH Aachen, Aachen, Germany, June 1992.
- [40] R.-F. Fung and R.-T. Yang. Application of vsc in position control of a nonlinear electrohydraulic servo system. *Computers & Structures*, 66(4):365–372, 1998.
- [41] J. B. Gamble. Robust sliding mode control of hydraulic valves. *IEE Colloquium on Advances in the Application of Robust Controllers*, Digest No.1993/220:4/1–4, 1993.
- [42] A. Gelb and W. E. V. Velde. *Multiple-Input Describing Functions and Nonlinear Systems Design*. McGraw-Hill Electronic Science Series. McGraw-Hill Book Company, New York St. Louis, 1968.
- [43] M. A. Ghazy. Variable structure control for electrohydraulic position servo system. In *IECON '01: The 27th Annual Conference of the IEEE Industrial Electronics Society*, 2001.
- [44] H. M. Handroos and M. J. Vilenius. The utilization of experimental data in modelling hydraulic single stage pressure control valves. *Journal of Dynamic Systems, Measurements and Control*, 112(3):482–488, 1990.
- [45] M. R. Hansen, T. O. Andersen, and F. Conrad. Experimentally based analysis and synthesis of hydraulically actuated loader crane. In *Bath Power Transmission and Motion Control Conference*, Bath, UK, 2001.
- [46] S. Helduser and M. Djurovic. Control strategies for load sensing in mobile machinery. In *Proceedings of the Sixth International Conference on Fluid Power Transmission and Control*, Hangzhou, China, 2005. International Academic Publishers World Publishing Corporation.
- [47] H. Hu and Q. Zhang. Realization of programmable control using a set of individually controlled electrohydraulic valves. *International Journal of Fluid Power*, 3(2):29–34, 2002.
- [48] C. L. Hwang. Sliding mode control using time-varying switching gain and boundary layer for electrohydraulic position and differential pressure control. *IEE Proceedings - Control Theory and Applications*, 143(4):325–332, 1996.
- [49] A. Jansson, P. Krus, and J.-O. Palmberg. Decoupling of response and pressure level in a hydraulic actuator. In *The Fourth Bath International Fluid Power Workshop*, Bath, UK, September 18-20 1991.

- [50] A. Jansson and J.-O. Palmberg. Separate controls of meter-in and meter-out orifices in mobile hydraulic systems. In *International Off-Highway & Powerplant Congress and Exposition*, Milwaukee, Wisconsin, USA, September 10-13 1990.
- [51] H. K. Khalil. *Nonlinear Systems*. Prentice Hall, 2002.
- [52] M. G. Kliffken and G. Geerling. New developments and trends in hydraulics for mobile applications. In *The Eighth Scandinavian International Conference on Fluid Power*, Tampere, Finland, May 7-9 2003. Bosch-Rexroth commercial paper.
- [53] V. Kneppová and S. Kozák.  $\mathcal{H}_\infty$ -optimal position control of a hydraulic drive. In *Proceedings of 2nd IFAC Workshop on New Trends in Design of Control Systems 1997*, 1997.
- [54] C. Kolbe. Digital valves raise machine performance, not cost. On: [http: www.machinedesign.com](http://www.machinedesign.com), May 2005. Husco International Inc.
- [55] P. Krus, K. Weddfelt, and J.-O. Palmberg. Fast pipeline models for simulation of hydraulic systems. *Transactions of the ASME Journal of Dynamic Systems, Measurement and Control*, 116(1):132–136, 1994.
- [56] T. Lang and H.-H. Harms. Concepts of mechatronics and distributed intelligence in mobile hydraulics. In *The Eighth Scandinavian International Conference on Fluid Power*, Tampere, Finland, May 7-9 2003.
- [57] B. Lantto, A. Jansson, and J.-O. Palmberg. A new concept of computer controlled electrohydraulic system the p-q pump and valve control. In *Second Bath International Fluid Power Workshop*, Bath, UK, September 21-22 1989.
- [58] M. Lebrun. A model for a four-way spool valve applied to a pressure control system. *The Journal of Fluid Control*, 17(4):38–54, 1987.
- [59] X. Liang, T. Virvalo, and M. Linjama. The influence of control valves on the efficiency of a hydraulic crane. In *The Sixth Scandinavian International Conference On Fluid Power*, Tampere, Finland, 1999.
- [60] J. D. Linerode and A. M. Egelja. Implement pressure control for hydraulic circuit. US Patent US 6 691 603 B2, February 2004. Caterpillar Inc.
- [61] M. Linjama and T. Virvalo. Low-order dynamical model for flexible hydraulic cranes. *Proc. of the Institution of Mechanical Engineers, Part I*, 213, 1997.
- [62] M. Linjama and T. Virvalo. Modelling of flexible hydraulic crane. In *5th Scandinavian International Conference on Fluid Power*, Linköping, Sweden, 1997.
- [63] M. Linjama and T. Virvalo. State-space model for control design of multi-link flexible hydraulic cranes. In *6th Scandinavian International Conference on Fluid Power*, Tampere, Finland, 1999.
- [64] G. Linyi and W. Qingfeng. Research on noninterference control of multiple actuators load sensing system with high inertia in construction machinery. In *The Fifth International Conference on Fluid Power Transmission and Control*, Hangzhou China, April 3-5 2001.

- [65] Y. Liu and H. Handroos. Technical note sliding mode control for a class of hydraulic hydraulic position servo. *Mechatronics*, 9:111–123, 1999.
- [66] Y. Liu and H. Handroos. Sliding mode control implementation for a large scale manipulator with hydraulic servo systems. In *The Seventh Scandinavian International Conference on Fluid Power*, 2001.
- [67] S. V. Lunzmann, X. Huang, K. S. Shively, and B. J. Holt. Control for electrohydraulic valve arrangement. US Patent US 6 598 391 B2, July 2003. Caterpillar.
- [68] N. D. Manring. Modeling spool-valve flow forces. In *Proceedings of IMECE04, 2004 ASME International Mechanical Engineering Congress and Exposition*, volume 2, Anaheim, California USA, November 13-19 2004. ASME, ASME.
- [69] J. Mattila. *On Energy-efficient Motion Control of Hydraulic Manipulators*. PhD thesis, Tampere University of Technology, 2000.
- [70] H. Merritt. *Hydraulic Control Systems*. John Wiley and Sons, Inc, 1967.
- [71] A. Mikkola and H. M. Handroos. Modelling and simulation of a flexible hydraulically driven log crane. In *9th Bath International Fluid Power Workshop - Fluid Power Systems*, Bath, UK, 1996.
- [72] J. Mäkinen, A. Ellman, and R. Piché. Dynamic simulations of flexible hydraulic-driven multibody systems using finite strain theory. In *5th Scandinavian International Conference on Fluid Power*, Linköping, Sweden, 1997.
- [73] M. E. Münzer. *Resolved Motion Control of Mobile Hydraulic Cranes*. PhD thesis, Aalborg University, 2003.
- [74] B. R. Munson, D. F. Young, and T. H. Okiishi. *Fundamentals of Fluid Mechanics*. John Wiley and Sons, Inc., New York, third edition, 1998.
- [75] H. Murrenhoff. *Servohydraulik*. Shaker Verlag, 2002.
- [76] K. S. Nair. Dither - the mysterious killer of friction in fluid power valves. *The Basic Fluid Power Research Journal*, 15(1):35–42, 1982.
- [77] P. N. Nikiforuk, P. R. Ukrainetz, and S. Tsai. Detailed analysis of a two stage four-way electrohydraulic flow control valve. *Journal Mechanical Engineering Science*, 11(2):168–174, 1969.
- [78] H. Ortlepp. Future trends in the development of mobile equipment. In *The Eighth Scandinavian International Conference on Fluid Power*, Tampere, Finland, May 7-9 2003.
- [79] J. L. Pfaff. Distributed electrohydraulic systems for telehandlers. In *Proceedings of the 50th National Conference on Fluid Power*, pages 779–784, Las Vegas, March 16-18 2005. HUSCO Commercial paper.
- [80] R. Piché, S. Pohjolainen, and T. Virvalo. Design of robust controllers for position servos using h-infinity theory. *Proc. IMechE Part I: Journal of Systems and Control Engineering*, 205:299–306, 1991.

- [81] R. Piché, S. Pohjolainen, and T. Virvalo. Design of robust controllers for position servos using h-infinity theory. *Proc. IMechE Part I: Journal of Systems and Control Engineering*, 206:135–142, 1992.
- [82] B. G. Poorman. Control system for controlling the speed of a hydraulic motor. US Patent US 6 131 391, October 2000. Caterpillar Inc.
- [83] I. Postlethwaite, J.-L. Lin, and D.-W. Gu. A loop-shaping approach to robust performance for siso systems. *Transactions of the Institute of Measurement and Control*, 13(5):262–268, 1991.
- [84] W. Qingfeng, G. Linyi, and L. Yongxiang. Research on digital control of meter-in and meter-out independent regulating for high inertia load. *ASME Fluid Power Systems and Technology*, 6:109–114, 1999.
- [85] R. Rahmfeld and M. Ivantysynova. New displacement controlled linear actuator technology - a suitable control element for active oscillation damping. In *The Eighth Scandinavian International Conference on Fluid Power*, pages 1139–1154, Tampere, Finland, May 1-9 2003.
- [86] R. Rahmfeld, M. Ivantysynova, and J. Weber. Displacement controlled wheel loader - a simple and clever solution. In *4th International Fluid Power Conference Dresden Vol. 2*, pages 183–196, Dresden, Germany, March 2004.
- [87] J. L. Shearer. Digital simulation of a coulomb-damped hydraulic servosystem. *Transactions of the ASME, Journal of Dynamic Systems, Measurement, and Control*, 105(4):215–221, December 1983.
- [88] S. Skogestad and M. Morari. Some new properties of the structured singular value. *IEEE Transactions on Automatic Control*, 33(12):1151–1154, 1988.
- [89] S. Skogestad and I. Postlethwaite. *Multivariable Feedback Control Analysis and Design*. John Wiley & Sons, 1996.
- [90] J.-J. E. Slotine and W. Li. *Applied Nonlinear Control*. Prentice Hall, 1991.
- [91] H. L. Sørensen. *Fluidmekanisk design af hydrauliske sædeventiler*. Report no. iks 99.41.b, Institut for Konstruktions- og Styreteknik, DTU, 1999. (Danish).
- [92] D. B. Stephenson and J. L. Pfaff. Hydraulic circuit with a return line metering valve and method of operation. US Patent US 6 457 487 B1, October 2002. Husco International Inc.
- [93] T. Sugiyama and U. Kenko. Gain-scheduled velocity and force controllers for electrohydraulic servo system. *Electrical Engineering in Japan*, 146(3):65–73, 2004. Translated from Denki Gakkai Ronbunshi, Vol. 122-D, No. 11, November 2002, pp. 1051–1058.
- [94] T. Sugiyama and U. Kenko. Gain scheduling control for electrohydraulic servo system considering time-delay modelling error. In *Proceedings of the 2004 IEEE International Conference on Control Applications*, Taipei, Taiwan, September 2-4 2004.

- [95] K. A. Tabor. Velocity-based method for controlling an electrohydraulic proportional control valve. European patent application EP 1 403 524 A2, March 2004. Husco International Inc.
- [96] K. A. Tabor and J. L. Pfaff. Apparatus and method for providing vibration to an appendage of a work vehicle. European Patent Application EP 1 361 312 A1, November 2003. Husco International Inc.
- [97] K. A. Tabor and J. L. Pfaff. Method for preventing bounce oscillations of internal masses caused by accelerations in hydraulically powered equipment. European Patent Application EP 1 403 438 A1, March 2004. Husco International Inc.
- [98] K. A. Tabor and J. L. Pfaff. Method of selecting a hydraulic metering mode for a function of a velocity based control system. European Patent Application EP 1 403 526 A1, March 2004. Husco International Inc.
- [99] G. Tao and P. V. Kokotović. *Adaptive Control of Systems with Actuator and Sensor Nonlinearities*. John Wiley and Sons, 1996.
- [100] A. Taware and G. Tao. An adaptive dead-zone inverse controller for systems with sandwiched dead-zones. *International Journal of Control*, 76(8):755–769, 2003.
- [101] A. Taware, G. Tao, and C. Teolis. An adaptive dead-zone inverse controller for systems with sandwiched dead-zones. In *Proceedings of the American Control Conference*, pages 2456–2461, Arlington VA, June 25-27 2001.
- [102] R. J. Theodore and A. Ghosal. Modelling of flexible-link manipulators with prismatic joints. *IEEE Transactions on systems, man and cybernetics - Part B: Cybernetics*, 27(2):296–305, April 1997.
- [103] J. U. Thoma. *Modern Oilhydraulic Engineering*. Trade and Technical Press Ltd., 1970.
- [104] S. B. Turner and D. F. Lakin. Electrohydraulic proportional control valve assemblies. European patent EP 0 809 737 B1, June 1999 1997. Ultronics Limited.
- [105] J. Watton. *Fluid power systems: modelling, simulation, analog and microcomputer control*. Prentice Hall, New York, 1989.
- [106] E. Weishaupt and B. Völker. Energisparende elektrohydraulische schaltungskonzepte. *Ölhydraulik und Pneumatik*, 39(2):106–112, 1995.
- [107] D. Wu, R. Burton, and G. Schoenau. An empirical discharge coefficient model for orifice flow. *International Journal of Fluid Power*, 3(3), December 2002.
- [108] D. Wu, R. Burton, G. Schoenau, and D. Bitner. Modelling of orifice flow rate at very small openings. *International Journal of Fluid Power*, 4(1):31–39, April 2003.
- [109] B. Yao and C. DeBoer. Energy-saving adaptive robust motion control of single-rod hydraulic cylinders with programmable valves. In *Proceedings of the American Control Conference*, Anchorage AK, May 8-10 2002. IEEE.

- [110] B. Yao and S. Liu. Energy-saving control of hydraulic systems with novel programmable valves. In *Proceedings of the 4th World Congress on Intelligent Control and Automation*, Shanghai China, June 10-14 2002. IEEE.
- [111] L. Yongxiang. A systematic philosophy consideration on the fluid power driven and control technology. In *Proceedings of the Sixth International Conference on Fluid Power Transmission and Control*, Hangzhou, China, 2005. International Academic Publishers World Publishing Corporation.
- [112] K. D. Young and Ümit Özgüner. Frequency shaping compensator design for sliding mode. *International Journal of Control*, 57(5):1005–1019, 1993.
- [113] K. D. Young, V. I. Utkin, and Ümit Özgüner. A control engineer's guide to sliding mode control. *IEEE Transactions on Control Systems Technology*, 7(3):328–342, 1999.
- [114] M. K. Zavarehi, P. D. Lawrence, and F. Sassani. Nonlinear modeling and validation of solenoid-controlled pilot-operated servovalves. *IEEE/ASME Transactions on Mechatronics*, 4(3):324–334, September 1999.
- [115] B. Zähe, M. Eschweiler, and K. Herzog. Regelung hydraulischer antriebe mit veränderlichem versorgungsdruck. *Ölhydraulik und Pneumatik*, 35(9):717–723, 1991.
- [116] B. Zähe, R. Schmitz, and M. Eschweiler. Elektrohydraulisches loadsensing. *Ölhydraulik und Pneumatik*, 34(8):548–553, 1990.